DEVELOPMENT OF A JOINT FAULTING MODEL FOR UNBONDED CONCRETE OVERLAYS OF EXISITNG CONCRETE PAVEMENTS THROUGH A LABORATORY AND NUMERIC ANALYSIS

by

Steven G. Sachs

BS, University of Pittsburgh, 2012

Submitted to the Graduate Faculty of

Swanson School of Engineering in partial fulfillment

of the requirements for the degree of

Doctor of Philosophy

University of Pittsburgh

2016

UNIVERSITY OF PITTSBURGH

SWANSON SCHOOL OF ENGINEERING

This dissertation was presented

by

Steven G. Sachs

It was defended on

November 30, 2016

and approved by

John C. Brigham, PhD, Associate Professor, Department of Civil and Environmental Engineering, University of Pittsburgh

Lev Khazanovich, PhD, Professor, Department of Civil, Environmental, and Geo-Engineering, University of Minnesota

Mark J. Magalotti, PhD, Senior Lecturer, Department of Civil and Environmental Engineering, University of Pittsburgh

Luis E. Vallejo, PhD, Professor, Department of Civil and Environmental Engineering, University of Pittsburgh

Dissertation Director: Julie M. Vandenbossche, PhD, Associate Professor, Department of Civil and Environmental Engineering, University of Pittsburgh

DEVELOPMENT OF A JOINT FAULTING MODEL FOR UNBONDED CONCRETE OVERLAYS OF EXISITNG CONCRETE PAVEMENTS THROUGH A LABORATORY AND NUMERIC ANALYSIS

Steven G. Sachs, PhD

University of Pittsburgh, 2016

An unbonded concrete overlay of an existing concrete pavement (UBOL) is a Portland cement concrete (PCC) overlay separated from the existing concrete slab by an interlayer (Smith, Yu, and Peshkin, 2002). The purpose of the interlayer is to reduce stress transfer between the existing concrete layer and the overlay. Interlayers commonly consist of asphalt or nonwoven geotextile fabric. A laboratory investigation is used to characterize the behavior of interlayers within UBOLs. Beam specimens are tested to evaluate four different mechanisms. Both asphalt and nonwoven geotextile fabric interlayer systems are considered. The mechanisms considered are: 1) deflection characteristics of the interlayer, 2) friction developed along the interface between the interlayer and the overlay, 3) ability of the interlayer to prevent reflective cracking, and 4) bond strength at the interfaces of the interlayer (direct tension test). Each interlayer system considered will be described in this chapter followed by the test procedures for each of the four developed tests. The results, findings, and conclusions from each of the tests in the laboratory investigation are presented.

The structural model development for UBOL faulting is then discussed. This includes the choice of modeling software and convergence and validation checks. The modeling parameters to characterize the interlayer using data from the laboratory testing are also outlined. Also, the modeling parameters used for the factorial of finite element runs are outlined as well as

the critical response parameters which will be used in the faulting model. Finally, the development of neural networks to predict the critical responses will be described.

A developed mechanistic-empirical faulting model for UBOL is then presented. This includes the development of an improved erosion model, which is implemented into a series of equations used to predict joint faulting for UBOL. The handling of climatic factors as well as traffic will also be outlined within the calculation framework established. The calibration sections used to calibrate the faulting model will be presented followed by the results of the calibration of the model and the development of a reliability and standard deviation model. Finally, a sensitivity analysis of the model is conducted.

TABLE OF CONTENTS

LIST OF TABLES

LIST OF FIGURES

PREFACE

I would like to thank my advisor Professor Julie M. Vandenbossche for her educational and financial support through my PhD study. My thanks also to the other faculty members on my committee: Professors John C. Brigham, Lev Khazanovich, Mark J. Magalotti, and Luis E. Vallejo. I would also like to thank Mr. Charles C. Hager for his guidance and assistance with the laboratory investigation. I would also like to extend my appreciation to my fellow graduate and undergraduate students who have helped conduct the laboratory experiments, i.e. Mr. Kevin Alland, Mr. John DeSantis, Mr. Nathan Bech, Dr. Zichang Li, Mr. Alex Voutto, Mr. Scott Sachs, Ms. Veronica Boyce, Ms. Erica Reiser, Mr. Andrew Rogers, Mr. Alexander Melo de Sousa, and Mr. Aldo Ferreira Montenegro.

I would also like to acknowledge the assistance provided by Andrew Bennett, John Staton, and Benjamin Krom of the Michigan Department of Transportation, Thomas Burnham, Robert Strommen, and Jack Herndon at the MnROAD Research Facility, Derek Tompkins of the University of Minnesota, Rob Golish from the Minnesota Department of Transportation, the McCrossan Company, the Pennsylvania Department of Transportation District 11, and Golden Triangle Construction. Additionally, the supply of the nonwoven geotextile fabrics and technical expertise provided by Eric Littel from Propex is also greatly appreciated.

Finally, I would like to thank my parents and brother for their love and support.

1.0 INTRODUCTION

An unbonded concrete overlay of an existing concrete pavement (UBOL) is a Portland cement concrete (PCC) overlay separated from the existing concrete slab by an interlayer (Smith, Yu, and Peshkin, 2002). The purpose of the interlayer is to reduce stress transfer between the existing concrete layer and the overlay. Interlayers commonly consist of asphalt or nonwoven geotextile fabric. UBOL systems are becoming an increasingly popular pavement rehabilitation technique. This is due to the fact that they are durable, mitigate reflective cracking, require minimal pre-overlay repairs and preparation, and can be placed with traditional concrete pavement paving methods. Additionally, unbonded overlays have performed very well over the last 30 years (Harrington, Degraaf, and Riley, 2007).

The interlayer is a critical component of the UBOL structure. The interlayer acts as a shear plane by inhibiting the mechanical bonding between the two pavement structures, which allows the two slabs to move independently of one another (Harrington, Degraaf, and Riley, 2007). The interlayer should be designed such that it meets the following criteria: 1. separate the overlay from the existing concrete slab to prevent reflective cracking, 2. maintain a sufficient amount of bond and friction so the joints form in the overlay, 3. provide uniform support for the overlay, 4. act as a leveling course where necessary, and 5. be cost effective (ERES, 1999).

The asphalt interlayer can be newly placed or an existing aged layer and is typically 1 to 4 in (ERES, 1999). If the existing PCC pavement was previously overlaid with asphalt to create a composite pavement, surface defects in the existing asphalt can be removed through milling. Milling will also act to increase the bond between the interlayer and the overlay PCC. In addition to dense graded asphalt, open graded asphalt courses have been used in order to improve drainage characteristics of the interlayer and prevent pressure buildup. Recently, nonwoven geotextile fabrics have become a popular alternative as an interlayer in these structures. The use of fabrics is an adaptation of the German application of using fabrics to separate newly constructed PCC pavements from cement stabilized bases (Rasmussen and Garber, 2009). The potential cost savings as well as the ease and quick installation of nonwoven geotextiles have made this type of interlayer an attractive alternative.

1.1 BACKGROUND AND PROBLEM STATEMENT

Joint faulting in traditional JPCP is the change in elevation between the approach and leave sides of a transverse joint (perpendicular to the direction of vehicle travel) as a result of pumping of material beneath the PCC slab. Figure 1.1 demonstrates the pumping mechanism. The pumping mechanism requires four components: 1) water, 2) unstabilized fines, 3) differential deflections between the approach and leave slab, and 4) traffic loading. As a wheel load approaches a joint, the approach slab deflects downward resulting in the movement of water from beneath the approach slab to underneath the leave slab. As the wheel load moves across the joint onto the leave slab, the approach slab rebounds upward and the leave slab is forced downward. This results in a pushing of water and fines from beneath the leave slab to the approach slab. With repeated traffic loadings over time, this results in the accumulation of a wedge of injected fines beneath the approach slab and a void beneath the leave slab creating the fault.

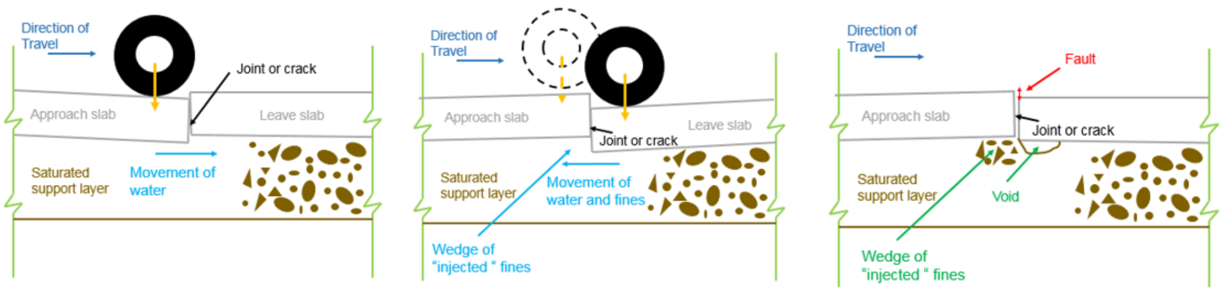

Figure 1.1. Pumping mechanism beneath PCC pavements (Van Wijk, 1985)

Current faulting design procedures, such as that incorporated into Pavement ME (ARA, 2004), were developed considering only Jointed Plain Concrete Pavements (JPCP). It is possible to use the current design software to predict joint faulting for UBOL, but the procedure is directly adapted from that used to predict joint faulting for JPCP. This procedure is not able to account for the characteristics of the interlayer itself on the performance prediction of joint faulting in the overlay of an UBOL. More importantly, the interaction between the interlayer and the two PCC layers is not directly considered, as will be outlined in more detail below. A description of just a few of the limitations in the ability of Pavement ME to predict faulting in UBOL is presented below. For the purposes of the problem formulation, only asphalt interlayers will be directly considered.

In the current model used to predict faulting, a large factorial of finite element runs were generated to predict critical corner deflections using the finite element software ISLAB (Khazanovich et al, 2000). These finite element runs were then used to train neural networks to predict the critical deflections for any scenario within the factorial of parameters, which can be found in ARA (2004). A number of equivalency concepts were employed to simplify the analysis, which include equivalent thickness, equivalent temperature gradient and equivalent slab. The equivalent slab was employed to combine the effects of the PCC layer and the base to simplify the analysis. While this may be appropriate for JPCP, the breakdown of a UBOL structure using the equivalent slab procedure is not applicable. If an asphalt interlayer is used to separate the PCC overlay from the existing PCC pavement, then the model simplifications shown in Figure 1.2 are made. Note that the separator layer is considered the base for all structural and non-structural analyses and that the existing concrete layer is then combined with all other layers beneath the existing PCC slab to create an effective modulus of subgrade reaction. Also of note is that if no interlayer is used between the PCC layers, then the existing PCC pavement will be used as the base layer. In combining the PCC overlay and the interlayer base, the layers are assumed to be unbonded to create a new effective thickness, which has the same stiffness and Poisson's ratio as the overlay PCC. This over simplification of a UBOL structure is not appropriate to capture the mechanics of the complex sandwich of layers in which the faulting will develop. Therefore, a new structural model must be employed to mimic the behavior of an UBOL more closely.

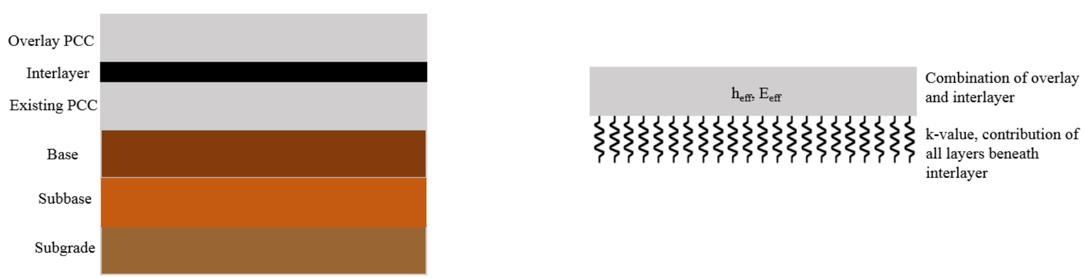

Figure 1.2. Pavement ME UBOL structural model

The erodibility index is also not appropriate for use in the design process for UBOL. Currently, there is only a numeric value between 1 and 5, referred to as the erodibility index, which is used to establish the erosion potential of a base material (in the case of UBOL, the interlayer). This classification was based upon the recommendation of the Permanent International Association of Road Congresses (PIARC). The recommendations in the Pavement ME design guide are shown in Table 1.1 below (adapted from Christory (1990) and PIARC (1987)). With these values, the erodibility ratio between two classes is about 5, such that materials with an index of 1 are five times more erosion resistant than materials with an index of 2 (ARA, 2004). The design guide acknowledges that results from laboratory testing and material test results should be used to represent the erodibility of material beneath the PCC slab but were not developed to the point for inclusion into the design guide. ARA (2004) mentions the following tests which are being used to assess the erodibility of paving materials: rotational shear device for cohesive and stabilized materials, jetting test (Bhatti et al, 1996), linear and rotational brush tests (Dempsey, 1982), and the South African erosion test (De Beer, 1990).

Since the interlayers used are typically asphalt, there is currently no definitive way to distinguish between asphalt layers, other than binder content, for UBOL. If an asphalt is used as the interlayer and meets stripping requirements, then the erodibility index will be 1, as defined in Table 1.1. This is because all asphalt interlayers will meet either criteria b or c in Table 1.1 for an erodibility index of 1. Therefore, at this time there is no way to distinguish between the erodibility of asphalt interlayers in UBOL. This limitation must be addressed in the development of a faulting model to be used specifically for UBOL, by characterizing the erosion potential of the interlayer materials using a more mechanistic approach. This leads to a more fundamental issue in that currently there is no way to deal with degradation of the interlayer material with time. As the initiation of pumping and erosion of the interlayer begins, the damage of the interlayer material must also be quantified for UBOL.

Table 1.1. Erodibility index recommendations (ARA, 2004)

Erodibility Index	Material Description and Testing
1	(a) Lean concrete with approximately 8 percent cement; or with long-term compressive strength > 2,500 psi (>2,000 psi at 28-days) and a granular subbase layer or a stabilized soil layer, or a geotextile fabric is placed between the treated base and subgrade, otherwise class 2. (b) Hot mixed asphalt concrete with 6 percent asphalt cement that passes appropriate stripping tests and aggregate tests and a granular subbase layer or a stabilized soil layer (otherwise class 2). (c) Permeable drainage layer (asphalt treated aggregate or cement treated aggregate and with an appropriate granular or geotextile separation layer placed between the treated permeable base and subgrade.
2	(a) Cement treated granular material with 5 percent cement manufactured in plant, or long-term compressive strength 2,000 to 2,500 psi (1,500 to 2,000 psi at 28-days) and a granular subbase layer or a stabilized soil layer, or a geotextile fabric is placed between the treated base and subgrade; otherwise class 3. (b) Asphalt treated granular material with 4 percent asphalt cement that passes appropriate stripping test and a granular subbase layer or a treated soil layer or a geotextile fabric is placed between the treated base and subgrade; otherwise class 3.
3	(a) Cement-treated granular material with 3.5 percent cement manufactured in plant, or with long-term compressive strength 1,000 to 2,000 psi (750 psi to 1,500 at 28-days). (b) Asphalt treated granular material with 3 percent asphalt cement that passes appropriate stripping test.
4	Unbound crushed granular material having dense gradation and high quality aggregates.
5	Untreated soils (PCC slab placed on prepared/compacted subgrade)

The above limitations of the current faulting framework in Pavement ME must be addressed in an improved faulting model for UBOL. Currently, it is not possible to select the optimum overlay system based on the contribution of the interlayer to improved performance of the concrete overlay. There is a need to characterize the performance of interlayer systems and the impact it has on the performance of UBOL. The characterization of interlayer systems combined with field data analysis will be used to develop an improved method for predicting the development of faulting in UBOL.

1.2 RESEARCH OBJECTIVE AND OUTLINE

The primary objective of this study is to develop a mechanistic-empirical model for faulting in UBOLs. In order to accomplish this task, a joint laboratory and numeric investigation is performed. A laboratory investigation is employed to provide a greater understating of interlayer behavior within an UBOL. A framework for the faulting model is then developed. The mechanistic-empirical framework considers the improved understanding of UBOL structures from the laboratory investigation in conjunction with field performance data.

. Chapter 2 introduces laboratory tests used to characterize the behavior of interlayers within UBOLs. Beam specimens are tested to evaluate four different mechanisms. Both asphalt and nonwoven geotextile fabric interlayer systems are considered. The mechanisms considered are: 1) deflection characteristics of the interlayer, 2) friction developed along the interface between the interlayer and the overlay, 3) ability of the interlayer to prevent reflective cracking, and 4) bond strength at the interfaces of the interlayer (direct tension test). Each interlayer system considered will be described in this chapter followed by the test procedures for each of the four developed tests. Chapter 3 will present the results, findings, and conclusions from each of the tests in the laboratory investigation.

Chapter 4 covers the structural model development for UBOL faulting. This includes the choice of modeling software and convergence and validation checks. The modeling parameters to characterize the interlayer using data from the laboratory testing are also outlined. Also, the modeling parameters used for the factorial of finite element runs are outlined as well as the critical response parameters which will be used in the faulting model. Finally, the development of neural networks to predict the critical responses will be described.

Chapter 5 details the development of the mechanistic-empirical faulting model for UBOL. This includes the development of an improved erosion model, which is implemented into a series of equations used to predict joint faulting for UBOL. The handling of climatic factors as well as traffic will also be outlined within the calculation framework established. The calibration sections used to calibrate the faulting model are presented followed by the results of the calibration of the model and the development of a reliability and standard deviation model. Finally, a sensitivity analysis is presented.

In the final chapter, all the findings from this study are summarized and recommendations for future research are made.

2.0 DEVELOPMENT OF LABORATORY TEST PROCEDURES FOR CHARACTERIZATION OF INTERLAYER BEHAVIOR OF UBOL

2.1 INTRODUCTION

In this study, a laboratory investigation is employed to examine the effects of the interlayer on the response of the pavement structure under load. Four different mechanisms are investigated. Both asphalt and nonwoven geotextile fabric interlayer systems are considered. The objective of this study is to establish parameters for these interlayers that can be used to develop structural models, which, in turn can is used in the development of a mechanistic-empirical design procedure for UBOL.

Four mechanisms are investigated using four separate test setups. The mechanisms considered are:

1. Deflection characteristics of the interlayer
2. Friction developed along the interface between the interlayer and the overlay
3. Ability of the interlayer to prevent reflective cracking
4. Bond strength at the interfaces of the interlayer

The specimens for evaluating mechanisms 1 through 3 consist of an overlay beam cast on top of the interlayer and existing concrete beam representing the UBOL pavement structure, as shown in Figure 2.1. The depth and width of both the overlay and the existing beams are 6 in.

Later in this chapter is will be discussed how the width, depth, and length of the UBOL beam specimens are established. The measured deflection characteristics and interface friction are used to establish stiffness and shear transfer for validating the structural models. The results from mechanism 3 testing are used to assess the potential for reflective cracking and, if necessary, to develop a reflective cracking model. Each interlayer system considered is outlined below followed by the test procedures for each of the four tests developed.

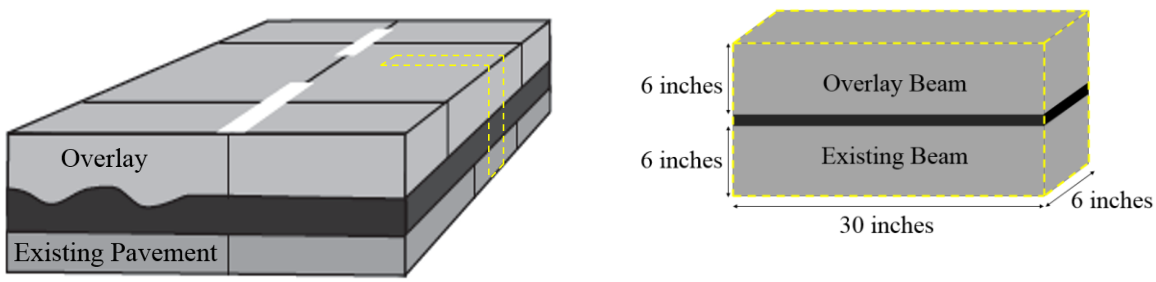

a. In-service pavement　　　　b. UBOL specimen

Figure 2.1. Replicating the UBOL in the laboratory

2.2 INTERLAYER SYSTEMS

Both nonwoven geotextile fabric and asphalt interlayers are considered in the laboratory testing. Two different weight fabrics from Propex are used along with dense and open graded asphalts retrieved from in-service pavements across the country.

2.2.1 Nonwoven Geotextile Fabric Interlayers

The nonwoven geotextile fabrics used for this study were manufactured by Propex and consisted of a dense (thicker) and a less dense (thinner) fabric. The thicker fabric (F15) is sold under the brand Propex and weighs 15 oz/yd^2. It is bleached white to minimize temperature rise due to solar radiation during construction. The thinner fabric (F10) was made specifically for this study and weighs 10 oz/yd^2. It was not bleached and is black. These fabrics can be seen in Figure 2.2. When comparing the 15 oz/yd^2 fabric to the 10 oz/yd^2, it is possible that the less dense fabric (10 oz) may allow for greater mortar penetration. However, there is also less thickness available to allow for mortar penetration. Therefore, these two factors may act to confound one another.

The fabric should have sufficient thickness to absorb the differential deflections between the loaded side of a crack/joint in the existing pavement and the unloaded side as a wheel traverses across the joint/crack. Otherwise stress concentrations will develop at the bottom of the overlay in the vicinity of the joint/crack and the crack will propagate up into the overlay. The selection of the fabric thickness must not only consider the magnitude of the differential deflections across the joint/crack but also the overlay thickness. A thicker overlay on a thin fabric may compress the fabric to the point that there is insufficient cushioning for the interlayer to absorb the differential deflections in the existing slab. Likewise, a thicker fabric with a thinner PCC overlay may not have sufficient weight to compress the fabric, which would result in high deflections in the overlay and therefore higher fatigue stresses.

a) 15 oz/yd^2 fabric (F15)

b) 10 oz/yd^2 fabric (F10)

Figure 2.2. Nonwoven geotextile fabrics used in this study

Beams simulating the existing concrete pavement were cast using the mixture design designated as Mixture 1 in Table 2.1. The concrete mix for the lower beam of the specimens with the fabric interlayer has a water to cementitious material ratio (w/cm) of 0.36 with a target flexural strength of approximately 850 psi. The fabrics are then attached to the existing concrete beams with a geotextile glue manufactured by 3M and sold under the brand name Scotch-Weld HoldFast 70 Adhesive. Historically, the geotextile fabric is pinned with metal fasteners to the existing concrete but the use of a geotextile adhesive is becoming more common. The adhesive helps to avoid damage to the existing beam. Also, the use of the adhesive eliminates any effects in the performance due to the location and spacing of the fasteners. Once the fabric was attached, concrete beams simulating the overlay were cast on top of the fabric. The mixture design, designated Mixture 2 in Table 2.1, was used for casting the overlay beam for all specimens. Mixture 2 has a w/cm of 0.42 and a target flexural strength of 650 psi and a target slump of 1 to 3 in. Concrete having a higher target strength was used for casting the overlay beams to simulate the effect of age on long-term strength gain that would occur in existing in-service pavement.

A 30-in beam, a 24-in modulus of rupture beam, and 2 to 3 4-in by 8-in cylinders were cast from each batch of concrete. Therefore, each beam had a measure of flexural strength, elastic modulus, and compressive strength. All specimens were cured according to ASTM C192.

Table 2.1. Target mixture designs for casting the UBOL specimens

<table>
<tr><th colspan="4">Mixture 1 for Casting Beams Representative of the Existing Slab</th></tr>
<tr><td>Material</td><td>Weight (lb/cy)</td><td>Volume (cft/cy)</td><td>Volume fraction</td></tr>
<tr><td>Coarse aggregate</td><td>1918</td><td>11.34</td><td>0.42</td></tr>
<tr><td>Fine aggregate</td><td>1163</td><td>6.98</td><td>0.26</td></tr>
<tr><td>Cement</td><td>650</td><td>3.31</td><td>0.12</td></tr>
<tr><td>Water</td><td>234</td><td>3.75</td><td>0.14</td></tr>
<tr><td>Air content (6%)</td><td>-</td><td>1.62</td><td>0.06</td></tr>
<tr><td>Superplasticizer, Sikament SPMN</td><td colspan="3">17 oz per100 lbs of cement</td></tr>
<tr><td>Air entrainer, Sika AIR-360</td><td colspan="3">3 oz per100 lbs of cement</td></tr>
<tr><th colspan="4">Mixture 2 for Casting Beams Representative of the Overlay</th></tr>
<tr><td>Material</td><td>Weight (lb/cy)</td><td>Volume (cft/cy)</td><td>Volume fraction</td></tr>
<tr><td>Coarse aggregate</td><td>2053</td><td>12.15</td><td>0.45</td></tr>
<tr><td>Fine aggregate</td><td>1023</td><td>6.14</td><td>0.23</td></tr>
<tr><td>Cement</td><td>600</td><td>3.05</td><td>0.11</td></tr>
<tr><td>Water</td><td>252</td><td>4.04</td><td>0.15</td></tr>
<tr><td>Air content (6%)</td><td>-</td><td>1.62</td><td>0.06</td></tr>
<tr><td>Air entrainer, Sika AIR-360</td><td colspan="3">2 oz per100 lbs of cement</td></tr>
</table>

2.2.2 Asphalt Interlayers

The beam representing the existing pavement and interlayer for the asphalt UBOL specimens were sawn as asphalt-PCC composite beams from in-service pavements. This ensures the mixture proportioning, density, particle orientation, and aging of the asphalt interlayers are typical of those found in the field. The asphalt-PCC composite beams were obtained from the

Minnesota Department of Transportation (MnDOT), Michigan Department of Transportation (MDOT), and the Pennsylvania Department of Transportation (PennDOT).

MDOT provided asphalt-PCC composite beams consisting of the overlay and the bonded asphalt interlayer from in service UBOLs. Full-depth concrete repairs were being performed and the asphalt interlayer was still bonded to the PCC overlay when the area to be repaired was cut and removed from the in-service pavement. The PCC portion of the beam served as the existing beam on the bottom of the UBOL specimens. The fact that this PCC might not have the exact same strength as that for Mixture 2 used for construction the UBOL specimens with the fabric interlayer is not consequential, since only the strength of the overlay beam has a substantial influence on the potential for reflective cracking. Specimens were cut from two separate in-service pavements. One had a dense graded asphalt interlayer, and with the other an open graded asphalt interlayer. The dense graded asphalt interlayer is approximately 1-in thick and the open graded asphalt interlayer is approximately 2 in thick.

MnDOT provided specimens cut from a concrete pavement that had previously been overlaid with asphalt. Some of the beams were cut prior to milling the aged, dense graded asphalt overlay and the others were cut after the asphalt was milled. They also provided beams cut immediately after an open graded asphalt was placed a distressed PCC pavement, prior to the placement of an unbonded concrete overlay. All of the asphalt interlayers from had been in-service for several years prior to being collected for the laboratory study with the exception of the open graded interlayer from Minnesota and the dense graded asphalt from Pennsylvania.

A summary of the sources of the UBOL specimens is provided in Table 2.2. Once the beams were brought to the laboratory, each specimen had to be cut to the desired dimensions using a wet saw to ensure that the exact dimensions desired were achieved. For each of the beam specimens, sand patch testing (ASTM E 965) was performed to characterize the surface roughness and dimensions were measured. The overlay was cast on top of the asphalt in the same manner as the fabric specimens using Mixture 2 from Table 2.1.

Table 2.2. Description of the UBOL specimens tested

UBOL Specimen	Overlay Beam	Existing Beam	Interlayer	Ave. Asphalt Thickness	Roadway
F15	Mixture 2	Mixture 1	15 oz/yd^2 fabric	-	-
F10	Mixture 2	Mixture 1	10 oz/yd^2 fabric	-	-
MIDAU	Mixture 2	JPCP (15 yrs old)	Dense graded, aged, unmilled (15 yrs old)	1 in	US-131 Rockford, MI
MIOAU	Mixture 2	JPCP (11 yrs old)	Open graded, aged, unmilled (11 yrs old)	2 in	US-131 Kalamazoo, MI
MNDAM	Mixture 2	JPCP (5 yrs old)	Dense graded, aged, milled (5 yrs old)	0.875 in	I-94, Albertville, MN (MnROAD)
MNDAU	Mixture 2	JPCP (5 yrs old)	Dense graded, aged, unmilled (5 yrs old)	2.75 in	I-94, Albertville, MN (MnROAD)
MNONU	Mixture 2	JRCP (≈ 26 yrs old)	Open graded, new, unmilled (≈1 week)	1.75 in	US-169, MN
PADNU	Mixture 2	JRCP (40 yrs old)	Dense graded, new, unmilled (≈1 week)	1 in	SR 50, PA

2.3 DEFLECTION CHARATERISTICS TEST SETUP

The deflection characteristics of the interlayer were established using the setup shown in Figure 2.3. The composite section consists of a beam representing the existing slab (in strength and stiffness), the interlayer system, and a beam representing the overlay (in strength and stiffness). A load is applied to one side of a joint sawed in the overlay and deflections in the overlay and existing beams are measured by linear variable displacement transducers (LVDTs). A discussion of the finite element modeling performed to insure the beam test is representative of the response (deflection and rotation) of the pavement structure is provided. This is followed by a discussion of the specimen preparation, hardware used in the setup, and the test procedure.

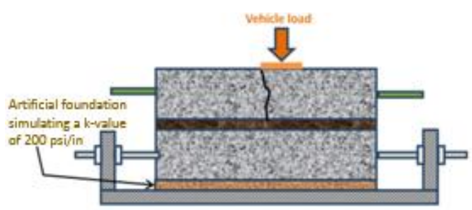

a.

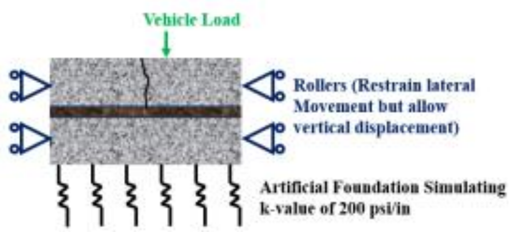

b.

Figure 2.3. (a) Schematic and (b) boundary conditions of deflection characteristics test setup

2.3.1 Beam Size, Load Location and Magnitude

In order to establish and confirm an appropriate setup and boundary conditions for the specimens, a finite element analysis was employed through the commercially available software ABAQUS™. The goal of the modeling is to establish the specimen length, boundary conditions, and load magnitude and location required to create deflections and rotations representative of those in an overlay loaded by a 9,000 lb design load.

In the computational model, all components were assumed to be elastic solids, no load transfer was provided across the joint. Tthe three contact conditions between the layers assumed included: 1, fully bonded, 2. unbonded, and 3. an intermediate level of bond where some shear transfer is allowed. The contact for both interfaces at the interlayer was modified such that every reasonable permutation of contact conditions at the interfaces was considered. For simplicity, however, the final model used assumed fully bonded conditions at both interfaces.

For the concrete, an elastic modulus of 4 million psi with a Poisson's ratio of 0.18 was assumed for the overlay concrete, while a stiffness of 4.5 million was assumed for the existing concrete to simulate an older concrete layer. The asphalt stiffness was defined as 750,000 psi with a Poisson's ratio of 0.35, while the fabric stiffness was defined as 1,000 psi.

Before any analyses were conducted, it was determined that rods would be cast into the ends of the beams so they could be connected to the testing frame to provide restraint in the transverse directions. This restraint helps the short beam respond in a more similar nature to a longer slab. At the start of modelling, a few preliminary analyses were conducted to determine how to restrain the beam specimen so that it remained in contact with the support layer when a dynamic load was applied. It was eventually determined that bearings needed to be placed through the overlay beam when testing for deflection characteristics. Also, a roller bearing was applied to create a pinned condition for facilitating rotation. The location for this was chosen as 3.5 in from the end of the beam on both sides, as shown in Figure 2.4.

Both the overlay and existing beam were chosen to be 6 in wide and 6 in deep. Next, the required length of the beam was established through a finite element analysis. Three lengths were considered: 24 in, 30 in, and 36 in. Since a modulus of rupture beam is 24 in long, this was chosen as the minimum value. Due to the considerable depth (slightly over one foot since the depth of both the overlay and existing are 6 in) of the two beam high structure, it was thought that the length of the overlay specimen should be increased to maintain a length to height ratio similar to a modulus of rupture beam. However, the length should remain as short as possible due to the significant increase in the weight of the stacked beam structure that would have to be moved on and off of the testing frame for each test. Neglecting the interlayer, the specimens would weight approximately 150 and 225 lbs for the 24-and 36-in long specimens, respectively. All three beam lengths (24, 30, and 36 in) were considered in the finite element analyses, and it was found that the beam had to be at least 30 in long to maintain deflection and rotation characteristics similar to those of a slab. Therefore, it was decided to make each overlay specimen 30 in long.

Finally, the load location and magnitude is established to mimic the deflections and rotations of the slab as closely as possible with the beam model. Static analyses are carried out with the beam and slab models shown in Figure 2.4 and Figure 2.5, respectively. A 9-kip FWD load is applied in the outside wheelpath to the slab model, which consisted of two 6-in thick 15-ft by 12-ft overlay slabs, the interlayer, and a continuous existing concrete slab. The asphalt interlayer is 1-in thick and the fabric interlayer is 0.125-in thick. No load transfer is applied across the joint in either model. A foundation stiffness of 200 psi/in was used in both models. A line load is applied to the beam model, where the location and the load magnitude are varied. Through trial and error, the location that most closely represented the slab model deflection and slope was 4.5 in from the overlay joint. Both the fabric and asphalt interlayers were considered.

The load magnitudes which produced the most similar results are summarized in Table 2.3. Based upon the analysis results, the load to be applied to the beam is chosen as 600 lbs.

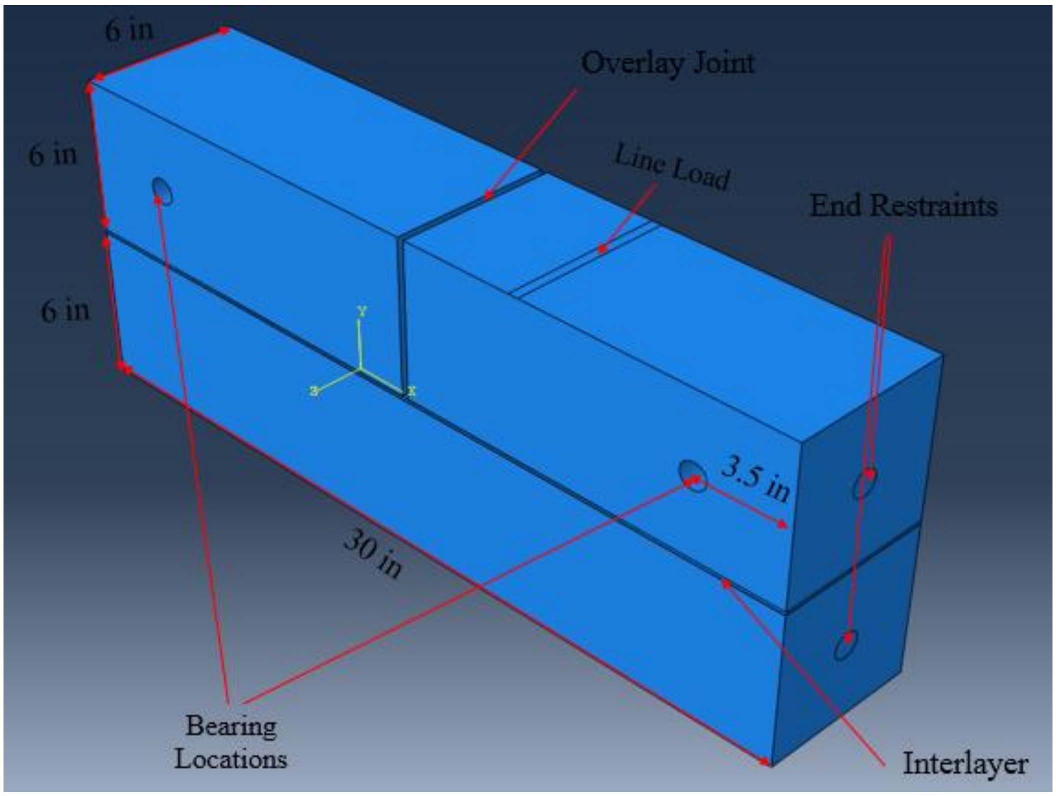

Figure 2.4. Beam finite element model

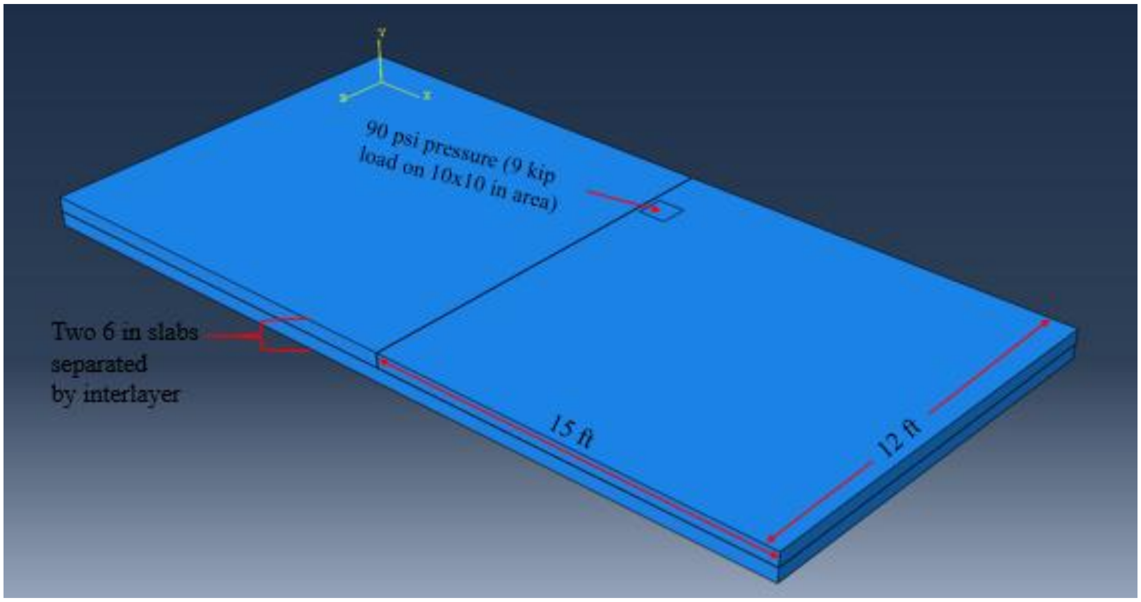

Figure 2.5. Slab finite element model

Table 2.3. Comparison of slab and beam finite element models

Slab Model				
Slab Load (lbs)	Interlayer	Max Deflection (in)	Loaded Slope (in/in)	Unloaded Slope (in/in)
9000	Asphalt	3.32E-03	3.63E-05	3.56E-05
9000	Fabric	3.50E-03	3.79E-05	3.74E-05
Beam Model				
Beam Equivalent Load (lbs)	Interlayer	Max Deflection (in)	Loaded Slope (in/in)	Unloaded Slope (in/in)
640	Asphalt	3.34E-03	3.80E-05	3.74E-05
580	Fabric	3.52E-03	4.03E-05	3.60E-05

2.3.2 Specimen Preparation

A discussion on the steps taken to fabricate the beam specimens is provided in this section. The fabric and asphalt beams are discussed separately and include all prep work, the forms used, the casting procedure and other pertinent information. Existing 6-in by 6-in by 30-in beams are cast using Mixture 1 from Table 2.1. The beam molds for the existing beams can be seen in Figure 2.6. Molds were constructed from plywood with ¾ in Schedule 40 PVC embedded in the concrete at 3.5 in from the ends and at mid-depth in the overlay of the 30-in long beams. End rods were also embedded into the concrete at a depth of approximately 2 in. Each beam is cast in a separate 1.5 ft^3 batch of concrete after the mixer has been buttered with a 0.5 ft^3 batch. This allows for one 30-in beam, one 24-in modulus of rupture beam, and 2 to 3 4-in by 8-in cylinders. Three beams are cast at a time. The air is measured for the first batch and slump is measured for every batch, which can be seen in Figure 2.7. Specimens were then rodded, finished, and cured according to ASTM C 192.

The fabrics are then attached to the existing concrete beams with a geotextile glue manufactured by 3M and sold under the brand name Scotch-Weld HoldFast 70 Adhesive. The surface of the existing concrete beam was completely covered with glue using a paint roller just prior to casting the overlay. Overlay molds were then attached to the existing concrete beams, as shown in Figure 2.8. The molds are placed such that the depth of the overlay will be 6 in. The PVC and end rods are placed in the same manner as the existing beams. The same casting procedure carried out with the exiting beams is used except that Mixture 2 from Table 2.1 is used for the overlay concrete. Once the specimens have cured for the requisite time, they are removed from the cure room and a 1/8-in wide joint is sawed into the overlay at mid length (15 in from either end) with a wet saw. The joint is sawed as close to as possible through the overlay beam but being sure not to saw into the interlayer.

Figure 2.6. Existing beam molds

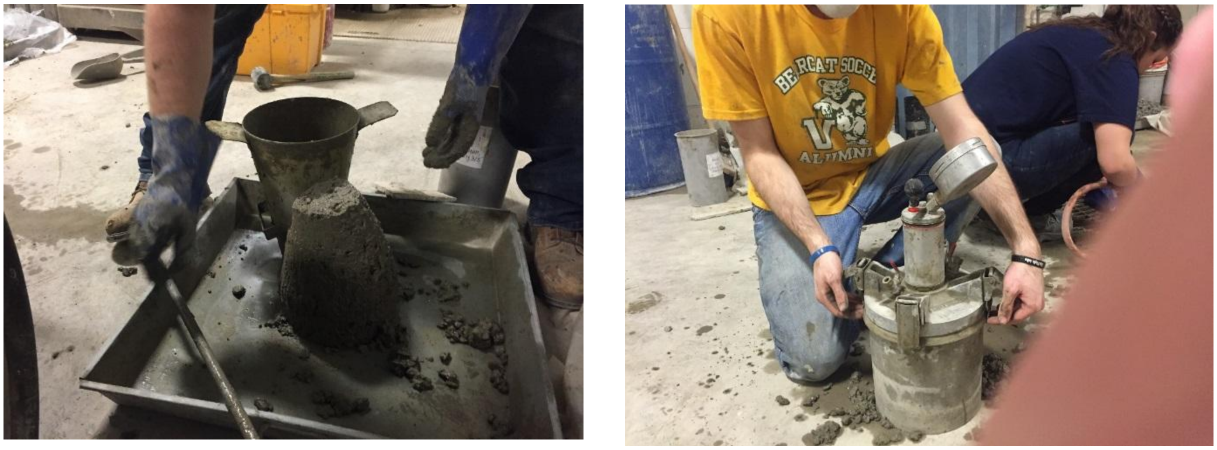

Figure 2.7. Slump and air meter testing

Figure 2.8. Overlay molds

Asphalt interlayer specimens are first sawed such that the concrete is as close to 6 in by 6 in by 30 in in size as possible. The surface of the asphalt is then cleaned with a brush and compressed air to remove any debris and slurry from the surface. Then, the dimensions are recorded as there is slight variability between specimens. Sand patch testing is then measured according to ASTM E 965 at three locations on each asphalt beam. The overlay molds are then placed, as shown above in Figure 2.8, in the same manner as the fabric specimens. Casting the overlay beams for the asphalt specimens is identical to that used for the fabric specimens. Three specimens are cast per day using Mixture 2 from Table 2.1. All specimens are then cured according to ASTM C 192. The same joint sawing procedure is also employed.

2.3.3 Components of Test Setup

Figure 2.9 shows a specimen in the testing frame for Mechanism 1. The loading head contains a ball joint and is part of the same loading head used for testing the modulus of rupture beams. As discussed in Section 1.3.2, the location of the load is 4.5 in from the overlay joint. The foundation support provided by the lower layers under the concrete slab in an in-service pavement was replicated by an artificial foundation of two layers of neoprene pads, known as Fabcel 25 (http://www.fabreeka.com/Products &productId=24). Figure 2.10 shows the Fabcel 25 waffle-shaped neoprene pads. The stiffness of the two combined Fabcel layers was determined by conducting a plate load test (ASTM D1195/D1195M), and was found to be 200 psi/in.

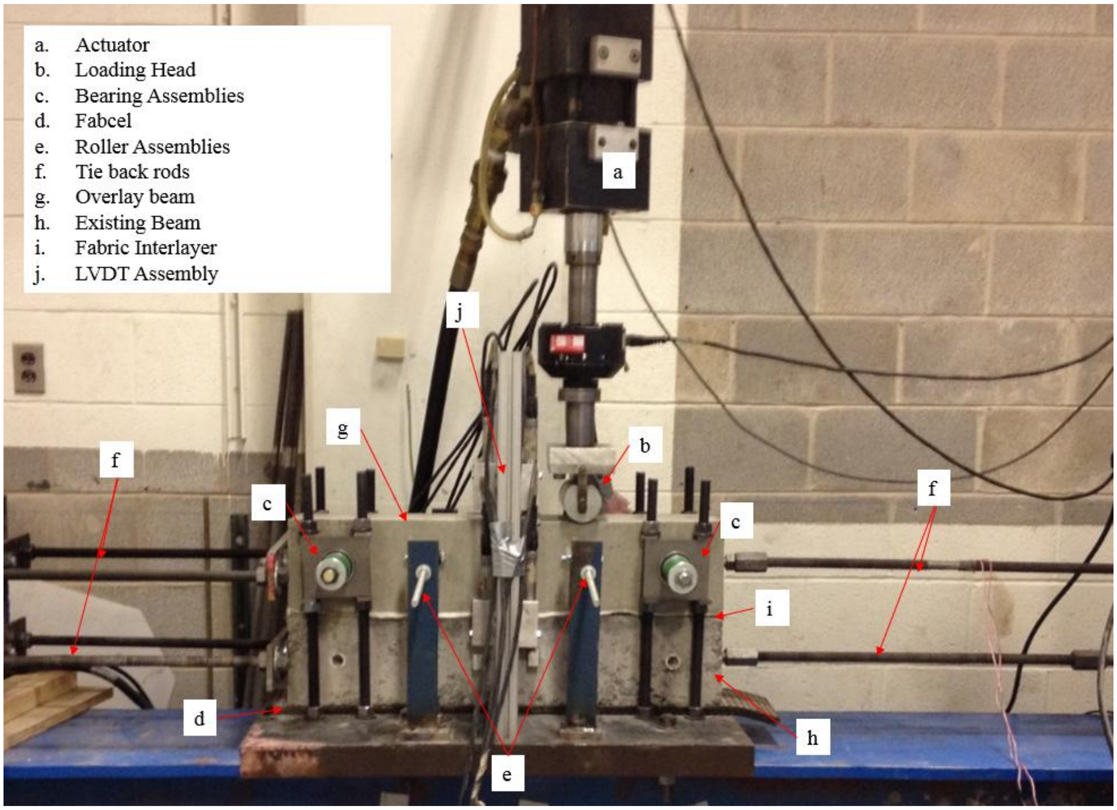

Figure 2.9. Deflection characteristics test setup

Figure 2.10. Neoprene Fabcel 25

The bearing assembly used to initiate points of rotation can be seen in Figure 2.11. The location of the bearings is 3.5 in from each end of the beam where the PVC was cast into the concrete. The collars provide a fixed point of rotation so that no moment is transferred to the beam from the restraint. Roller bearings are socketed into steel housings, which are placed onto over ¾ in threaded rod with 10 threads/in that are threaded into the base plate. Both the front and the back of the beam have bearing housings. Machined collars are then placed into the front and back of the bearing housing. One collar rests against the concrete beam while the other supports nuts to clamp down onto the specimen. The bearing housings are secured via washers, a lock washer, and hexagonal nuts on each rod. Each inside collar is forced into surface to surface contact with the side walls of the beam, by a horizontal force. The horizontal force is applied through a ¾ in threaded rod, referred to as the loading rod. This rod runs through a spring (with a stiffness of 3000 lb/in), collars at the front bearing housing, a pre-made PVC hole (located at the mid-depth of the specimen and at 3.5-in on center from the end) and collars at the rear bearing housing. Nuts on this loading rod on each side of the beam are tightened to apply the horizontal force. A torque wrench is used to insure the same compression is achieved in every setup. A torque of 40 in-lbs is applied to the bearings for all specimens. The 40 in-lbs was established through trial and error during shakedown testing. Applied torques greater than 40 in-lbs began restricting the rotation of the beam, while smaller torques did not apply sufficient clamping force.

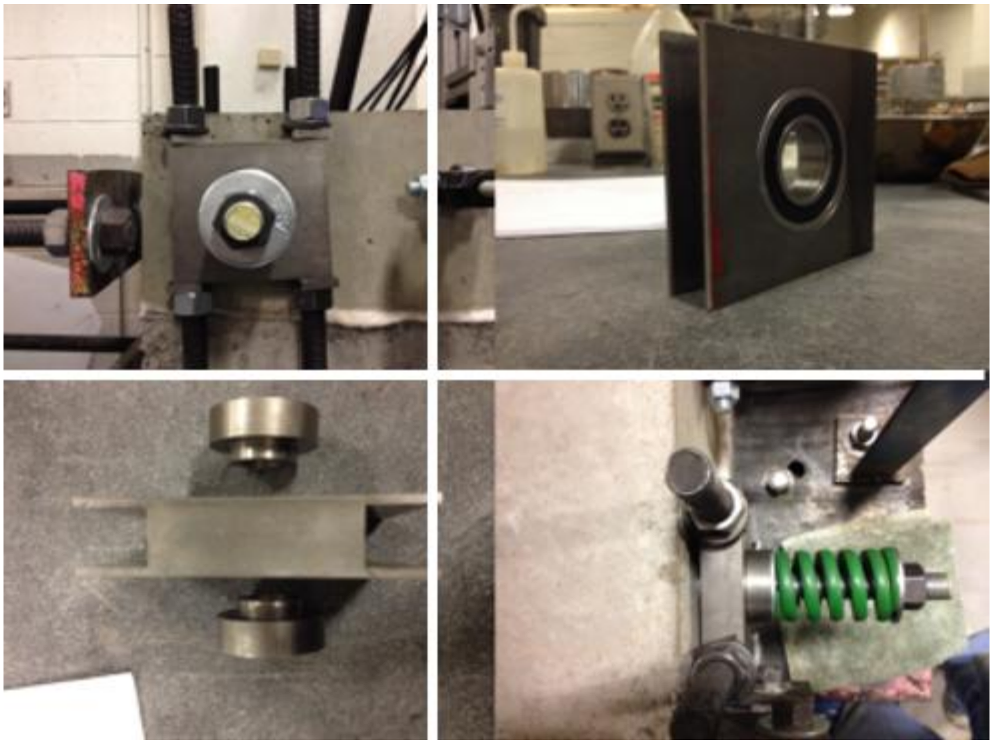

Figure 2.11. Bearing assembly

Additional restraint is provided by vertical rollers on both the loaded and unloaded sides of the beam on the front and back to prevent horizontal displacement of the specimen. Bearings are fitted into a yoke and secured via a nut and bolt. The rear of the yoke is threaded with threaded rod and brought back to a vertical 2 in x 2 in x ¼ in angle and held into a drilled hole with nuts. The base of the angle is then welded to a steel plate with a ¾ in hole, which is then fixed in a strategically placed tapped hole with all thread and a nut. The bearings then rest against the beam in the vertical orientation. This allows for vertical rotation of the specimen but prohibits the beam from a forward or backwards motion. The bearings rest at mid depth of the overlay beam at approximately 4 in from the middle of the sawed joint. Figure 2.12 shows the components of this assembly.

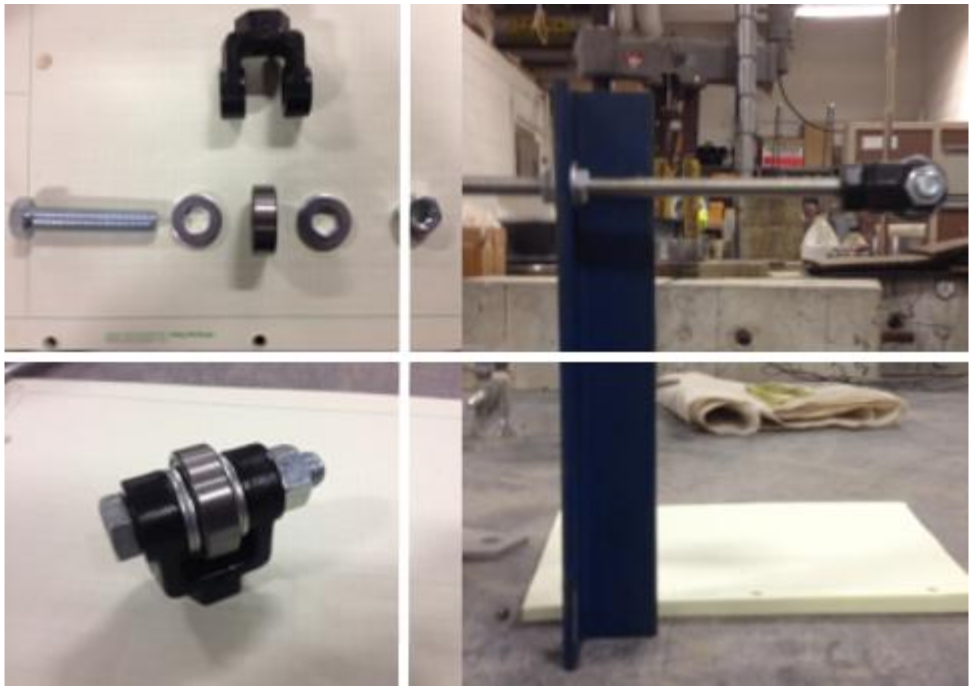

Figure 2.12. Roller assembly

The ends of the beam were restrained by running threaded rod back out of the beam, as shown in Figure 2.9 above. This allowed for vertical motion of the beams but prevented translational movement of the beam to either the left or the right. While casting the specimen, a ¾-in threaded rod was embedded in each end of the beam along the longitudinal axis. The embedded length of the rod is about 2 in, while the exposed length is around 1.5 to 2 in. On the left hand side of the beam, the exposed end of the tension rod is connected to a horizontally aligned steel angle running across the width of the beam. Two more parallel ¾-in diameter threaded rods coming out from this steel angle were connected to a vertical column through one more steel angle and a bracket. On the right hand side, the rod was lengthened with the help of a coupler. The right end of the extended rod was directly attached to the vertical column through a bracket. The beam is restrained by tightening the hexagonal nuts on both sides of the beam. For the fabric specimens, both the overlay and existing beams were restrained in this fashion. However, only the overlay was restrained for the asphalt interlayer beams.

Displacement is measured using eight Linear Variable Differential Transducers (LVDTs). The LVDT locations are shown in Figure 2.13. 80/20 T-slotted framing strut is used to place aluminum holsters for the LVDTs against the aluminum blocks, which are epoxied onto the beam. Displacement is measured at 1.5 in from the center saw cut joint on the top of the overlay beam and at mid depth of the lower beam representing the slab being overlaid. The locations of LVDTs 5, 6, 7, and 8 are opposite of 1, 2, 3, and 4. Therefore, displacements measured by LVDTs 2 and 6 are averaged to obtain the overlay loaded (OL) deflection, 1 and 5 are averaged to obtain the overlay unloaded (OU) deflection, 3 and 7 are averaged to obtain the existing unloaded (EU) deflection, and 4 and 8 are averaged to obtain the existing loaded deflection (EL). The force and deflection data is recorded by a controller such that the time history is synced.

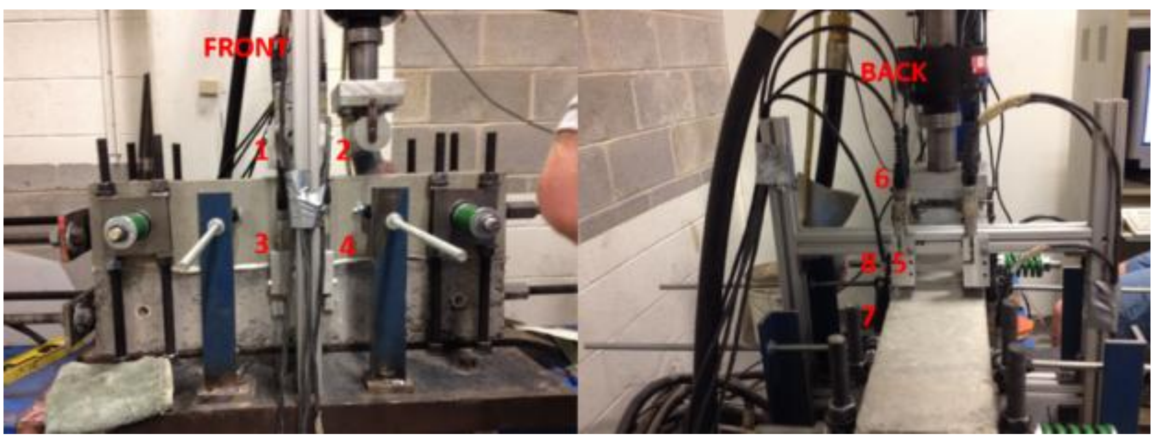

Figure 2.13. LVDT locations

2.3.4 Test Procedure

The beam specimen is placed into the loading frame and the components described in the previous section are attached to the beam. The beam is first placed onto the artificial foundation and adjusted until the beam is in the desired location after the aluminum blocks are epoxied onto the specimen to measure displacement. Then, the vertical rods used to house the bearings are screwed into the base plate and nuts and washers are placed on each rod underneath where the bearing housings are be located. The bearing housings with collars are then placed onto the vertical threaded rods. The horizontal clamping rods with springs are then placed through the beams on both sides but are not yet clamped down. Washers, lock washers, and nuts are then placed on top of each rod but are not yet tightened onto the bearing housings.

The ends of the beam are then restrained via the threaded rod embedded in each end of the beam along the longitudinal axis. These nuts are tightened down at this time. Next, the roller assemblies on the left and right, of both the front and back of the beam, are attached and oriented such that they are just in contact with the beam. The LVDT frame is then attached and secured to the base plate and the LVDTs are rested onto the aluminum blocks. The cables are then connected to the LVDTs and the reading values of displacement are analyzed. If the value of displacement read by the LVDTs is not +/- 10 mils then the vertical height of the LVDT is adjusted until between -10 and +10 mil reading is achieved. Once the LVDTs are secure, the actuator is brought down onto the beam and a load of 25 lbs is placed onto the specimen. Once the seat load is applied, then the horizontal clamping force is applied via the springs to 40 in-lbs. The bearing housings are secured by tightening down the nuts until the lock washers are compressed. Finally, the LVDTs are zeroed and the loading sequence can begin.

The dynamic load applied to the specimen to test for deflection characteristics is intended to simulate a vehicle traveling 65 mph over 10 in and the specimen is loaded at a rate of 7 Hz. A 7-Hz was selected because enables testing of specimens to occur in a reasonable time while still allowing for data to be sampled and show a clear time history of load and displacement. A constant 25-lb minimum load is maintained for a 0.134 second rest period. A haversine load, which approximates the stress pulse of a moving vehicle, is applied over a 0.0087 second duration with a peak load of 600 lbs. A load cycle time history can be seen in Figure 2.14 below. Testing was carried out for at least 300,000 cycles for each specimen. A static sweep from the seat load of 25 lbs to 600 lbs is conducted at 50, 100, 500, 1000, 2000, 5000, 10k, 20k, and every 10k loading cycles afterwards. The 600-lb load induced a similar deflection and angular rotation in the beam to that of a 9-kip falling weight deflectometer load applied to an overlay in the field.

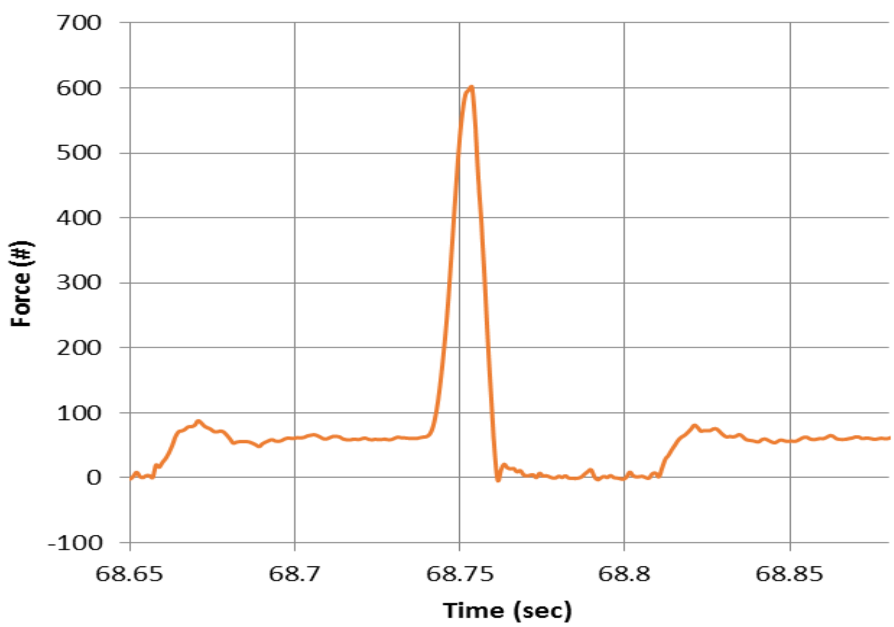

Figure 2.14. Deflection characteristic test load pulse

2.4 MODIFIED PUSH-OFF TEST

Shear transfer at the interlayer is a critical parameter in the design of unbonded overlays because the interlayer system must be able to provide a slip plane to allow the overlay to move freely with respect to the existing pavement. On the other hand, field observations have indicated that some interlayer systems do not provide sufficient restraint to allow for joint deployment. This can lead to high curling stresses, and the joints that actually do crack are wide. Therefore, an unbonded overlay interlayer system must both have sufficient slip to allow free movement of the overlay and provide sufficient restraint for joint deployment.

Interaction between a concrete slab and a granular or stabilized base layer is traditionally characterized using the Push-Off Test (Maitra, Reddy, & Ramachandra, 2009)(Ruiz, Kim, Schindler, & Rasmussen, 2001)(Rasmussen and Rozycki 2001). In this test, a small section of pavement is cast a short distance away from a paved lane. The paved lane acts as a rigid support and a hydraulic jack or actuator is used to displace the test section. The displacement of the test section is measured using a displacement measurement device rigidly fixed to the subgrade. The resistance to sliding is reported either as a force per unit area of interface or as a friction coefficient. The friction coefficient is the frictional force divided by the weight of the slab. When a chemical bond exists between the slab and the base, the sliding resistance will not be proportional to the slab weight, therefore it is more logical to report the force per unit area than the friction coefficient. In order to characterize the resistance to sliding of each interlayer system, a modified push-off test was performed in the laboratory where the force-displacement relationship is recorded for each interlayer type.

2.4.1 Modified Push-off Test Specimen Setup

For this test, identical specimens as those use fabricated for the deflection characterization test are used. The existing and overlay concrete beams are 6 in by 6 in by 30 in. The height of the interlayer varies and is 6 in wide by 30 in long. An approximately 1/8-in wide joint is sawed in the middle of the overlay concrete beam as deep as possible without going into the interlayer. A schematic of this test setup can be seen in Figure 2.15, along with actual fabric and asphalt interlayer specimens in Figure 2.16 and Figure 2.17 respectively.

a. b.

Figure 2.15. (a) Schematic and (b) boundary conditions of the modified push-off test setup

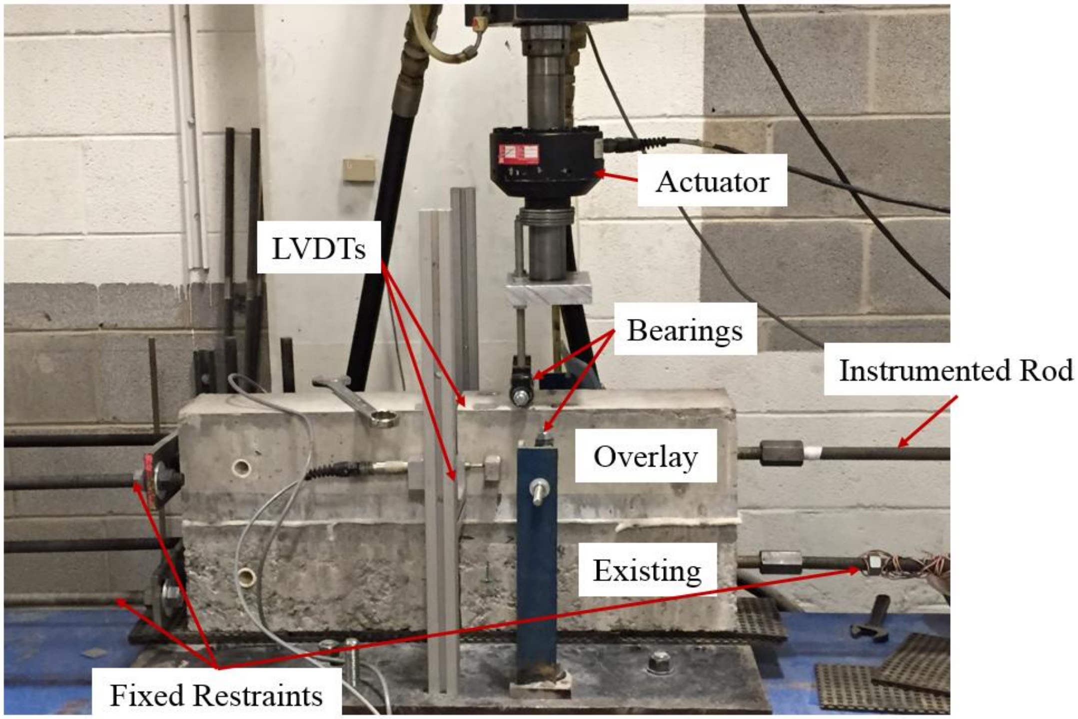

Figure 2.16. Fabric modified push-off specimen

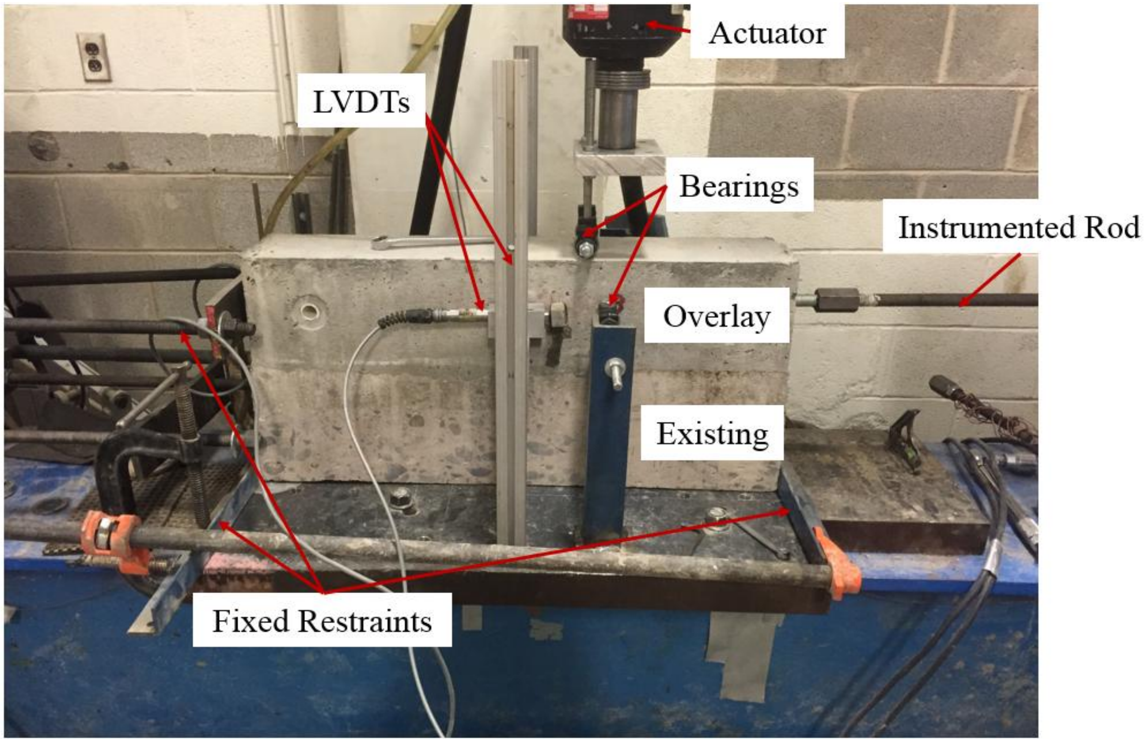

Figure 2.17. Asphalt modified push-off specimen

The bottom beam is restrained with the use of threaded rods for fabric interlayer specimens, which had threaded rod cast in to the beam using 0.36 w/cm concrete mixture. Note that all threaded rod is ¾ in with 10 threads/inch. For the asphalt interlayer specimens, where the concrete was obtained from in-service pavements, the bottom beam was restrained with steel angle and pipe clamps and C clamps, as shown in Figure 2.17. The top left half of the 0.42 w/cm overlay is restrained with threaded rod, while the top right half of the beam specimen is attached to an instrumented threaded rod, where the threads were machined off and strain gauges attached on opposite sides, as shown in Figure 2.18. All nuts and clamps are tightened down with the exception of the instrumented threaded rod. The instrumented rod is used to manually apply a translational force to the top right half of the overlay. The strain is recorded using a Campbell

Scientific CR 1000 datalogger. With the known cross sectional area and the modulus of elasticity of the steel, the force in the rod is calculated. To measure displacement, two LVDTs are utilized. Aluminum blocks are epoxied onto the front and back of the right half of the overlay at mid depth (3 in) and at a distance of 2.5 in from the sawed joint. Aluminum holsters for the LVDTs are mounted using 80/20 T-slotted framing strut. In order to read the LVDTs off of the same datalogger as the strain gauges for the instrumented rod, the signal from the LVDTs is conditioned from AC to DC and read as a differential voltage by the datalogger. Therefore, both the force and displacement are reported with the same time history. The data for the force and displacement is recorded at a frequency of 2 Hz.

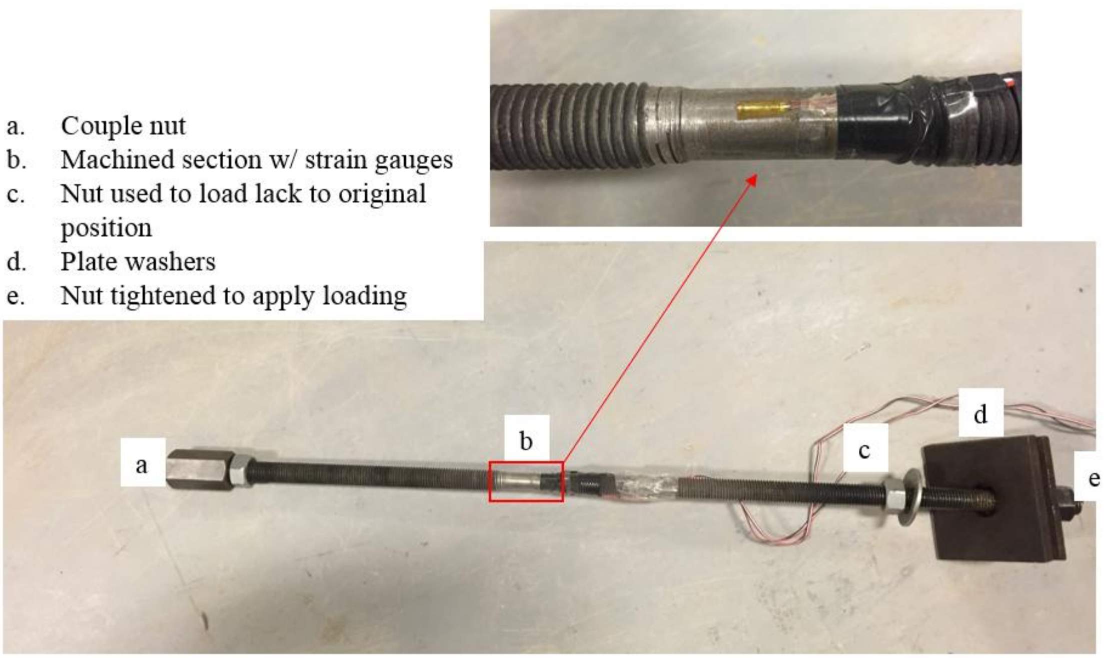

Figure 2.18. Instrumented threaded rod

The final step of the setup is the placement of rollers on both the top and the sides of the right half of the overlay, which is to be pulled via the instrumented rod. The bearings attached to the yokes are rotated 90 degrees from the direction used for the deflection characteristics test to only allow movement horizontally. Two other bearings are attached to the hydraulic actuator shown to create a trust bearing. The actuator is used to place a load of 25 pounds on the top of the right half of the overlay beam. The actuator is then put into displacement control to prevent vertical displacement of the concrete beam during testing. A variable force is then applied by the actuator to prevent rotation of the loaded half of the overlay and a subsequent tensile debonding failure near the joint.

2.4.2 Modified Push-off Testing Procedure

Prior to initiating the test, the displacement of the LVDTs as well as the strain in the instrumented rod are zeroed. In order to monitor force and displacement during loading while manually tightening the instrumented threaded rod, the datalogger is connected to a computer to view the information in near real time. A slight delay of a second or two exists between the time the force is applied and the time the data can be read on the screen, which must be accounted for during testing. Note that prior to testing, axle grease is applied to the threads to minimize heat built up due to friction between the rod and the hexagonal nut used to apply the load. This reduces the chances of galling occurring on the threads of the instrumented rod. Immediately before the instrumented rod is tightened, a level is used to ensure that the rod is parallel to the direction of loading so that there is as little eccentricity as possible. Throughout testing, the specimens are examined for damage or cracking in the asphalt and are then documented by photographing the specimens.

Testing is carried out in two phases. Phase 1 is the cyclic loading phase. In this phase, load is applied until the loaded portion of overlay reaches approximately 80 mils of displacement, as read by the LVDTs. The 80 mil displacement corresponds to a 100 degree Fahrenheit drop in temperature for a 12 foot slab cast of concrete with a thermal coefficient of expansion of 5.3 microstrain per degree F. The load is then held constant to observe the relaxation of the interlayer system until the force is relatively constant over time. The load is then removed from the rod by loosening the hexagonal nut. To account for non-elastic displacement, a load is applied in the opposite direction of the initial load until the overlay section returns to its initial position. This position is then held until the force is relatively constant over time. The load, relaxation, and opposite load cycle is repeated between 6 to 8 times for each test. During testing, it was determined that the interlayer system stiffness stabilized between 6 and 8 load cycles. The stiffness is said to have stabilized when no observed difference between the force experienced between cycles at the maximum observed displacement is present. This stiffness is relevant when calculating the stress in the overlay caused by the interlayer resisting uniform volume changes due to a decrease in temperature and/or moisture. An overly stiff unbonded overlay system can prevent true debonding, cause high stresses to develop in the overlay, and prevent proper joint activation.

Phase 2 is the ultimate loading phase. Once the final loading cycle from Phase 1 is finished, load is applied, via the hexagonal nut, until the interlayer system fails, or very large displacements (over one inch) are observed. This allows the ultimate resistance of each interlayer system to be determined. Once the specimen has been failed, the force is slowly removed from the rod by loosening the hexagonal nut. Then, the vertical thrust bearings attached to the actuator are lifted off of the specimen in displacement control mode. All restraints are then removed from the beam specimens and the location of failure is noted. Data is then collected from the datalogger, as soon as possible after testing, to ensure that the correct recorded values are obtained.

2.5 REFLECTIVE CRACKING TEST

Reflective cracking is a potential concern in unbonded concrete overlays of existing distressed concrete pavements (UBOLs). The interlayer acts to minimize interaction between the overlay and the existing concrete pavement, which helps prevent distress in the existing pavement from propagating into the overlay. A laboratory test was conducted using stacked beam specimens separated by an interlayer to evaluate the potential for a discrete crack in the lower beam to reflect up through the interlayer and into the overlay.

2.5.1 Reflective Crack Test Setup

Beam specimens for the reflective cracking test setup are cast in the same manner as those for the Deflection Characteristics and Modified Push-off tests. The existing and overlay concrete beams are 6 in by 6 in by 30 in. The height of the interlayer varies but is 6 in wide by 30 in long. However, the approximately a 1/8-in joint is sawed in the bottom beam, representing a joint or crack in the existing concrete pavement.

Figure 2.19 shows a specimen placed in the loading frame. The actuator is attached to a cylindrical loading head containing a ball joint. This allows a uniform line load along the transverse width of the beam to be applied directly above the joint. The foundation support provided by the lower layers under the existing PCC layer is replicated by an artificial foundation consisting of two layers of neoprene pads, known as Fabcel 25 (http://www.fabreeka.com/Products &productId=24). The stiffness of the two combined Fabcel layers is 200 psi/in as determined by conducting a plate load test according to ASTM D1195/D1195M. LVDTs are used to record the displacement in the front and back of the beam on the overlay and existing beams. Aluminum blocks are epoxied to both the front and back of the existing beams at mid depth as well on the top of the overlay beam. The LVDTs are located 3.5 in to the left of the applied load, as can be seen in Figure 2.19. The same 80/20 T-slotted framing strut is then used mount aluminum holsters for holding the LVDT's, such that the plunger of the LVDT rests on top of the aluminum blocks.

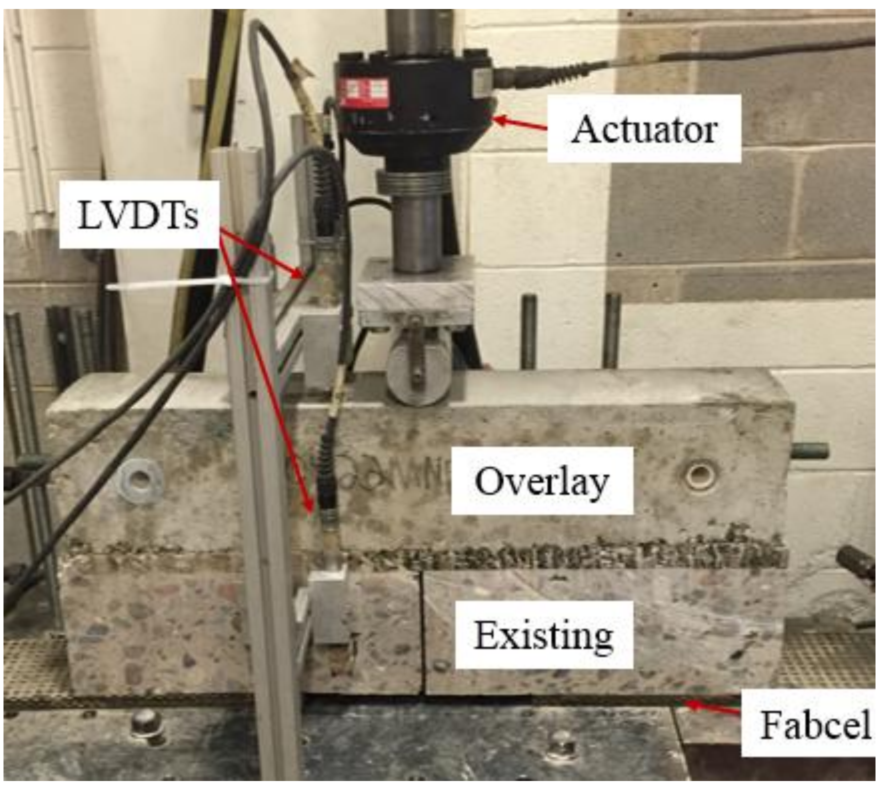

Figure 2.19. UBOL specimen in loading frame

The load is applied under load control at 30 lbs per second until a reflective crack is generated in the overlay beam. This is the same quasi-static load rate used in testing the flexural strength of concrete using ASTM C78. The load cell and LVDTs are sampled at 10 Hz. The maximum load is then recorded as the load required to propagate a reflective crack.

Preliminary testing was performed on specimens with the F15 interlayer, and uniform foundation support beneath the existing PCC layer. Three specimens were tested and a reflective crack could not be generated. The load was increased until a crack initiated at the top of the overlay, under the loading head, and then propagated through the overlay. This indicates that the failure is due to the stress concentration and crushing under the loading head and not a crack reflecting up from the underlying cracked beam. In order to investigate reflective cracking, a gap was created under the central portion of the beam by removing part of the artificial foundation such that there was no support for a length spanning 10 inches in the central portion of the beam. This non uniform support under the beam simulates a void under the existing pavement, and can also be representative of a distressed region. Figure 2.20 shows the gap in the Fabcel. A plywood template was used when placing the Fabcel support layer prior to placing the beam in the loading frame to ensure the gap was consistently 10 in wide and that the front edge of the Fabcel was directly perpendicular to direction of the UBOL specimen. A plumb bob was used to ensure that a 5-in gap was present between the loading axis and the front edge of the Fabel in both directions. Once the alignment of the Fabcel foundation was correct, the plywood templates were removed and the UBOL specimen was set in place. With the unsupported region under the joint, reflective cracking, which propagated from the bottom up, was generated. The fact that reflective cracking could not be generated when the specimen was fully supported indicates that unless a void is present in the vicinity of a joint or crack, or a distressed region is present, then the potential for reflective cracking to occur in the field is extremely low for UBOLs. This supports previous work performed by Hoegh, et al. (2012), who also investigated the potential for reflective cracking in a fully supported UBOL with a nonwoven fabric interlayer.

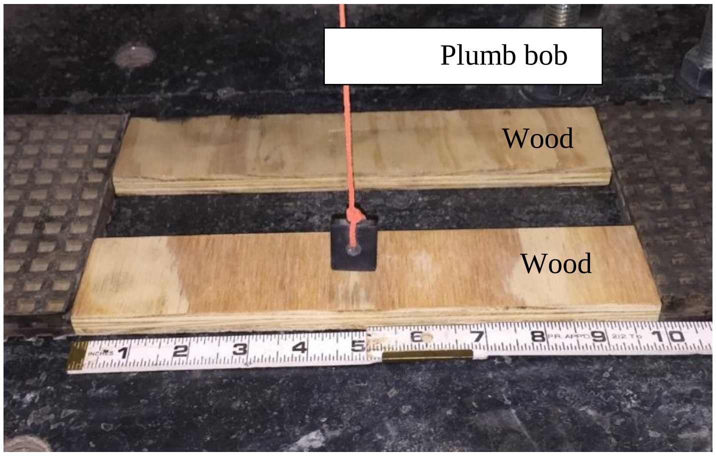

Figure 2.20. Alignment of the Fabcel foundation

Figure 2.21 shows the revised schematic and boundary conditions for the reflective crack test. Three replicates for each interlayer systems were tested. Testing was carried out after 5 days (120 hours) of curing. Both the modulus of rupture specimens and the reflective cracking specimens were tested after 120 hours +/- 1.5. This tolerance is more stringent than the permissible time tolerance required for testing the flexural strength at 5 days per ASTM C 78.

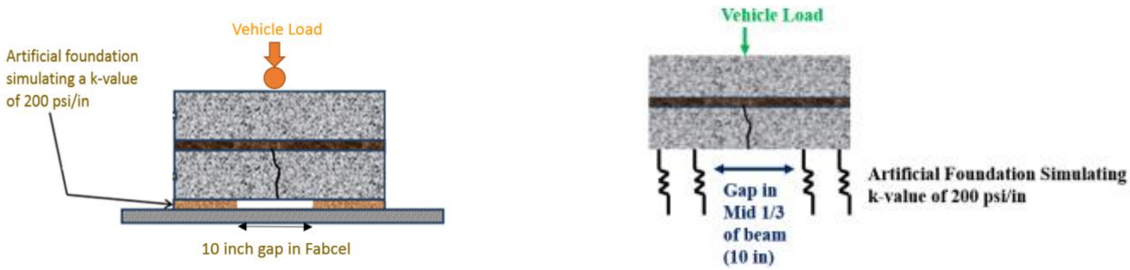

a. b.

Figure 2.21. (a) Schematic and (b) boundary conditions of reflective cracking test setup

2.6 DIRECT TENSION TEST (DTT)

The fourth mechanism examined to evaluate different interlayers for use in UBOL is a direct tension test (DTT). The purpose of this test is to characterize the bond strength at the interfaces of the interlayer with the concrete. A wedge splitting test is typically employed to analyze interface strengths, however a different approach is taken. A schematic of this test setup can be seen in Figure 2.22. The vertical force-displacement relationship is measured in tension to provide insight into how debonding between the existing and overlay concrete layers develops in the field and to determine if curling can result in debonding between the interlayer and the concrete layers.

Figure 2.22. Schematic of DTT test setup

2.6.1 DTT Specimen Preparation

Specimens were prepared differently for fabric and asphalt interlayers to facilitate the creation by taking advantage of casting required for beam testing outlined previously. Fabric specimens are cast in cylindrical molds, where the existing 0.36 w/cm concrete mixture is cast in a 4-in diameter by 4-in high mold. The geotextile fabric is then cut into a 4-in diameter circle and glued to the top of the 4 in tall cylinder made from the existing PCC mixture. The bottom cylinder, consisting of the existing PCC mixture and geotextile fabric, is then placed into a 4-in diameter by 8-in high plastic cylinder mold where 0.42 w/cm overlay PCC mixture is cast on top of the fabric. This creates the 4-in diameter by approximately 8-in height UBOL cylinder seen in Figure 2.23. A concrete wet saw is used to create DTT specimens for asphalt interlayers from reflective cracking beam specimens as seen in Figure 2.23. Two 4-in square by approximately

12-in tall specimens for each asphalt interlayer are extracted from each half of the beam, as seen in Figure 2.24. It is assumed that little to no damage is experienced where the direct tension specimens are sawed from the reflective cracking beam specimens and would therefore not affect the results of the DTT. Additionally, great care is taken while handling the specimens so as not to damage or fatigue the asphalt or the bonds to either of the concrete layers.

a. b.

Figure 2.23. DTT specimen with (a) fabric interlayer and (b) asphalt interlayer

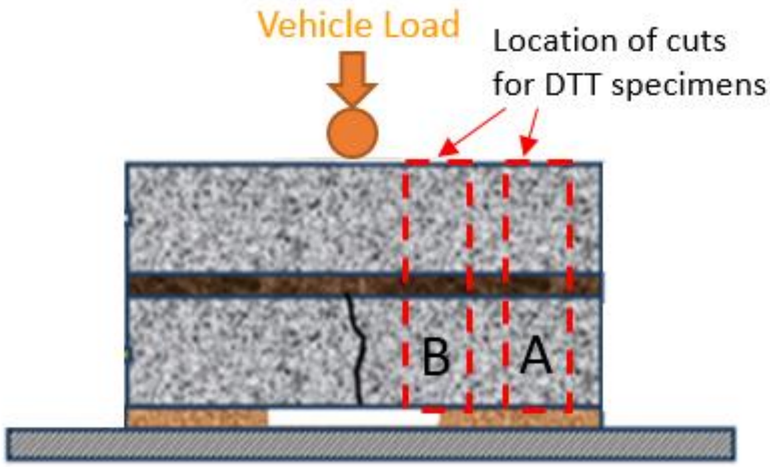

Figure 2.24. Location of asphalt DTT specimens

The next step prior to loading is to attach caps to the top and bottom. The caps are tapped and threaded to accommodate 7/8 in coarse threaded rod, which is gripped by the loading clamps. This requires very precise preparation to ensure that the top and the bottom surfaces are as parallel as possible to one another, as well as that the line of loading at both ends is straight. This is necessary so that as little moment as possible is induced during loading thereby creating, as close as possible, a pure tensile load condition. The end caps and rods can be seen in Figure 2.25. Note that different caps are used for the different specimens. The caps for the cylindrical fabric specimens have a machined 4-in diameter recess whereas those for the asphalt interlayers are 4-in square aluminum blocks.

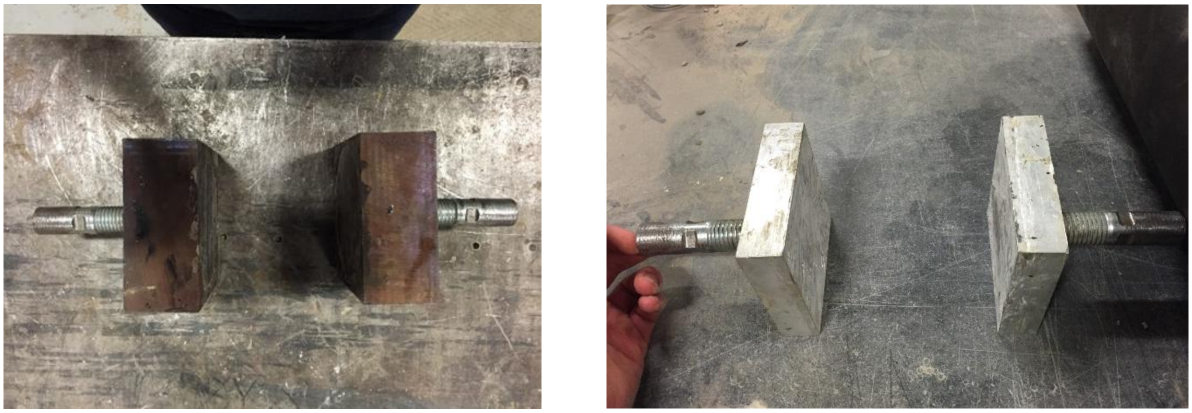

a. b.

Figure 2.25. DTT specimen end caps and rods for (a) fabric interlayer and (b) asphalt interlayer

If it was deemed that the top and bottom surfaces were not parallel enough with the use of a level, a grinder was used to grind the surfaces sufficiently level. With the top and bottom parallel, a two part epoxy is used to adhere the caps to the top and bottom surfaces. For the asphalt interlayer specimens, a reference corner was established so and the edge of the cap was aligned flush against it to ensure the line of loading was straight through the. For the fabric interlayer specimens, the circular recess is used to make sure that the loading was as symmetric as possible across the entire specimen. The epoxy was allowed to cure for sufficiently long so that failure did not occur in the epoxy.

The loading machine is capable of recording force and displacement, however due to concern of deformation of the epoxy during loading, LVDTs are attached to the sides of the specimens so that only the displacement observed in the interlayer is measured. Plastic blocks are epoxied onto the concrete, as seen in Figure 2.26, such that the gauge length between the blocks was approximately 3 in. Two LVDTs on opposite sides, 180 degrees from each other, are placed on the specimens which are those used for the modified push off test. The LVDTs are conditioned and recorded on a Campbell Scientific CR 1000 datalogger and recorded at a frequency of 2 Hz. Due to the concern of a moment being applied to the specimens, two additional LVDTs, oriented 90 degrees from the first two, are read off of read out boxes. Monitoring the displacement of all four facilitates the ability to determine if any one side is displacing at a different rate from another, which would indicate bending is occurring. When it is established that a large difference in displacement is occurring on a sample, either from the LVDT data or if it could be seen that the interface is "unzipping" from one side, the test results were not used and another specimen with that interlayer is prepared and tested.

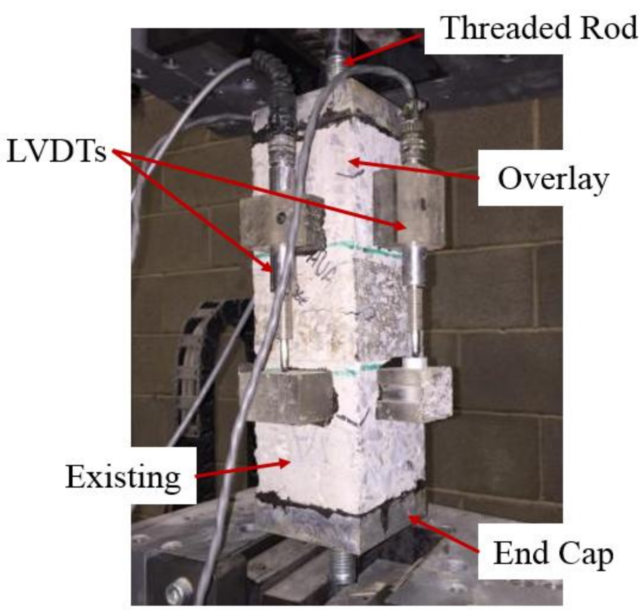

Figure 2.26. Mechanism 4 test setup (asphalt interlayer)

2.6.2 DTT Test Procedure

An Instron loading machine was used to apply the direct tensile load. A photo of the test setup is shown in Figure 2.26. To begin testing, LVDTs are placed onto the plastic blocks, which are glued to the sides and the rods are threaded into the end caps and then the bottom rod is secured in the tensile loading grip. The load cell is then zeroed to account for the weight of the specimen. Significant care then needs to be taken when lowering the top loading grips. As the top loading grips are brought down, the specimen is put into compression as the clamps are secured. In order to minimize the amount of compression applied to the DTT specimen, the bottom of the specimen is moved down via the fine position of the Instron to maintain as close to zero load as possible without allowing tension to be applied. It is impossible to avoid a minor compressive load with the procedure and loading machine available. After the specimen is secure in the loading frame, the LVDTs are zeroed. The test is then run by the Instron, which performs displacement controlled tensile loading. The test is run in displacement control mode at a rate of 1 mil/sec for fabric specimens and 0.5 mils/sec for asphalt specimens and the force is recorded by the load machine. The loading rates were chosen based on the displacement at the peak load for the interlayers and the limitations of the internal LVDT of the Instron. Once the test is initiated, the LVDTs connected to the readout boxes are recorded manually as displacement reported by the Instron are called out. The specimen is also examined to look for signs of bending or non-uniform loading. Failure is defined when complete separation is achieved. The LVDT data recorded by the datalogger is then time synched with the load from the Instron to achieve a force-displacement relationship for each specimen.

3.0 RESULTS AND CONCLUSIONS OF LABORATORY TESTS FOR CHARACTERIZATION OF INTERLAYER BEHAVIOR OF UNBONDED CONCRETE OVERLAYS OF EXISTING CONCRETE PAVEEMNTS (UBOL)

3.1 INTRODUCTION

This chapter summarizes key results obtained from the laboratory testing for each of the test setups described in Chapter 2. The results will focus particularly on how the performance of UBOL is affected by different interlayer types and characteristics based upon what is observed in the laboratory. Additional information for each of the specimens tested are located in Appendices A through E. Four mechanisms are being examined using four separate test setups. The mechanisms considered are:

1. Deflection characteristics of the interlayer
2. Friction developed along the interface between the interlayer and the overlay
3. Ability of the interlayer to prevent reflective cracking
4. Bond strength at the interfaces of the interlayer

3.2 DEFLECTION CHARATERISTICS TEST SETUP

The vertical stiffness of an interlayer system will define the response of the overlay to vehicle loading. Problems can develop if an interlayer system is either too stiff or insufficiently stiff. Ideally, an interlayer system is not so stiff that it is unable to provide cushion and act as a stress absorbing layer between the two concrete layers. This in turn would allow distress or cracks to reflect up into the overlay. If an interlayer is not sufficiently stiff, then issues can arise as a result of large deflections in the overlay. This can potentially lead to slab rocking in the overlay or joint damage from large deflections, which can adversely affect fatigue life. Another issue that can arise in asphalt interlayers is consolidation deformation. Consolidation deformation is a decrease in thickness of the interlayer due to a reduction in air voids, as traffic loading compacts the mix beyond the initial construction compaction. New asphalt interlayers placed for UBOL can especially be susceptible to this kind of distress. Additionally, if an interlayer is too drainable with significant air voids, it may be subjected to consolidation deformation. Permanent deformation of this nature can lead to the development of a gap between the overlay and the interlayer. This can be problematic as this gap can lead to stress increases that contribute to the development of longitudinal cracking in the wheelpath.

For the dynamic loading defined in Chapter 2 for the deflection characteristics test, there is a defined elastic response for the loaded overlay part of the beam. The elastic response is consistent for each interlayer type for the duration of the test and across specimens. Table 3.1 presents the average magnitude of the elastic response for each interlayer type and the standard deviation for the number of cycles examined for each of the two specimens tested per interlayer. Both fabrics have a larger amplitude of deflection than any asphalt interlayer. Since the 10 oz/yd^2 fabric is thinner, it does not compress as much as the 15 oz/yd^2 fabric. For the asphalt interlayers, the magnitudes are similar to one another, with the exception of the open graded asphalt from Minnesota. The deflections for this interlayer are higher than the other asphalt interlayers tested. The permanent deformation reported in Table 3.1 is the overlay loaded deflection at the end of testing. Each value represents the average obtained for two specimens. For both the 10 and 15 oz/yd^2 fabrics, the response remains relatively constant throughout the duration of the test and are therefore more consistent in time than the asphalt specimens. For asphalt interlayers, permanent deformation was observed within the interlayer. The open graded asphalt from Minnesota resulted in the largest magnitude of permanent deformation, followed by the dense graded asphalt from Minnesota. The open graded asphalt from Michigan resulted in the least amount of permanent deformation.

Table 3.1. Elastic deflection and permanent deformation under cyclic loading for deflection characteristics test

Interlayer	Ave. Elastic Deflection (mils)	Std. Dev. Ave. Elastic Deflection (mils)	Permanent Deformation (mils)
F15	5.70	0.59	5.7
F10	4.31	0.38	4.3
MNDAU	1.97	0.55	10.1
MNDAM	2.21	0.49	7.4
MNONU	3.51	0.88	18.4
MIDAU	2.05	0.55	6.8
MIOAU	1.94	0.61	4.9
PADNU	2.24	0.48	7.1

Asphalt interlayers can have the potential to breakdown under repeated traffic loading. This effect is exacerbated by the presence of moisture. Excessive moisture can cause an accumulation of hydraulic pressure, which can result in material distresses such as stripping and erosion. From a durability stand point, the interlayer must be able to withstand repeated traffic loads, without compromising the matrix of the interlayer. Whereas consolidation deformation described in the section above refers to additional compaction of the interlayer system. An asphalt interlayer that is not durable will breakdown, strip, or crumble even without the presence of moisture to degrade the stability of the asphalt matrix.

Of the interlayer types used for UBOL, the one most susceptible to this kind of damage is an open graded asphalt that lacks sufficient stiffness for the mixture to remain stable during loading. For the different interlayer types tested in the laboratory, the one most susceptible to this is the open graded asphalt from Minnesota. Great care had to be taken when handling the open graded asphalt from Minnesota to prevent crumbling of the asphalt interlayer. As can be seen for the discussion on consolidation deformation above for the Minnesota open graded asphalt, most of the permanent deformation observed was the result of a decrease in volume due to a reduction in air voids as the specimen was loaded.

In conclusion, deflections with fabric interlayers are greater than those for asphalt interlayers. This can potentially make the overlay more susceptible to slab rocking and joint damage resulting from wear out of aggregate interlock. Additionally, both fabrics maintained the same magnitude of deflection and load transfer throughout testing, which can be an indication that they are more resistant to fatigue damage and less susceptible to loss of support from degradation of the interlayer. Finally, large permanent deformation occurred in some of the asphalt interlayers. This can lead to a loss of support under the overlay in the wheelpath. The Minnesota open graded asphalt had the most permanent deformation. The mixture is more open graded than the others tested and damage is possibly occurring. Less stable open graded mixes have an increased risk of breaking down and causing a loss of support. The asphalt interlayer mixture design information in conjunction with the results of the permanent deformation of the asphalt interlayers will be used to develop criteria for consolidation of the asphalt interlayer in UBOL.

3.3 MODIFIED PUSH-OFF TEST

Testing of the modified push-off specimens is carried out in two phases. Phase 1 is the cyclic loading phase. In this phase, load is applied until the loaded portion of the overlay is displaced by approximately 80 mils. The 80-mil displacement corresponds to a 100 ^{o}F drop in temperature for a 12-ft slab cast of concrete having a thermal coefficient of expansion of 5.3 microstrain per ^{o}F. The relaxation of the interlayer system is then observed until the force is relatively constant over time. The load is then completely removed from the rod by loosening the hexagonal nut. To account for non-elastic displacement, a load is applied in the opposite direction of the initial load until the overlay section returns to its initial position. This position is then held until the force is relatively constant over time. The load, relaxation, and opposite load cycle is repeated 5 to 8 times for each test. Phase 2 is the ultimate loading phase. Force versus displacement for each different specimen can be seen in Figure 3.1. Once the final loading cycle from Phase 1 is completed, load is applied via the hexagonal nut until the interlayer system fails. Failure is defined as the point in which very large displacements (over 1 in) are observed and is referred to as the ultimate resistance of the interlayer system.

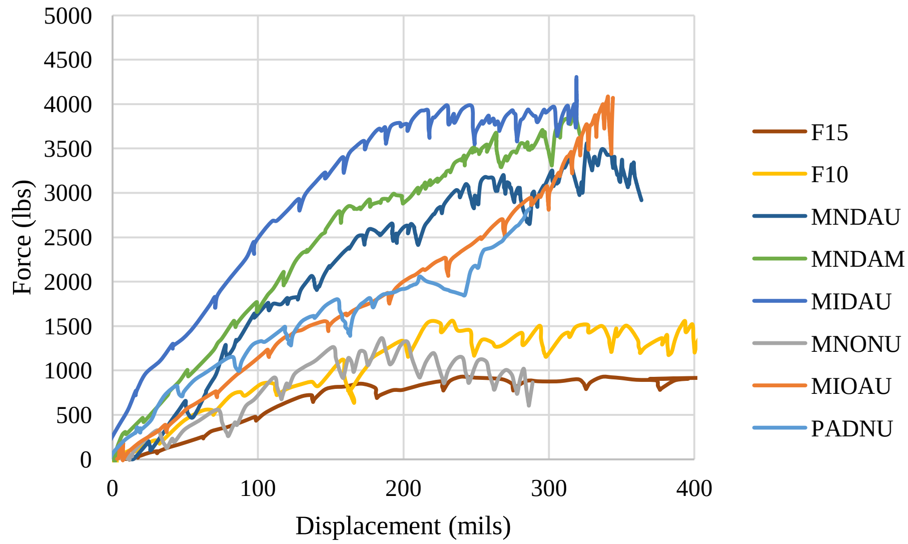

Figure 3.1. Force versus displacement for modified pull-off test phase 2 loading

The first cycle of each test provided information on the material properties relevant in determining when and where joints in the overlay would activate. The stiffness for each test was calculated as the force over displacement at a displacement of 80 mils. If the first cycle did not reach 80 mils of displacement, the stiffness was calculated at the maximum displacement. Two specimens for each interlayer type were tested using the modified push off test. The average initial stiffness of each interlayer system is provided in Table 3.2.

During testing, it was determined that the final stiffness would stabilize after between 5 and 8 load cycles. The stiffness is said to have stabilized when no difference between the force experienced between cycles at the maximum observed displacement is observed. This stiffness is relevant when calculating the stress in the overlay caused by the interlayer resisting uniform volume changes due to a decrease in temperature and/or moisture. An overly stiff system can prevent true debonding, and cause high stresses to develop in the overlay and prevent proper joint activation. The average final stiffness for each interlayer is summarized in Table 3.2. The definition of the initial and final stiffness is provided in Figure 3.2. The ultimate strength of each interlayer system was tested to establish the ultimate resistance to sliding for each interlayer system. The average ultimate resistance is provided in Table 3.2 for each interface.

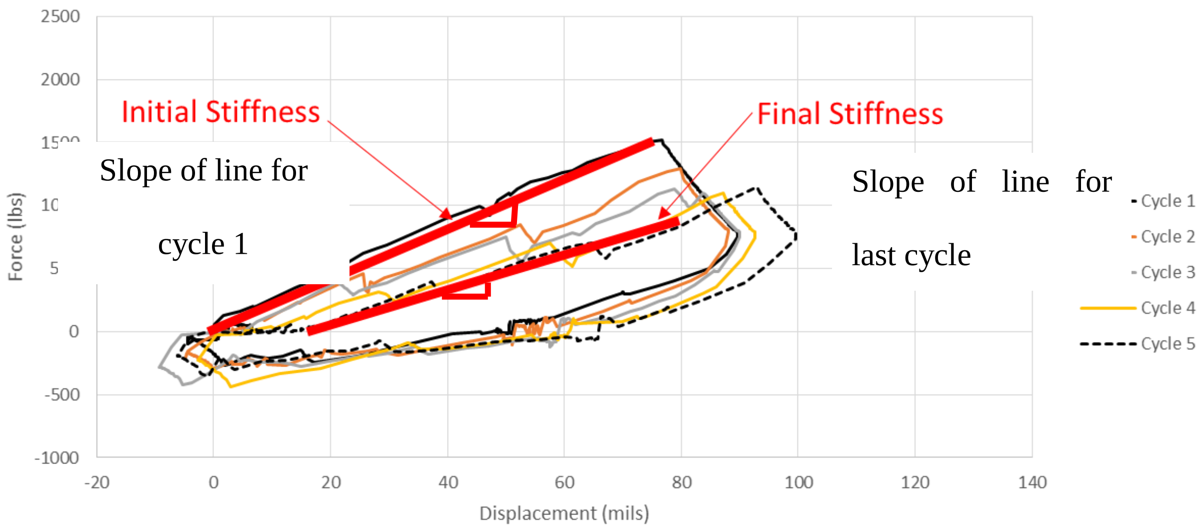

Figure 3.2. Example of initial and final stiffness definition

Table 3.2. Summary results from modified push off test

Interlayer (Code)	Initial Stiffness (psi/in)	Final Stiffness (psi/in)	Ultimate Resistance (psi)
F15-Glued	61	37	13
F15-Pinned	50	40	26
F10-Glued	104	87	22
F10-Pinned	98	29	21
MNDAU	234	167	39
MNDAM	333	263	59
MIDAU	336	317	62
MNONU	217	55	16
MIOAU	169	136	63
PADNU	215	124	32

From the results presented in Table 3.2, it can be seen that the specimens with a fabric interlayer have a lower stiffness than the specimens with an asphalt interlayer. Within the fabric specimens, the 10 oz/yd^2 fabric had a higher stiffness than the 15 oz/yd^2 fabric. This is most likely due to decreased thickness, which limits in plane deformation of the interlayer. The specimens with the milled interlayer from Minnesota have a higher initial and final stiffness than the specimens with the unmilled interlayer. It can also be seen that the ultimate resistance of the specimens with the milled interlayer was much greater than the specimens with the unmilled interlayer. This is possibly due to the decreased thickness of the milled specimens. The largest reduction in stiffness can be seen for the specimens with the open graded asphalt interlayer from Minnesota, which was visibly distressed during testing and led to the very small ultimate resistance. The specimens with the open and dense graded asphalt interlayers from Michigan exhibited the smallest decreases in stiffness and also had the largest ultimate resistance. The ultimate resistance for the thicker asphalt interlayers was lower with the exception of the open graded interlayer for the specimens from Minnesota, which damaged due to the lower strength.

In general, with the exception of the specimens with the open graded asphalt interlayer from Minnesota, the fabric interlayers provide less restraint than the asphalt layers, as expected.

In order to examine the significance between the different interlayers, hypothesis testing is performed. The partitioned error rate, Bonferroni method is utilized to compare the different interlayers. The null hypothesis is that the means of the two interlayer types compared are equal, while the alternative hypothesis is that the mean of one of the two interlayer types differs from the other. Table 3.3 presents all comparisons that were able to be made, some comparisons were not able to be performed since an insufficient number of specimens were tested. Also, the pinned fabric specimens are not used in the statistical testing. A P-Value < 0.05/3 = 0.017 indicates means are significantly different at a 95% experiment confidence level. The P-values from significant observations at 95% confidence (defined as having a P-value of less than 0.05), which emerged from this two-tailed hypothesis testing analysis will be discussed and are presented in Table 3.3.

Table 3.3. Significant results from hypothesis testing of different interlayers

	P-Value	
Compared Interlayers	Initial Stiffness	Final Stiffness
Fabric vs Open Graded	**<0.0001**	0.20
Fabric vs Dense Graded	**<0.0001**	**<0.0001**
Open Graded vs Dense Graded	**<0.0001**	**<0.0001**
Fabric, initial vs final	0.057	
Dense Graded, initial vs final	**0.004**	
Open Graded, initial vs final	0.055	

***Bold font indicates comparisons that are statistically significant.**

When comparing the different interlayer systems, both the initial and final stiffness were examined. For initial stiffness comparisons at a 95% confidence, fabric, open graded, and dense graded asphalt are significantly different from one another. However, the final stiffness comparison between fabric and open graded asphalt is not significant. The final stiffness for fabric and dense graded asphalt, as well as between open graded and dense graded asphalt are statistically significant. It is also shown that the initial and final stiffness for the fabric, as well as the open graded asphalt are not significantly different. The comparison between the initial and final stiffness for the dense graded asphalt is significantly different.

3.4 REFLECTIVE CRACKING TEST

3.4.1 Results

Figure 3.3 presents photos of the UBOL specimens after failure. For the UBOL specimens with the fabric interlayer, the crack did not propagate through the fabric, although on a few occasions a few of the fibers within the 10 oz/yd^2 fabric failed. There was partial failure at the glued interface with the existing concrete beam for three of the six fabric specimens (one 15 oz/yd^2 fabric and two 10 oz/yd^2 fabrics). By examining the depth of mortar penetration into the fabrics, it is apparent that there is penetration down into the fabric. However, no observable difference between the 15 oz/yd^2 and 10 oz/yd^2 fabrics was discernable. The interface with the overlay beam was completely intact except for the small area where the crack propagated. Once the crack began to initiate in the asphalt for the UBOL specimens with an asphalt interlayer, the crack immediately propagated up through the overlay beam. In all of the asphalt beams tested, the bond between the overlay and interlayer and the bond between the interlayer and the existing remained intact. Post failure analysis showed that more mortar penetration was noted in the open graded asphalts than the dense graded asphalts, as would be expected. In comparing the two open graded asphalts, the MNONU appeared to have a greater depth of mortar penetration than the MIOAU samples. While a crack was generated through the interlayer into the overlay, the primary difference between the fabric specimens and the asphalt specimens is that the fabrics remained fully or partially intact, whereas the asphalt samples cracked straight through the asphalt interlayer and the concrete once the crack initiated.

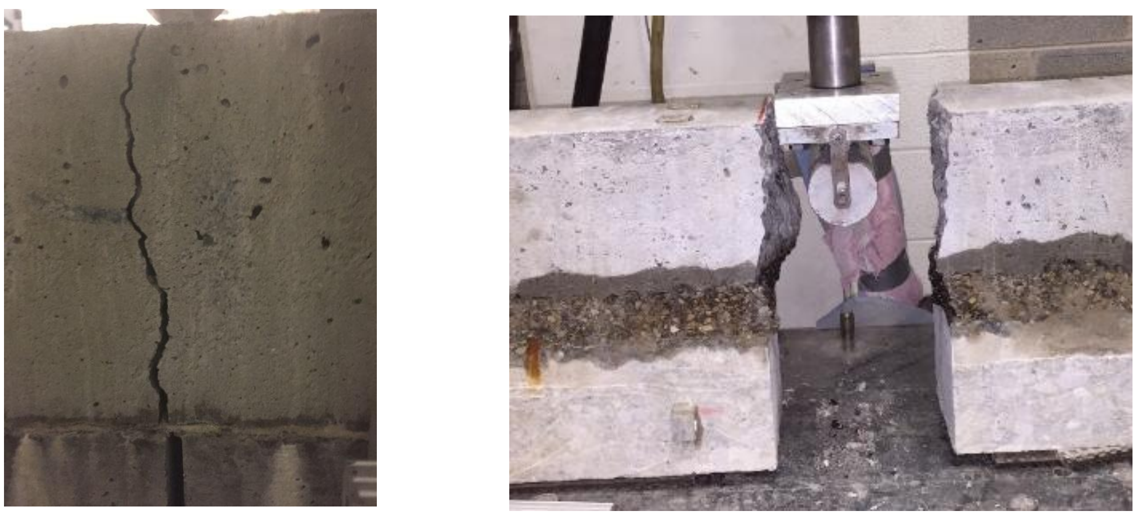

a) F15

b) MIOAU

Figure 3.3. Post failure of reflective cracking specimens

The results from the reflective crack testing for the UBOL specimens is provided in Table 3.4. Three specimens were tested for each interlayer system. Table 3.4 provides the specimen name (See Table 2.2 for additional information); the ultimate load sustained by the reflective cracking specimen, P_{RC},; the ultimate load sustained by the companion modulus of rupture beams tested in third point loading cast in conjunction with the UBOL overlay beam (tested in accordance with ASTM C 78), P_{MOR},; and the average and standard deviation of the load ratio. The load ratio is defined in Equation 3.1. The use of the load ratio helps to account for any minor differences in strengths between batches for the Mixture 2 concrete.

$$load\ ratio = \frac{P_{RC}}{P_{MOR}} \qquad \textbf{Equation 3.1}$$

where P_{RC} is the ultimate load sustained by the reflective cracking specimen in pounds and P_{MOR} is the ultimate load sustained by the modulus of rupture specimen in lbs. When establishing P_{MOR}, the modulus of rupture strength was first calculated using the measured dimensions of the specimen. This strength was then converted back into a load assuming a specimen depth and width of 6 in. This eliminates the effects due to slight variations in the dimensions of the modulus of rupture beams.

It should be noted that P_{MOR} is greater than P_{RC} for all specimens tested. While a single point center loading should be greater for two identical specimens, this was not the case. The type of specimens and the loading conditions used to evaluate P_{RC} and P_{MOR} are not the same. For the UBOL reflective cracking beams, there is a singularity present in the existing beam coupled with the gap in support in the middle third of the beam. The singularity under the load creates a stress concentration at the bottom of the interlayer, which can be attributed to the lower strength for the UBOL reflective cracking beams over the 24-in MOR beams. The increased length may also have contributed to the decrease in strength.

Table 3.4. Results from UBOL reflective cracking laboratory test

UBOL Specimen[1]	P_{RC} (lbs)	MOR for the Overlay Mixture (psi)	P_{MOR} (lbs)	Load Ratio	Average Load Ratio for Each Interlayer	Std. Dev. of Load Ratio for Each Interlayer
F15	6218	610	7417	0.838	0.842	0.016
	6605	644	7980	0.828		
	7508	682	8730	0.860		
F10	6565	628	7707	0.852	0.869	0.015
	6984	641	7920	0.882		
	7517	701	8620	0.872		
MNDAU	5562	590	7480	0.744	0.725	0.031
	6345	738	9217	0.688		
	6052	658	8155	0.742		
MNDAM	5923	623	7767	0.763	0.753	0.014
	6638	690	8730	0.760		
	5912	649	8020	0.737		
MNONU	6414	694	8594	0.746	0.767	0.034
	6678	724	8925	0.748		
	6460	636	8015	0.806		
MIDAU	5777	652	8140	0.710	0.711	0.014
	6438	717	8874	0.725		
	5896	663	8460	0.697		
MIOAU	6957	697	8675	0.802	0.787	0.033
	7129	711	8798	0.810		
	6471	698	8637	0.749		
PADNU	6512	691	8292	0.785	0.768	0.015
	5859	641	7692	0.762		
	5967	656	7872	0.758		

[1] A description for each UBOL specimen is provided in Table 2.2.

Hypothesis testing is performed to evaluate the effects of the different interlayers. Tukey's range test is utilized to compare all possible pairs of means (Montgomery, 2012). The null hypothesis is that the means of the two interlayers compared are equal, while the alternative hypothesis is that the mean of one of the two interlayers differs from the other.

Table 3.5 presents all pair-wise comparisons between each interlayer. The difference in means is the result of the subtraction of the averages of the two compared interlayers. The 95 percent confidence intervals on the difference between interlayers are also presented. The two interlayers are statistically different at 95 percent if the range of the confidence interval does not contain zero. The P-values from significant observations at 95 percent confidence (defined as having a P-value of less than 0.05), which emerged from this two-tailed hypothesis testing analysis will be discussed and are presented below in Table 3.6.

.

Table 3.5. Pair-wise interlayer comparisons

Comparison	**Difference of Means Between Interlayers**	**95% Confidence Interval of Difference**
F10 - F15	0.0267	(-0.0395, 0.0929)
MNDAU - F15	**-0.1173**	**(-0.1835, -0.0511)**
MNDAM - F15	**-0.0887**	**(-0.1549, -0.0225)**
MNONU - F15	**-0.0753**	**(-0.1415, -0.0091)**
MIDAU- F15	**-0.1313**	**(-0.1975, -0.0651)**
MIOAU - F15	-0.055	(-0.1212, 0.0112)
PADNU - F15	**-0.0737**	**(-0.1399, -0.0075)**
MNDAU - F10	**-0.144**	**(-0.2102, -0.0778)**
MNDAM - F10	**-0.1153**	**(-0.1815, -0.0491)**
MNONU - F10	**-0.1020**	**(-0.1682, -0.0358)**
MIDAU- F10	**-0.158**	**(-0.2242, -0.0918)**
MIOAU - F10	**-0.0817**	**(-0.1479, -0.0155)**
PADNU - F10	**-0.1003**	**(-0.1665, -0.0341)**
MNDAM - MNDAU	0.0287	(-0.0375, 0.0949)
MNONU - MNDAU	0.042	(-0.0242, 0.1082)
MIDAU - MNDAU	-0.014	(-0.0802, 0.0522)
MIOAU - MNDAU	0.0623	(-0.0039, 0.1285)
PADNU - MNDAU	0.0437	(-0.0225, 0.1099)
MNONU - MNDAM	0.0133	(-0.0529, 0.0795)
MIDAU - MNDAM	-0.0427	(-0.1089, 0.0235)
MIOAU - MNDAM	0.0337	(-0.0325, 0.0999)
PADNU - MNDAM	0.015	(-0.0512, 0.0812)
MIDAU - MNONU	-0.056	(-0.1222, 0.0102)
MIOAU - MNONU	0.0203	(-0.0459, 0.0865)
PADNU - MNONU	0.0017	(-0.0645, 0.0679)
MIOAU - MIDAU	**0.0763**	**(0.0101, 0.1425)**
PADNU - MIDAU	0.0577	(-0.0085, 0.1239)
PADNU - MIOAU	-0.0187	(-0.0849, 0.0475)

***Bold font indicates comparisons that are statistically significant.**

Table 3.6. Significant results from hypothesis testing of different interlayers

Compared Interlayers		P-value
F15	MNDAU	0.000
F15	MNDAM	0.005
F15	MNONU	0.020
F15	MIDAU	0.000
F15	PADNU	0.024
F10	MNDAU	0.000
F10	MNDAM	0.000
F10	MNONU	0.001
F10	MIDAU	0.000
F10	MIOAU	0.011
F10	PADNU	0.002
MIDAU	MIOAU	0.018

From these values, it becomes evident that statistically, both the 15 and 10 oz/yd^2 fabrics have higher load ratios at a confidence level of 95 percent than all of the asphalt interlayers with the sole exception of the 15 oz/yd^2 fabric and MIOAU. The fact that the nonwoven geotextile fabric interlayer load ratios are statistically shown to be greater than the asphalt interlayers indicate that more energy (a higher load) is required to propagate a crack through the nonwoven geotextile fabric interlayers. This shows that the fabric interlayers have an increased resistance to the development of reflective cracking when compared with the asphalt interlayers tested. Comparing the fabric interlayers to one another, a P-value of 0.824 was obtained. Therefore, no meaningful difference was noted between the heavier 15 oz/yd^2 fabric and the lighter 10 oz/yd^2 fabric. However, on average, the load ratio for the 10 oz/yd^2 fabric was greater than that for the thicker 15 oz/yd^2 fabric. Further investigation into the effects of different weight fabrics is needed to say if there is an advantage of lighter, thinner fabrics over heavier, thicker fabrics in alleviating reflective cracking. This investigation should include at least two additional fabric weights, such as 5 and 20 oz/yd^2. The inclusion of the extrema would allow for comparison against a greater range to see if statistically significant differences can be gleaned. Additional testing, could also be beneficial in determining if there is a limit as to how thin the fabric can get before it becomes ineffective in preventing reflective cracking.

No meaningful trends were obtained that show a difference in the performance between dense graded, open graded, milled, or unmilled asphalt interlayers. This might be attributed to the fact that there is a significant amount of variability in the asphalt retrieved from in-service pavements coupled with the fact that only three samples were tested per interlayer type. No statistical difference between the milled and unmilled asphalt interlayers from Minnesota was seen, even though the average load ratio for the milled asphalt interlayer was greater than the unmilled. This could possibly be due to the drastic difference in thickness confounding the effect of the milling. Comparisons between the different asphalt interlayers yielded only one significant difference and it was between the MIDAU and the MIOAU. The load ratio for the Michigan open graded asphalt interlayer was greater than that for the Michigan dense graded interlayers and had the highest average load ratio as compared to the other asphalt interlayers. On average, both open graded asphalts have load ratios greater than the dense graded asphalts. This most likely can be attributed to a higher stress dissipation in the asphalt with the higher void contents. On average, the load ratio for MIOAU was greater than MNONU. This can be due to the fact that the gradation of MNONU was more open graded and contained more rounded aggregate particles than MIOAU. While both interlayers were open graded, the Minnesota open graded interlayer has a substantially lower strength and stiffness then the Michigan open graded asphalt. The differences between the two open graded asphalts can be seen in Figure 3.4.

a) Michigan open graded asphalt

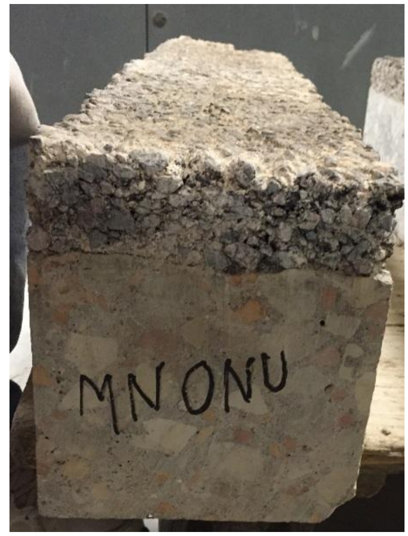

b) Minnesota open graded asphalt

Figure 3.4. Open graded asphalt samples tested

It should be noted that even though the fabric interlayer had a higher load ratio than the asphalt interlayers, a relatively large load was required to generate reflective cracking regardless of the interlayer type (asphalt or fabric). Therefore, both appear to be suitable interlayer alternatives and additional work should be performed to establish what minimum load ratio requirements should be set.

3.4.2 Conclusions

An important conclusion from this study is that a true reflective crack could not be generated when the UBOL specimens were fully supported. For the three specimens tested while fully supported, the overlay crack propagated from the top down. The stress concentration at the crack tip of the joint in the existing beam was not sufficiently high before the concrete failed due to stress concentrations and crushing directly under the loading head. When a gap in the Fabcel foundation support was introduced, the crack in the overlay propagated from bottom up through the interlayer at the sawed joint. The gap in the support underneath the beam simulates a void that would exist under a joint or crack in the field. Therefore, unless a void is present near a joint or crack in the existing pavement, the probability of reflective cracking occurring in UBOLs is extremely low.

Another significant finding is that at a confidence level of 95 percent, the nonwoven geotextile fabrics provided increased resistance to the development of reflective cracking. The ability of the fabrics to absorb additional deflection by providing a cushion for the overlay adds to this improved resistance as the crack initiates in the bottom of the overlay with the fabric remaining fully or partially intact. Whereas with the asphalt interlayers, once the crack initiates at the bottom of the asphalt it propagates straight through the concrete overlay. Within the asphalt interlayers, the open graded asphalt from Michigan was shown to better resist reflective cracking than the dense graded from Michigan. This most likely can be attributed to a higher stress dissipation in the asphalt with the higher void contents. It should be mentioned that a relatively large load was required to generate reflective cracking regardless of the interlayer type (asphalt or fabric). Therefore, both asphalt and fabric interlayers might be suitable alternatives to retard reflective cracking. Additional work should be performed to establish what minimum load ratio requirements should be set to assure good performance. Interlayer selection at a project level should be made based on a number of different factors and not solely on the ability to prevent reflective cracking. Also, pre-overlay work should be performed to address any void present beneath the existing slab to insure reflective cracking will not occur.

3.5 DIRECT TENSION TEST (DTT)

The resistance of the interlayer system to vertical uplift as a result of curling/warping forces affects the level of bond present at the edges of the slabs near the joints. Any debonding that occurs as a result of this loading will affect the performance of the overlay. The goal of the laboratory vertical pull off test is to observe how debonding develops between the existing and overlay concrete and if curling stresses are significant.

Figure 3.5 shows specimens after failure. Note that the overlay concrete is on the left hand side of each picture in Figure 3.5. Figure 3.5(a) is a fabric DTT specimen with the 10 oz/yd^2 nonwoven geotextile. For all fabric specimens, failure occurred within the glued interface with the existing concrete. Some of the adhesive remains attached to the existing concrete while the majority remains attached to the fabric as shown in Figure 3.5(a). More variability exists between the asphalt specimens tested. The location of failure is either completely at an interface with the asphalt, within the middle of the asphalt, or a combination of the two. For the specimens shown in Figure 3.5(b), failure occurred at the interface with the existing concrete, while failure occurred within the asphalt for the specimens in Figure 3.5(b) and (c). Table 3.7 shows the load and displacement at failure as well as the location of the failure within the interlayer for each specimen tested.

(a) F10

(b) PADNU

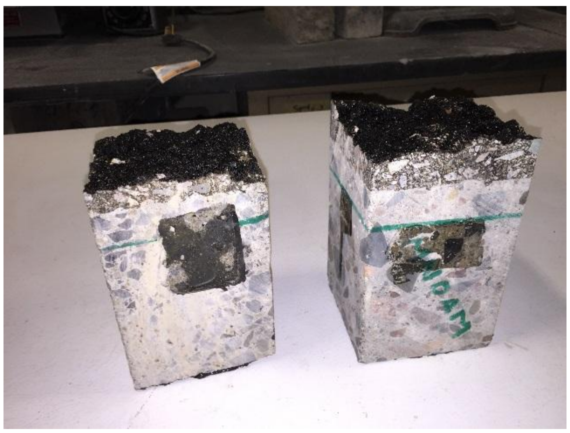

(c) MNDAM

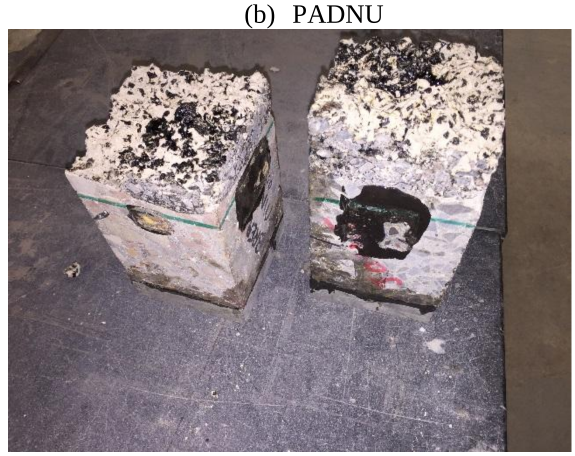

(d) MNONU

Figure 3.5. Post failure of direct tension specimens

As shown in Table 3.7, both NWGFs tested had comparable values of peak force and displacement at peak force. The F10 specimens resulted in a peak load of 30 - 40 lbs at a displacement ranging between 120 mils to 140 mils and the F15 specimens maintained a peak load of 15 to 20 lbs at a displacement of approximately 60 mils. The variation observed between fabric specimens can be partly attributed to the quality and quantity of geotextile adhesive placed at the glued interface. Overall, these results indicate that the fabrics would provide insignificant resistance to upward curl of the concrete overlay.

Greater variability was observed with the asphalt interlayers than the NWGF interlayer specimens. Higher strength and smaller displacements at the peak load for the asphalt specimens was observed as compared to the fabric specimens, as one would expect. The magnitude of the peak load varied with the location of the failure within the interlayer system. Both the Minnesota and Michigan open graded asphalts produced the smallest peak loads, followed by the Minnesota dense unmilled, Minnesota dense milled, and Michigan dense unmilled, which had the greatest peak load. It was also noted that the location of failure within the specimens was identical for all except the open graded asphalts from Michigan and Minnesota, where failure either occurred at the existing interface or in the asphalt. Additionally, the only interlayer that failed at the interface with the overlay is the dense graded asphalt from Michigan, which also has the largest peak load. While there was variability within the different specimens, general trends between the different types of asphalt could still be gleaned.

Table 3.7. Results of vertical pull off test

Code	Peak Load (lbs)	Displacement at Peak Load (mils)	Location of Break
F15	18	64	Glued Interface
	16	61	Glued Interface
F10	31	139	Glued Interface
	38	120	Glued Interface
MNDAU	255	33	Middle of asphalt
	251	42	Middle of asphalt
MNDAM	262	10	Bond w/ Existing Concrete (into asphalt)
	392	13	Bond w/ Existing Concrete (into asphalt)
MNONU	169	12	Middle of asphalt
	208	12	Bond w/ Existing Concrete (into asphalt)
MIDAU	586	22	Bond w/ Overlay Concrete
	411	13	Bond w/ Overlay Concrete
MIOAU	206	4	Bond w/ Existing Concrete (into asphalt)
	142	6	Bond w/ Existing Concrete
PADNU	305	9	Bond w/ Existing Concrete
	289	13	Bond w/ Existing Concrete

The asphalt specimens were taken from either close to the location of the break of the reflective cracking specimens or further away as shown in Figure 2.24. It is desired to see if there was a difference in interface strength between these two locations. Therefore, a t-test is performed to examine if there is any difference in the resulting interface strength. Testing the null hypothesis that the strength of the location closer to the break is equal to the strength of the location further from the break versus the alternative hypothesis that they are unequal yields a P-value of 0.845. This indicates that there is no statistical difference between locations. Therefore, the assumption that no damage occurred to the reflective cracking beams outside of the location of the crack was reasonable. Finally, hypothesis testing was performed to examine the difference between the three types of interlayers: fabric, dense graded asphalt, and open graded asphalt. T-tests to examine the null hypothesis of two types of interlayers being equal versus the alternative that they are not equal yielded the results shown in Table 3.8. From these results, the null hypothesis is rejected and it can be seen that the fabric has the smallest interface strength, followed by the open graded asphalts, and the dense graded asphalt has the largest interface strength.

Table 3.8. Results of hypothesis testing of DTT interlayer types

Compared Interlayer Types		**P-value**
Fabric	Dense graded	0.0001
Fabric	Open graded	0.0007
Dense graded	Open graded	0.005

In conclusion, nonwoven geotextile fabric interlayers provide essentially no resistance to upward curling. Asphalt interlayers provided varying degrees of resistance based upon the type of asphalt and the degree of bond strength at the interfaces with the existing and overlay concrete. In the field, the resistance to upward curling will remain negligible for UBOLs with nonwoven geotextile fabric interlayer. However, the restraint provided by asphalt interlayers in the field is subject to change depending upon the asphalt temperature and any stripping, erosion, or consolidation which will occur in the interlayer from the effect of water and traffic loading. Hypothesis testing showed that there was no statistical difference between the asphalt interlayer specimens taken from the reflective cracking beam specimens indicating that no damage occurred to the reflective cracking beams outside of the location of the crack. Finally, it was shown that the fabric interlayers had the smallest interface strength followed by the open graded asphalt then the dense graded asphalt with the largest resistance.

4.0 STRUCTURAL MODELING OF UNBONDED CONCRETE OVERLAYS OF EXISTING CONCRETE PAVEMENTS (UBOL) FOR JOINT FAULTING

4.1 INTRODUCTION

In order to determine faulting, the UBOL pavement response is needed from structural modeling. Incremental faulting calculations require many time consuming finite element runs, so the creation of Neural Networks to predict the response greatly decreases run time. This chapter details the choice of finite element software for modeling the UBOL structure followed by convergence and validation checks of the finite element model. Calibration of the Totsky interlayer parameter is then presented. The range of parameters used to generate a factorial of finite element runs and the critical responses to be used in the faulting model are defined. Finally, the development of neural networks to predict the critical responses for the UBOL structure using MATLAB’s Neural Network Toolbox is discussed (MATLAB, 2013).

4.2 ABAQUS VERSUS ISLAB

Two primary choices of finite element modeling software are available to model the UBOL structure, ABAQUS and ISLAB. ABAQUS is a commercial software package that has become the standard in the development of detailed finite element modeling, while ISLAB is a software package developed exclusively for the response of rigid pavements to loading under a wide variety of conditions.

While commercial software tools, are extremely powerful, the use of this software has some disadvantages. Robust software, such as ABAQUS, requires extensive user experience to efficiently develop and run structural models. In addition, should a model be set up incorrectly, tracking down the error and making the correct adjustments are not easy. Finally, ABAQUS requires significant computational resources and simulations can take considerable time.

Alternatively, ISLAB is specifically designed to model pavement structures. ISLAB was developed and tested explicitly for the response of multilayered rigid slabs on grade. Additionally, neural networks developed using ISLAB are currently used to predict the critical responses in the AASHTO Pavement ME design guide (ARA, 2004). Furthermore, projects can be quickly built and run in ISLAB, allowing for more adjustments and a greater number of runs to be performed in a reasonable timeframe.

ISLAB includes the use of the Totsky model to simulate the interlayer in an UBOL pavement system (Totsky 1981, Khazanovich 1994, Khazanovich and Ioannides 1994). The Totsky assumption is summarized in Figure 4.1, where the overlay rests on the Totsky spring interlayer and the existing slab rests on a Winkler subgrade.

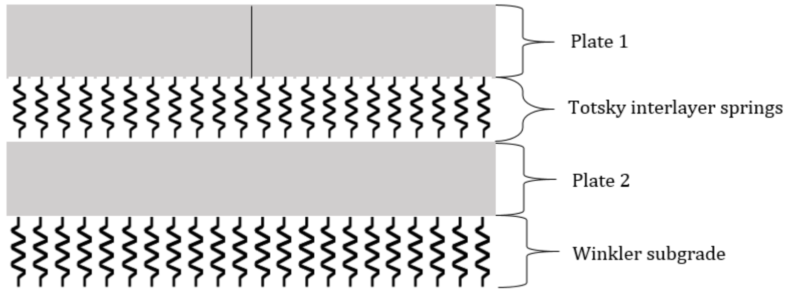

Figure 4.1. Totsky model for layer interface in UBOL system adopted in ISLAB

The advantage of the Totsky model is that it can model the "cushioning" property of the interlayer in a straightforward, computationally efficient manner. The Totsky model was specifically implemented in ISLAB to model UBOLs. The elements of the Totsky model are 8 node, 24 degree of freedom elements, which can be seen in Figure 4.2 (Kazanovich et al, 2000). The first four nodes of the overlay plate are placed at the neutral axis of this upper plate, while the other four nodes of the existing plate are placed at the neutral axis of the lower plate. The plate elements model the bending, while the springs accommodate the direct compression occurring in the UBOL pavement structure. Within ISLAB, it is assumed that stiffness matrices of the spring interlayer and Winkler subgrade are dependent only on nodal displacements and not on the nodal rotations. In ABAQUS, the Totsky interlayer spring approach can also be taken, or the asphalt interlayer can be modeled as an elastic or viscoelastic solid.

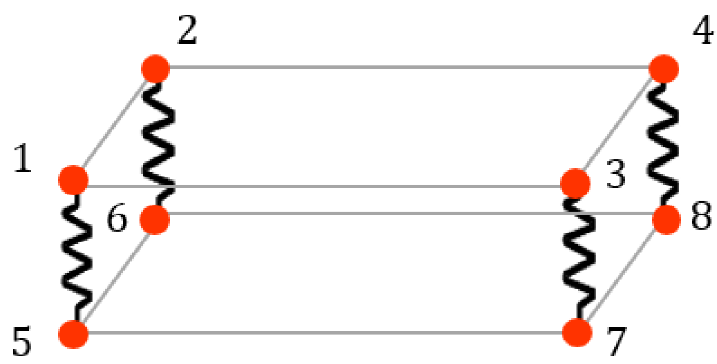

Figure 4.2. Representation of Totsky element in ISLAB

Therefore, due to the advantages and disadvantages outlined above, ISLAB is chosen as the modeling software for UBOL joint faulting. A convergence analysis was conducted and showed that the element size of 6 in is sufficient for the analysis. Example output for one of the mesh convergence checks performed is shown in Table 4.1. This mesh convergence analysis was carried out for a 12-ft joint spacing and a 6-in overlay on a 10-in existing concrete slab with a subgrade Winkler k-value of 150 psi/in. An 18-kip single axle load was applied at the joint. Additionally, validation checks were performed with Falling Weight Deflectometer (FWD) data from UBOLs in Michigan and Minnesota. An example validation with FWD data for two Michigan sections using interlayers tested in the lab study is shown in Table 4.2.

Table 4.1. Mesh convergence check in ISLAB

Mesh size (in)	Corner deflection (mils)	Maximum Interlayer compressive stress (psi)
12	70.2	25.72
8	80.5	26.07
6	80.7	26.21
3	80.8	26.34

Table 4.2. ISLAB validation with FWD data

	US 131 Kalamazoo (MIOAU)			US 131 Rockford (MIDAU)	
FWD Location	FWD (mils)	ISLAB (mils)		FWD (mils)	ISLAB (mils)
-12	4.6	5		3.7	3.9
0	5.1	5.4		3.8	4.1
12	4.4	4.7		3.5	3.7

4.3 CALIBRATION OF TOTSKY INTERLAYER PARAMETER

In order to accurately model the UBOL structure within ISLAB, the value of the Totsky interlayer k-value must be established for different interlayers. This section details the use of data from the reflective cracking laboratory testing as well as Falling Weight Deflectometer (FWD) data, to establish guidelines for the value of the interlayer Totsky k-value for UBOL design.

4.3.1 Reflective Cracking Laboratory Data Analysis

The reflective cracking test from Chapter 2.5 and 3.4 is modeled in ISLAB and the results from the LVDTs during the test are used to determine the corresponding value of the Totsky interlayer k-value. Please see Chapter 2.5 to give details of the reflective cracking test setup. Figure 4.3 provides a representation of the model used to determine the Totsky k-value for the different interlayers. Note that the simulated load is applied as a 0.25-in wide line-load along the beam depth of 6 in (indicated in blue in Figure 4.3a). Thus, the load contact area is 1.5 in^2. As the finite element model is static, a single load of 1 kip is applied to determine a response of the beam model to loading.

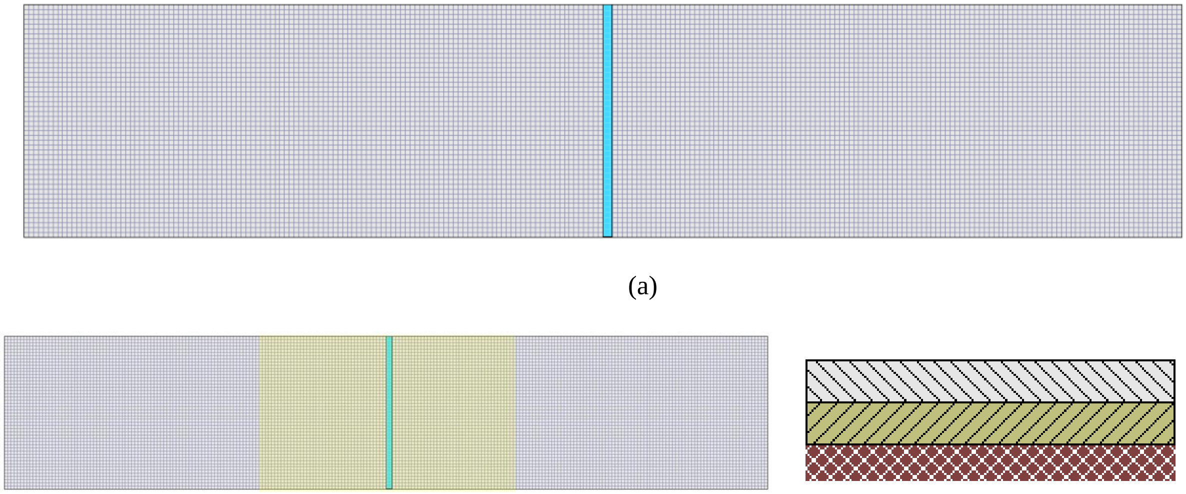
(a)
(b)
(c)

Figure 4.3. ISLAB two-dimensional model of Reflective Cracking test, where (a) shows the mesh and load area, (b) highlights the unsupported area in yellow, and (c) shows the structure profile

In ISLAB, the notch at mid-span in the existing concrete is modeled by inserting a joint at mid-span. In the upper layer (the overlay), this joint fully transfers load (the load-transfer efficiency is 100% treated as a rigid joint). However, in the lower layer (the existing concrete), the joint does not transfer the load at all (load transfer efficiency is near-zero). This allows for the test setup to be modeled the same as the laboratory test setup.

With the beam model, a factorial of cases is modeled to observe the response utilizing interlayers of different properties. In each case, only the Totsky interlayer k-value (k_{totsky}) assumed is varied, otherwise the modeled beam has the following properties:

- Layer 1: h_{OL} = 6 in, E_{OL} = 4,255,000 psi (average of all Reflective Cracking beam overlay elastic moduli), Poisson ratio ν = 0.15, unit weight γ = 0.087 lb/in^3
- Interlayer: k_{IL} varied from 100 to 50,000 psi/in

- Layer 2: h_{EX} = 6 in, E_{EX} = 4,790,000 psi (average of PCC elastic moduli for the "existing" beam of the reflective cracking laboratory specimens), Poisson ratio ν = 0.15, unit weight γ = 0.087 lb/in^3
- Mesh details: Mesh elements are square (0.125 in to a side) for the entire model, as illustrated in Figure 4.3a.
- A static load of 1-kip is applied to determine a linear beam response associated with interlayer properties.

Figure 4.4 illustrates the final relationship determined for the modeled beam response and the Totsky interlayer stiffness. Also included in the figure is an exponential relationship determined by transforming the variables and finding a linear least-squares fit. As shown in the figure, the R-squared valued for the fitness of the exponential relationship is 0.99, thus the model adequately describes the relationship between model response and the Totsky k-value for this range of values. With the relationship developed in ISLAB, interlayer Totsky k-values can be established for each beam specimen tested and therefore each type of interlayer system included in the laboratory study.

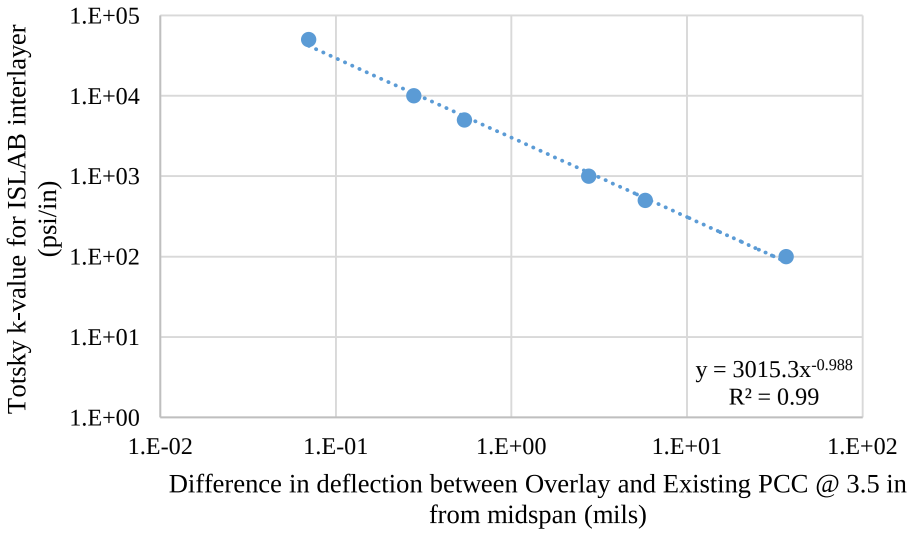

Figure 4.4. Relationship between difference in layer deflection (in mils) and Totsky k-value for interlayer from ISLAB

Table 4.3 presents the reflective cracking beam specimens for each interlayer and the corresponding Totsky k-value. Results for these beams are in Table 4.3 below. Given the response of the different interlayer beams under a 1-kip load in the lab, the modeled relationship was used to infer an associated Totsky interlayer stiffness. Average and standard deviation of the different interlayers tested in the laboratory are presented in Table 4.4.

Table 4.3. Established Totsky k-values for reflective cracking laboratory testing specimens

Overlay PCC			Fabric Type	Diff in defl @ 1 kip (mils)	Totsky k-value (psi/in)
Specimen	E (psi)	f'c (psi)			
0429F15OB	4280000	5059	F15	8.27	411
0429F15OC	4280000	5059	F15	10.41	325
0701F15OD	4430000	4632	F15	12.33	274
0402F10OA	3880000	4512	F10	10.58	320
0501F10OA	4170000	5069	F10	7.76	439
0402F10OA	3880000	4512	F10	9.48	358
			Asphalt Thickness		
0417MNDAUA	3880000	4590	2.9	0.93	3824
0507MNDAUA	4480000	5106	2.8	2.32	1504
0701MNDAUA	4430000	4632	2.8	0.76	4698
0422MNDAMC	4300000	4696	0.9	1.37	2581
0507MNDAMB	4480000	5105.75	1	1.25	2828
0709MNDAMB	4490000	4732	0.8	0.66	5431
0507MNONUC	4480000	5106	1.7	1.52	2324
0522MNONUC	4650000	5131	1.7	0.93	3824
0701MNONUB	4430000	4632	1.8	2.3	1518
0424MIDAUC	4230000	5106	1.1	0.65	5521
0515MIDAUB	4790000	5131	1	0.99	3584
0701MIDAUC	4430000	4632	1.3	1.17	3033
0513MIOAUC	4710000	5013	1.8	1.28	2760
0520MIOAUC	4620000	5073	1.9	0.68	5263
0709MIOAUA	4490000	4632	1.8	1.32	2675
0806PADNUC	4630000	4966	1.5	1.98	1766
0909PADNUA	4340000	4824	1.4	1.3	2717
0909PADNUC	4340000	4824	1.5	0.63	5690

Table 4.4. Average and standard deviation of Totsky k-value for different the different interlayer types

Interlayer Type	Average Totsky k	Standard Deviation
F15	336.7	63.4
F10	372.2	54.9
MNDAU	3342.3	1261.9
MNDAM	3613.4	1175.1
MNONU	2555.1	900.8
MIDAU	4046.1	965.9
MIOAU	3566.1	1095.2
PADNU	3390.8	1533.4

Hypothesis testing is performed to evaluate the effects of the different interlayers and determine if there is any statistical difference between the interlayers. Tukey's range test is utilized to compare all possible pairs of means. The null hypothesis is that the means of the two interlayers compared are equal, while the alternative hypothesis is that the mean of one of the two interlayers differs from the other. Table 4.5 presents all pair-wise comparisons between each interlayer. The difference in means is the result of the subtraction of the averages of the two compared interlayers. The 95 percent confidence intervals on the difference between interlayers are also presented. The two interlayers are statistically different at 95 percent, if the range of the confidence interval does not contain zero. As can be seen from Table 4.5, the means of the fabric interlayers are statistically different from each of the asphalts with the exception of the open graded asphalt from Minnesota. No statistical difference was detected between any of the asphalt interlayers or between the fabric interlayers.

Note that there does not appear to be a relationship between interlayer asphalt thickness and the inferred Totsky k-value. In addition, no relationship appears to be present between asphalt stiffness and the Totsky k-value. Based on the model and the lab data, other factors, including interlayer bond and perhaps loading/support conditions, must be considered if the inferred Totsky k-value is to be considered beyond an average across all asphalt lab beams.

Table 4.5. Pair-wise Interlayer Comparisons

Comparison	Difference of Mean Totsky coeff. Between Interlayers	95% Confidence Interval of Difference
F10 - F15	35	(-2762, 2833)
MNDAU - F15	**3006**	**(208, 5803)**
MNDAM - F15	**3277**	**(479, 6074)**
MNONU - F15	2218	(-579, 5016)
MIDAU- F15	**3709**	**(912, 6507)**
MIOAU - F15	**3229**	**(432, 6027)**
PADNU - F15	**3054**	**(257, 5852)**
MNDAU - F10	**2970**	**(173, 5768)**
MNDAM - F10	**3241**	**(444, 6039)**
MNONU - F10	2183	(-615, 4980)
MIDAU- F10	**3674**	**(876, 6471)**
MIOAU - F10	**3194**	**(396, 5991)**
PADNU - F10	**3019**	**(221, 5816)**
MNDAM - MNDAU	271	(-2526, 3069)
MNONU - MNDAU	-787	(-3585, 2010)
MIDAU - MNDAU	704	(-2094, 3501)
MIOAU - MNDAU	224	(-2574, 3021)
PADNU - MNDAU	49	(-2749, 2846)
MNONU - MNDAM	-1058	(-3856, 1739)
MIDAU - MNDAM	433	(-2365, 3230)
MIOAU - MNDAM	-47	(-2845, 2750)
PADNU - MNDAM	-223	(-3020, 2575)
MIDAU - MNONU	1491	(-1306, 4289)
MIOAU - MNONU	1011	(-1786, 3809)
PADNU - MNONU	836	(-1962, 3633)
MIOAU - MIDAU	-480	(-3278, 2318)
PADNU - MIDAU	-655	(-3453, 2142)
PADNU - MIOAU	-175	(-2973, 2622)

***Bold font indicates statistically significant comparisons.**

4.3.2 MnROAD Falling Weight Deflectometer Analysis

To supplement the use of the laboratory beam testing in establishing the Totsky interlayer k-value, an analysis was carried out using FWD data from MnROAD UBOLs to establish the interlayer k-values for comparison and validation of the lab interlayer k relationship. MnROAD Cells 105, 205, 304, 405, 505, and 605 are UBOLs constructed with either an open graded Permeable Asphalt Stabilized Stress Relief Course (PASSRC - denoted MNONU from the laboratory testing) or a non-woven geotextile fabric. The designs of these cells are summarized in Table 4.6 below. The existing concrete pavement in Cell 5 was constructed in 1993 and consisted of 7.1 in of PCC placed over 3 in of Class 4 aggregate base over 27 in of Class 3 aggregate subbase over a clay subgrade (Watson and Burnham, 2010). Cell 5 had a 20-ft long by 13-ft (passing lane) or 14-ft (driving lane) wide panels and bituminous shoulders. FWD data was available for each cell except 105.

Table 4.6. UBOL MnROAD cells

Cell	Construction Date	Slab Size* (Length x Width) (ft x ft)	Dowels (in)	Overlay Concrete Thickness (in)	Interlayer Thickness (in)	Interlayer Type	Existing Concrete Thickness (in)
105	10/8/08	15 x 14	None	4	1	Permeable Asphalt (PASSRC)	7.5
205	10/8/08	15 x 14	None	4	1	Permeable Asphalt (PASSRC)	7.5
305	10/8/08	15 x 14	None	5	1	Permeable Asphalt (PASSRC)	7.5
405	10/8/08	15 x 14	None	5	1	Permeable Asphalt (PASSRC)	7.5 (cracked)
505	8/24/11	6 x 7	None	5	-	Fabric	7.5 (cracked)
605	8/24/11	6 x 7	None	5	-	Fabric	7.5

*NOTE: Sizes shown for driving lane. For sections 15 x 14, passing lane is 15 x 13. For sections 6 x 7, passing lane is 6 x 6.5. This matches the width of Cell 5 driving and passing lanes.

Thermocouple data was available for Cells 205, 305, and 605 and were also used for Cells 105, 405, and 505 respectively since the overlay thickness and design are the same. The temperature profile through the PCC overlay, as well as an approximate temperature of the interlayer at the time of FWD testing, was then established for each cell and testing time. FWD testing performed in the wheelpath and adjacent to the transverse joint was used to establish the LTE to be used in the ISLAB finite element model. The slab stiffness was obtained either directly from an elastic modulus test for the existing PCC and through a correlation with strength for the overlay. The layers beneath the existing PCC are modeled as a Winkler foundation with a k-value of 250 psi/in established from backcalculation from Cell 5 FWD data.

ISLAB's Totsky formulation was then used to model the structure for FWD testing performed at center slab to establish what interlayer Totsky k-value produces the closest deflection response. Mesh convergence was achieved by examining the deflection and overlay slab stress beneath the center slab load. Three sensors were used to define the deflection, including one directly under the load plate, and the sensors at +/- 12 in from the applied FWD load. Slabs that exhibited cracking and had a corresponding center slab drop after the cracking had initiated were excluded from this analysis in an attempt to isolate the effect of the interlayer on the resulting response. A batch of runs were then generated for Totsky interlayer k-value in increments of 100 psi/in. The FWD deflections was then matched to the Totsky k-value which produced the same deflection using linear interpolation obtain the interlayer stiffness. The results of the Totsky k-value determination are presented in Figure 4.5. For the cells with the PAASRC interlayer, the range of interlayer k-values is 1180 to 8770 psi/in with an average value of 3900 psi/in. For the nonwoven geotextile fabric interlayer cells, the range of interlayer k-values is 135 to 900 psi/in with an average value of 425 psi/in.

As can be seen in Figure 4.5, there is no apparent trend between interlayer k-value and asphalt temperature, which is consistent with the laboratory data in that there was no apparent trend between different asphalts with varying stiffness. Statistical testing was carried out to see if a statistical difference could be identified between the k-values obtained from the laboratory specimens and those found from the FWD testing at MnROAD. Student t-tests were carried out using the null hypothesis that the mean laboratory k-values are equal to the mean k-values obtained from the FWD testing. These results are summarized in Table 4.7 below. Additionally, it can be seen that the FWD results for both asphalt and fabric interlayers are different from one another statistically.

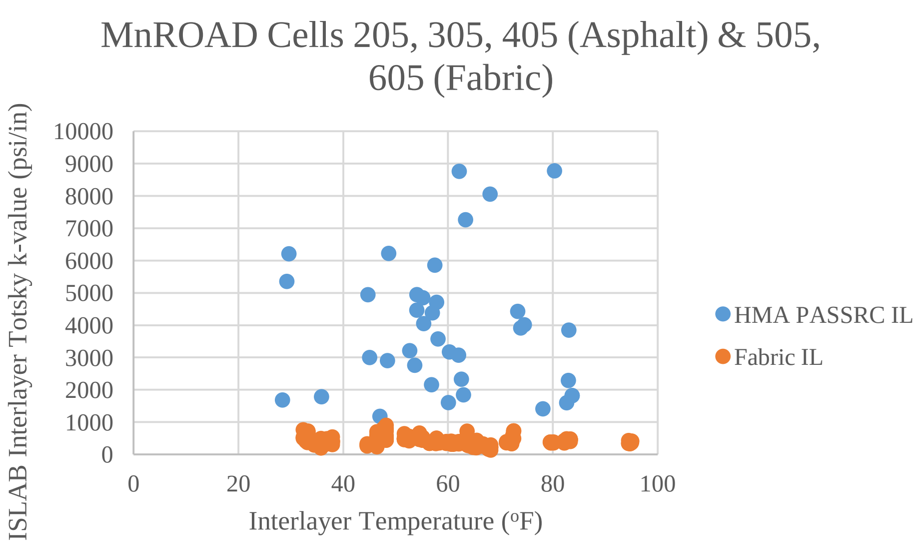

Figure 4.5. Interlayer Totsky k-value established from MnROAD FWD

Table 4.7. T-tests comparing FWD Totsky results

Comparison between means of established Totsky values	P-value of t-test for difference in means
Fabric LAB vs. MnROAD Fabric FWD	0.126
MNONU LAB vs. MnROAD Asphalt FWD	0.137
MnROAD Fabric FWD vs. MnROAD Asphalt FWD	<0.001

From the laboratory testing, the only significant comparisons were that all asphalt interlayers, except MNONU, were significantly different from the two fabric interlayers. Additionally, no apparent relationship exists between asphalt stiffness or thickness and Totsky k-values within the different asphalt interlayers tested. The k-values determined using FWD test data are not statistically different from the lab values for the same interlayer type, while the fabric and asphalt k-values established using FWD test data are statistically different from one another. Since there is not an apparent trend between different asphalt types or with temperature, one value is recommended as an average for all asphalt interlayer types and temperatures. Averaging the results from both the laboratory and FWD investigations produces an average Totsky value of approximately 3500 psi/in. This value is recommended for use in the development of a design procedure for UBOL with an asphalt interlayer. No discernable difference was detected between different weight fabrics; however, the fabric stiffness was shown to be statistically different from the asphalt stiffness. Therefore, one value is recommended as an average for all nonwoven geotextile fabrics. The average Totsky value of the laboratory and FWD results is 425 psi/in and this value should be used in the development of a design procedure for UBOL with a nonwoven geotextile fabric interlayer.

4.4 MODELING PARAMETERS

In performing the runs necessary to create a database of critical response parameters to train neural networks to predict the critical structural responses, the range of parameters for the UBOL structure had to be established. Additionally, the choice of the critical response parameter to be used as the predictor in the faulting model are chosen.

4.4.1 Structural Parameters

Critical responses from the structural model must be established for every combination of variables considered. The structural model considers a wide range of parameters for the overlay, interlayer, and existing concrete slab. In performing the database of runs to generate critical responses, a baseline case is established and one parameter at a time is allowed to vary. In order to decrease the number of finite element runs required, some parameters within the structure are combined with one another. This can be seen in Figure 4.6. A list of all variables and range of values considered are included in Table 4.8. This design matrix results in approximately 100,000 finite element runs to be conducted. The values of the existing thickness, stiffness, and k-value are combined into a radius of relative stiffness. The radius of relative stiffness is adjusted from 20, 50, and 80 in by leaving the stiffness of the existing concrete as 4,500,000 psi and the k-value as 100 psi/in and only adjusting the thickness. The range of existing thicknesses becomes 3.5 to 22 in. To further decrease the number of finite elements runs that need to be generated, only three different values of flexural stiffness for the PCC overlay are used. The overlay elastic modulus remains 4,000,000 psi and only the thickness of the overlay is increased.

The values of flexural stiffness of the overlay are $2*10^7$, $3*10^8$, and $9*10^8$ lb-in. These values of flexural stiffness result in overlay thicknesses between 3.9 and 13.8 in.

Table 4.8. UBOL parameters for structural model

<table>
<tr><th>Parameter</th><th colspan="8"></th><th colspan="8"></th><th colspan="8"></th></tr>
<tr><td>Existing slab and foundation radius of relative stiffness, ℓ (in)</td><td colspan="8">20</td><td colspan="8">50</td><td colspan="8">80</td></tr>
<tr><td>Interlayer Totsky k-value (psi/in)</td><td colspan="8">2,000</td><td colspan="8">6,000</td><td colspan="8">10,000</td></tr>
<tr><td>Overlay Flexural Stiffness, D (lb-in)</td><td colspan="8">2.00E+07</td><td colspan="8">3.00E+08</td><td colspan="8">9.00E+08</td></tr>
<tr><td>Overlay PCC joint spacing x slab width (ft)</td><td colspan="8">6 x 6</td><td colspan="8">12 x 12</td><td colspan="8">15 x 12</td></tr>
<tr><td>Overlay Temp Difference (^oF)</td><td colspan="3">-30</td><td colspan="3">-20</td><td colspan="3">-10</td><td colspan="3">0</td><td colspan="3">10</td><td colspan="3">20</td><td colspan="3">30</td><td colspan="3">40</td></tr>
<tr><td>PCC Poisson’s ratio</td><td colspan="8">0.18</td><td colspan="8"></td><td colspan="8"></td></tr>
<tr><td>Longitudinal Lane shoulder LTE (%)</td><td colspan="8">Tied PCC (90 %)</td><td colspan="8">Asphalt (0 %)</td><td colspan="8"></td></tr>
<tr><td>Transverse Joint AGG Factor (psi)</td><td colspan="4">100</td><td colspan="4">1000</td><td colspan="4">10000</td><td colspan="4">50000</td><td colspan="4">100000</td><td colspan="4">1000000</td></tr>
<tr><td>Wheel wander (in)</td><td colspan="8">0</td><td colspan="8">4</td><td colspan="8">16</td></tr>
<tr><td>Single axle (lb)</td><td colspan="8">0</td><td colspan="8">18</td><td colspan="8">30</td></tr>
<tr><td>Tandem axle (lb)</td><td colspan="8">0</td><td colspan="8">36</td><td colspan="8">60</td></tr>
</table>

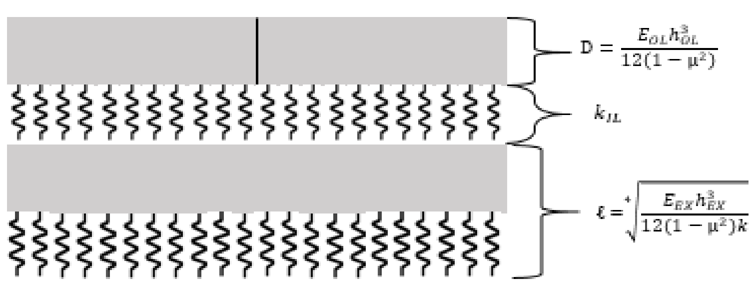

Figure 4.6. Consolidation of structural model for UBOL faulting model

The loading configuration of an axle is that shown in Figure 4.7. When considering tandem axles, the spacing between tires is defined as 40 in. For each different structure, 3 slabs are modeled in the driving lane and the passing lane is not modeled. If there is a tied shoulder then there is a shoulder modeled on the edge of the pavement, but in the case of an asphalt pavement no shoulder is modeled.

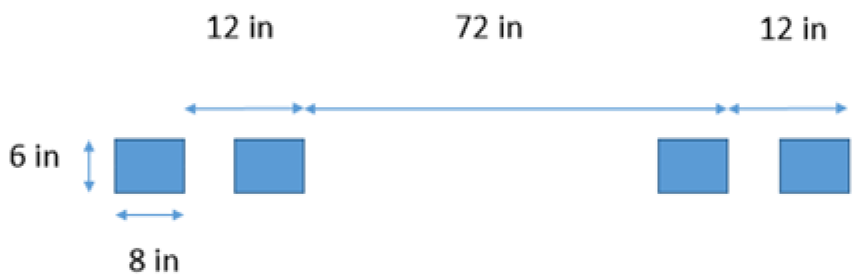

Figure 4.7. Axle configuration for structural modeling

4.4.2 Critical Response Parameters

The critical responses from the model will be used to calculate differential energy of the interlayer, which is shown in Equation 4.1. Within Pavement ME, the deflections on both the loaded and unloaded sides of the joint are taken to be the deflections at the corners of the approach and leave slabs. In order to more accurately represent the difference in energy density on both sides of the joint, a basin sum deflection is used as the critical response parameter for this structural model and design procedure. All of the vertical nodal displacements within a distance of 2 ft from the joint of interest are summed on both the loaded and unloaded sides of the joint to represent the deflections used to calculate the differential energy. This can be seen in Figure 4.8 below.

$$DE = \frac{1}{2}k(\delta_L^2 - \delta_{UL}^2) \qquad \textbf{Equation 4.1}$$

Where DE = differential energy, k = Totsky interlayer stiffness, δ_L = loaded slab deflection, and δ_{UL} = unloaded slab deflection.

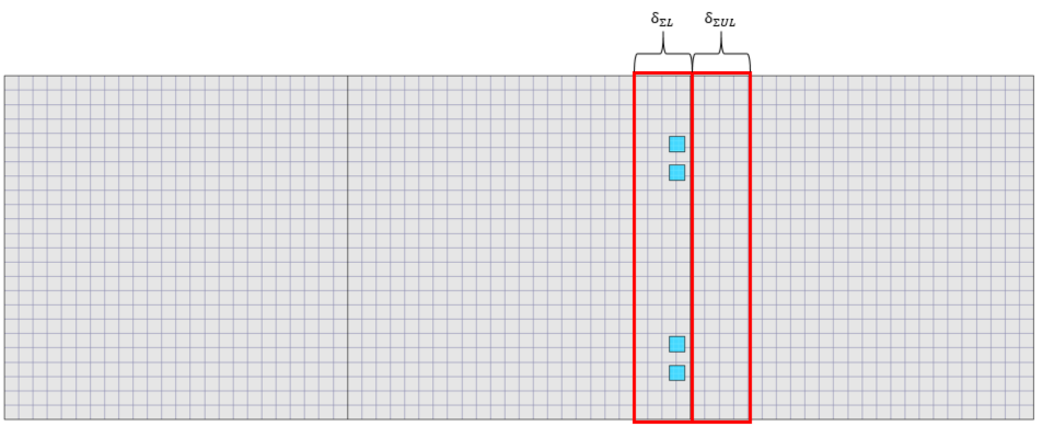

Figure 4.8. Representation of basin sum deflection on loaded and unloaded side of joint

For each combination of variables located in Table 4.8, an ISLAB structure is created and ran taking advantage of ISLABs batching capabilities. Then, all the nodes deflections within 2 ft of the joint on the loaded and unloaded side of the joint are calculated so they can be used to train neural networks for predicting the critical response parameters for any combination of structure, loading condition, joint stiffness, and overlay temperature difference.

4.5 NEURAL NETWORK DEVELOPMENT

Neural networks (NNs) are developed to predict the sum of the vertical nodal displacements within a distance of 2 ft from the joint on both the loaded and unloaded sides of the joint for the entire panel. The neural network toolbox in MATLAB is used to train, validate, and test the neural networks (MATLAB, 2013). Separate neural networks are developed for temperature loading only and for a combination of load and temperature. Due to symmetry of the temperature loading condition, only one NN is developed for both the loaded and unloaded sides of the joint. Four NNs are developed for the condition when there is a combination of load and temperature. These consist of the loaded and unloaded side for both single and tandem axles. The predictors for each of these NNs are presented along with pertinent network development information. Finally, the results of the training are presented.

Each of the NNs with each of their predictors are shown in Equation 4.2 through Equation 4.4.

$$\boldsymbol{NN_{\Sigma L,A}}(\boldsymbol{JTSpace}, \mathrm{l}_{\boldsymbol{OL}}, \mathrm{l}_{\boldsymbol{EX}}, \boldsymbol{LTE_{shoulder}}, \boldsymbol{AGG/k_{IL}}\mathrm{l}_{\boldsymbol{OL}}, \boldsymbol{\Phi}, \boldsymbol{q_i^*}, \boldsymbol{s}) \qquad \textbf{Equation 4.2}$$

$$\boldsymbol{NN_{\Sigma UL,A}}(\boldsymbol{JTSpace}, \mathrm{l}_{\boldsymbol{OL}}, \mathrm{l}_{\mathrm{EX}}, \boldsymbol{LTE_{shoulder}}, \boldsymbol{AGG/k_{IL}}\mathrm{l}_{\boldsymbol{OL}}, \boldsymbol{\Phi}, \boldsymbol{q_i^*}, \boldsymbol{s}) \qquad \textbf{Equation 4.3}$$

$$\boldsymbol{NN_{\Sigma T}}(\boldsymbol{JTSpace}, \mathrm{l}_{\boldsymbol{OL}}, \mathrm{l}_{\boldsymbol{EX}}, \boldsymbol{LTE_{shoulder}}, \boldsymbol{AGG/k_{IL}}\mathrm{l}_{\boldsymbol{OL}}, \boldsymbol{\Phi}) \qquad \textbf{Equation 4.4}$$

Where $NN_{\Sigma L,A}$ = Neural Network for the sum of the 2-ft deflection basin for the loaded slab for axle type A (= 1 for single and = 2 for double), $NN_{\Sigma UL,A}$ = Neural Network for the basin sum unloaded deflection for axle type A (= 1 for single and = 2 for double), $NN_{\Sigma T}$ = Neural Network for the basin sum deflection for the condition when only temperature is present. The predictors for the sum loaded and unloaded deflection are the same, while the NN to predict temperature load excludes the predictors related to axle loading. $JTSpace$ is the joint spacing in the overlay (ft). $l_{OL} = \sqrt[4]{\frac{E_{OL} h_{OL}^3}{12(1-\mu^2)k_{IL}}}$ is the radius of relative stiffness of the overlay (in), $l_{EX} = \sqrt[4]{\frac{E_{EX} h_{EX}^3}{12(1-\mu^2)k}}$ is the radius of relative stiffness of the existing pavement (in). $LTE_{shoulder}$ is the lane/shoulder LTE (%). $AGG/k_{IL}l_{OL}$ is the nondimensional joint stiffness where AGG = joint load transfer stiffness (psi), k_{IL} = Totsky interlayer k-value (psi/in), and l_{OL} = radius of relative stiffness for the overlay (in). $\Phi = \frac{2\alpha_{pcc}(1+\mu_{pcc})l_{OL}^2}{h_{OL}^2}\frac{k_{IL}}{\gamma_{pcc}}\Delta T$ is Korenev's nondimensional temperature gradient where α_{pcc} = coefficient of thermal expansion for the overlay concrete (in/in/^{o}F), γ_{pcc} = is the unit weight of the overlay concrete (pci), and ΔT is the temperature difference in the overlay. $q_i^* = \frac{P_i}{A * \gamma_{pcc} * h_{OL}}$ is the adjusted load/pavement weight ratio where P_i = axle load (lbs), A = parameter for axle type (= 1 for single and = 2 for tandem axles). s = wheel wander (in).

The NN architecture was established through trial and error and the same structure was used for each network. For each of the NNs trained, 2 hidden layers of 20 neurons each is used. The Levenberg-Marquardt backpropagation algorithm is used to train the network, and the default split is used between the training, validation, and the test sets (70%, 15%, and 15% of samples respectively). Each NN was trained 10 times and the results are averaged over the 10 networks. Figure 4.9 shows the results of the training, validation, and test sets for the single axle loaded and unloaded NNs. Figure 4.10 shows the results of the training, validation, and test sets for the tandem axle loaded and unloaded NNs. Figure 4.11 shows the results of the training, validation, and test sets for the temperature loading NN.

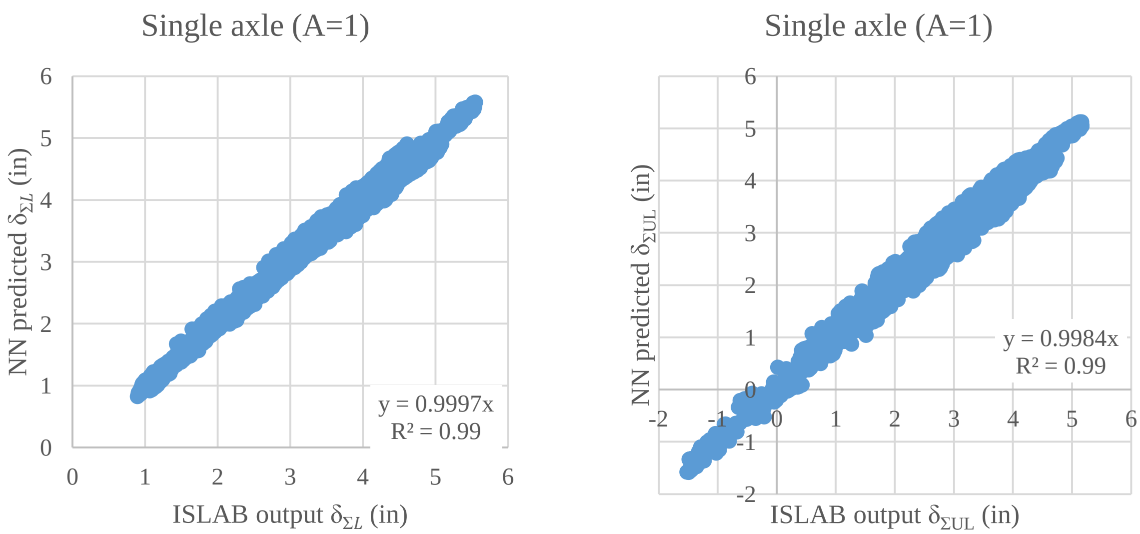

(a) (b)

Figure 4.9. Comparison of (a) $\mathbf{NN_{\Sigma L,A}}$ and (b) $\mathbf{NN_{\Sigma UL,A}}$ for A = 1 versus ISLAB

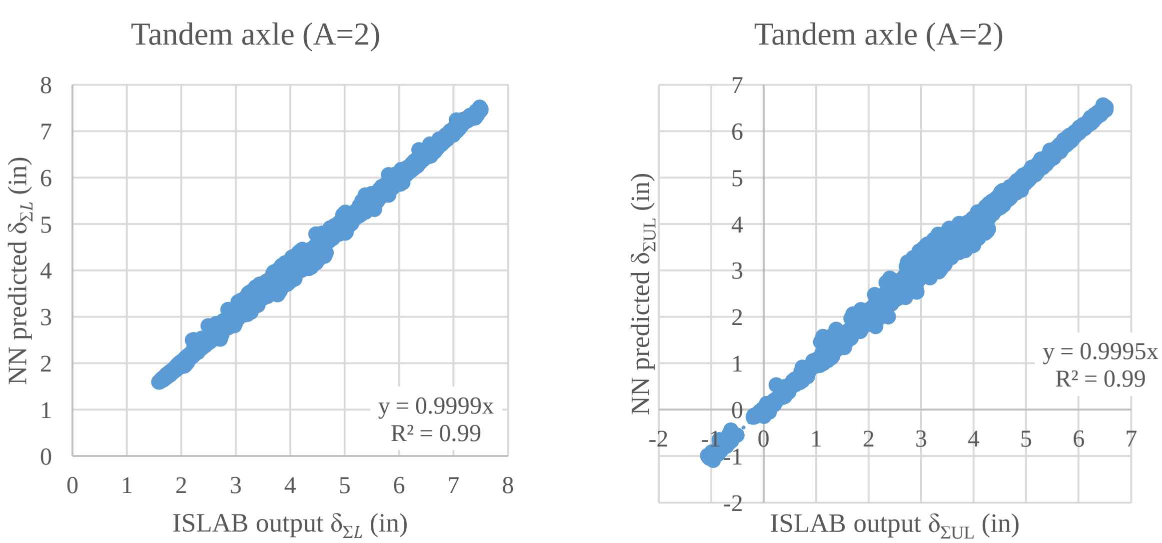

(a) (b)

Figure 4.10. Comparison of (a) $\mathbf{NN_{\Sigma L,A}}$ and (b) $\mathbf{NN_{\Sigma UL,A}}$ for A = 2 versus ISLAB

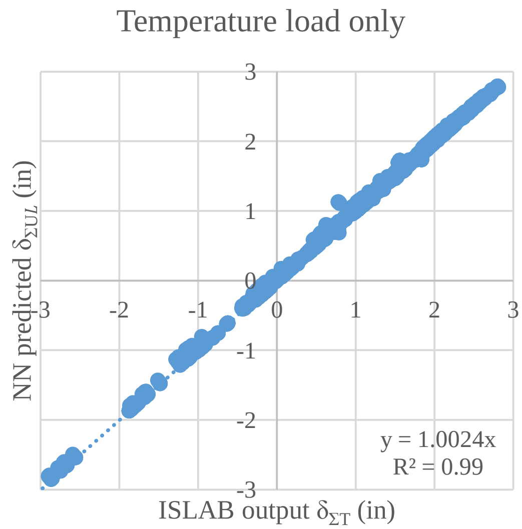

Figure 4.11. Comparison of $\mathbf{NN_{\Sigma T}}$ versus ISLAB

In addition to the testing of the neural networks using 15% of the runs from the database, an additional test of the networks was performed with independent, randomly generated, parameters which spanned the range of values defined in the matrix provided in Table 4.8. This was performed to test the robustness of the NNs. Approximately 3000 different points were tested for the combination of load and temperature for the single axle NNs and approximately 3000 different points were tested for the combination of load and temperature for the single axle NNs. About 1000 points were tested for the temperature load only NNs. The results of these predictions can be seen in Figure 4.12 for the single axle NNs, Figure 4.13 for the tandem axle NNs, and Figure 4.14 for the temperature load only NNs.

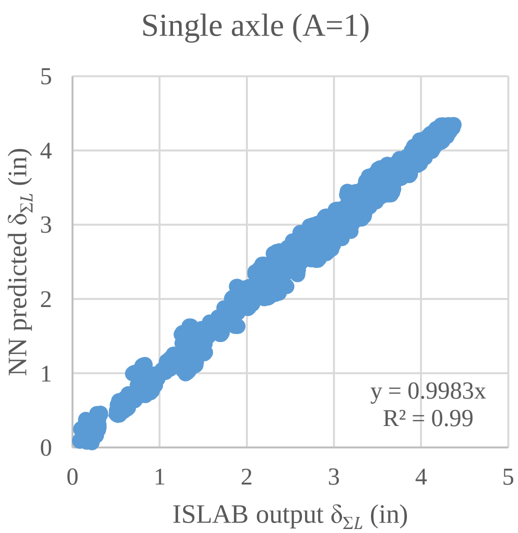

(a)

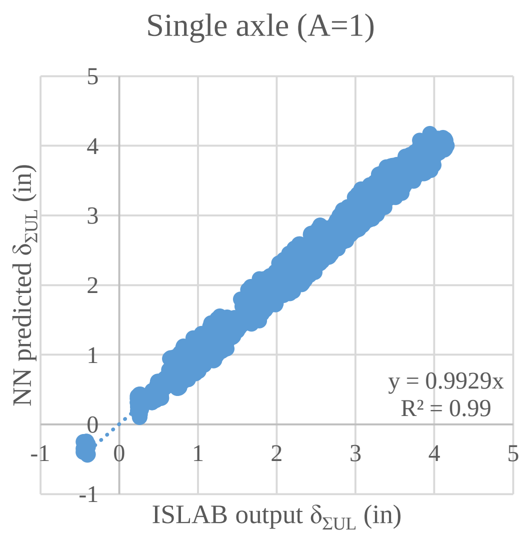

(b)

Figure 4.12. Predictability of (a) $\mathbf{NN_{\Sigma L,A}}$ and (b) $\mathbf{NN_{\Sigma UL,A}}$ for A = 1

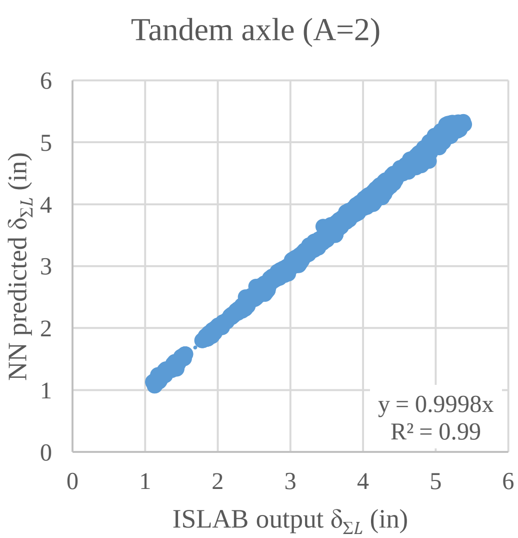

(a)

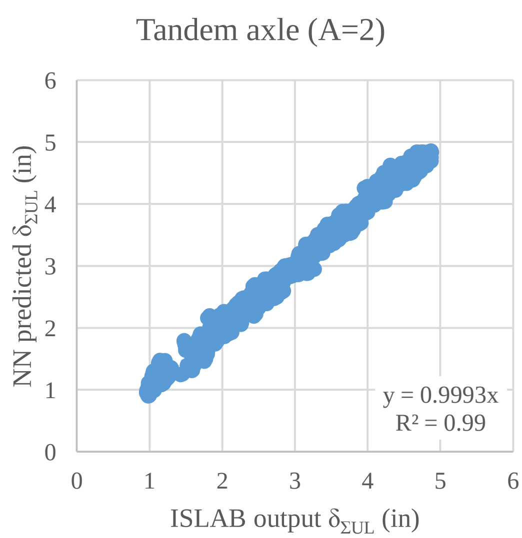

(b)

Figure 4.13. Predictability of (a) $\mathbf{NN_{\Sigma L,A}}$ and (b) $\mathbf{NN_{\Sigma UL,A}}$ for A = 2

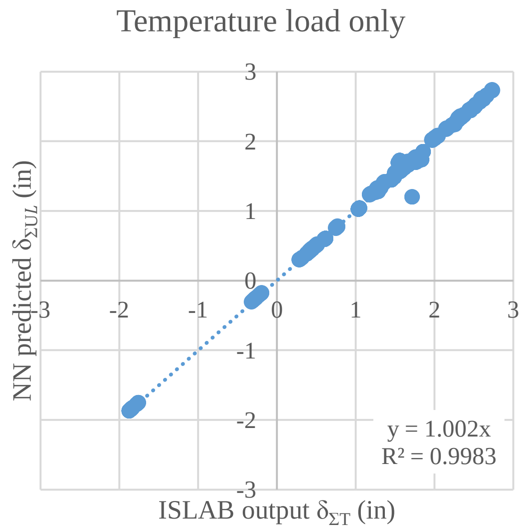

Figure 4.14. Predictability of (a) $\mathbf{NN_{\Sigma T}}$

4.6 CONCLUSIONS

In this chapter, ISLAB is established as the software to be used for the structural modeling. An investigation to establish the Totsky interlayer k-value parameter using both laboratory data from the reflective cracking test and a FWD analysis was conducted. This investigation yielded recommended values of the Totsky k-value of 3500 psi/in for asphalt interlayers and 425 psi/in for nonwoven geotextile fabric interlayers. Additionally, the factorial of design variables to generate a database of finite element runs was established and the critical response parameter of a nodal sum deflection within 2 ft from the joint along the entire panel is established. Finally, the details of the NNs developed were presented including the predictors along with the network architecture. Finally, plots comparing the results from ISLAB to that of the NNs are presented.

These NNs are then used within a framework to predict joint faulting for UBOL. The faulting model will be discussed in Chapter 5.

5.0 JOINT FAUTING MODEL DEVELOPMENT FOR UNBONDED CONCRETE OVERLAYS OF EXISTING CONCRETE PAVEMENTS

This chapter details the UBOL faulting model development. First, previously developed faulting models are presented and outlined. Then, the framework that is established for UBOL joint faulting is presented, focusing on the steps which go into the monthly incremental analysis. Information regarding the calibration sections is then provided with detailed section information presented in Appendix F. Results of the model calibration are discussed including the calibrated model coefficients as well as the developed standard deviation model for reliability. Finally, comparisons are made between the observed and predicted faulting and a sensitivity analysis is presented.

5.1 PREVIOUSLY DEVELOPED FAULTING MODELS

Many of the faulting models developed under previous research were reviewed. Specific attention to the variables chosen for inclusion in the models was made. The details of each of the faulting models reviewed under this study are described separately in the following sections. The faulting models presented are only for Jointed Plain Concrete Pavements (JPCP). Six different models presented.

ACPA JPCP Transverse Joint Faulting Model

The first model presented is a mechanistic-empirical faulting model for doweled and undoweled pavements developed for the American Concrete Paving Association (ACPA) by Wu et al. (1993). These models were expanded from models developed for the Portland Cement Association (PCA) by Packard (1977). The percent erosion damage is established using Miner's linear cumulative damage concept in Equation 5.1 (Wu et al, 1993). The allowable number of load applications is computed using Equation 5.2. The power of each axle pass at the corner of the slab is computed using Equation 5.3. The faulting for JPCP doweled and undoweled pavements can then be calculated using Equation 5.4 and Equation 5.5, respectively.

$$EROSION = 100 \sum_{i} \frac{C_2 n_i}{N_i}$$ **Equation 5.1**

where $EROSION$ = percent erosion damage, n_i = expected number of axle load repetitions for each axle group I, N_i = allowable number of axle load repetitions for each axle group I, and C_2 = a constant which takes into account the presence of a tied shoulder.

$$Log(N) = 14.524 - 6.777 * (C1 * P - 9.0)^{0.103}$$ **Equation 5.2**

where N = allowable number of axle load repetitions during the design period, P = power of each axle pass at the corner of the slab, $C1 = 1 - (\frac{k}{2000} * \frac{4}{h_{pcc}})^2$, k = modulus of subgrade reaction (psi/in), and h_{pcc} = slab thickness (in).

$$P = 268.7 * \frac{p^2}{h_{pcc}\, k^{0.73}}$$ **Equation 5.3**

where P = power of each axle pass at the corner of the slab, p = pressure at slab-foundation interface (psi).

$$FAULTD = EROSION^{0.25} * [0.0038332 * \left(\frac{PRECIP}{10}\right)^{1.84121} + 0.0057763 * JTSPACE^{0.38274}]$$ **Equation 5.4**

$$FAULTND = EROSION^{0.25} * [9.75873 * 10^{-4} * (PRECIP)^{0.91907} + 0.0060291 * JTSPACE^{0.54428} - 0.016799 * DRAIN]$$ **Equation 5.5**

where $FAULTD$ = mean transverse doweled joint faulting (in), $FAULTND$ = mean transverse undoweled joint faulting (in), $EROSION$ = percent erosion damage (Equation 5.1), $PRECIP$ = annual precipitation (in), $JTSPACE$ = transverse joint spacing (ft), $DRAIN$ = 1 (w/ edge drains) = 0 (w/o edge drains).

SHRP P-020 JPCP Transverse Joint Faulting Model

Simpson et al. (1994) conducted a Strategic Highway Research Program (SHRP) project looking at early Long Term Pavement Performance (LTPP) General Pavement Study data and developed both doweled and undoweled JPCP faulting models which are presented in Equation 5.6 and Equation 5.7, respectively.

$$FAULTD = CESAL^{0.25} * [0.0238 + 0.0006 * \left(\frac{JTSPACE}{10}\right)^2 + 0.0037 * \left(\frac{100}{k_{static}}\right)^2 + 0.0039 * \left(\frac{AGE}{10}\right)^2 - 0.0037 * EDGESUP - 0.0218 * DOWELDIA]$$ **Equation 5.6**

$$FAULTND = CESAL^{0.25} * [-0.07575 + 0.0251 * \sqrt{AGE} + 0.0013 * \left(\frac{PRECIP}{10}\right)^2 + 0.0012 * \left(FI * \frac{PRECIP}{1000}\right) - 0.0378 * DRAIN]$$ **Equation 5.7**

where $FAULTD$ = mean transverse doweled joint faulting (in), $FAULTND$ = mean transverse undoweled joint faulting (in), $CESAL$ = cumulative 18-kip ESALs in traffic lane (millions), $JTSPACE$ = transverse joint spacing (ft), k_{static} = mean backcalculated static k-value (psi/in), AGE = age since construction (yrs), $EDGESUP$ = edge support (1 = tied PCC shoulder, 0 = any other shoulder type), $DOWELDIA$ = diameter of dowel in transverse joints (in), $PRECIP$ = mean annual precipitation (in), FI = mean freezing index (^{o}F-days), $DRAIN$ = drainage type (1 = longitudinal subdrainage, 0 = otherwise).

FHWA RPPR 1997 JPCP Transverse Joint Faulting Model

Yu et al. (1996) developed both doweled and undoweled faulting models as part of the Federal Highway Administration (FHWA) RPPR project. These models are presented as Equation 5.8 and Equation 5.9 below.

$$\begin{aligned} FAULTD = CESAL^{0.25} * [&0.0628 - 0.0628 * C_d * + 0.3673 * 10^{-8} * BSTRESS^2 \\ &+ 0.4116 * 10^{-5} * JTSPACE^2 + 0.7466 * 10^{-9} * FI^2 * PRECIP^{0.5} \\ &- 0.009503 * BASE - 0.01917 * WIDENLANE + 0.0009217 \\ &* AGE] \end{aligned} \quad \textbf{Equation 5.8}$$

$$\begin{aligned} FAULTND = CESAL^{0.25} * [&0.2347 - 0.1516 * C_d - 0.00025 * \frac{h_{pcc}^2}{JTSPACE} - 0.0115 \\ &* BASE + 0.7784 * 10^{-7} * FI^{1.5} * PRECIP^{0.25} - 0.002478 \\ &* DAYS90^{0.5} - 0.0415 * WIDENLANE] \end{aligned} \quad \textbf{Equation 5.9}$$

where $FAULTD$ = mean transverse doweled joint faulting (in), $FAULTND$ = mean transverse undoweled joint faulting (in), $CESAL$ = cumulative 18-kip ESALs in traffic lane (millions), C_d = modified AASHTO drainage coefficient, $BSTRESS$ = maximum dowel/concrete bearing stress (psi), $JTSPACE$ = transverse joint spacing (ft), FI = mean freezing index (^{o}F-days), $PRECIP$ = mean annual precipitation (in), $BASE$ = base type (0 = nonstabilized base, 1 = stabilized base), $WIDENLANE$ = widened lane (0 = not widened, 1 = widened), AGE = age since construction (yrs), $DRAIN$ = drainage type (1 = longitudinal subdrainage, 0 = otherwise), h_{pcc} = slab thickness (in), $DAYS90$ = mean annual number of hot days (days with max temperature greater than 90 ^{o}F).

LTPP Data Analysis Study JPCP Transverse Joint Faulting Model

Titus-Glover et al. (1999) recalibrated the 1997 Nationwide Pavement Cost Model (NAPCOM) model (Owusu-Antwi et al, 1997) using only LTPP data. Equation 5.10 is the developed model for both doweled and undoweled pavements.

$$\begin{aligned} FAULT = DAMAGE^{0.3} * [&0.05 + 0.00004 * WETDAYS - 0.0024 * DOWELDIA \\ &- 0.025 * C_d * (0.5 + BASE)] \end{aligned} \quad \textbf{Equation 5.10}$$

where $FAULT$ = mean transverse joint faulting (in), $DAMAGE$ = n/N, n = cumulative 18-kip ESALs applied, N = cumulative 18-kip ESALs allowable, Log(N) = 4.27-1.6*Log(DE), DE

= differential subgrade elastic energy density, $WETDAYS$ = annual average number of wet days, $DOWELDIA$ = diameter of dowel in transverse joints (in), C_d = AASHTO drainage coefficient, $BASE$ = base type (0 = erodible base, 1 = nonerodible base).

NCHRP 1-34 Model

Yu et al. (1998) developed the model in Equation 5.11 as part of the National Cooperative Highway Research Program (NCHRP) project 1-34.

$$FAULT = DAMAGE^{0.2475} * [0.2405 - 0.00118 * DAYS90 + 0.001216 * WETDAYS - 0.04336 * BASETYPE - (0.004336 + 0.007059 * (1 - DOWEL)) * LCB] \quad \textbf{Equation 5.11}$$

where $FAULT$ = mean transverse joint faulting (in), $DAMAGE$ = n/N, n = cumulative 18 kip ESALs applied, N = cumulative 18 kip ESALs allowable, Log(N) = 0.785983-0.92991*(1+0.4*PERM*(1-DOWEL))*Log(DE), PERM = base permeability (0 = not permeable, 1 = permeable), DE = differential subgrade elastic energy density, $DAYS90$ = number of days per year with the maximum temperature greater than 90°F, $WETDAYS$ = annual average number of wet days, $BASETYPE$ = (0 if not stabilized, 1 if stabilized), $DOWEL$ = presence of dowels (1 = present, 0 = not present), LCB = presence of lean concrete base (1 if present, 0 if not present).

Pavement ME Model

The Pavement ME faulting model is a monthly incremental approach developed by ARA (2004). For each month of an analysis, a faulting increment, that is dependent on the faulting level from the previous month, is determined. Faulting is then determined by summing the faulting increments from all of the previous months. Equation 5.12 through Equation 5.15 detail the faulting models iterative process (ARA, 2004).

$$FMAX_0 = (C_1 + C_2 * FR^{0.25}) * \delta_{curl} * \left[Log(1 + C_5 * 5^{EROD}) * Log(\frac{P_{200} * WetDays}{p_s})\right]^{C_6}$$ **Equation 5.12**

$$FMAX_i = FMAX_{i-1} + C_7 * DE_i * [Log(1 + C_5 * 5^{EROD})]^{C_6}$$ **Equation 5.13**

$$\Delta Fault_i = (C_3 + C_4 * FR^{0.25}) * (FMAX_{i-1} - Fault_{i-1})^2 * DE_i$$ **Equation 5.14**

$$Fault_i = Fault_{i-1} + \Delta Fault_i$$ **Equation 5.15**

where $FMAX_0 =$ initial maximum mean transverse joint faulting (in), *FR* = base freezing index defined at the percentage of the time that the top of the base is below freezing, $\delta_{curl} =$ maximum mean monthly PCC upward slab corner deflection due to temperature curling and moisture warping, *EROD* = base/subbase erodibility index (Integer between 1 and 5), $P_{200} =$ percent of the subgrade soil passing No. 200 sieve, *WetDays* = average number of annual wet days (> 0.1 in of rainfall), $p_s =$ overburden on subgrade (lb), $FMAX_i =$ maximum mean transverse joint faulting for month i (in), $FMAX_{i-1} =$ maximum mean transverse joint faulting for month i-1 (in) (If i =1, $FMAX_{i-1} = FMAX_0$), $DE_i =$ differential energy density of subgrade accumulated during month i, $\Delta Fault_i =$ incremental monthly change in mean transverse joint faulting during month i (in), *FR* = base freezing index defined at the percentage of the time that the top of the base is below freezing (<32°F), $Fault_{i-1} =$ mean joint faulting at the beginning of month i (in) (0 if i = 1), C_1 ... $C_7 =$ calibration coefficients.

The one component of the faulting calculation that changes from month to month is the differential energy. The differential energy is computed using Equation 5.16. Neural networks are used to calculate the loaded and unloaded slab deflection for each axle and temperature loading condition, and then the differential energy is calculated for each axle crossing the pavement structure for each month of the analysis. This value of differential energy is then used in Equation 5.12 through Equation 5.15.

$$DE_m = \sum_{A=1}^{3}\sum_{i=1}^{N_A}\frac{1}{2}n_{i,A}k_m\left(\delta_{L,i,A}^2 - \delta_{U,i,A}^2\right)$$ **Equation 5.16**

where $DE_m =$ differential energy density of subgrade deformation accumulated for month m, $n_{i,A}$ = number of axle load applications for current month and load group i, k_m = modulus of subgrade reaction for month m, $\delta_{L,i,A} =$ corner deflections of the loaded slab caused by axle loading, $\delta_{L,i,A} =$ corner deflections of the unloaded slab caused by axle loading.

Of the procedures which have been presented, important predictive parameters include the following: the differential energy between the loaded and unloaded slabs, an indication of the amount of precipitation, an estimate of the traffic, the presence of dowel bars, and an indication of the erodibility of the base material. The Pavement ME faulting model is the standard mechanistic-empirical framework currently available. Therefore, the framework for the UBOL faulting model will adopt a similar approach in predicting joint faulting.

5.2 FAULTING MODEL FRAMEWORK

The framework to determine faulting involves using the NNs developed in Chapter 4 to determine the differential energy. For this model, an iterative monthly incremental analysis is performed. The treatment of climatic considerations and the calculation of joint stiffness is outlined. A discussion on the calculation of differential energy and the functional form of the faulting calculation will then follow.

5.2.1 Climatic Considerations

This sections deals primarily with the treatment of temperature gradients in the overlay since it was established that there is no significant relationship between interlayer temperature and the resulting Totsky k-value. Within the current framework, a separate analysis for each structure must be carried out within the Enhanced Integrated Climatic Model (EICM) (Larson and Dempsey 2003). EICM is used to perform an hourly incremental analysis for predicting the temperature profile in the pavement structure at specified depths. This is then used to help establish gradients for use in the design process. For each calibration section, an EICM file is created. Within EICM, the structure must be defined including layer thicknesses, the number of nodes for each layer. Additionally, thermal properties, permeability, porosity, and water content must be defined to model moisture movement in granular layers. Within the overlay, nodes are placed at one inch increment depths. Additionally, the nearest weather stations to the calibration sites are chosen to give hourly values of air temperature, precipitation, wind speed, and percent sunshine for several years that can be output as a file with an .icm extension. The program is then run to give hourly nodal temperature depths throughout the structure that is output as a file with a .tem file extension by the software. This information is then used to determine the mean monthly mid-depth overlay temperature, establish hourly equivalent strain gradients, and determine the freezing ratio (FR), which is the percentage of time that the interlayer is less than 32^{o}F. The .icm file for each EICM analysis is used to establish mean monthly air temperature and the number of wet days in a year.

The equivalent strain gradients are calculated using the temperature-moment concept (Janssen and Snyder 2000) that converts the nonlinear temperature profile for a specific hour generated by the EICM into an equivalent linear temperature gradient (ELTG) using Equation

5.17 through Equation 5.19. This method establishes an ELTG that would impose the same deformation in the overlay as would be imposed by the nonlinear temperature distribution.

$$T_{ave} = \sum_{i=1}^{n} \left[\frac{0.5(t_i + t_{i+1})(d_i - d_{i+1})}{(d_1 - d_n)} \right] \qquad \textbf{Equation 5.17}$$

$$TM_0 = -0.25 \sum_{i=1}^{n} [(t_i + t_{i+1})(d_i^2 - d_{i+1}^2) - 2(d_1^2 - d_n^2)T_{ave}] \qquad \textbf{Equation 5.18}$$

$$ELTG = -\frac{12 \cdot TM_0}{h^3} \qquad \textbf{Equation 5.19}$$

where ELTG is the equivalent linear temperature gradient (°F/in), T_{ave} is the average temperature (°F), TM_0 is the temperature moment (°F·in^2), d_i is the depth of the i^{th} node (in), and t_i is the temperature at depth d_i (°F).

In order to perform a monthly analysis instead of an hourly incremental analysis, it is necessary to create an effective equivalent linear temperature gradient so that hourly incremental damage can be equated to monthly incremental damage. For each month, the differential energy is summed with the hourly ELTGs for each calibration section. Then, fminsearch in MATLAB is used to find a single temperature gradient, which causes the same value of differential energy calculated using the NNs from Chapter 4. For this analysis, 1 million ESALs (18-kip single axle loads) are applied over the course of the year, distributed hourly according to the percentages established in Pavement ME based on LTPP traffic data and presented in Table 5.1 (ARA, 2004). Monthly joint and overlay stiffness are also used in this analysis. The following section describes how the inputs for the NNs are established.

Table 5.1. Hourly truck traffic distributions from Pavement ME (ARA, 2004)

Time period	Distribution (percent)	Time period	Distribution (%)
12:00 a.m. - 1:00 a.m.	2.3	12:00 p.m. - 1:00 p.m.	5.9
1:00 a.m. - 2:00 a.m.	2.3	1:00 p.m. - 2:00 p.m.	5.9
2:00 a.m. - 3:00 a.m.	2.3	2:00 p.m. - 3:00 p.m.	5.9
3:00 a.m. - 4:00 a.m.	2.3	3:00 p.m. - 4:00 p.m.	5.9
4:00 a.m. - 5:00 a.m.	2.3	4:00 p.m. - 5:00 p.m.	4.6
5:00 a.m. - 6:00 a.m.	2.3	5:00 p.m. - 6:00 p.m.	4.6
6:00 a.m. - 7:00 a.m.	5.0	6:00 p.m. - 7:00 p.m.	4.6
7:00 a.m. - 8:00 a.m.	5.0	7:00 p.m. - 8:00 p.m.	4.6
8:00 a.m. - 9:00 a.m.	5.0	8:00 p.m. - 9:00 p.m.	3.1
9:00 a.m. - 10:00 a.m.	5.0	9:00 p.m. - 10:00 p.m.	3.1
10:00 a.m. – 11:00 a.m.	5.9	10:00 p.m. – 11:00 p.m.	3.1
11:00 a.m. – 12:00 p.m.	5.9	11:00 p.m. – 12:00 a.m.	3.1

5.2.2 Model Inputs

The iterative faulting calculations are performed using the equivalent temperature gradients defined for each calibration section while the monthly differential energy is determined using Equation 5.20 through Equation 5.22. The inputs for the neural networks are defined below.

$$\Sigma\delta_{L,m} = [NN_{\Sigma L,m}(JTSpace, \ell_{OL}, \ell_{EX}, LTE_{shoulder}, AGG/k_{IL}\ell_{OL}, \Phi, q_m^*, s) - NN_{\Sigma L,m}(JTSpace, \ell_{OL}, \ell_{EX}, LTE_{shoulder}, AGG/k_{IL}\ell_{OL}, \Phi, 0, s)] \quad \textbf{Equation 5.20}$$

$$\Sigma\delta_{UL,m} = [NN_{\Sigma UL,m}(JTSpace, \ell_{OL}, \ell_{EX}, LTE_{shoulder}, AGG/k_{IL}\ell_{OL}, \Phi, q_m^*, s) - NN_{\Sigma UL,m}(JTSpace, \ell_{OL}, \ell_{EX}, LTE_{shoulder}, AGG/k_{IL}\ell_{OL}, \Phi, 0, s)] \quad \textbf{Equation 5.21}$$

$$DE_m = \frac{1}{2} n_m k\left(\Sigma\delta_{L,m}^2 - \Sigma\delta_{UL,m}^2\right) \quad \textbf{Equation 5.22}$$

where the variables in Equation 5.20 and Equation 5.21 are defined in Chapter 4, DE_m = differential energy density deformation accumulated for month m, n_m = number of ESAL applications for the current month, k = Totsky interlayer stiffness (psi/in), $\Sigma\delta_{L,m}$ = basin sum deflection of the loaded slab for month m (in), $\Sigma\delta_{UL,m}$ = basin sum deflection of the unloaded slab for month m (in).

For each calibration section, the four files needed to perform the faulting calculation include the input, traffic, .tem, and .icm files. The .tem and .icm EICM files have been previously discussed along with the climatic considerations. Example input and traffic text files are shown in Table 5.2. Twenty one different inputs are specified for each calibration section, as can be seen in Table 5.2a. The traffic file has four columns which from left to right are the overall month in the analysis, the calendar month of the year, the year, and the ESALs observed for that month.

Table 5.2. Examples of (a) an input text file and (b) a traffic text file

(a)

6.4	Thickness of overlay (in)
3812505	Elastic modulus of the overlay (psi)
5338	28 day compressive strength of overlay (psi)
808	28 day modulus of rupture of overlay (psi)
0.1	Thickness of interlayer (in)
6.31	Percent passing N0. 200 sieve in interlayer (%)
8.5	Percent air voids in interlayer (%)
11	Effective percent binder content in interlayer (%)
3500	k-value of interlayer (psi/in)
8.1	Thickness of existing pavement (in)
3900000	Elastic modulus of the existing pavement (psi)
250	k-value of all layers beneath the existing pavement (psi/in)
15.5	Joint spacing of the overlay (ft)
0	Presence of dowels (0=none, 1=yes)
0	dowel diameter (in)
40	Lane-shoulder LTE (%)
0.0000055	Overlay Coefficient of thremal expansion (in/in/degF)
408	Months of the design analysis
-0.868	EELTG established from ELTGfault.m for each calibration site
5	Numeric month of overlay construction
564	Cement content for overlay concrete (lbs)

(b)

Month	Month	Year	ESALs
1	2	1986	40900
2	3	1986	40900
3	4	1986	40900
4	5	1986	40900
5	6	1986	40900
6	7	1986	40900
7	8	1986	40900
8	9	1986	40900
9	10	1986	40900
10	11	1986	40900
11	12	1986	40900
12	1	1987	40900
13	2	1987	40900
14	3	1987	40900
15	4	1987	40900
16	5	1987	40900

Looking at the inputs to the NNs, the joint spacing and the radius of relative stiffness of the overlay and existing pavements can be gleaned from the information provided in the NN input file. Note that a default value of 0.18 is assumed for the Poisson's ratio of the concrete. Additionally, $LTE_{shoulder}$ is defined as 40% when there is a tied concrete shoulder and 0% when an asphalt shoulder is used. The long-term LTE for a tied shoulder joint in Pavement ME is also 40% (ARA, 2004). The normalized load-pavement weight ratio, $q_m^* = \frac{P_i}{\gamma_{pcc} * h_{OL}}$. P_i is taken to be 18,000 lbs and the unit weight of the concrete, γ_{pcc}, is 150 lbs/ft^3 for all calibration sections. The wheel wander, s, is assumed to be normally distributed in the wheelpath with a standard deviation of 10 in. Korenev's nondimensional temperature gradient, Φ, is defined according to the equation in Chapter 4. All variables in this equation have been discussed previous with the exception of the temperature difference, ΔT. In this procedure, the temperature difference is defined as the monthly transient equivalent temperature difference plus the effective built-in temperature difference. The default value of -10 ^{o}F used in Pavement ME was also adopted here (ARA, 2004). The final NN input is $AGG/k_{IL}\ell_{OL}$. This variable is also referred to as the nondimensional joint stiffness. In order to calculate the nondimensional joint stiffness, the contribution of both aggregate interlock and the dowels in the overlay must be considered.

In order to examine the effects of aggregate interlock on joint stiffness, the joint width must be estimated. The joint width for each month is calculated according to Equation 5.23. The two variables that still need to be determined to calculate the joint width are the PCC set temperature and the PCC overlay shrinkage strain. The concrete set temperature is estimated using Table 5.3, which requires the mean monthly temperature for the month when the overlay was paved as well as the cement content of the paving mixture. The concrete overlay shrinkage strain is established using the tensile strength (correlated from compressive strength) based on the recommendations in AASHTO 93. This recommendation is shown in Table 5.4. The nondimensional aggregate joint stiffness is then calculated for each month using Equation 5.24 and Equation 5.25 adopted from Zollinger et al. (1998). Note that ΔS_{tot} is equal to zero for the first month of the analysis and the individual monthly increments of loss in shear capacity is calculated using Equation 5.26.

$$JW(m) = max\,(12000 * c * JTSpace * (CTE * (T_c - T(m)) + \varepsilon_{sh}), 0) \qquad \textbf{Equation 5.23}$$

where $JW(m)$ = joint width for month m (mils), c = friction factor (0.65 for asphalt interlayers, 1.74 for fabric interlayers), $JTSpace$ = joint spacing in the overlay (ft), CTE = overlay PCC coefficient of thermal expansion (in/in/^oF), T_c = concrete set temperature (^oF), $T(m)$ = mean mid-depth PCC overlay temperature for month m (^oF), ε_{sh} = PCC overlay shrinkage strain (in/in).

Table 5.3. PCC set temperature based on cement content and mean temperature during month of paving (^oF)

	Cement Content (lbs)			
Mean Monthly Air Temp (^oF)	400	500	600	700
40	52	56	59	62
50	66	70	74	78
60	79	84	88	93
70	91	97	102	107
80	103	109	115	121
90	115	121	127	134
100	126	132	139	145

Table 5.4. PCC overlay shrinkage strain relationship

Tensile Strength (psi)	Shrinkage Strain (in/in)
400	0.0008
500	0.0006
600	0.00045
700	0.0003
800	0.0002

$$S = 0.5 * h_{pcc} * e^{-0.032*JW} - \Delta S_{tot}$$ **Equation 5.24**

$$\log(J_{AGG}) = -28.4 * e^{-e^{-\left(\frac{S-e}{f}\right)}}$$ **Equation 5.25**

where S = aggregate joint shear capacity, JW = joint opening (mils), $\Delta S_{tot} = \sum_{i=1}^{m} \Delta S_i$ = cumulative loss of shear capacity at the beginning of the current month, J_{AGG} = nondimensional aggregate joint stiffness for current monthly increment, e = 0.35, f = 0.38.

$$\Delta S_i = \begin{Bmatrix} 0 & if\ JW < 0.001h_{PCC} \\ n_i * \dfrac{0.005 * 10^{-6}}{1.0 + \left(\dfrac{JW}{h_{PCC}}\right)^{-5.7}}\left(\dfrac{\tau_i}{\tau_{ref}}\right) & if\ 0.001 < JW < 3.8h_{PCC} \\ n_i * \dfrac{0.068 * 10^{-6}}{1.0 + 6.0 * \left(\dfrac{JW}{h_{PCC}} - 3\right)^{-1.98}}\left(\dfrac{\tau_i}{\tau_{ref}}\right) & if\ JW > 3.8h_{PCC} \end{Bmatrix}$$ **Equation 5.26**

where ΔS_i = loss of shear capacity from all ESALs for current month i, h_{PCC} = overlay slab thickness (in), JW = joint opening (mils), $\tau_i = J_{AGG} * (\Sigma\delta_{L,m} - \Sigma\delta_{UL,m})$ = shear stress on the transverse joint surface from the response model, $\tau_{ref} = 111.1 * \exp(-\exp(0.9988 * \exp(-0.1089 * \log(J_{AGG}))))$ = reference shear stress derived from the PCA test results.

For a doweled pavement, the model adopted for the nondimensional dowel stiffness is that provided by ARA (2004). The initial nondimensional dowel joint stiffness is calculated using Equation 5.27 and the critical nondinemsional dowel joint stiffness is calculated using Equation 5.28. The nondimensional dowel stiffness is then calculated using Equation 5.29 and the dowel damage parameter is presented Equation 5.30.

$$J_0 = \frac{38.20 * A_d}{h_{pcc}}$$ **Equation 5.27**

$$J_d^* = \begin{Bmatrix} 118, if\ \dfrac{A_d}{h_{pcc}} > 0.835 \\ 52.52\dfrac{A_d}{h_{pcc}} - 19.8,\ if 0.039 \leq \dfrac{A_d}{h_{pcc}} \leq 0.835 \\ 0.4,\ if\ \dfrac{A_d}{h_{pcc}} < 0.039 \end{Bmatrix}$$ **Equation 5.28**

$$J_d = J_d^* + (J_0 - J_d^*) exp\ (-\ DOWDAM) \quad \textbf{Equation 5.29}$$

$$\Delta DOWDAM = \frac{J_d * \left(\Sigma\delta_{L,m} - \Sigma\delta_{UL,m}\right) * DowelSpace}{d * f_c'} \quad \textbf{Equation 5.30}$$

where A_d = area of dowel bar (in^2), h_{pcc} = overlay PCC thickness (in), J_0 = initial nondimensional dowel stiffness, J_d^* = critical nondimensional dowel stiffness, J_d = nondimensional dowel stiffness for current month, $DOWDAM$ = cumulative dowel damage for the current month, $DowelSpace$ = dowel bar spacing (in), d = dowel bar diameter (in), f_c' = PCC compressive stress estimated based on the modulus of rupture (psi).

With the differential energy calculated, the faulting can then be predicted using Equation 5.31 through Equation 5.34.

$$F_0 = (C_1 + C_2 * FR^{0.25}) * \delta_{curl} * [C_5 * E]^{C_6} * log(WETDAYS * P_{200}) \quad \textbf{Equation 5.31}$$

$$F_i = F_{i-1} + C_7 * C_8 * DE_i * [C_5 * E]^{C_6} \quad \textbf{Equation 5.32}$$

$$\Delta Fault_i = (C_3 + C_4 * FR^{0.25}) * (F_{i-1} - Fault_{i-1})^2 * C_8 * DE_i \quad \textbf{Equation 5.33}$$

$$Fault_i = Fault_{i-1} + \Delta Fault_i \quad \textbf{Equation 5.34}$$

F_0 =initial maximum mean transverse joint faulting (in), FR = base freezing index defined at the percentage of the time that the top of the base is below freezing (<32^{o}F), δ_{curl} = maximum mean monthly PCC upward slab corner deflection due to temperature curling and moisture warping (in), E = erosion potential of interlayer: f(% binder content, % air voids, P_{200}), $P_{200} =$ Percent of interlayer aggregate passing No. 200 sieve, *WETDAYS* = Average number of annual wet days (> 0.1 in of rainfall), F_i =maximum mean transverse joint faulting for month i (in), F_{i-1} = maximum mean transverse joint faulting for month i-1 (in)(If i =1, $FMAX_{i-1} = FMAX_0$), DE_i = Differential energy density accumulated during month i, $\Delta Fault_i$ = incremental monthly change in mean transverse joint faulting during month i (in), $C_1 \dots C_8$ = calibration coefficients, $Fault_{i-1}$ = mean joint faulting at the beginning of month i (0 if i = 1), $Fault_i$ = mean joint faulting at the end of month i (in).

5.3 CALIBRATION SECTIONS

The calibration database used to calibrate the UBOL faulting model consists of 34 different sections from 9 different states across the United States and 1 province in Canada. The calibration sections are comprised of 14 Long Term Pavement Performance (LTPP) sections, 6 sections from the Minnesota Road Research Facility (MnROAD), and 14 Michigan Department of Transportation (MDOT) pavement sections. Table 5.6 presents a range of the values represented in the calibration database for some of the more pertinent calibration parameters. Of the sections, 16 are undoweled and the remainder of the sections are doweled. The dowel diameter for the doweled sections ranged from 1 - 1.5 in. If the pavement section has a random joint spacing, the mean joint spacing was used in the analysis. Considering the number of time series observations available, a total of 163 data points are available for calibration of the model.

The age of the sections ranged from approximately 2.5 to 33.5 years with an average of 13.5 years of age. In terms of ESALs, the traffic ranged from approximately 0.85 million to 22.4 million with an average value of around 7 million ESALs. Over half of the sections had experienced over 6 million ESALs, while 15% of the sections had experienced over 10 million ESALs. Only one undoweled section was exposed to more than 10 million ESALs. Detailed information for each calibration section can be found in Appendix F.

Table 5.5. Range of parameters for calibration sections

Parameter	Minimum	Maximum	Average
Age, yrs	2.5	33.5	13.5
Estimated ESALs	8.56E+05	2.45E+07	7.79E+06
Ave. Jt. Spacing, ft	6	27	14.6
Interlayer Thickness, in	0.1	8.6	1.5
Overlay thickness, in	4.5	10.3	7.1
Overlay Elastic Modulus, psi	3.09E+06	4.85E+06	3.93E+06
Overlay MOR, psi	530	1022	684
Existing thickness, in	7.1	10.2	8.5
Existing EMOD, psi	3.50E+06	5.00E+06	4.46E+06
Overlay Cement Content, lbs	354	594.5	540.7

5.4 RESULTS OF MODEL CALIBRATION

Calibration of the faulting model requires adjusting the calibration coefficients from Equation 5.31 through Equation 5.34 to minimize the error function defined by Equation 5.35. Additionally, the shape of the erosion function had to be fit based upon the interlayer characteristics influential in the development of faulting. The erosion model developed is shown in Equation 5.36 and Equation 5.37. A macro driven excel spreadsheet was used to calibrate the model and the following steps were taken to minimize the error. Several calibration parameters were fixed at a constant value while the remaining coefficients were varied until the lowest values of the error function could be identified. Once the error is minimized for the varied coefficients, these values are kept constant while the coefficients previously held constant are allowed to vary until the lowest possible value of the error function is achieved. These two sets of coefficients are varied in this manner until the error can be minimized no further. These steps do not guarantee a global minimum error but should provide a reasonable result. Minimization of the bias in the model with the calibration parameters must also be performed in addition to error minimization when selecting the final set of calibration coefficients. Predicted versus measured transverse joint faulting is presented in Figure 5.1. Table 5.6 summarizes all of the calibration coefficients that have been chosen.

$$\mathrm{ERROR}(C_1, C_2, C_3, C_4, C_5, C_6, C_7, C_8) = \sum_{i=1}^{N} (\mathrm{FaultPredicted_i} - \mathrm{FaultMeasured_i})^2$$ **Equation 5.35**

where ERROR = error function, $C_1, C_2, \dots, C_8 =$ calibration coefficients, $FaultPredicted_i =$ predicted faulting for i^th observation in dataset (in), $FaultMeasured_i =$ measured faulting for i^th observation in dataset (in), N = number of observations in the dataset.

$$\alpha = \log\left(1 + a * \%Binder + b * \%AV + c * P_{200}\right)$$ **Equation 5.36**

$$E = \begin{cases} (1.1974 * \alpha^2 - 0.9933 * \alpha + 0.306) & \mathit{Undoweled\ Pavements} \\ (1.0178 * \alpha^2 - 0.8443 * \alpha + 0.26) & \mathit{Doweled\ Pavements} \\ (1.0178 * \alpha^2 - 0.8443 * \alpha + 0.1) & \mathit{Non\ woven\ geotextile\ fabric\ interlayer} \end{cases}$$ **Equation 5.37**

where α = erodibility index, a, b, c = calibration coefficients, $* \%Binder$ = binder content of the interlayer (%), $\%AV$ = air voids percentage of interlayer, P_{200} = percent aggregate passing No. 200 sieve in interlayer (%), E = erosion factor to be used in predictive equations.

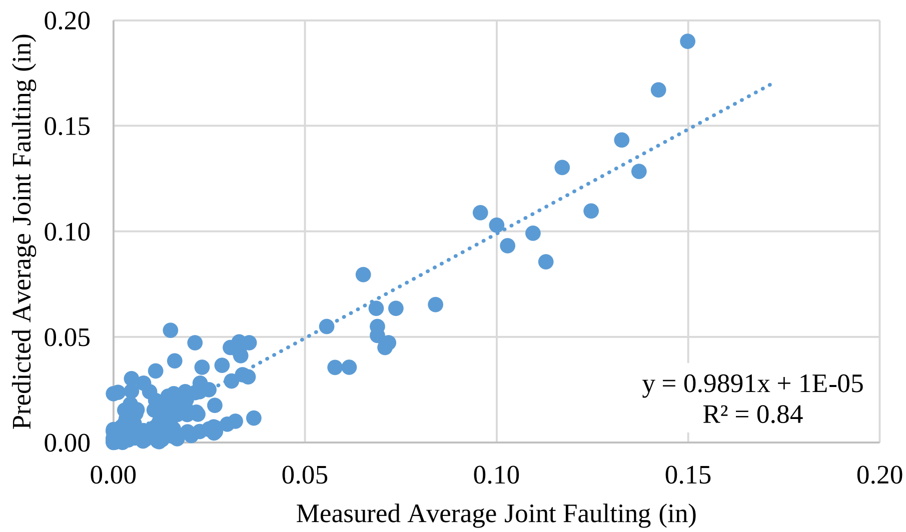

Figure 5.1. Measured vs. predicted UBOL transverse joint faulting

Table 5.6. UBOL transverse joint faulting calibration coefficients

Calibration Coefficient	
C_1	8.3
C_2	0.9
C_3	2.3
C_4	0.001
C_5	0.17
C_6	4
C_7	4.4
C_8	0.0000036

JPCP Transverse Joint Faulting Model Adequacy Checks

A series of model adequacy checks were performed to ensure the model coefficients provided reasonable values in terms of predictability and reasonableness. The tests outlined by Mallela et al. (2009) have been performed and are summarized below. For the model, an overall SEE of 0.019 in of faulting and a coefficient of determination, R^2, of 0.84 was deemed reasonable and are comparable to values achieved when calibrating the Pavement ME JPCP transverse joint faulting model (Sachs et al, 2014). The model bias was checked using the three hypothesis tests outlined in Table. The null and alternative hypothesis outlined in Table 5.7 were tested and the results are summarized in Table 5.8. A significance level of 0.05 is assumed for hypothesis testing. From Table 5.8, none of the three null hypotheses are rejected indicating that model bias has been removed through the calibration.

Table 5.7. Null and Alternative hypothesis tested for JPCP faulting

Hypothesis 1	Null hypothesis H_o: Linear regression model intercept = 0
	Alternative hypothesis H_a: Linear regression model intercept ≠ 0
Hypothesis 2	Null hypothesis H_o: Linear regression model slope = 1.0
	Alternative hypothesis H_a: Linear regression model slope ≠ 1.0
Hypothesis 3	Null hypothesis H_o: Mean ME Design faulting = Mean LTPP measured faulting
	Alternative hypothesis H_a: Mean ME Design faulting ≠ Mean LTPP measured faulting

Table 5.8. Results from transverse joint faulting model hypothesis testing

Hypothesis Testing and t-Test			
Test Type	Value	95% CI	P-value
Hypothesis 1: Intercept = 0	0.00001	-0.00194 to 0.00196	0.968
Hypothesis 2: Slope = 1	0.989	0.952 to 1.026	0.564
Paired t-test	-	-	0.801

UBOL Joint Faulting Model Reliability

The UBOL transverse joint faulting model reliability (standard deviation) was defined in a similar way as was conducted for the JPCP faulting model in Pavement ME (ARA, 2004). The resulting standard deviation model developed for a design at a specified level of reliability using data from Table 5.9 is presented as Equation 5.38 and Figure 5.2.

$$Stdev(FLT) = 0.0477 * (FLT^{0.3842}) \qquad \textbf{Equation 5.38}$$

where Stdev(FLT) = transverse joint faulting standard deviation (in), FLT = predicted UBOL transverse joint faulting (in).

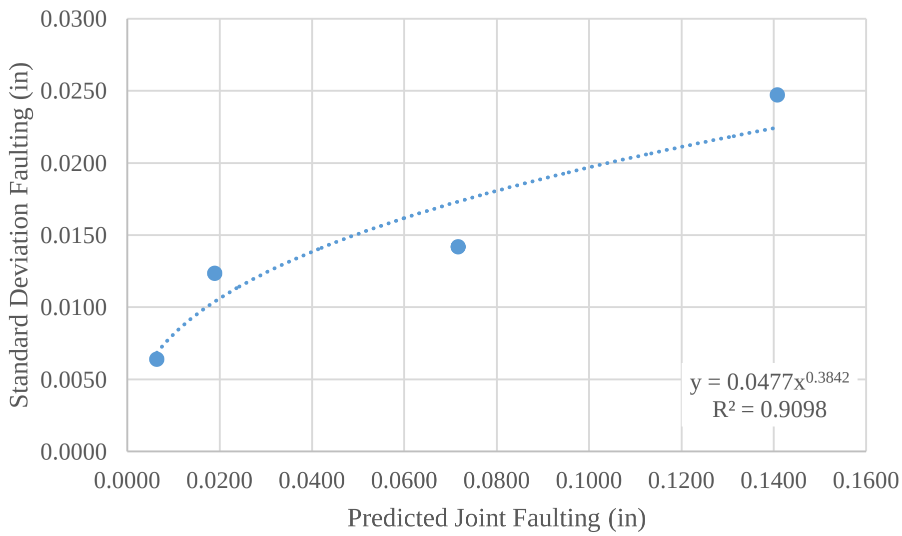

Figure 5.2. Predicted faulting versus faulting standard deviation

Table 5.9. Predicted faulting data used to develop faulting standard deviation model

Mean Predicted Joint Faulting, in	Std. Dev. Of Predicted Joint Faulting, in
0.0064	0.0063
0.0189	0.0123
0.0716	0.0142
0.1408	0.0247

5.5 SENSITIVITY ANALYSIS

A sensitivity analysis of the predicted faulting to various parameters of interest is conducted to further evaluate the model. The base design parameters used in the sensitivity analysis are as follows: 6-in undoweled PCC overlay (elastic modulus of $4*10^6$ psi and modulus of rupture of 600 psi), 1-in dense graded MIDAU asphalt, 10-in existing PCC slab (elastic modulus of $5*10^6$ psi), joint spacing is 12 ft, asphalt shoulder, and 20 million ESALs uniformly distributed over 30 years. The default climate was Pittsburgh, Pennsylvania (Wet-Freeze). One parameter was allowed to vary at a time. The effect of the joint spacing on the resulting predicted faulting can be seen in Figure 5.3. As can been seen, there is a small decrease in faulting as the joint spacing decreases from 20 to 12 ft. Currently the model does not consider 6 x 6 ft slabs. It should be noted that as the joint spacing decreases the decrease in faulting may not result in the same level of roughness. As there are more joints with a smaller joint spacing, the amount of average faulting does not need to be as large to produce the same ride for a section with more faulting and a larger joint spacing (DeSantis et al, 2016). The significance of the presence and diameter of the dowels can be seen in Figure 5.4. The use of dowels greatly reduces the potential for faulting to develop.

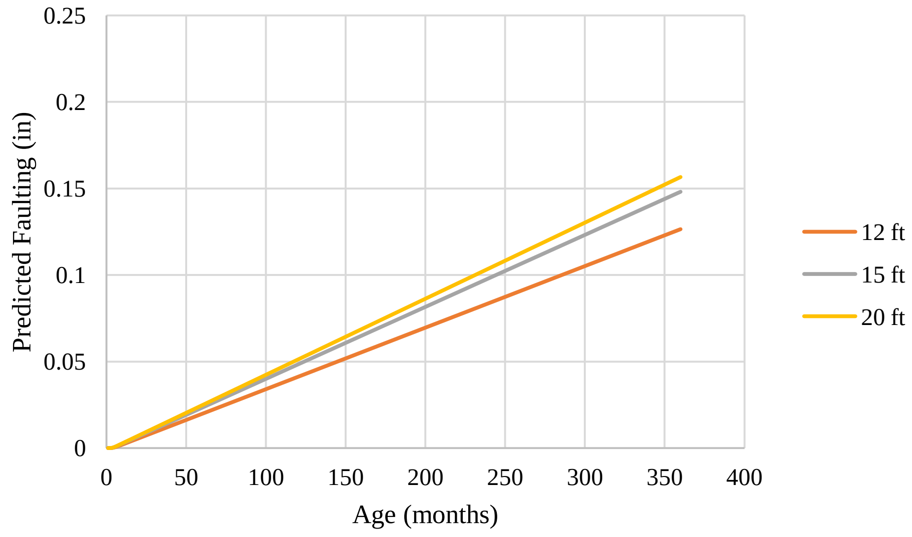

Figure 5.3. Sensitivity of joint spacing on predicted faulting

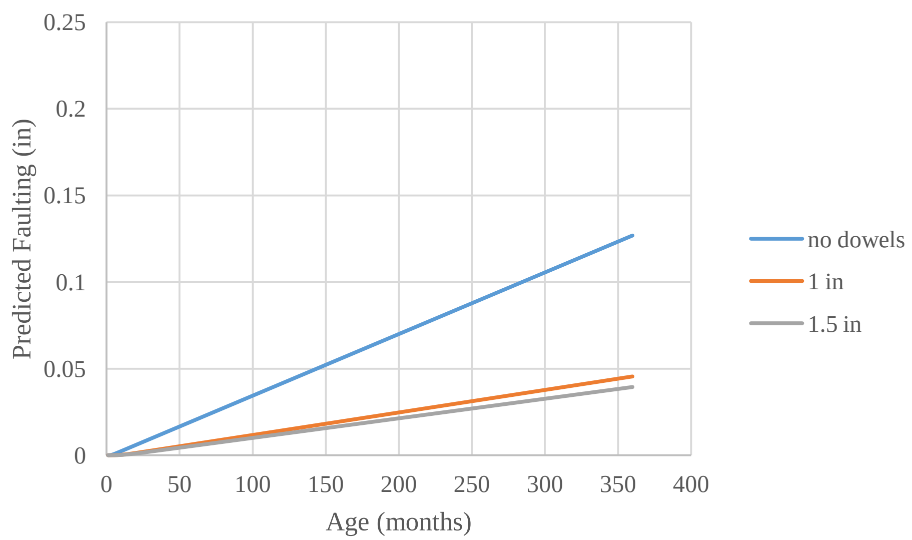

Figure 5.4. Sensitivity of dowels on predicted faulting

The effect of thickness on the predicted faulting can be seen in Figure 5.5. The trend observed is opposite of what would be expected. That is to say that an increase in slab thickness resulted in a slight increase in predicted joint faulting. Deflections at the corners and joints should decrease with increasing slab thickness and this is the case. However, is appears that this difference is the result of a decrease in the load transfer efficiency (LTE), as slab thickness increases. This is, at least in part, why the predicted joint faulting increases with increasing slab thickness. As can be seen from Figure 5.6, there is a small decrease in predicted faulting with an increase in the radius of relative stiffness for the existing PCC pavement and underlying layers.

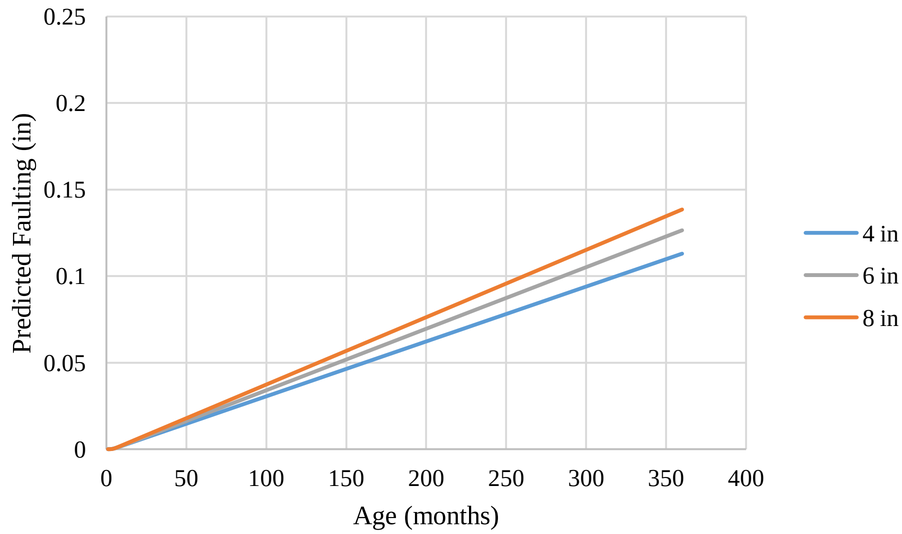

Figure 5.5. Sensitivity of thickness on predicted faulting

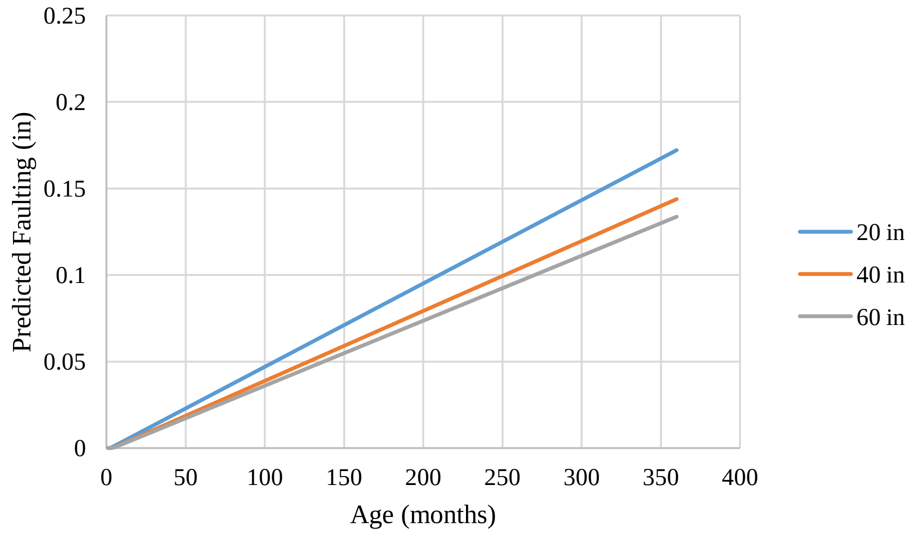

Figure 5.6. Sensitivity of existing PCC slab on predicted faulting

The effect of a tied versus asphalt shoulder can be seen in Figure 5.7. The support condition at the shoulder reduces the deflections and stresses of the PCC slab. The greater the support, the greater the reduction in stress and deflections, which results in increased pavement performance. This trend is observed in Figure 5.7. The PCC shoulder reduces the predicted faulting with respect to when an asphalt shoulder is used.

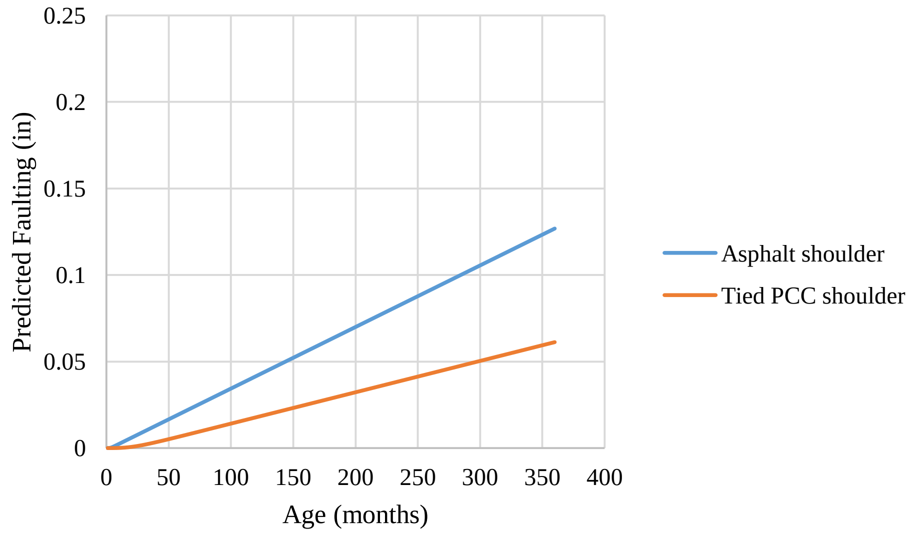

Figure 5.7. Sensitivity of shoulder support on predicted faulting

The interlayer was varied from a dense graded (MIDAU) to an open graded (PASSRC) with the results shown in Figure 5.8 by modifying Equation 5.36 and Equation 5.37 to change the calibrated erosion parameter. It should be noted that the open graded interlayer shown in Figure 5.8 had insufficient stability and exhibited deterioration under traffic in the field.

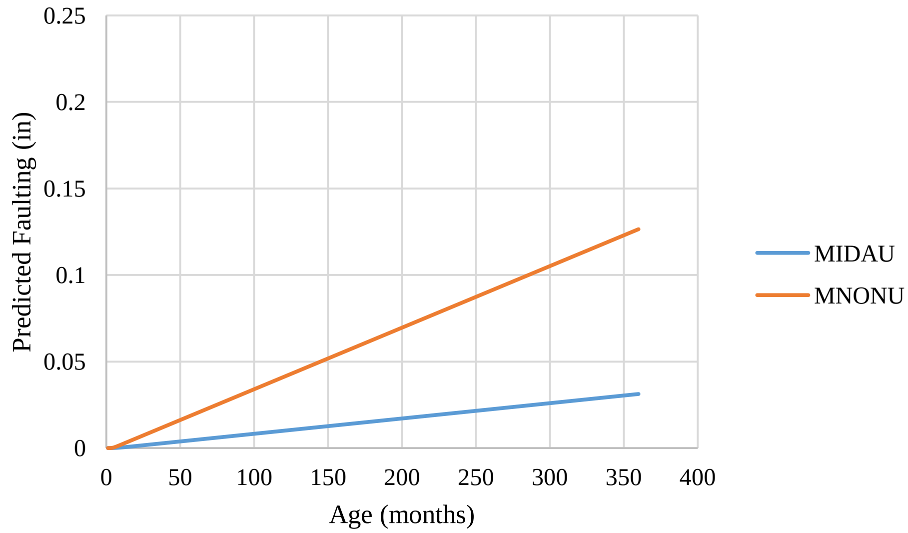

Figure 5.8. Sensitivity of interlayer type on predicted faulting

It can be seen from Figure 5.9 that an increase in traffic results in an increase in joint faulting, as would be expected. Increased truck traffic will result in an increase in the differential energy for joint faulting as there is an increase in the number of load applications at the joints.

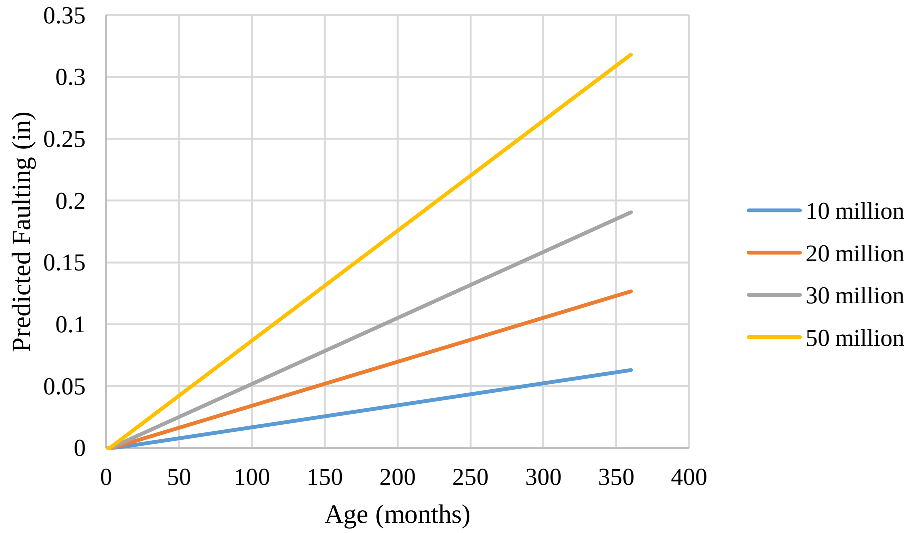

Figure 5.9. Sensitivity of traffic on predicted faulting

The flexural strength of the overlay was varied along with the modulus of elasticity since an increase in strength corresponds to an increase in stiffness. The effect of the increased strength on faulting is minimal, as is seen in Figure 5.10.

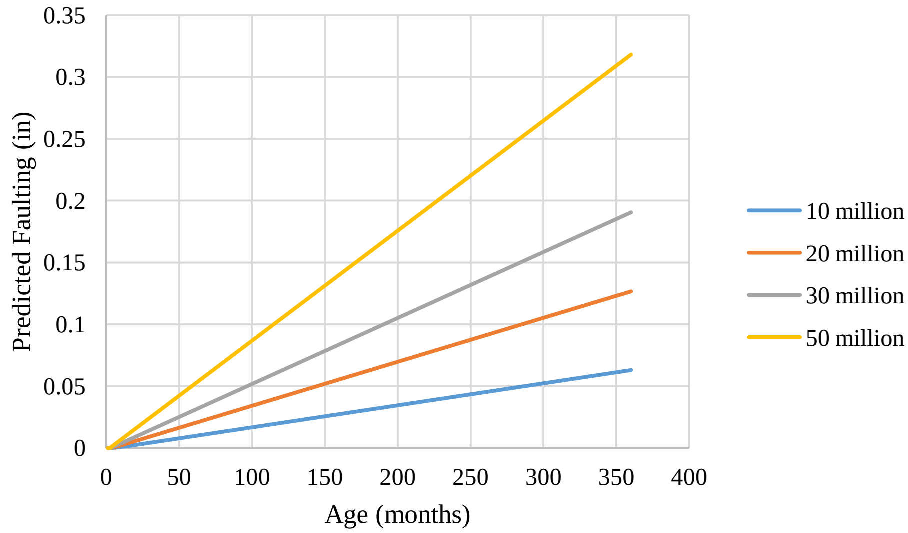

Figure 5.10. Sensitivity of overlay flexural strength on predicted faulting

The effect of climate on predicted faulting can be seen in Figure 5.11. The wet-freeze (WF) climates exhibited the most faulting followed by the wet-non freeze (WNF) and then the dry-freeze (DF) and dry-non freeze (DNF) which predicted the smallest amount of faulting. These relationships are as expected since the wet climates exhibited the highest predicted faulting and free moisture beneath the overlay is an essential component to the development of faulting.

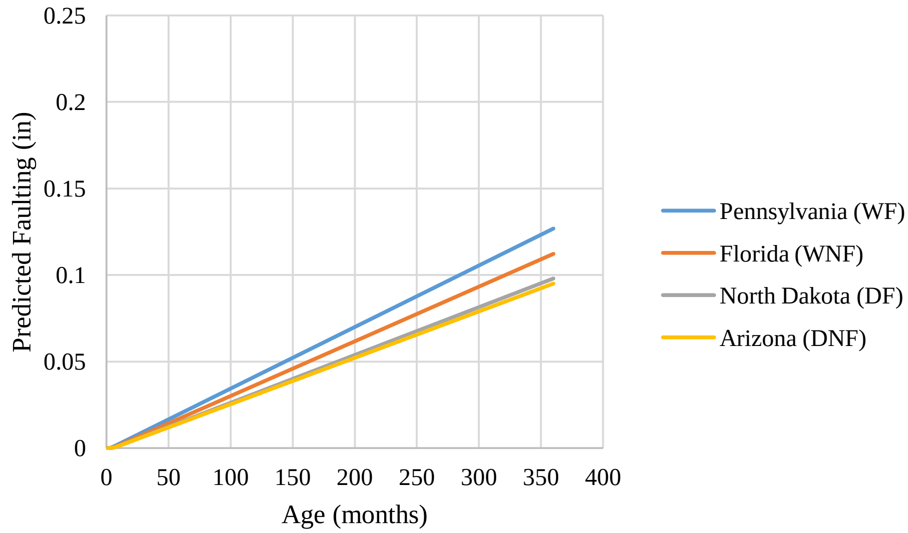

Figure 5.11. Sensitivity of climate type on predicted faulting

The effect of the reliability model is presented in Figure 5.12. It shows that higher amounts of faulting are predicted at higher levels of reliability.

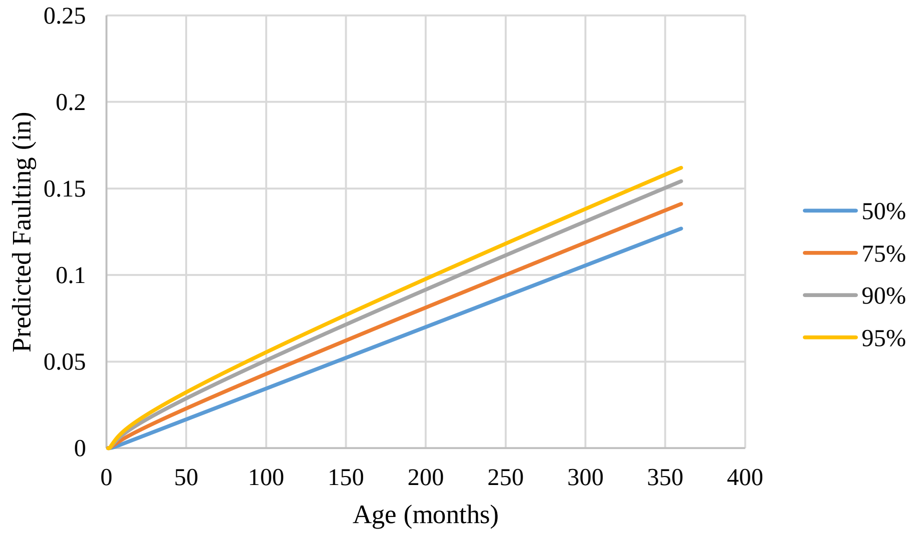

Figure 5.12. Sensitivity of reliability on predicted faulting

The evaluation of the calibrated model is continued with plots that show the faulting versus traffic for three of the calibration sections. Figure 5.13 shows MnROAD Cells 305 and 405, which consist of the same design. The design is a 5-in undoweled overlay with an asphalt shoulder, 15-ft joint spacing, and a 1-in MNONU interlayer. Figure 5.14 shows LTPP Section 89_9018 in Quebec, Canada. The structure is a 6-in undoweled overlay with an asphalt shoulder, a 15-ft joint spacing, and a chip seal interlayer. Figure 5.15 is LTPP Section 06_9107 in California. The structure is a 9-in undoweled overlay with an asphalt shoulder, 12-ft joint spacing, and a 1-in dense graded interlayer.

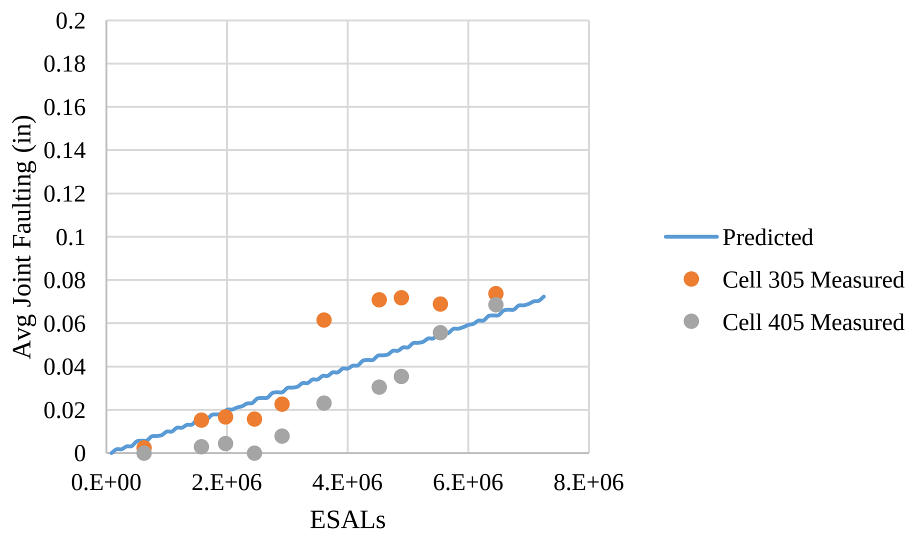

Figure 5.13. MnROAD Cells 305 and 405 predicted and measured joint faulting

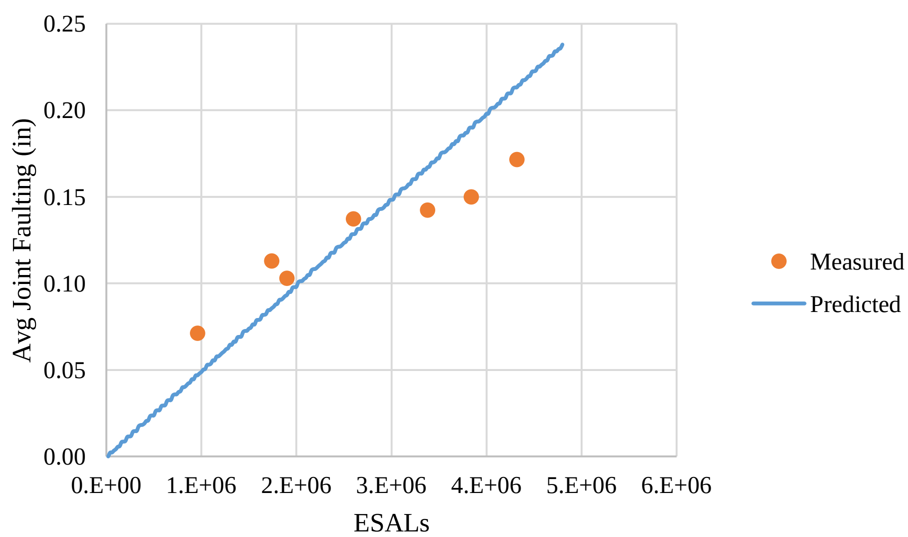

Figure 5.14. LTPP Section 89_9018 predicted and measured joint faulting

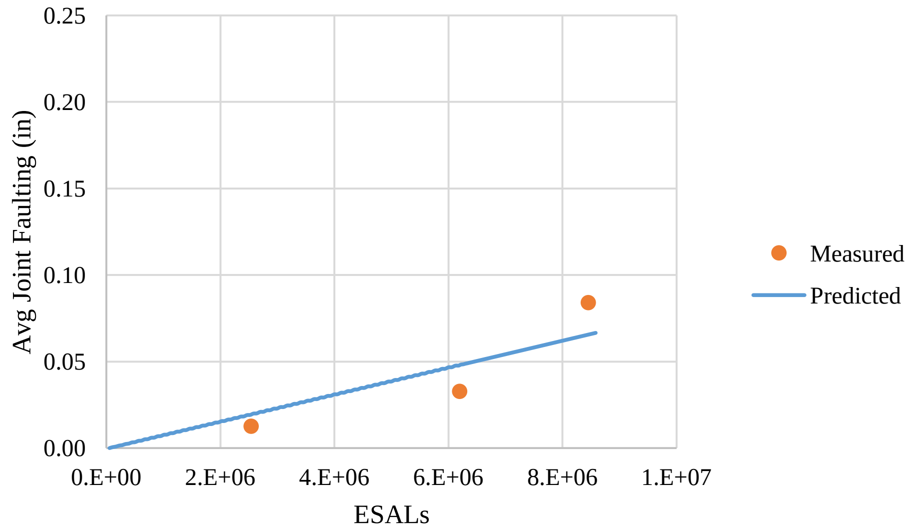

Figure 5.15. LTPP Section 6_9107 predicted and measured joint faulting

5.6 CONCLUSIONS

In this chapter, many previous faulting models were examined to evaluate the key predictive variables considered along with frameworks used to predict faulting for JPCP pavements. The framework developed to predict faulting for UBOL was then presented. This includes how climatic factors are treated. Then a discussion on the calculation of differential energy is with the steps necessary for establishing the inputs for the NNs is provided. Finally, the incremental faulting equations are presented. With the framework presented, a discussion of the data available to calibrate the faulting model is made that includes the location of the pavement sections and a summary of the relevant design features included in the calibration. The calibrated model is then presented. Finally, an assessment of the model is performed by comparing predicted to observed faulting and determining the sensitivity of the predicted faulting to several critical variables.

6.0 CONCLUDING REMARKS AND FUTURE WORK

In this study, laboratory tests were devised and carried out to investigate the effect of different interlayers on the performance of UBOL. An important conclusion obtained from the deflection characteristics test was that deflections for the specimens with the fabric interlayers are greater than those for asphalt interlayers. This can potentially make the overlay more susceptible to slab rocking and joint damage resulting from wear out of aggregate interlock. Additionally, both fabrics maintained the same magnitude of deflection and load transfer throughout the duration of the test, which can be an indication that they are more resistant to fatigue damage and less susceptible to loss of support from degradation of the interlayer. Finally, large permanent deformation occurred in some of the asphalt interlayers. This can lead to a loss of support under the overlay in the wheelpath.

Results from the modified push-off test show at a 95% confidence, that the initial stiffness comparisons of the fabric, open graded, and dense graded asphalt interlayers are significantly different from one another. However, the final stiffness between fabric and open graded asphalt is not statistically significant. The difference between final stiffness (stiffness after repeated loading) of the fabric and dense graded asphalt interlayers, and the open graded and dense graded asphalt interlayers are statistically significant. It is also shown that the initial and final stiffness for the fabric interlayer, as well as the open graded asphalt interlayer are not significantly different. The comparison between the initial and final stiffness for the dense graded asphalt interlayer is significantly different.

An important conclusion of the reflective cracking laboratory study is that a true reflective crack cannot be generated when the UBOL specimen is fully supported. The stress concentration at the crack tip of the joint in the existing beam was not sufficiently high before the concrete failed due to stress concentrations and crushing directly under the loading head. When a gap in the Fabcel foundation support was introduced in the central portion of the beam, the crack in the overlay propagated from bottom up through the interlayer at the sawed joint. The gap in the support underneath the beam simulates a void that could exist under a joint or crack in the field. Another significant finding is that, at a confidence level of 95 percent, the nonwoven geotextile fabric interlayers provided increased resistance to the development of reflective cracking. The ability of the fabrics to absorb additional deflection by providing a cushion for the overlay adds to this improved resistance as the crack initiates in the bottom of the overlay with the fabric remaining fully or partially intact.

Results from the direct tension laboratory test show that nonwoven geotextile fabric interlayers provide essentially no resistance to upward curling. Asphalt interlayers provided varying degrees of resistance based upon the type of asphalt and the degree of bond strength at the interfaces with the existing and overlay concrete. In the field, the resistance to upward curling will remain negligible for UBOLs with nonwoven geotextile fabric interlayer. However, the restraint provided by asphalt interlayers in the field is subject to change depending upon the asphalt temperature and any stripping, erosion, or consolidation/degredation that might occur in the interlayer from the effect of water and traffic loading. Finally, it was shown that the fabric interlayers had the smallest interface strength followed by the open graded asphalt then the dense graded asphalt had the largest resistance.

ISLAB was the finite element software selected for the structural modeling of the UBOL. An investigation to establish the Totsky interlayer k-value using both data from the reflective cracking laboratory test and a FWD analysis was conducted. This investigation yielded recommended values for the Totsky k-value of 3500 psi/in for asphalt interlayers and 425 psi/in for nonwoven geotextile fabric interlayers. Additionally, the factorial of design variables used to generate a database of finite element runs was established. The critical response parameterwas identified as a sum of deflection at all nodes lying between the lane/shoulder and centerline longitudinal joints and within 2 ft from the transverse joint. Finally, the details of the NNs developed were presented. This includes the predictors as well as the network architecture. Finally, plots comparing the results from ISLAB to that of the NNs are presented.

These NNs are then used within a framework to predict joint faulting for UBOL. A discussion on the calculation of the differential energy and all the steps needed to establish the inputs for the NNs is provided. Finally, the incremental faulting equations are presented. With the framework presented, a discussion of the data available to calibrate the faulting model is made that includes the location of the pavement sections and the range of relevant design features included in the calibration of the database. The calibrated model is presented and an evaluation of the model is performed.

A number of improvements need to be made to the model before it can be implemented into a design procedure to UBOL. First, the calibrated model needs to be expanded to include shorter joint spacings (6 by 6 ft slabs). These shorter slabs are becoming increasingly popular for UBOL. The NNs are able to predict differential energy for the shorter slabs, however, the only data in the calibration database for short panels were from MnROAD Cells 505 and 605 with nonwoven geotextile fabric. The model must be calibrated with data for short panels with asphalt interlayers to be used for this application. Currently, there is insufficient UBOL data on short slabs to add to the calibration database. It is thought that short slab data for Bonded Concrete Overlays of Asphalt Pavements (BCOA) can be used for calibration if the joints have not propagated through the asphalt.

Next, the model should account for a wide range of axle types and loads instead of only accounting for ESALs. Accounting for different load spectra provides a more realistic representation of the deflections occurring in the field as compared to just using ESALs. A similar approach to that incorporated into Pavement ME could be used where national average values for load spectra are used for the purposes of calibration. Additionally, the calibration database is not as robust as desired. Very few sections were exposed to high level interstate traffic. It is anticipated that a primary use of this predictive model will be for the design of UBOL on heavily trafficked interstate roadways. In order to improve the predictive capability of the model, a larger number of calibration sections with larger traffic volumes should be incorporated into the calibration. Alternatively, simulations should be run at a variety of high interstate traffic volumes to ensure that reasonable values of faulting are still obtained and if not then the model should be modified accordingly.

Finally, in order to improve the implementation of the design procedure, a framework should be established for determining the effective equivalent temperature gradient without the use of EICM. This would require developing effective equivalent temperature gradients for a wide range of climatic conditions and structures. A predictive model can then be developed so the ELTG can be estimated as a function of structural and climatic features.

APPENDIX A

MATERIAL TEST DATA FOR LABORATORY INVESTIGATION

Table A.1 through Table A.3 contain all material test data from the study with averages and standard deviations for each test date as well as concrete age at testing. Elastic modulus, compressive strength, and modulus of rupture tests were conducted according to ASTM C469, ASTM C39, and ASTM C78 respectfully. Additionally, Table A.4 provides dimensions of each of the existing asphalt beam specimens are provided along with sand patch test information for each of the asphalt beams tested according to ASTM E 965. Three sand patch measurements are taken along the length of the beam. 10 mL of Ottawa sand are used for each patch for all beams except those with MNDAM interlayer which used 20 mL of sand. The average of three measurements of each patch is reported.

Table A.1. Summary of Elastic Modulus test data

	Elastic Modulus			
	14 Day		28 Day	
Cast Date	Avg	Std Dev	Avg	Std Dev
Existing Beam Mixture				
2/11/2015	5.24E+06	90000	5.34E+06	47000
2/19/2015	4.53E+06	13000	4.92E+06	81000
3/2/2015			4.80E+06	63000
3/12/2015	4.77E+06	67000	4.83E+06	109000
3/16/2015			5.03E+06	149000
	29 Day		31 Day	
4/6/2015			4.64E+06	111000
4/9/2015	4.60E+06	171000		
	14 Day		28 Day	
4/13/2015			4.83E+06	171000
Overlay Beam Mixture				
	14 Day		28 Day	
2/20/2015	2.81E+06	14000	3.11E+06	50000
2/22/2015	3.11E+06	69000	3.24E+06	64000
2/23/2015			3.28E+06	112000
2/26/2015			3.11E+06	251000
3/3/2015			3.04E+06	49000
	5 Day		7 Day	
Cast Date	Avg	Std Dev	Avg	Std Dev
3/30/2015			3.81E+06	315000
4/2/2015			3.88E+06	187000
4/17/2015			3.88E+06	339000
4/22/2015			4.30E+06	142000
4/24/2015			4.23E+06	43000
	5 Day		6 Day	
4/29/2015			4.28E+06	155000
5/1/2015			4.17E+06	88000
5/6/2015	4.36E+06	258000		
5/7/2015	4.48E+06	218000		
5/13/2015			4.71E+06	47000
5/15/2015			4.79E+06	54000
5/20/2015			4.62E+06	88000
5/22/2015			4.65E+06	89000
7/1/2015	4.43E+06	165000		
7/9/2015	4.49E+06	112000		
8/6/2015			4.82E+06	67000
9/9/2015			4.56E+06	72000

Table A.2. Summary of compressive strength test data

	Compressive Strength			
	14 Day		28 Day	
Cast Date	Avg	Std Dev	Avg	Std Dev
	Existing Beam Mixture			
2/11/2015	7610	533	7411	271
2/19/2015	6232	61	6471	96
3/2/2015	6196	160	6991	129
3/12/2015	6325	170	7059	263
3/16/2015	6443	298	7093	459
	29 Day		31 Day	
4/6/2015			6982	170
4/9/2015	6806	303		
	14 Day		28 Day	
4/13/2015			6847	177
	Overlay Beam Mixture			
	14 Day		28 Day	
2/20/2015	1977	199	2666	61
2/22/2015	2608	31	2905	242
2/23/2015	2352	129	2326	119
2/26/2015	2140	168	2237	32
3/3/2015	2242	24	2156	303
	5 Day		7 Day	
Cast Date	Avg	Std Dev	Avg	Std Dev
3/30/2015			3881	262
4/2/2015			4512	247
4/17/2015			4590	285
4/22/2015			4696	267
4/24/2015			4694	100
	5 Day		6 Day	
4/29/2015			5059	64
5/1/2015			5069	184
5/6/2015	5334	310		
5/7/2015	5106	225		
5/13/2015			5013	353
5/15/2015			5357	275
5/20/2015			5073	186
5/22/2015			5131	195
7/1/2015	4632	279		
7/9/2015	4732	235		
8/6/2015	4716	137		
9/9/2015	4812	218		

Table A.3. Summary of modulus of rupture test data

	Modulus of Rupture			
	14 Day		28 Day	
Cast Date	Avg	Std Dev	Avg	Std Dev
Existing Beam Mixture				
2/11/2015			932	86
2/19/2015			878	17.5
3/2/2015				
3/12/2015	838	20		
3/16/2015				
	29 Day		31 Day	
4/6/2015			884	3
4/9/2015	863	12		
	14 Day		28 Day	
4/13/2015			905	55
Overlay Beam Mixture				
	14 Day		28 Day	
2/20/2015			584	13
2/22/2015			573	-
2/23/2015				
2/26/2015				
3/3/2015			552	-
	5 Day		7 Day	
Cast Date	Avg	Std Dev	Avg	Std Dev
3/30/2015			688	58
4/2/2015	613	18		
4/17/2015	617	31		
4/22/2015	642	30		
4/24/2015	643	8		
	5 Day		6 Day	
4/29/2015	643	47		
5/1/2015	645	23		
5/6/2015	685	53		
5/7/2015	707	27		
5/13/2015	695	10		
5/15/2015	719	6		
5/20/2015	725	27		
5/22/2015	708	18		
7/1/2015	660	19		
7/9/2015	683	29		
8/6/2015	690	25		
9/9/2015	651	21		

Table A.4. Asphalt beam measurements and sand patch test results

Beam	Sand Patch (Characteristic depth in mils)			Average Dimensions			
	1	2	3	Length	Width	Height (PCC)	Height (HMA)
0223MNDAUC	34.4	31.1	29.6	30.9	6.0	6.1	2.9
0223MNDAUB	34.4	30.8	31.3	30.7	6.2	6.0	2.8
0223MNDAUA	31.9	30.3	31.3	30.3	6.2	6.0	2.8
0226MNONUC	102.7	84.0	91.3	30.1	5.9	6.0	1.6
0226MNONUB	95.4	84.0	94.0	30.2	5.9	5.8	1.6
0226MNONUA	87.5	84.0	91.3	30.6	5.9	6.0	1.7
0319MNDAMC	93.2	82.8	71.4	30.5	5.9	5.8	1.2
0319MNDAMB	76.7	76.7	79.7	30.3	6.1	5.9	1.1
0319MNDAMA	86.0	71.4	76.7	30.3	6.1	6.0	1.0
0417MNDAUC	31.1	29.3	31.1	30.0	5.9	6.1	2.9
0417MNDAUB	29.1	24.9	33.3	30.2	6.3	6.0	2.8
0417MNDAUA	28.2	30.1	25.7	30.3	6.2	6.0	2.9
0422MNDAMC	79.7	71.4	67.7	30.1	6.3	5.8	0.8
0422MNDAMB	89.5	71.4	71.4	30.8	6.0	6.0	0.9
0422MNDAMA	93.2	82.8	93.2	30.1	5.8	6.0	0.9
0424MIDAUC	35.7	38.4	34.4	30.1	5.9	6.0	1.1
0424MIDAUA	35.7	37.7	34.4	30.0	6.0	6.1	1.2
0424MIDAUB	32.1	37.7	34.4	30.3	5.9	5.8	1.1
0507MNDAUA	38.4	40.6	48.6	30.2	6.0	5.9	2.8
0507MNDAMB	79.7	74.0	95.1	30.3	6.2	6.0	1.0
0507MNONUA	91.3	84.0	81.7	30.1	5.8	5.9	1.7
0513MIOAUA	63.4	57.8	57.8	30.1	5.9	5.8	1.8
0513MIOAUB	63.4	52.9	48.6	30.0	6.0	5.9	1.8
0513MIOAUC	73.6	63.4	50.6	30.0	6.1	5.7	1.9
0515MIDAUC	28.2	33.3	32.1	30.5	6.0	6.0	1.1
0515MIDAUB	43.6	46.6	44.8	30.1	5.9	6.0	1.0
0515MIDAUA	31.1	37.0	44.8	29.9	5.9	6.0	1.1
0520MIOAUC	77.5	59.1	49.6	30.0	5.8	6.0	1.9
0520MIOAUB	77.5	54.0	63.4	30.0	5.8	6.0	2.1
0520MIOAUA	60.5	66.6	65.0	30.1	5.9	6.1	2.0
0522MNONUC	77.5	86.3	90.0	30.2	6.1	6.0	2.0
0522MNONUB	86.3	86.3	86.3	29.9	5.8	5.9	1.7
0522MNONUA	102.8	88.8	73.6	30.0	5.9	6.0	1.7
0701MNDAUA	41.4	47.6	41.4	30.2	6.1	6.1	2.8
0701MNONUB	86.3	81.7	91.3	30.0	6.1	5.9	1.8
0701MIDAUC	44.8	44.8	42.2	30.3	6.0	5.9	1.3
0709MIOAUA	63.4	60.5	79.6	30.6	6.1	6.1	1.8
0709MNDAMB	91.0	86.8	89.5	30.1	6.0	5.9	0.8
0806PADNUA	45.7	46.6	46.6	30.1	6.0	6.0	1.4
0806PADNUB	52.9	52.9	52.9	30.0	6.0	6.0	1.6
0806PADNUC	55.3	47.1	46.6	30.4	6.0	6.0	1.5
0909PADNUA	47.6	46.6	43.0	30.5	6.0	6.1	1.4
0909PADNUB	41.4	39.8	41.4	30.3	6.0	6.0	1.5
0909PADNUC	41.4	46.6	46.6	30.2	6.0	6.0	1.5
0909PADNUD	39.8	41.4	43.0	30.2	6.0	6.2	1.4

APPENDIX B

RESULTS FROM DEFLECTION CHARATERISTICS TEST SETUP

Two different plots for each specimen tested are shown in Figure B.1 through Figure B.32. Plots of the measured deflection at each of the four locations versus the cycle number are shown below for each specimen as well as plots of load transfer efficiency (LTE) and interlayer compression. LTE is defined as the ratio of the deflection of the unloaded side to the loaded side of the joint in the overlay and is reported as a percent. Interlayer compression is the overlay loaded deflection minus the existing beam loaded deflection. Please see Chapter 2 for a description of the test setup. Note the following nomenclature:

OL = Overlay Loaded side
OU = Overlay Unloaded side
EL = Existing Loaded side
EU = Existing Unloaded side

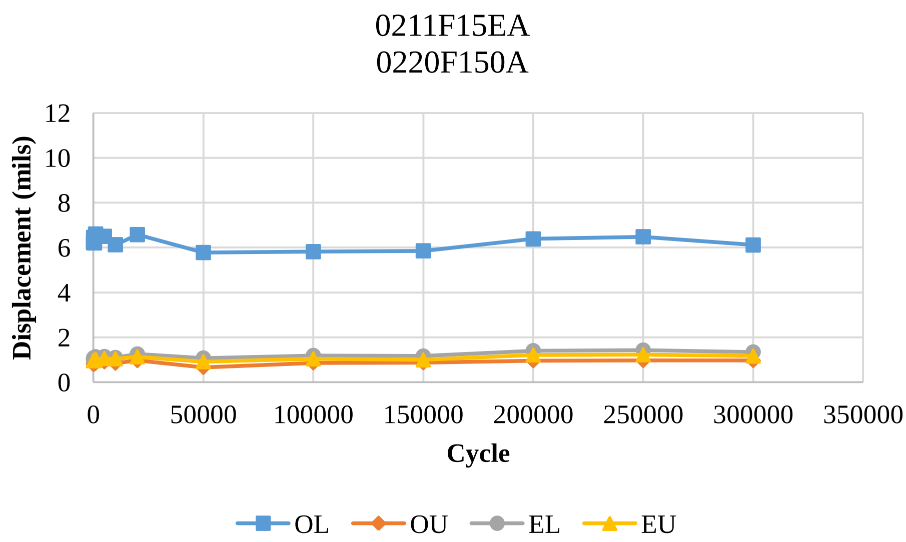

Figure B.1. F15 Displacement vs. Load Cycle (Tested on 3/20/15)

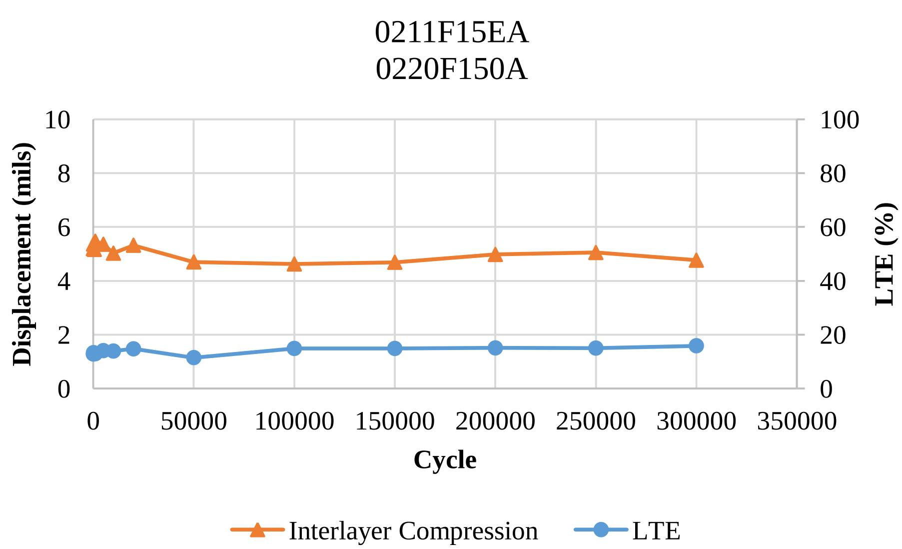

Figure B.2. F15 Interlayer Compression and LTE vs. Load Cycle (Tested on 3/20/15)

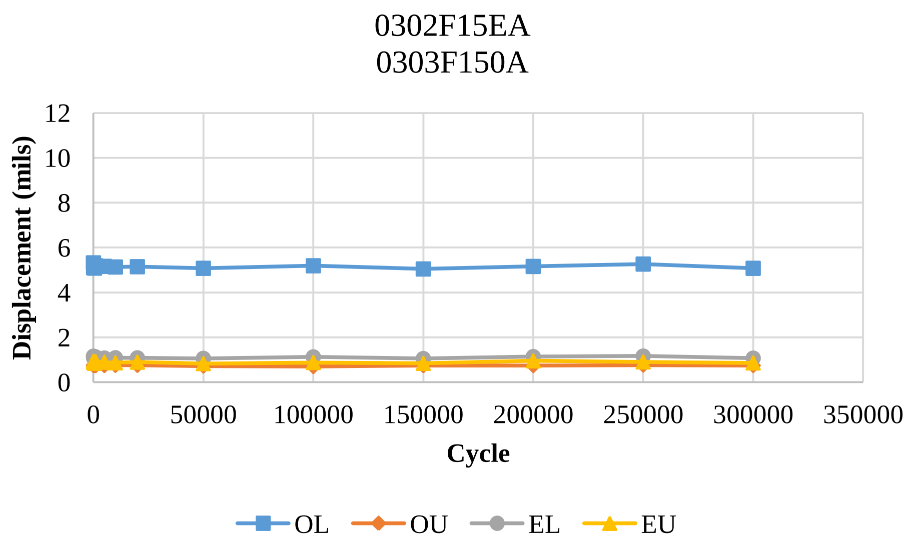

Figure B.3. F15 Displacement vs. Load Cycle (Tested on 4/1/15)

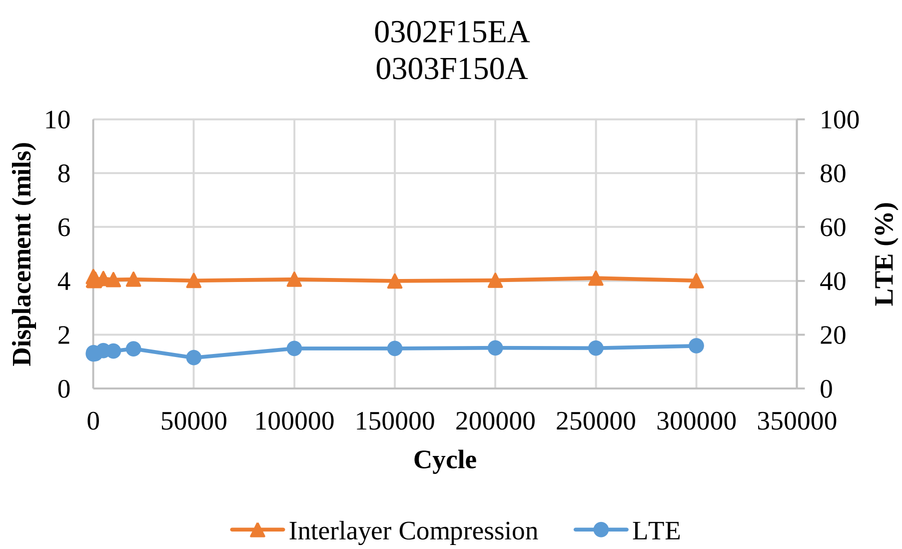

Figure B.4. F15 Interlayer Compression and LTE vs. Load Cycle (Tested on 4/1/15)

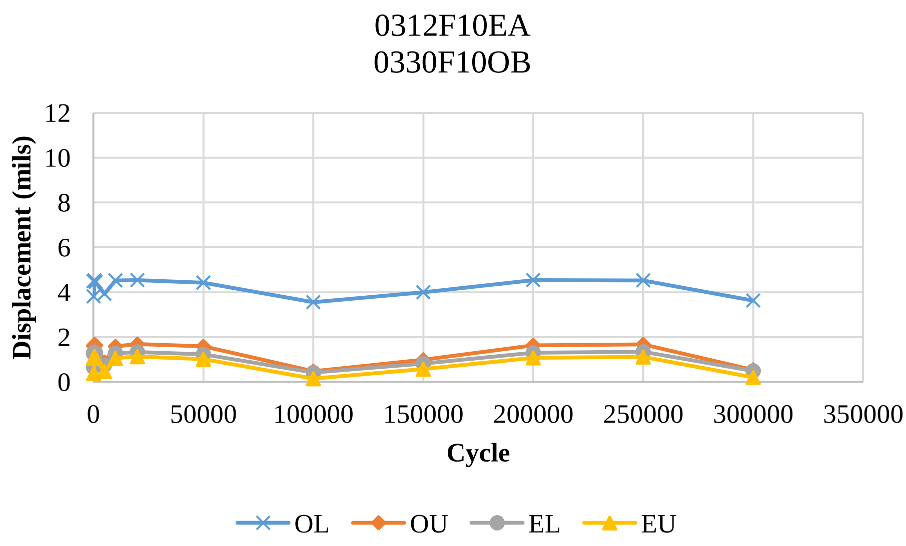

Figure B.5. F10 Displacement vs. Load Cycle (Tested on 4/8/15)

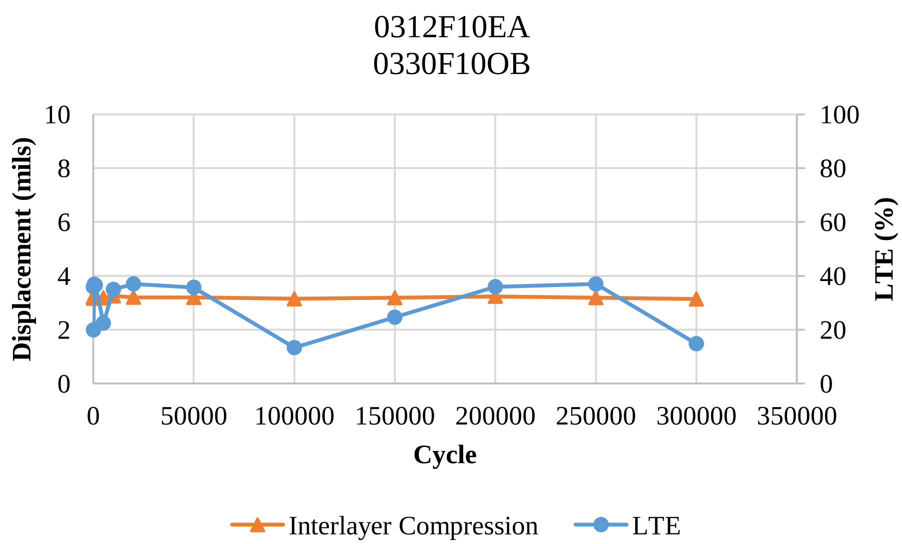

Figure B.6. F10 Interlayer Compression and LTE vs. Load Cycle (Tested on 4/8/15)

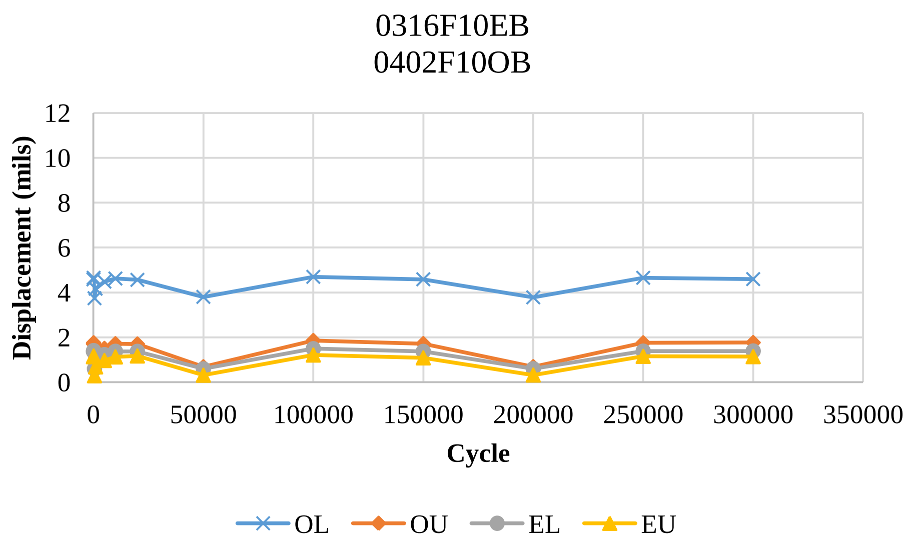

Figure B.7. F10 Displacement vs. Load Cycle (Tested on 4/9/15)

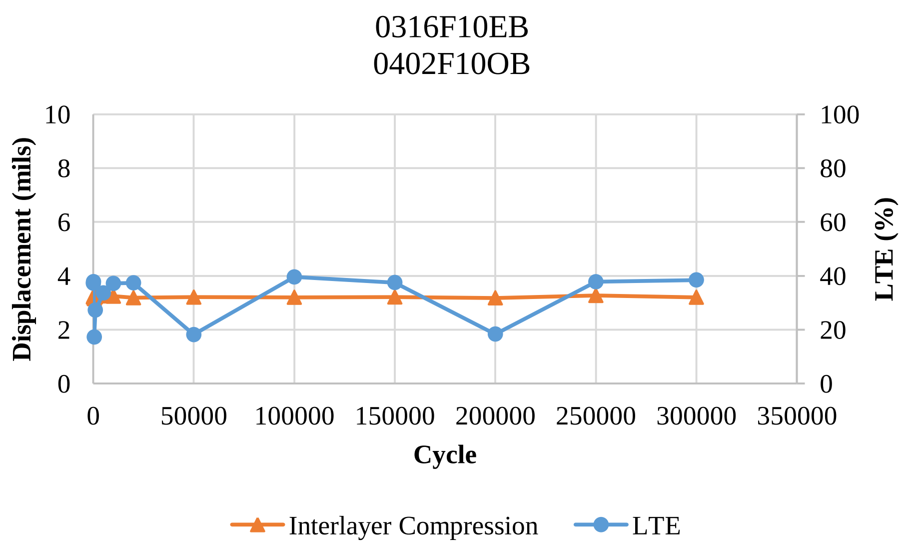

Figure B.8. F10 Interlayer Compression and LTE vs. Load Cycle (Tested on 4/9/15)

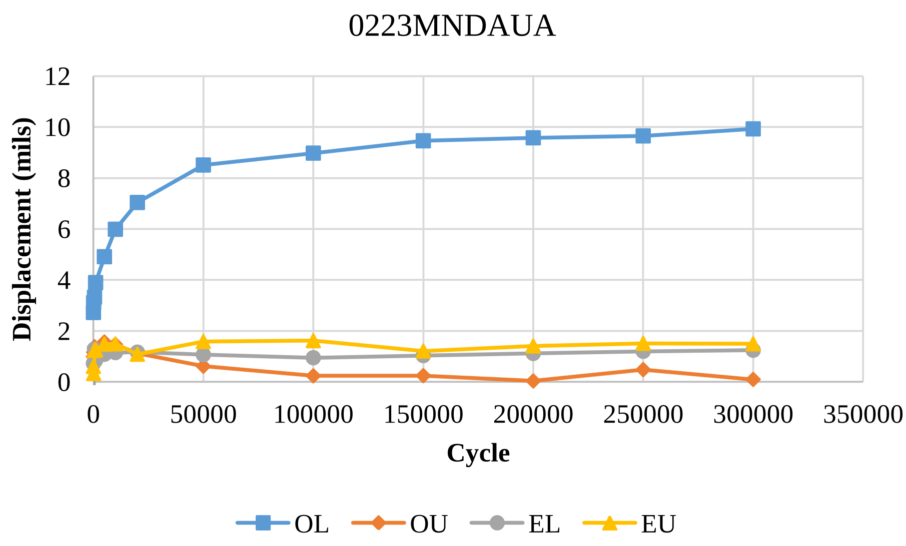

Figure B.9. MNDAU Displacement vs. Load Cycle (Tested on 3/25/15)

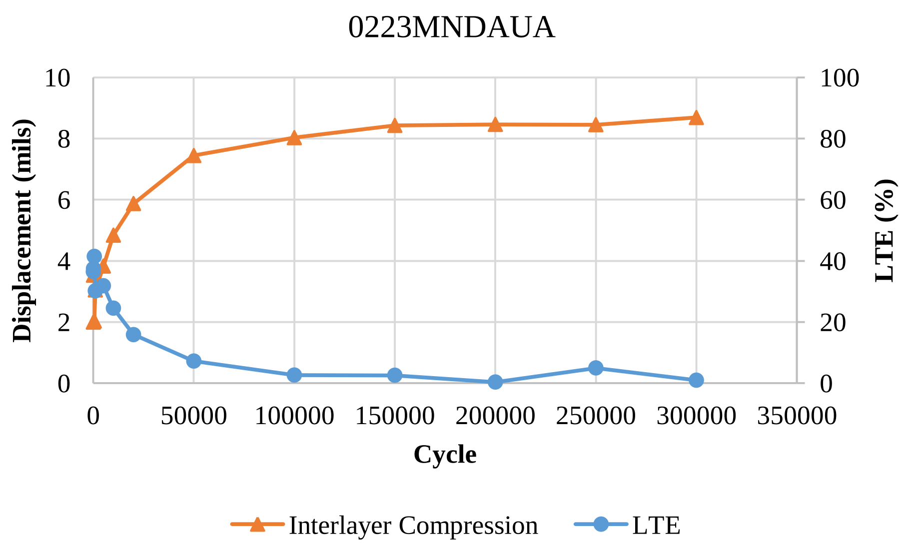

Figure B.10. MNDAU Interlayer Compression and LTE vs. Load Cycle (Tested on 3/25/15)

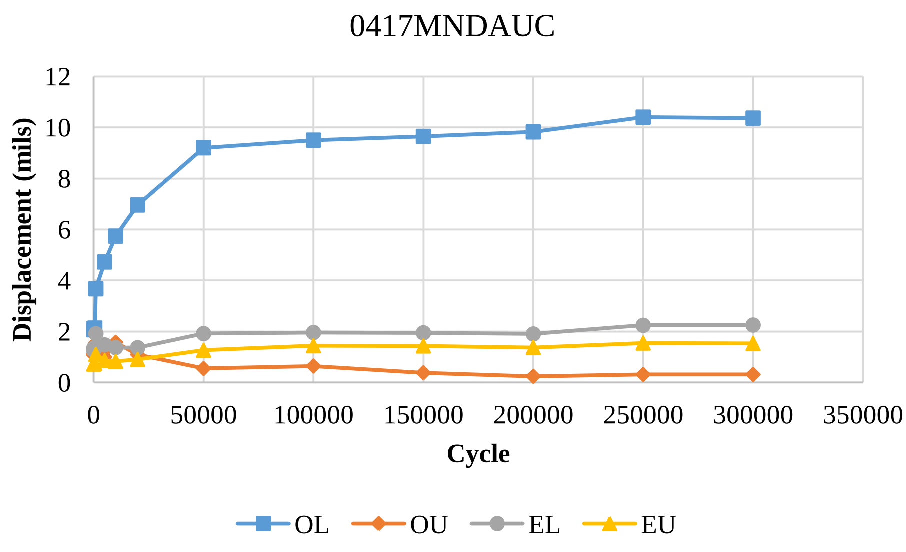

Figure B.11. MNDAU Displacement vs. Load Cycle (Tested on 4/23/15)

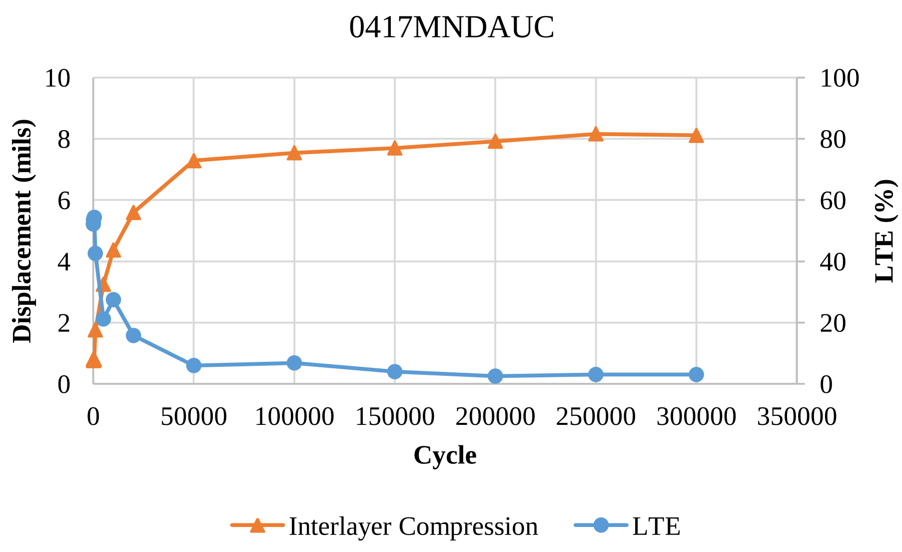

Figure B.12. MNDAU Interlayer Compression and LTE vs. Load Cycle (Tested on 4/23/15)

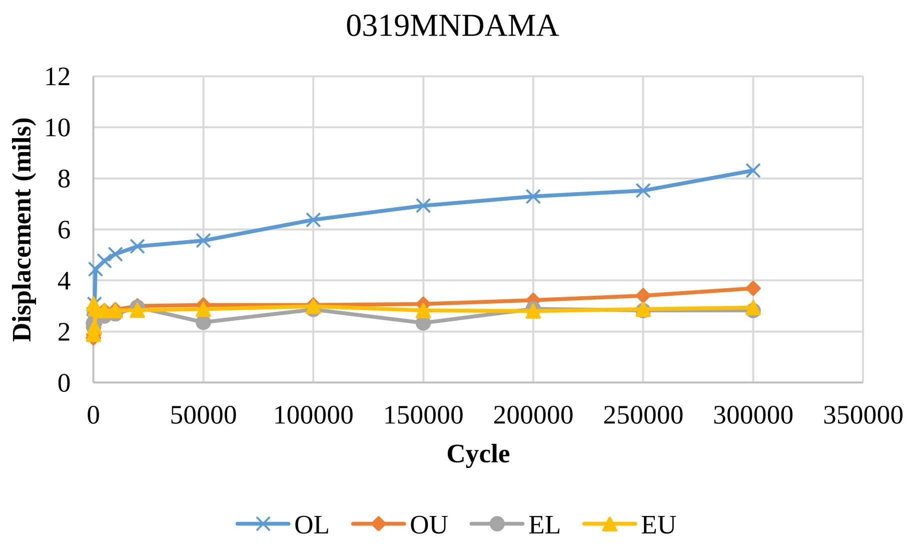

Figure B.13. MNDAM Displacement vs. Load Cycle (Tested on 4/2/15)

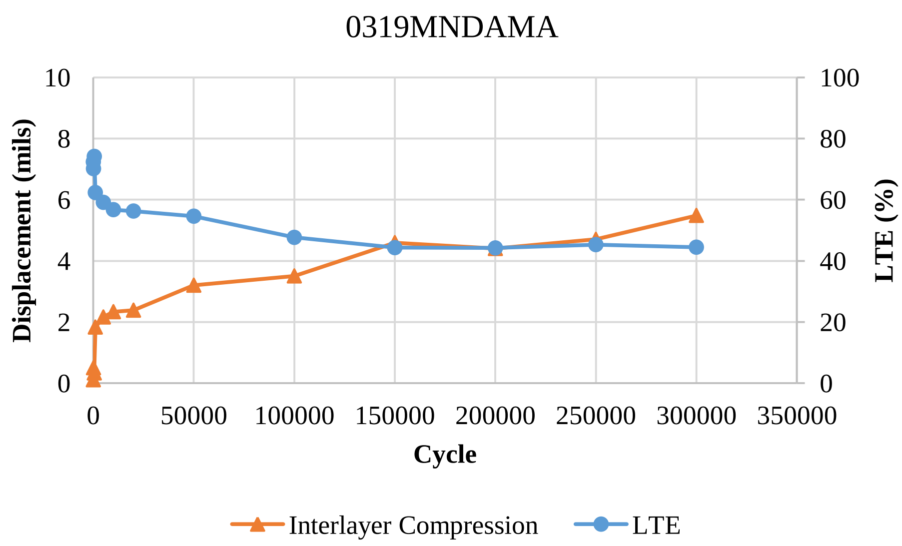

Figure B.14. MNDAM Interlayer Compression and LTE vs. Load Cycle (Tested on 4/2/15)

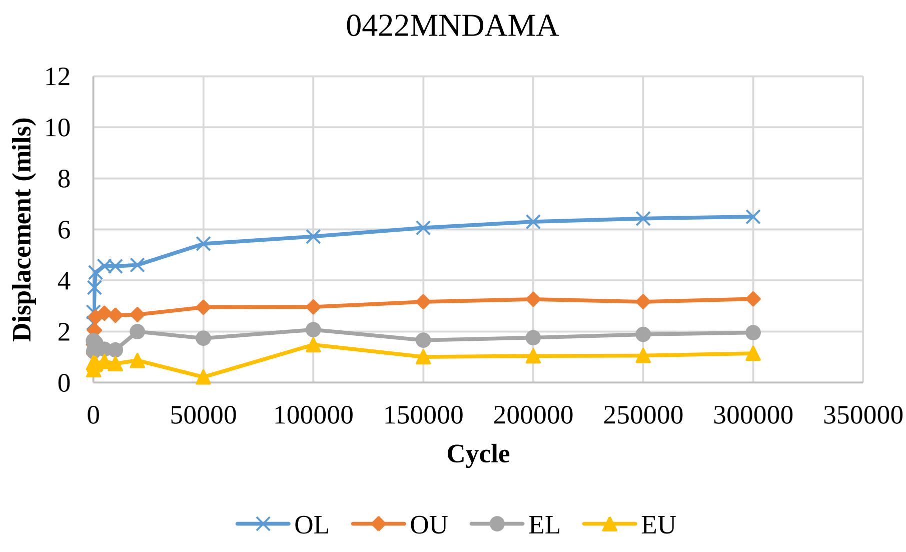

Figure B.15. MNDAM Displacement vs. Load Cycle (Tested on 4/28/15)

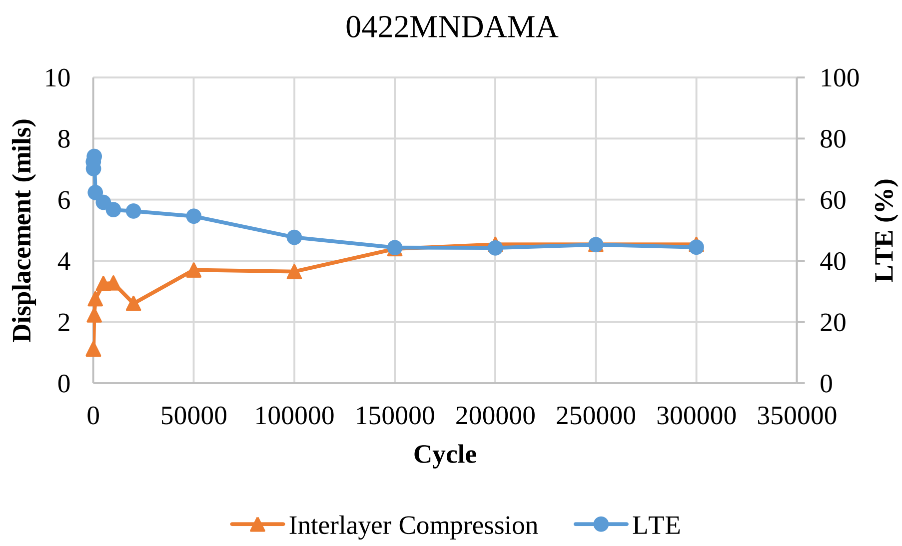

Figure B.16. MNDAM Interlayer Compression and LTE vs. Load Cycle (Tested on 4/28/15)

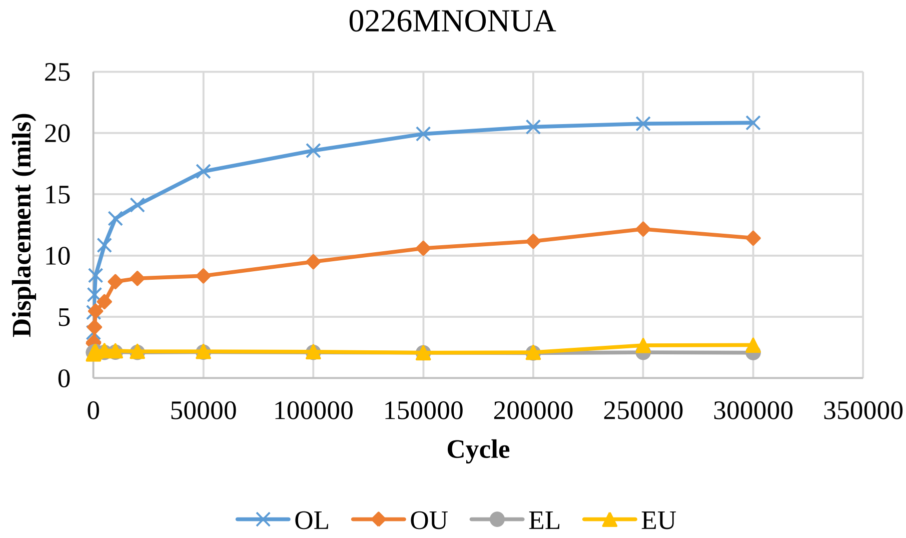

Figure B.17. MNONU Displacement vs. Load Cycle (Tested on 3/27/15)

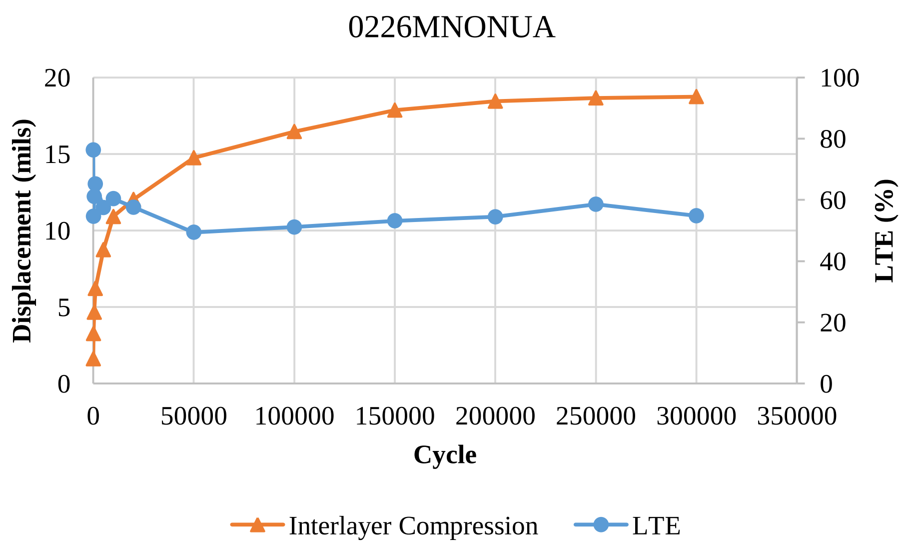

Figure B.18. MNONU Interlayer Compression and LTE vs. Load Cycle (Tested on 3/27/15)

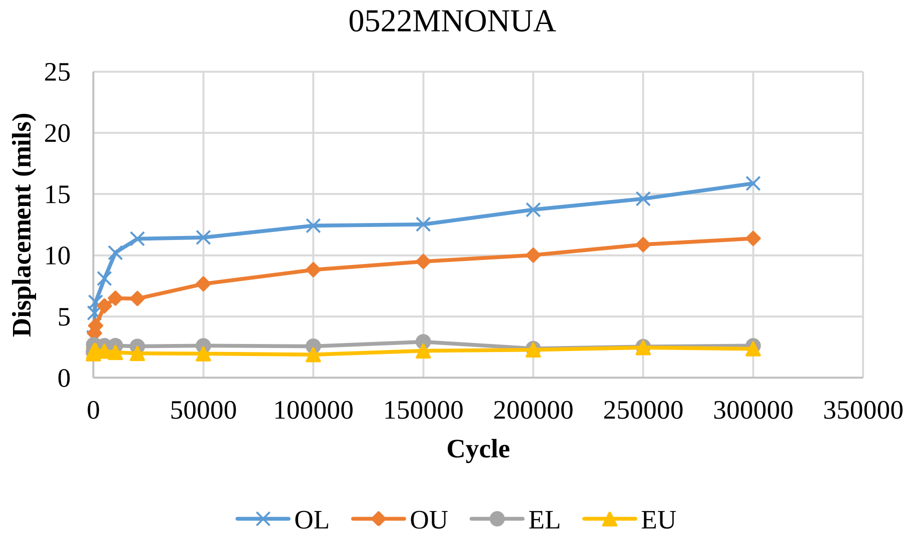

Figure B.19. MNONU Displacement vs. Load Cycle (Tested on 5/27/15)

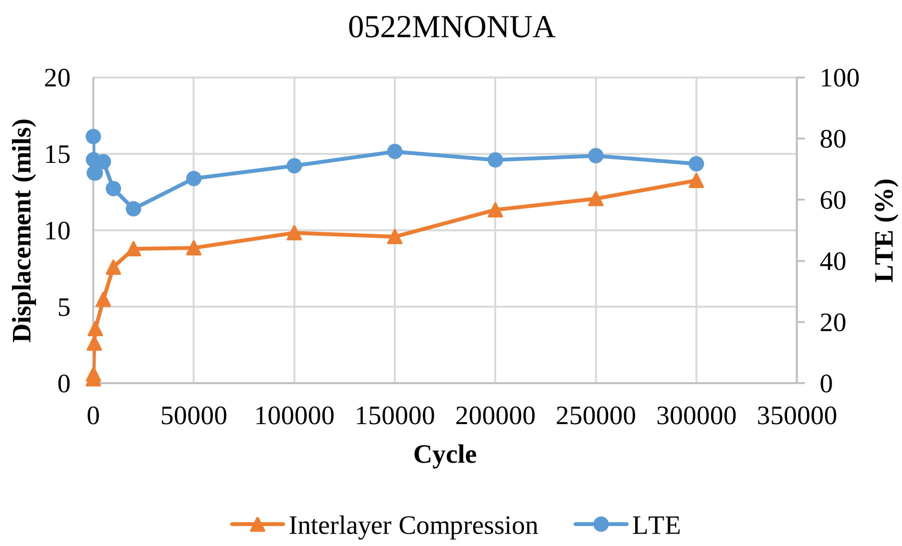

Figure B.20. MNONU Interlayer Compression and LTE vs. Load Cycle (Tested on 5/27/15)

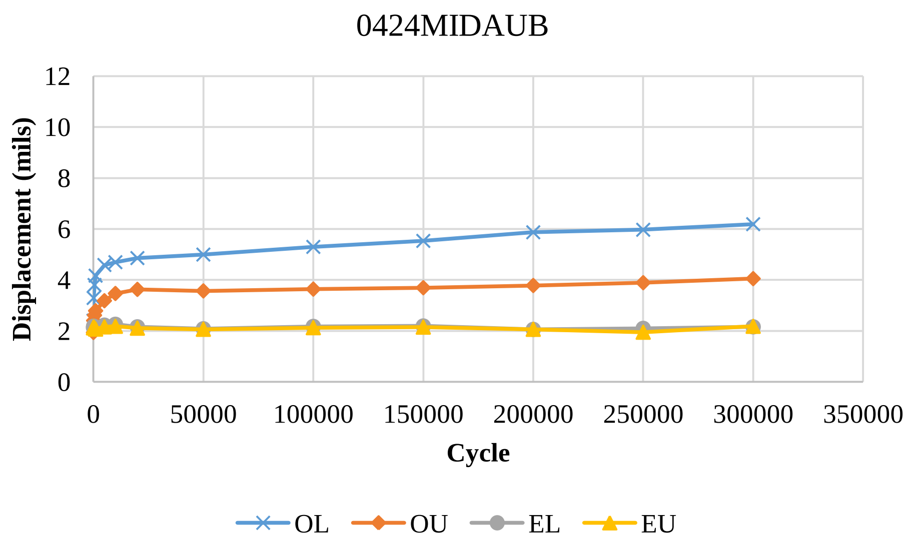

Figure B.21. MIDAU Displacement vs. Load Cycle (Tested on 4/29/15)

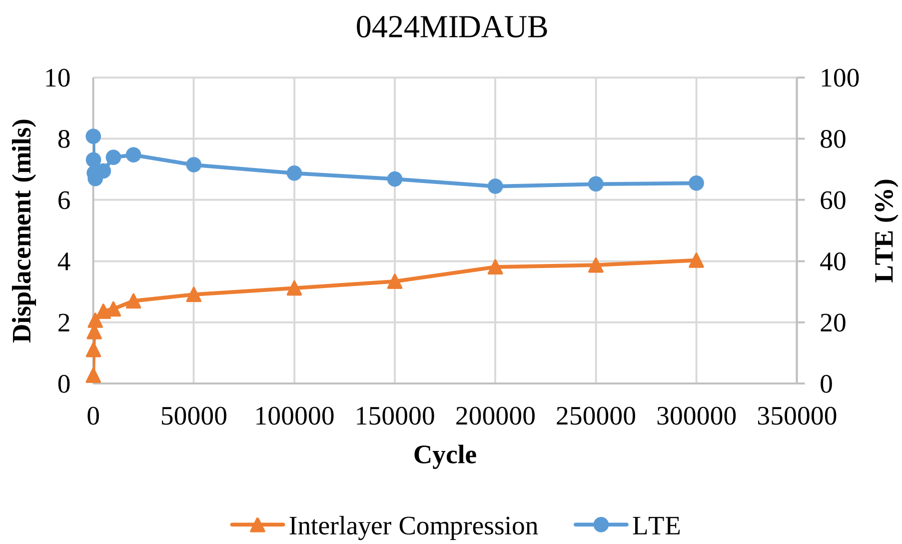

Figure B.22. MIDAU Interlayer Compression and LTE vs. Load Cycle (Tested on 4/29/15)

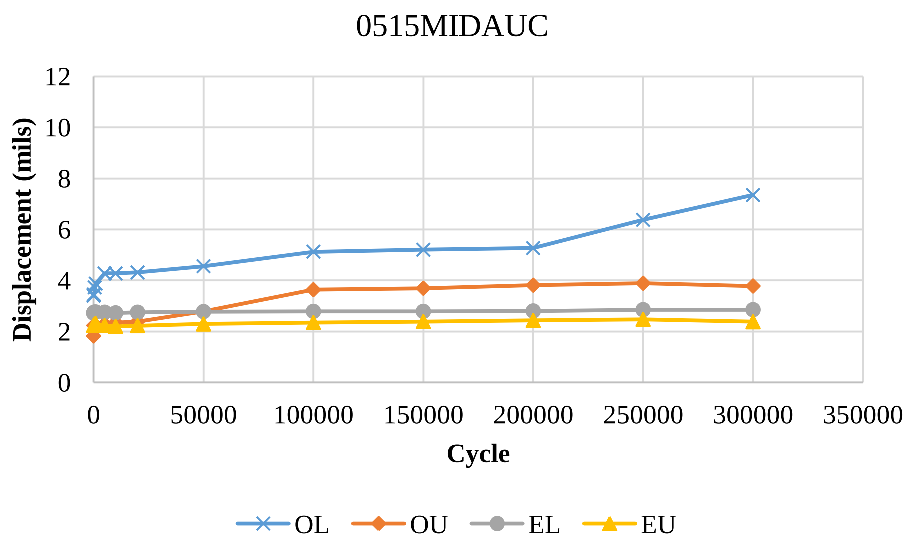

Figure B.23. MIDAU Displacement vs. Load Cycle (Tested on 5/20/15)

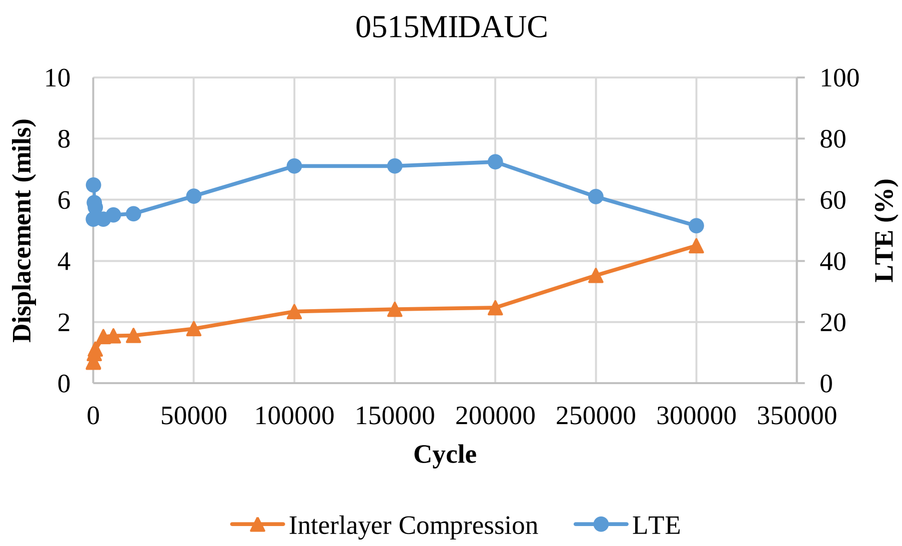

Figure B.24. MIDAU Interlayer Compression and LTE vs. Load Cycle (Tested on 5/20/15)

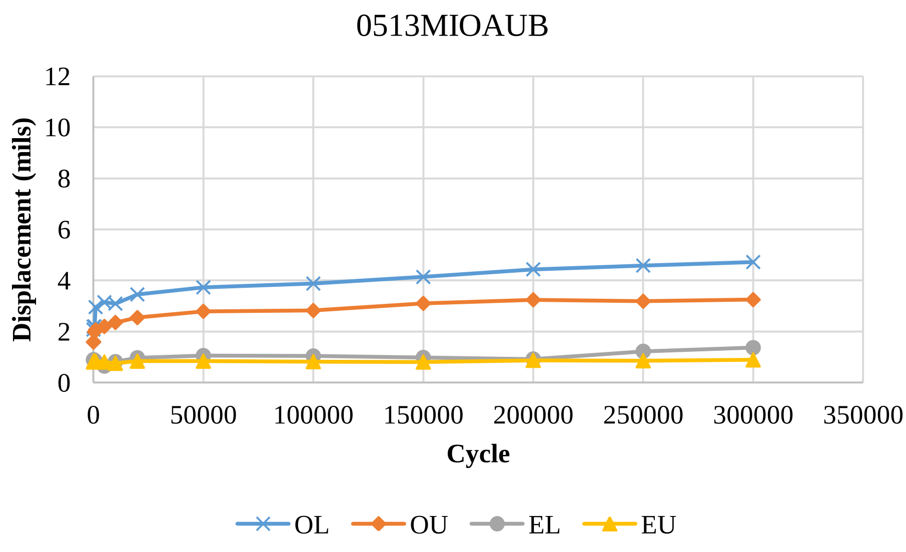

Figure B.25. MIOAU Displacement vs. Load Cycle (Tested on 5/19/15)

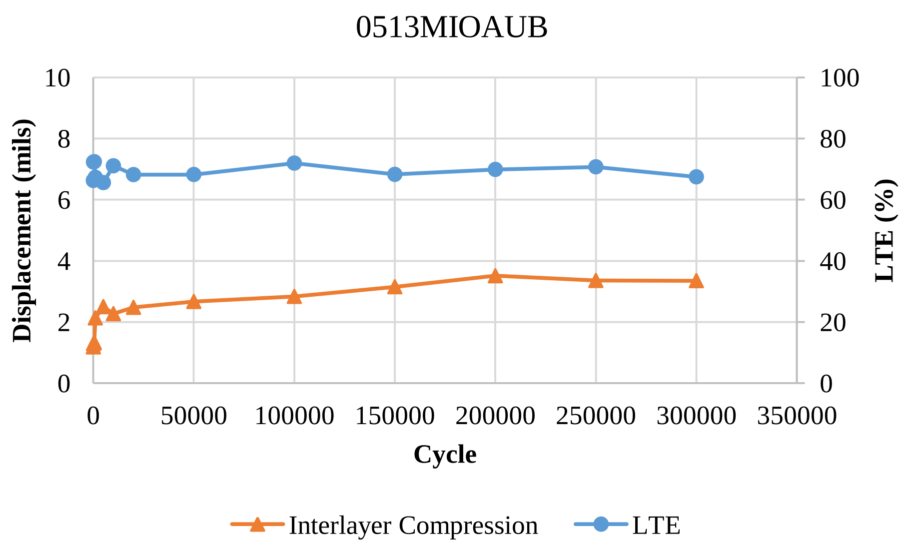

Figure B.26. MIOAU Interlayer Compression and LTE vs. Load Cycle (Tested on 5/19/15)

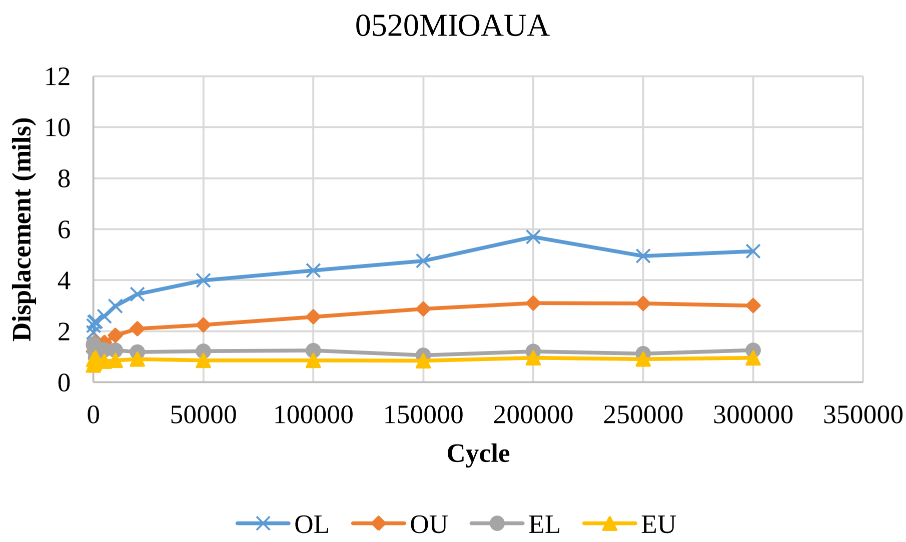

Figure B.27. MIOAU Displacement vs. Load Cycle (Tested on 5/26/15)

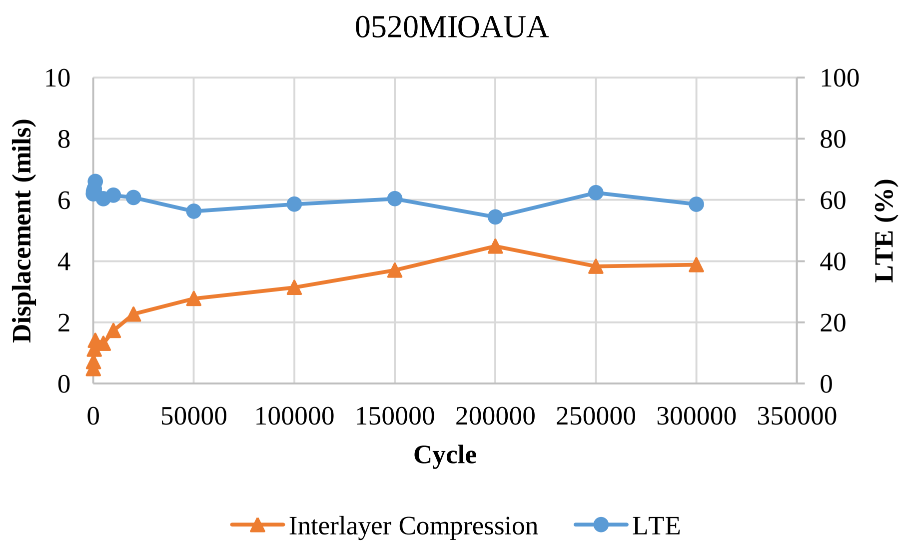

Figure B.28. MIOAU Interlayer Compression and LTE vs. Load Cycle (Tested on 5/26/15)

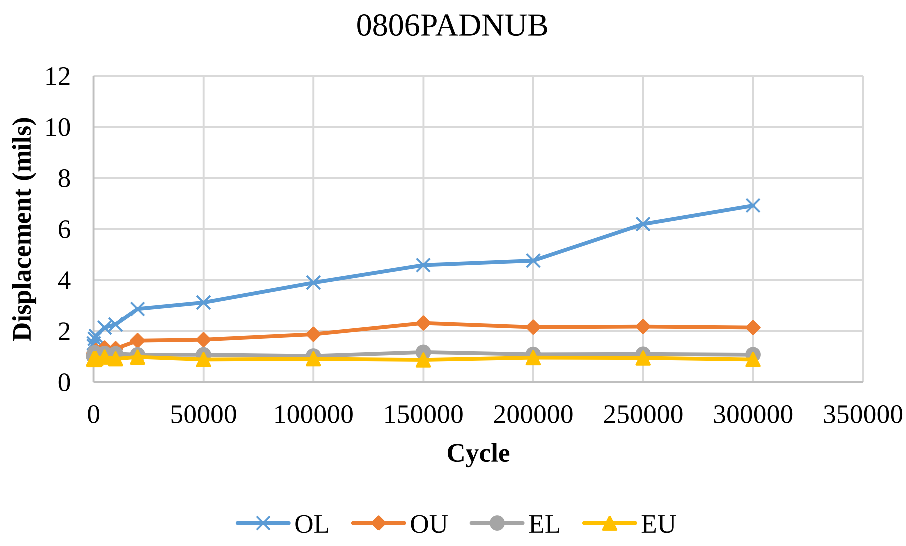

Figure B.29. PADNU Displacement vs. Load Cycle (Tested on 8/11/15)

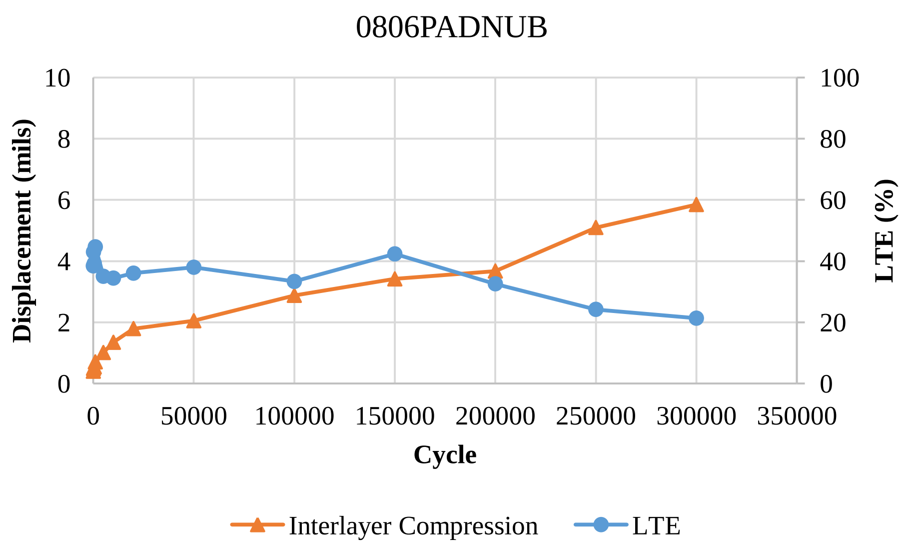

Figure B.30. PADNU Interlayer Compression and LTE vs. Load Cycle (Tested on 8/11/15)

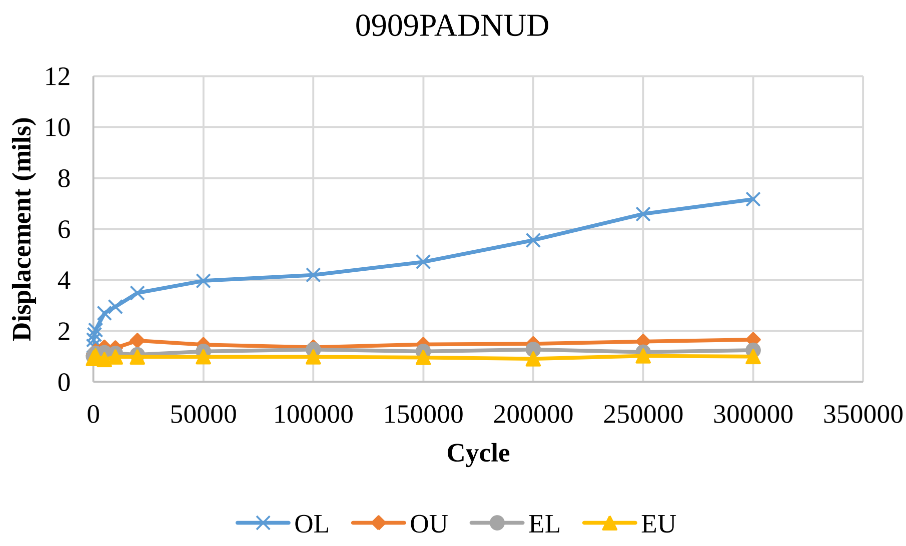

Figure B.31. PADNU Displacement vs. Load Cycle (Tested on 9/16/15)

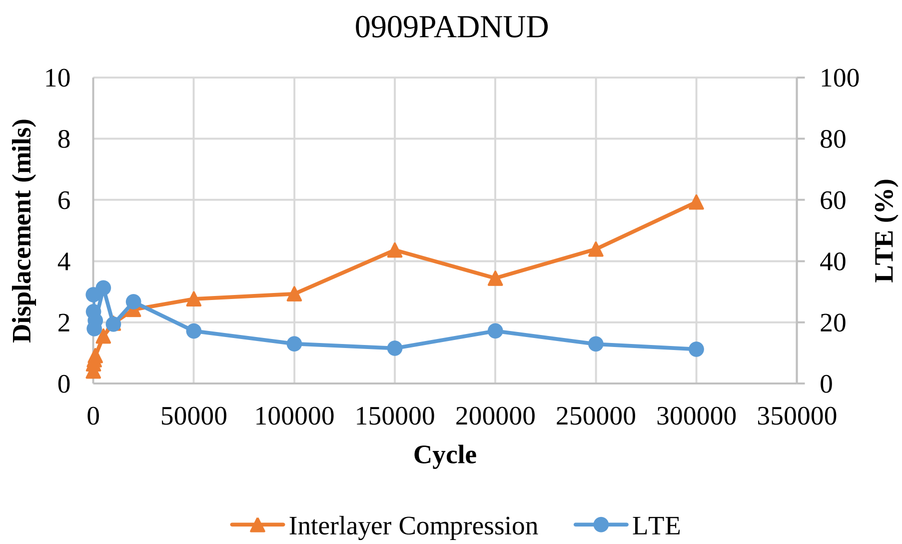

Figure B.32. PADNU Interlayer Compression and LTE vs. Load Cycle (Tested on 9/16/15)

APPENDIX C

RESULTS FROM MODIFIED PUSH-OFF TEST

Two different plots for each specimen tested are shown in Figure C.1 thorough Figure C.38. The first plot show the force and displacement versus time for each of the Phase 1 loading cycles. The second figure shows the force versus displacement for each of the Phase 1 loading cycles. In this phase load is applied until the test block reaches approximately 80 mils of displacement. The 80 mil displacement corresponds to a 100 degree Fahrenheit drop in temperature for a 12 foot slab cast of concrete with a thermal coefficient of expansion of 5.3 microstrain per degree F. The load is then held constant to observe the relaxation of the interlayer system until the force is relatively constant over time. The load is then removed from the rod. To account for non-elastic displacement load is applied in the opposite direction until the test block returns to its initial position. This position is then held until the force is relatively constant over time. This cycle is then repeated between 6 and 8 times for each test. Please refer to Chapter 2 as necessary for the modified push-off testing setup.

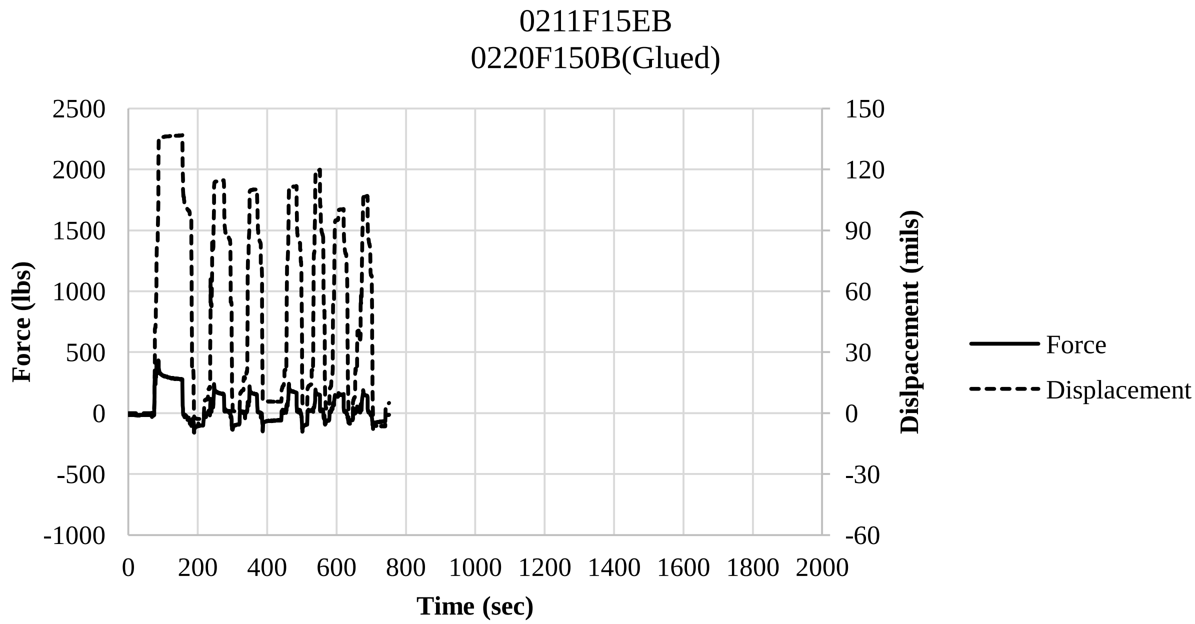

Figure C.1. F15(Glued) Force and Displacement vs. Time (Tested on 3/20/15)

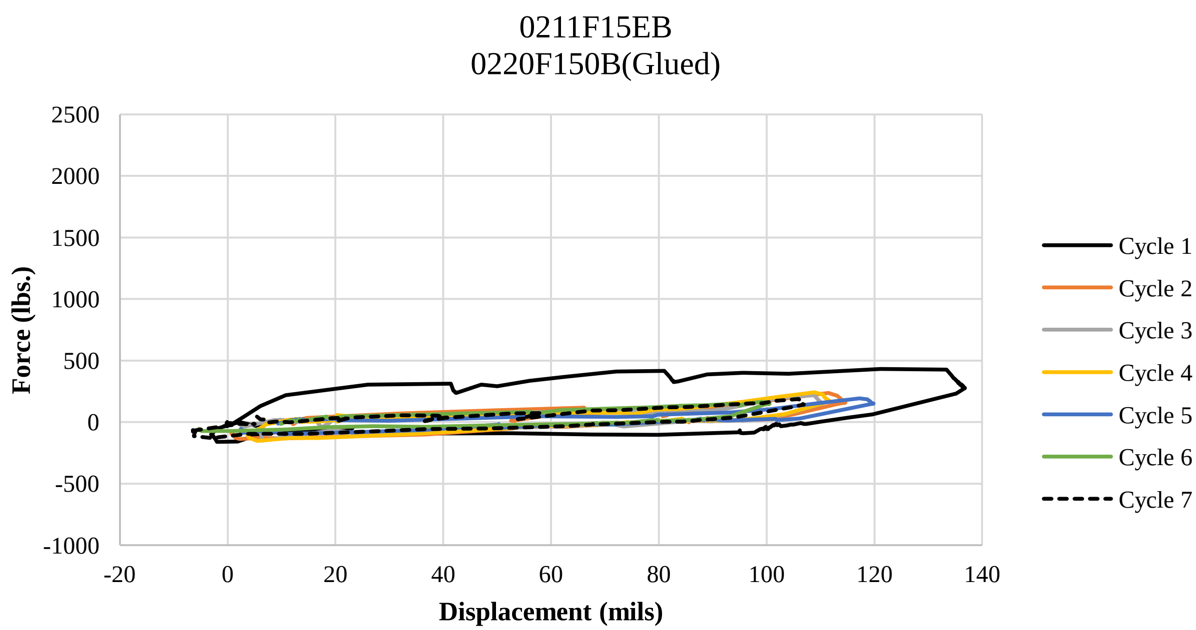

Figure C.2. F15(Glued) Force vs. Displacement (Tested on 3/20/15)

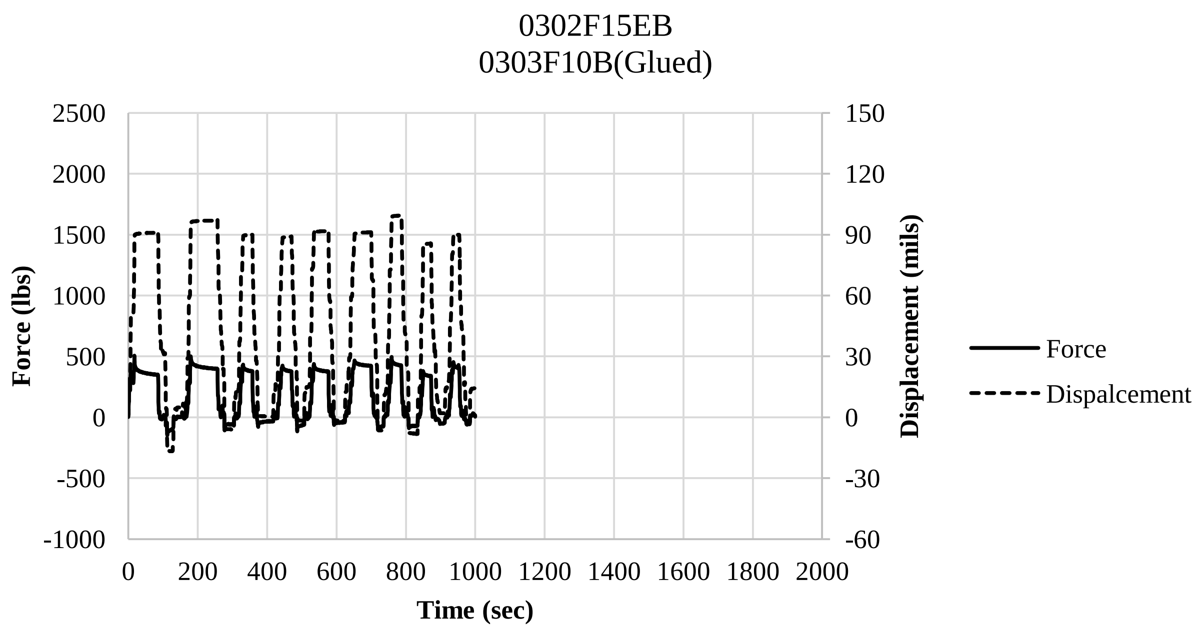

Figure C.3. F15(Glued) Force and Displacement vs. Time (Tested on 4/1/15)

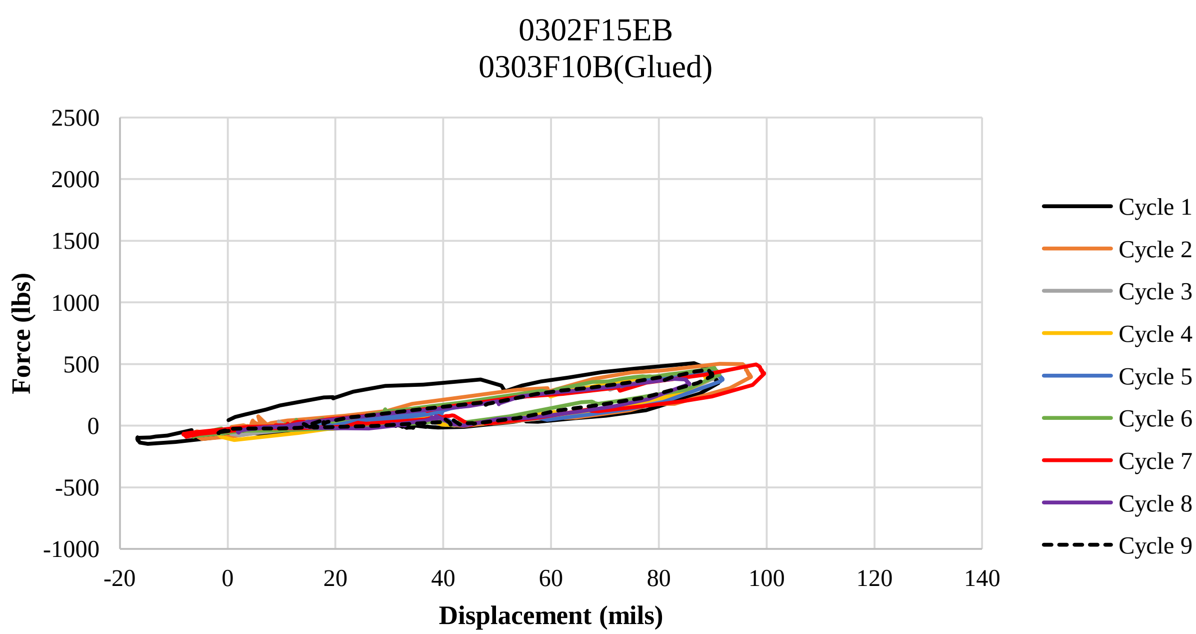

Figure C.4. F15(Glued) Force vs. Displacement (Tested on 4/1/15)

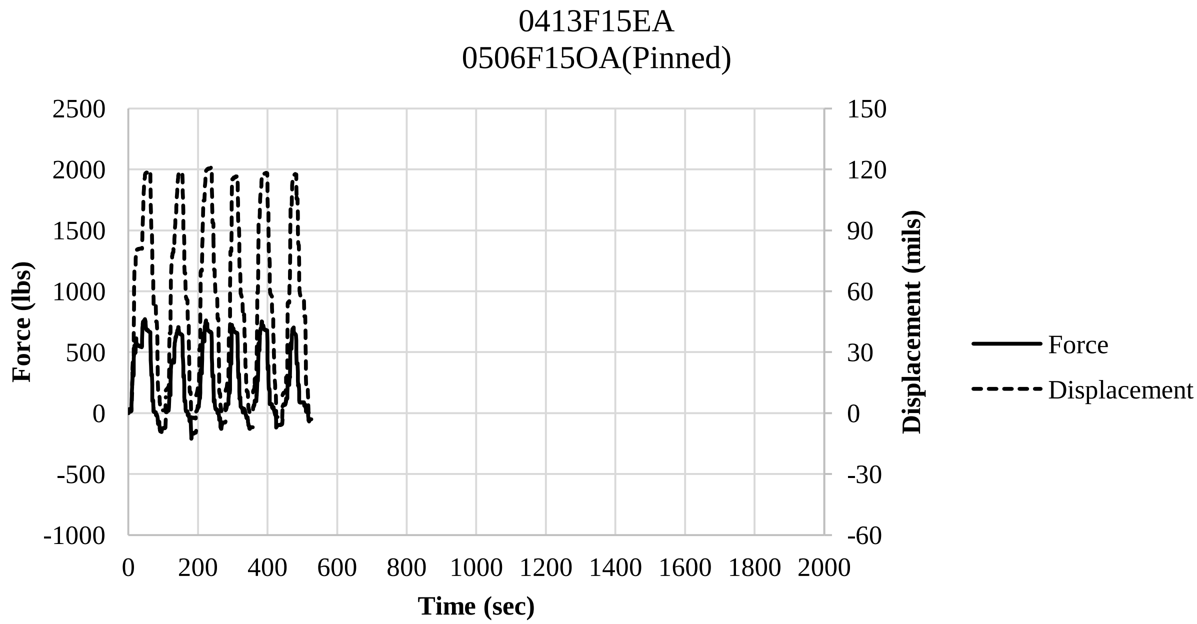

Figure C.5. F15(Pinned) Force and Displacement vs. Time (Tested on 5/11/15)

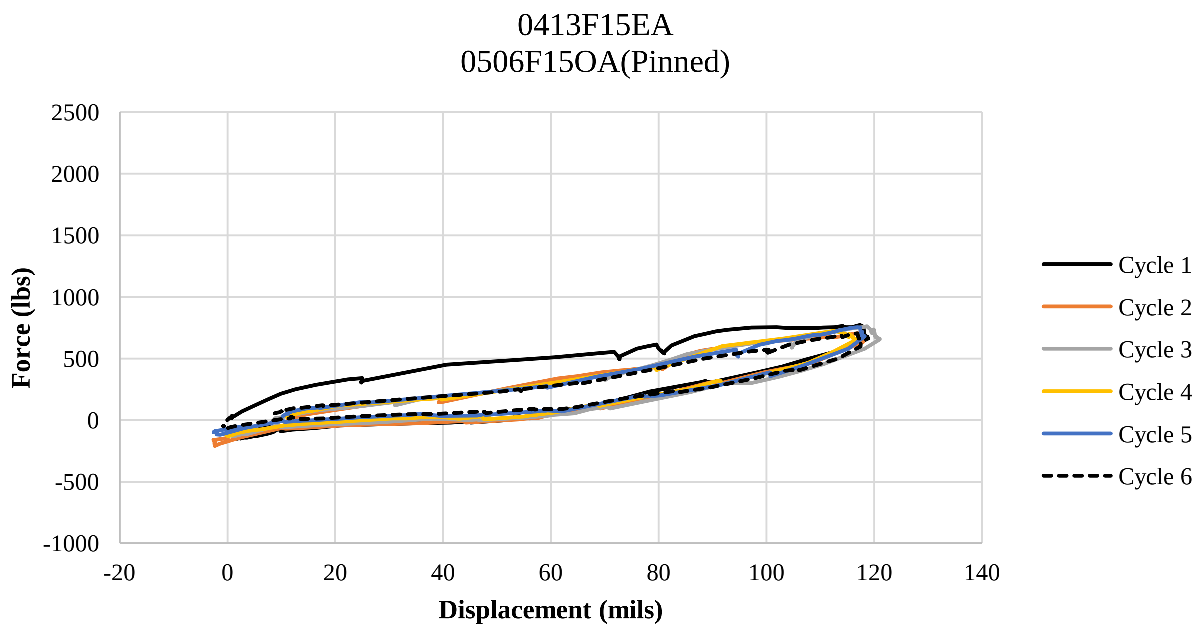

Figure C.6. F15(Pinned) Force vs. Displacement (Tested on 5/11/15)

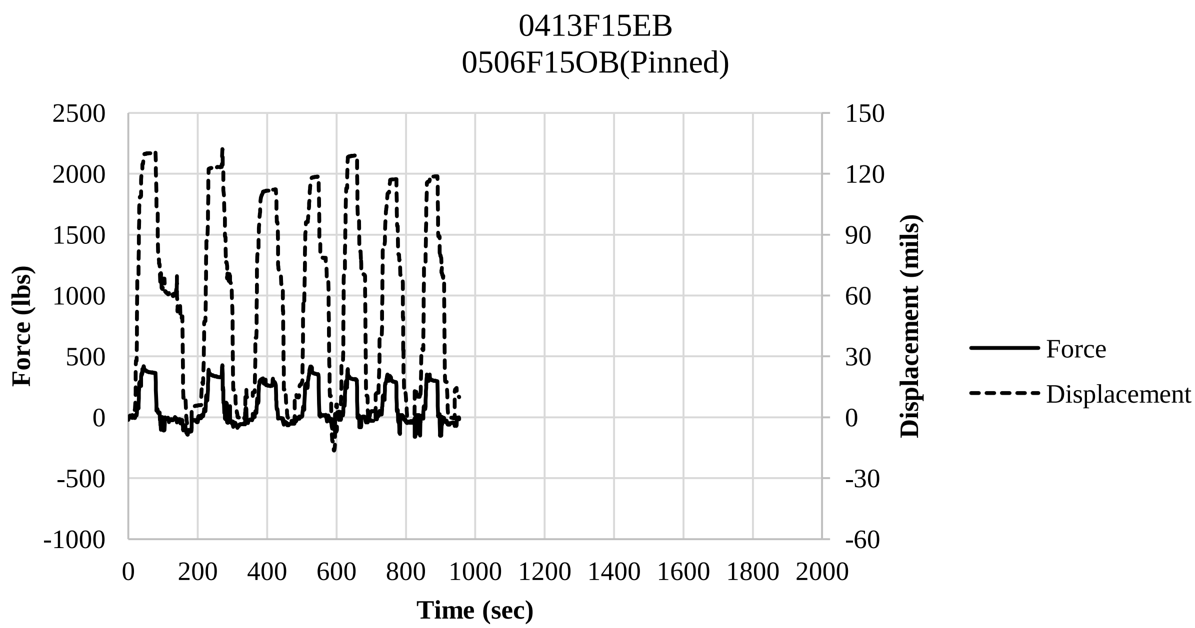

Figure C.7. F15(Pinned) Force and Displacement vs. Time (Tested on 5/12/15)

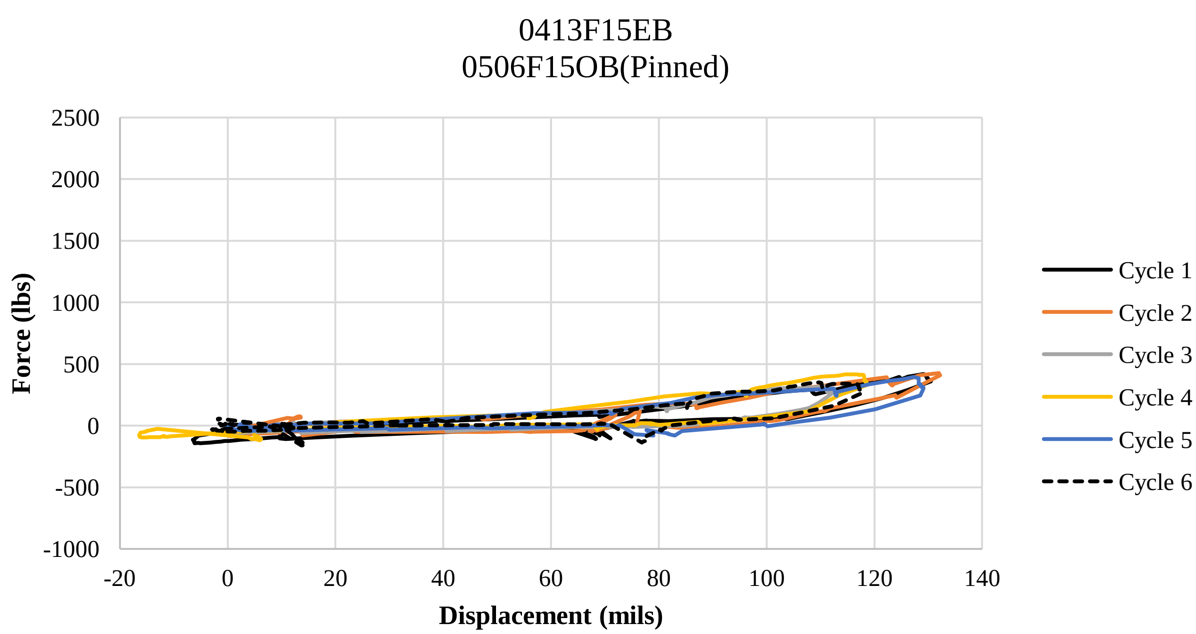

Figure C.8. F15(Pinned) Force vs. Displacement (Tested on 5/12/15)

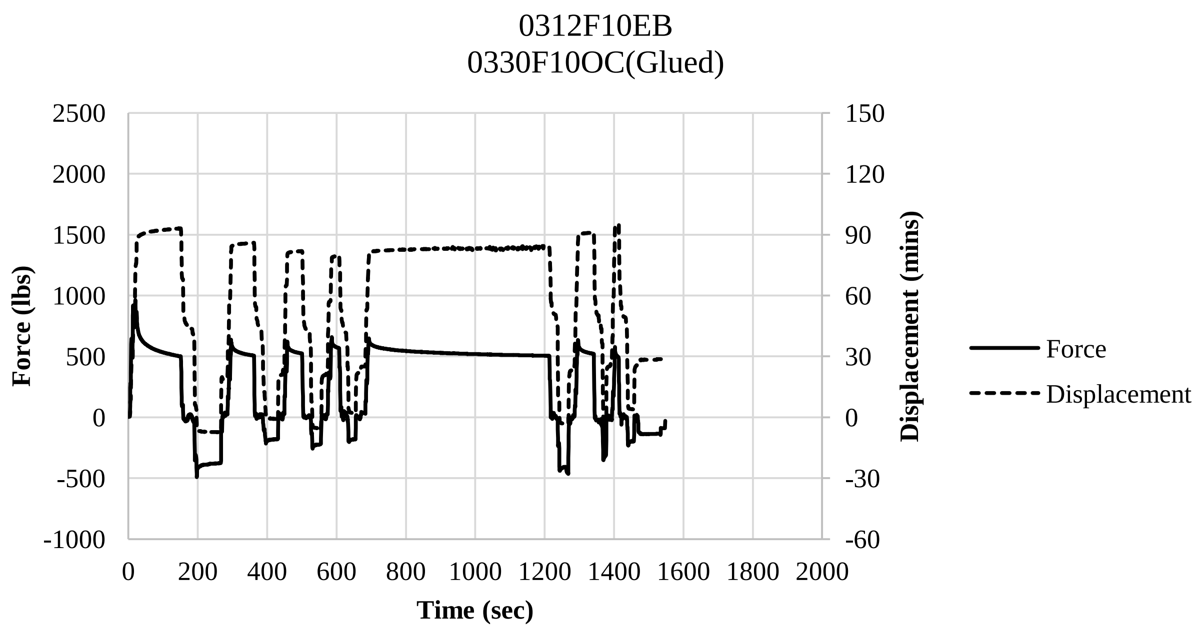

Figure C.9. F10(Glued) Force and Displacement vs. Time (Tested on 4/10/15)

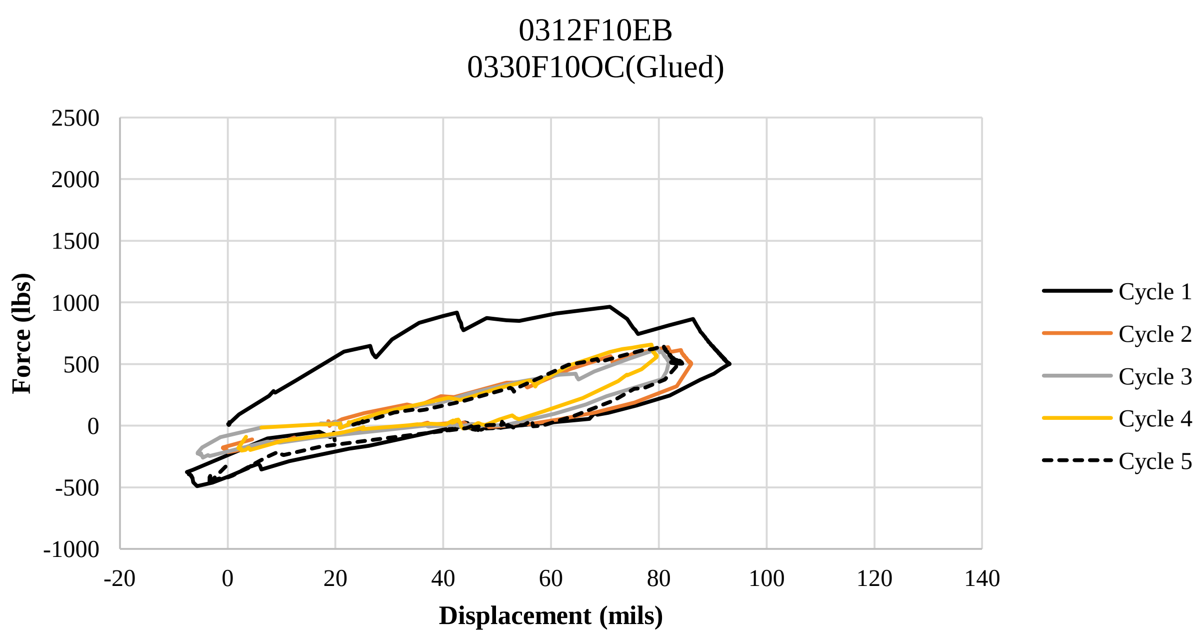

Figure C.10. F10(Glued) Force vs. Displacement (Tested on 4/10/15)

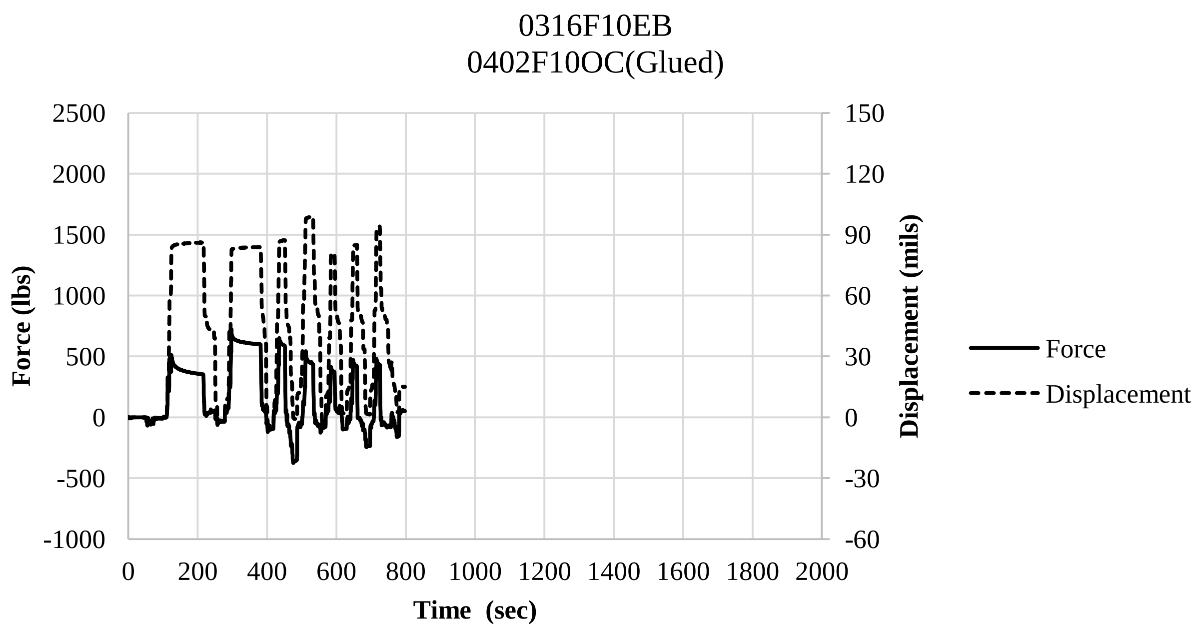

Figure C.11. F10(Glued) Force and Displacement vs. Time (Tested on 4/10/15)

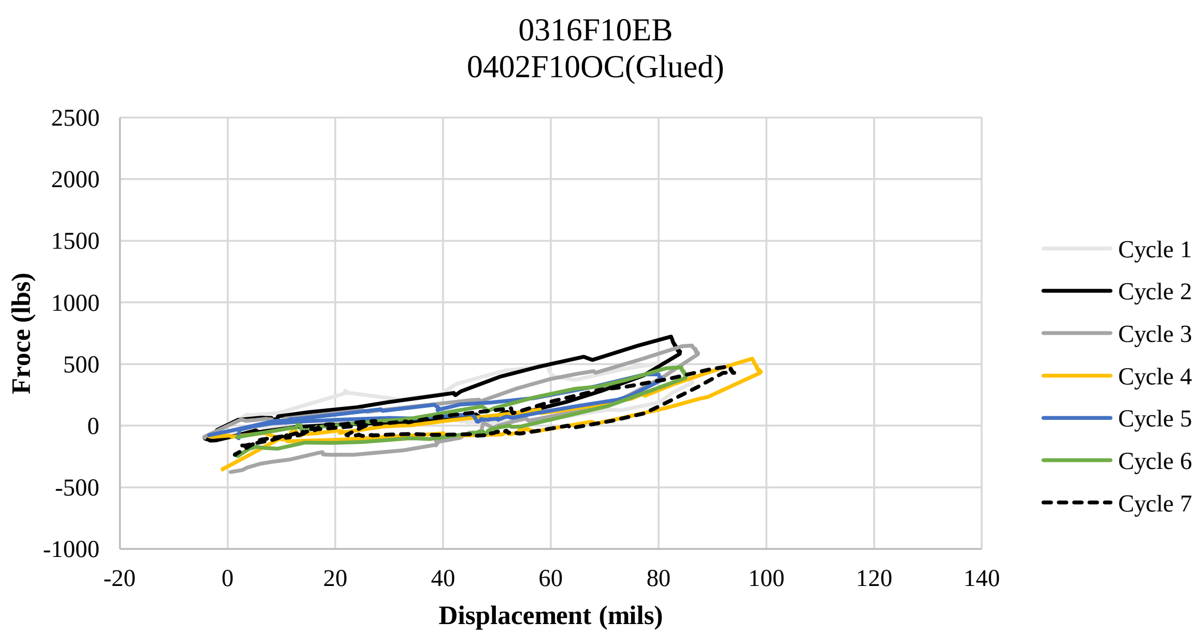

Figure C.12. F10(Glued) Force vs. Displacement (Tested on 4/10/15)

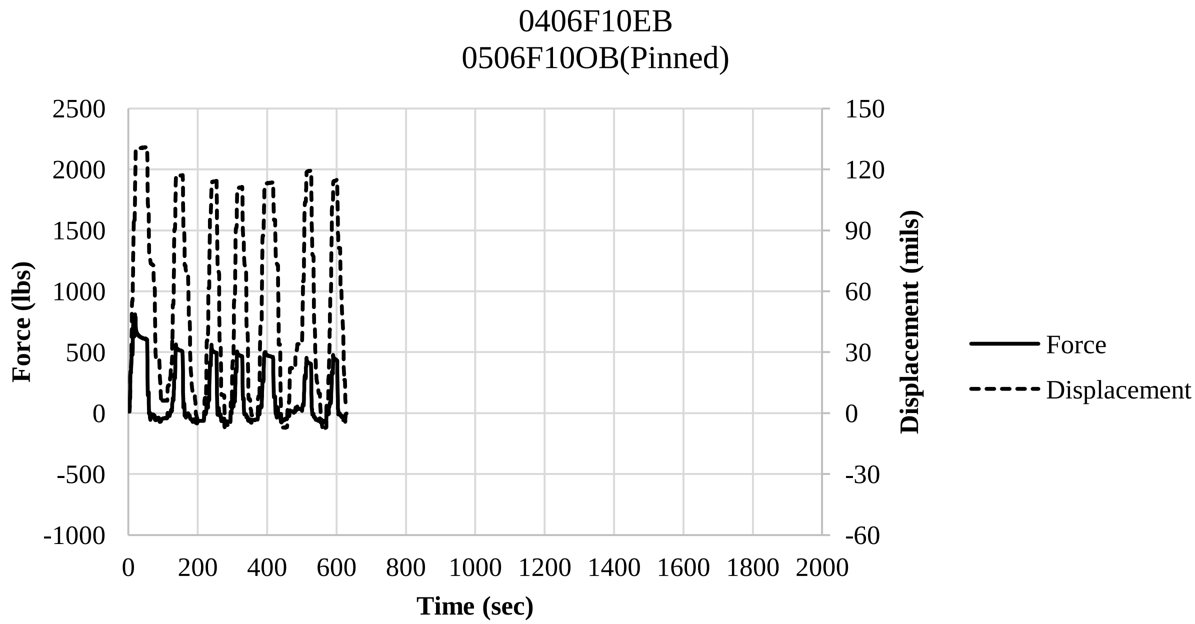

Figure C.13. F10(Pinned) Force and Displacement vs. Time (Tested on 5/11/15)

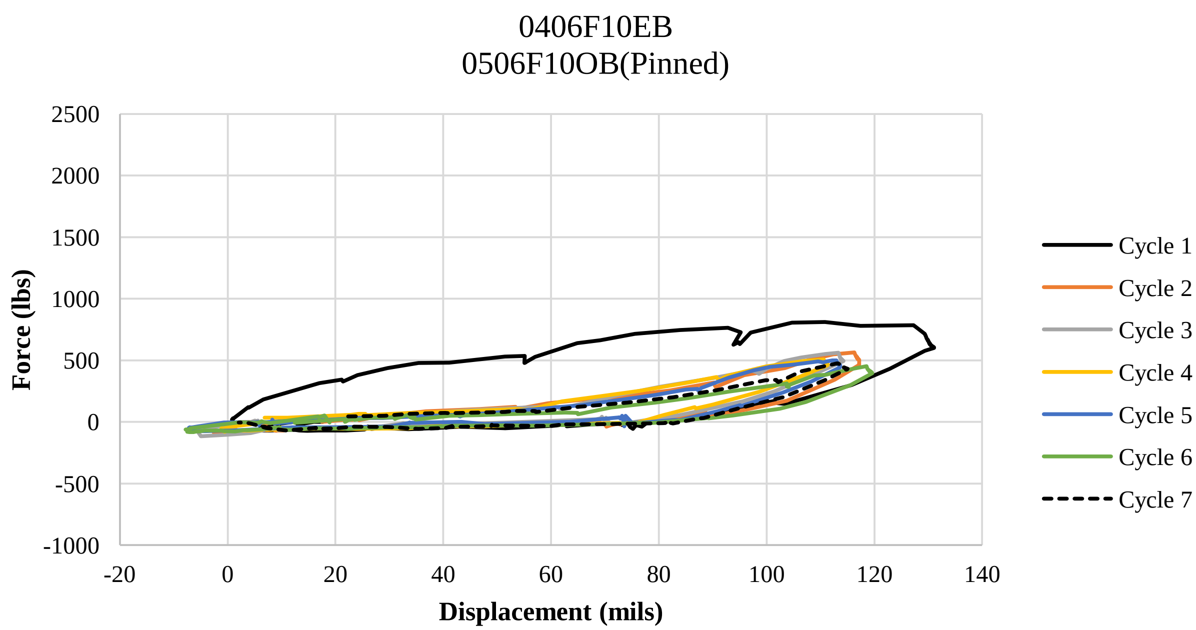

Figure C.14. F10(Pinned) Force vs. Displacement (Tested on 5/11/15)

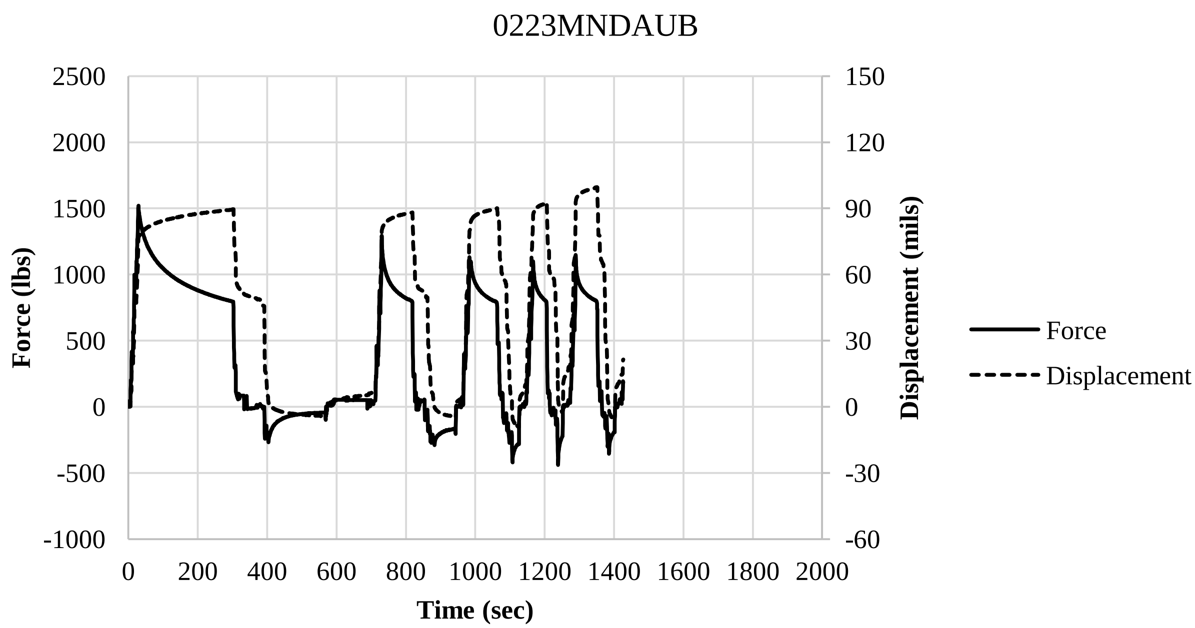

Figure C.15. MNDAU Force and Displacement vs. Time (Tested on 3/24/15)

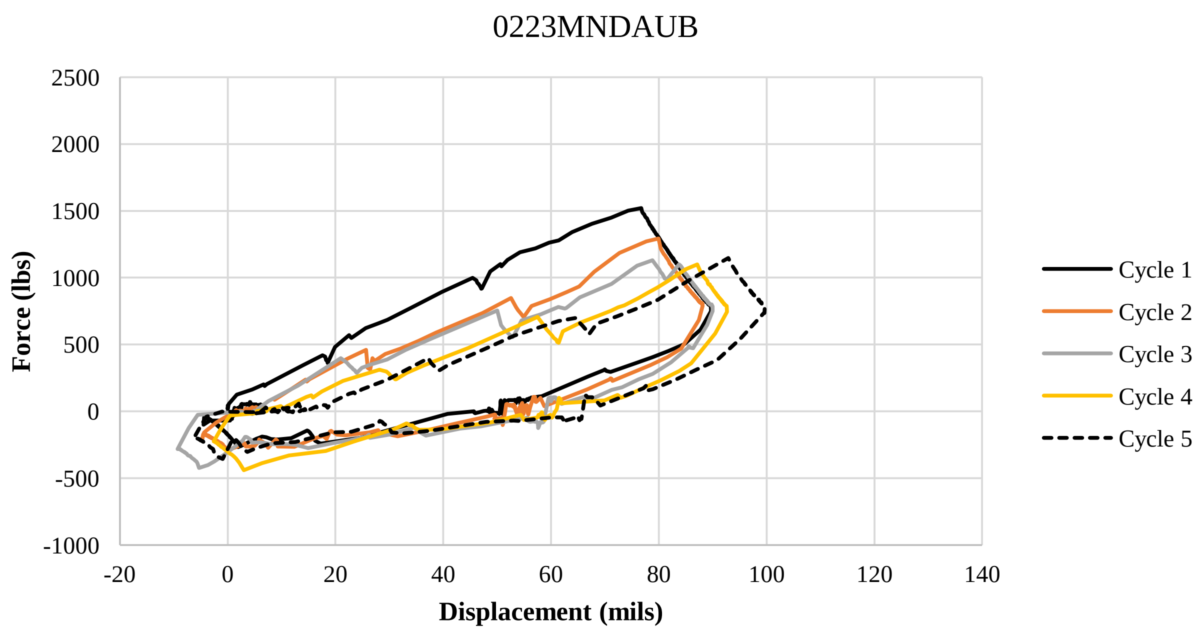

Figure C.16. MNDAU Force vs. Displacement (Tested on 3/24/15)

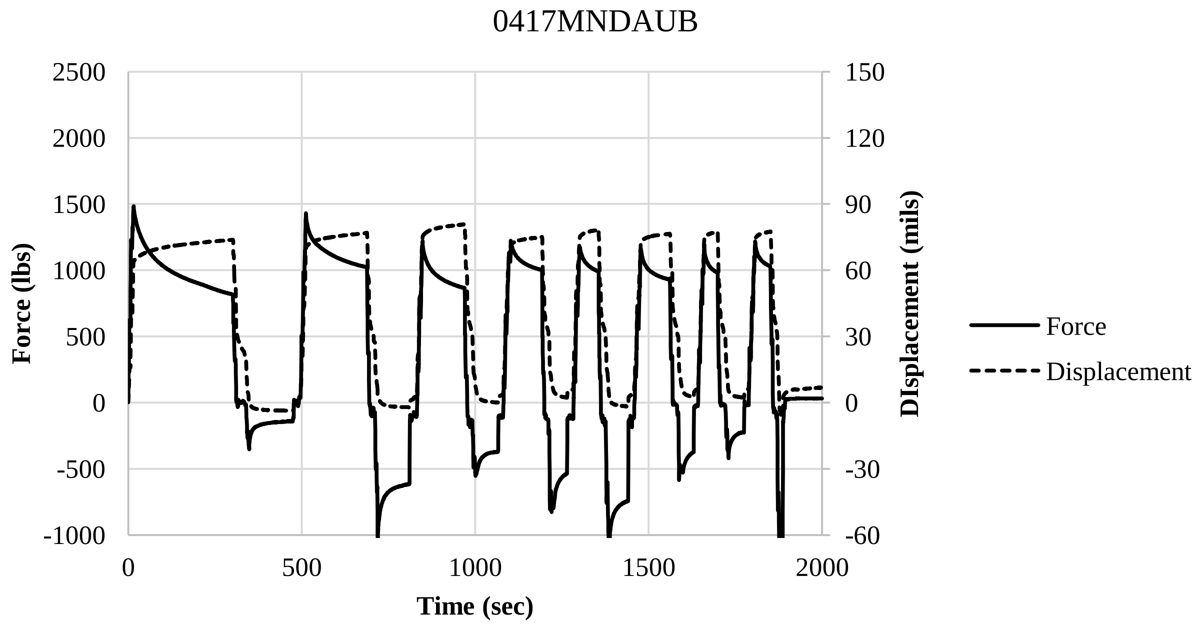

Figure C.17. MNDAU Force and Displacement vs. Time (Tested on 4/23/15)

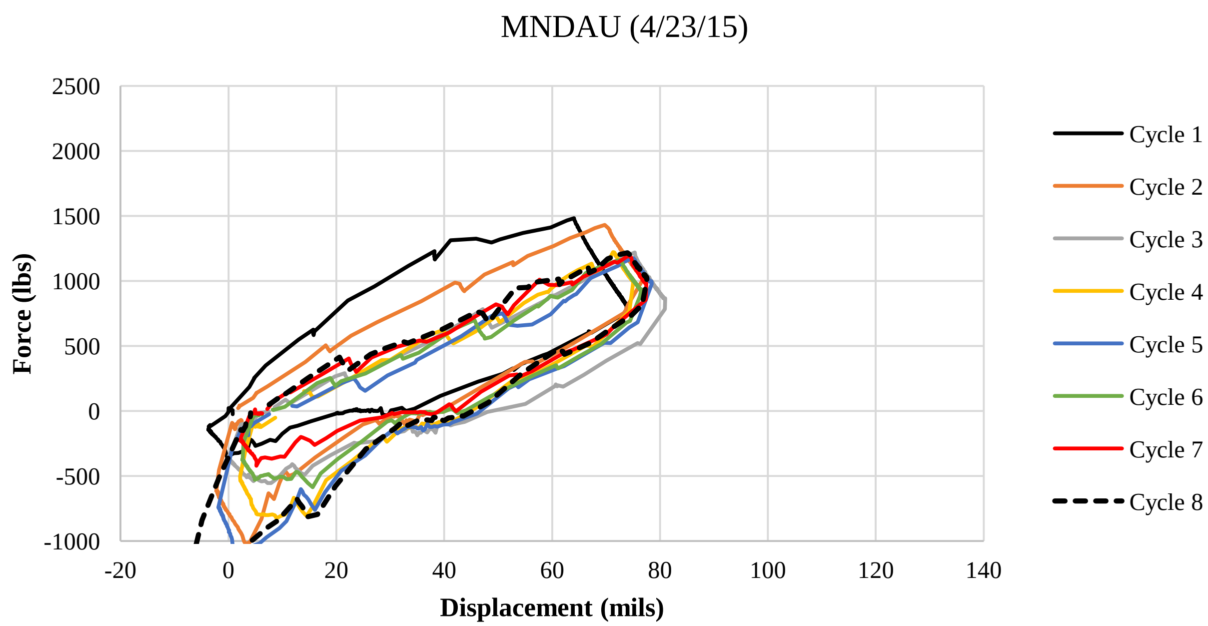

Figure C.18. MNDAU Force vs. Displacement (Tested on 4/23/15)

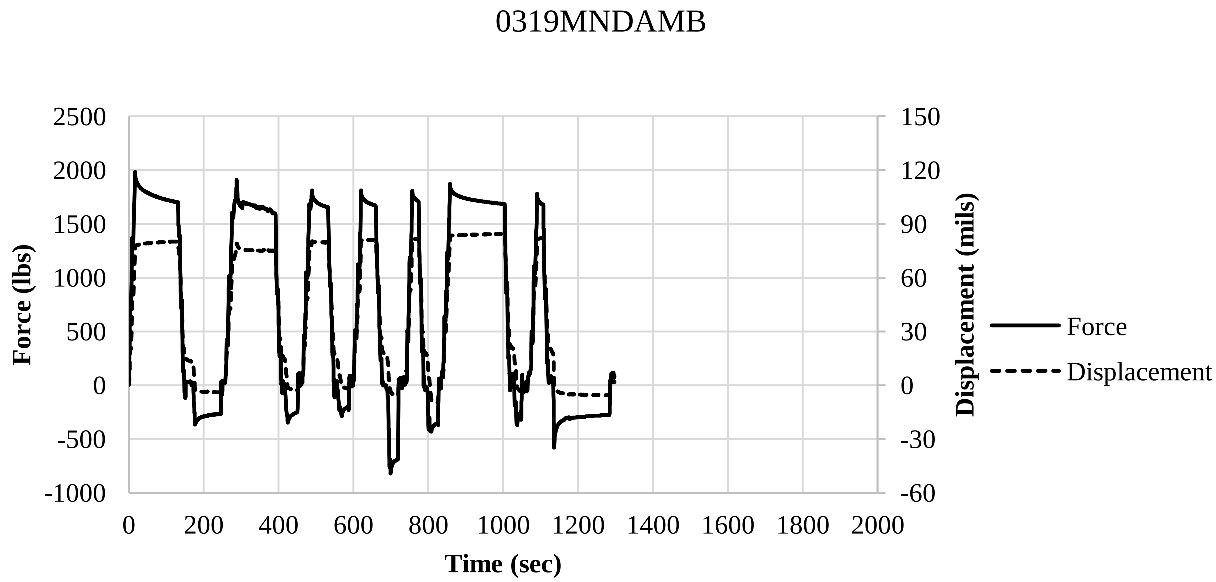

Figure C.19. MNDAM Force and Displacement vs. Time (Tested on 4/3/15)

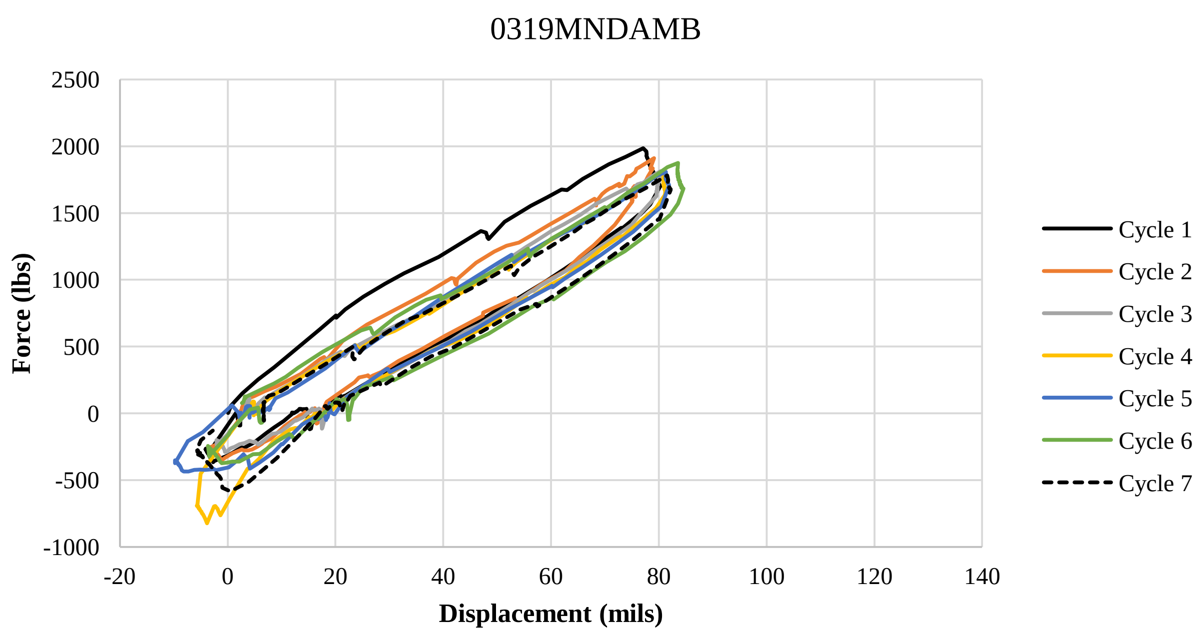

Figure C.20. MNDAM Force vs. Displacement (Tested on 4/3/15)

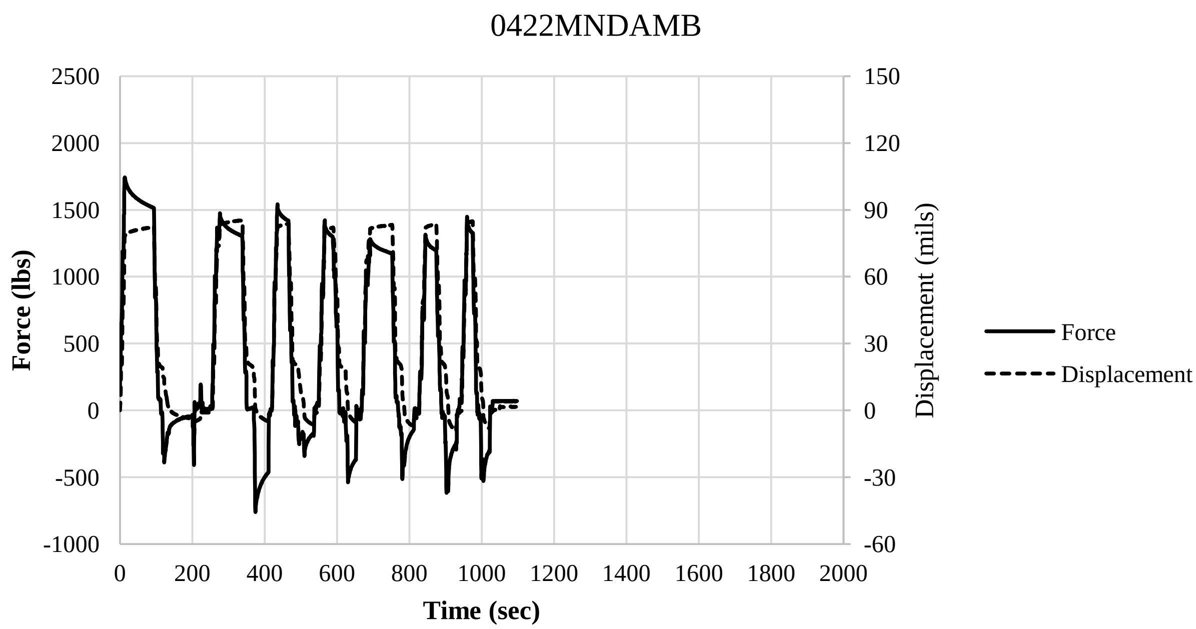

Figure C.21. MNDAM Force and Displacement vs. Time (Tested on 4/27/15)

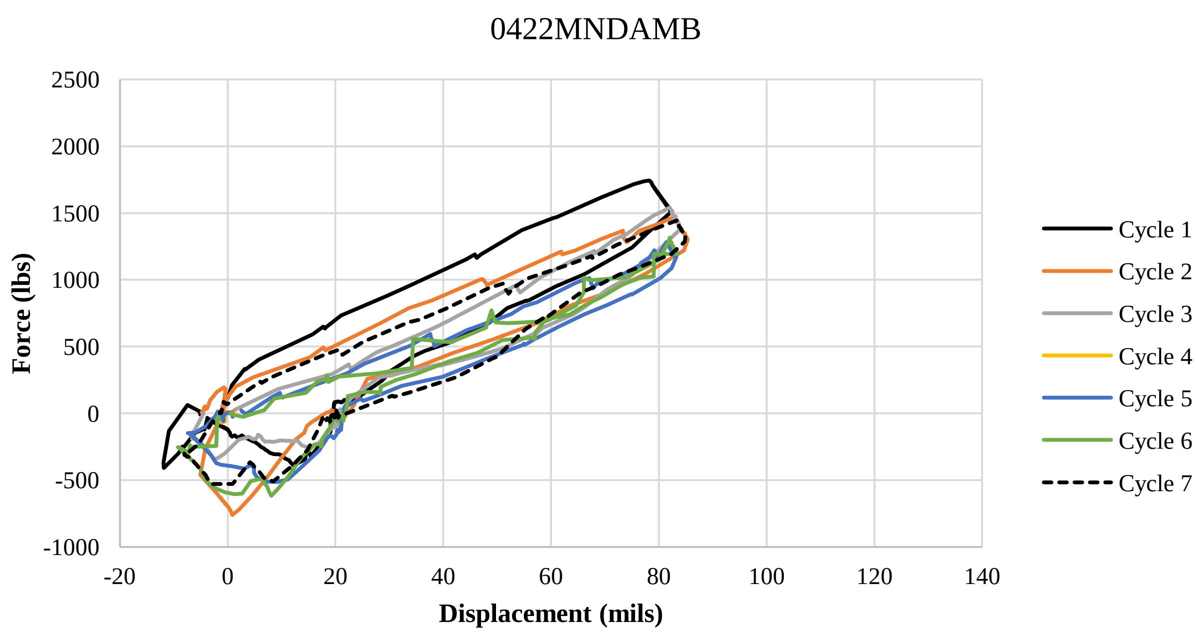

Figure C.22. MNDAM Force vs. Displacement (Tested on 4/27/15)

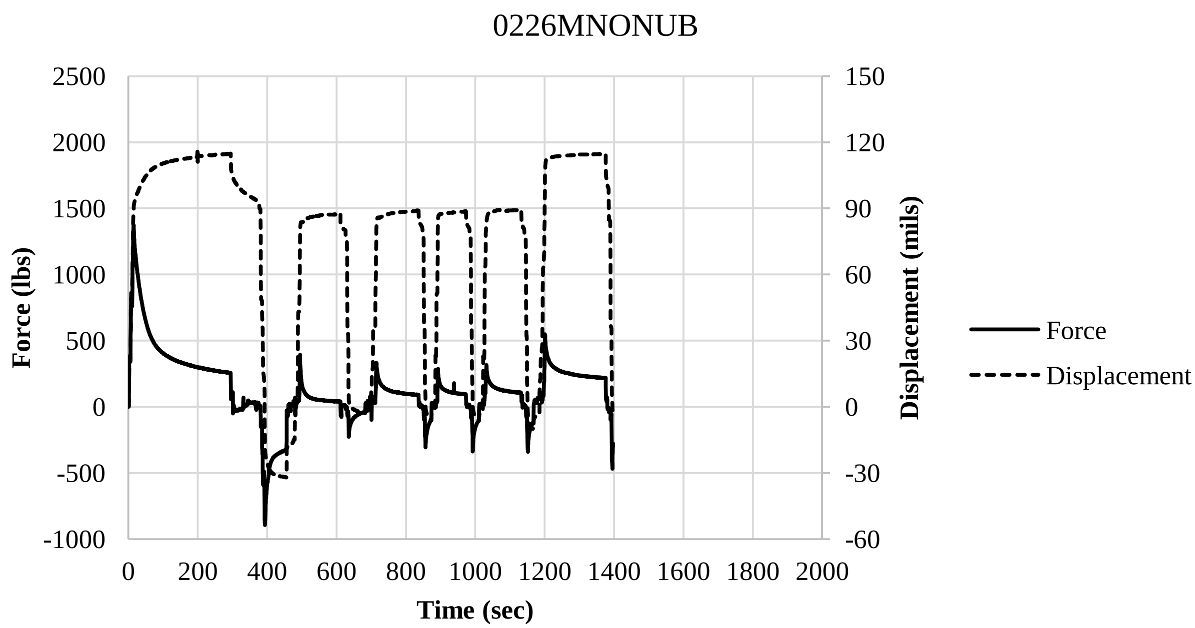

Figure C.23. MNONU Force and Displacement vs. Time (Tested on 3/30/15)

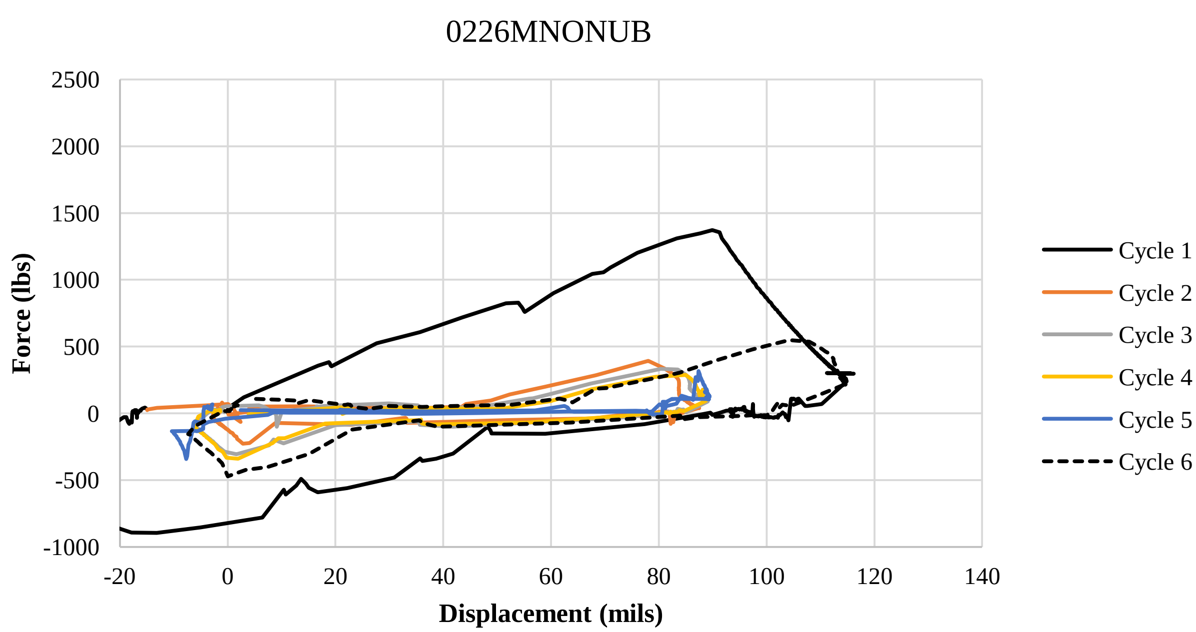

Figure C.24. MNONU Force vs. Displacement (Tested on 3/30/15)

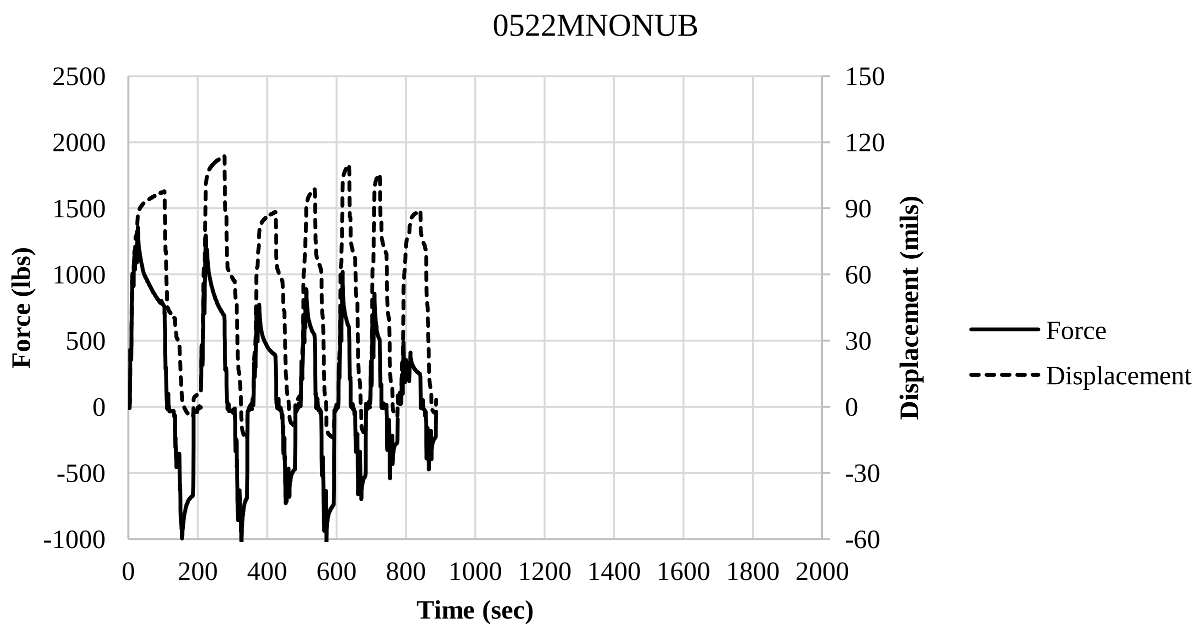

Figure C.25. MNONU Force and Displacement vs. Time (Tested on 5/26/15)

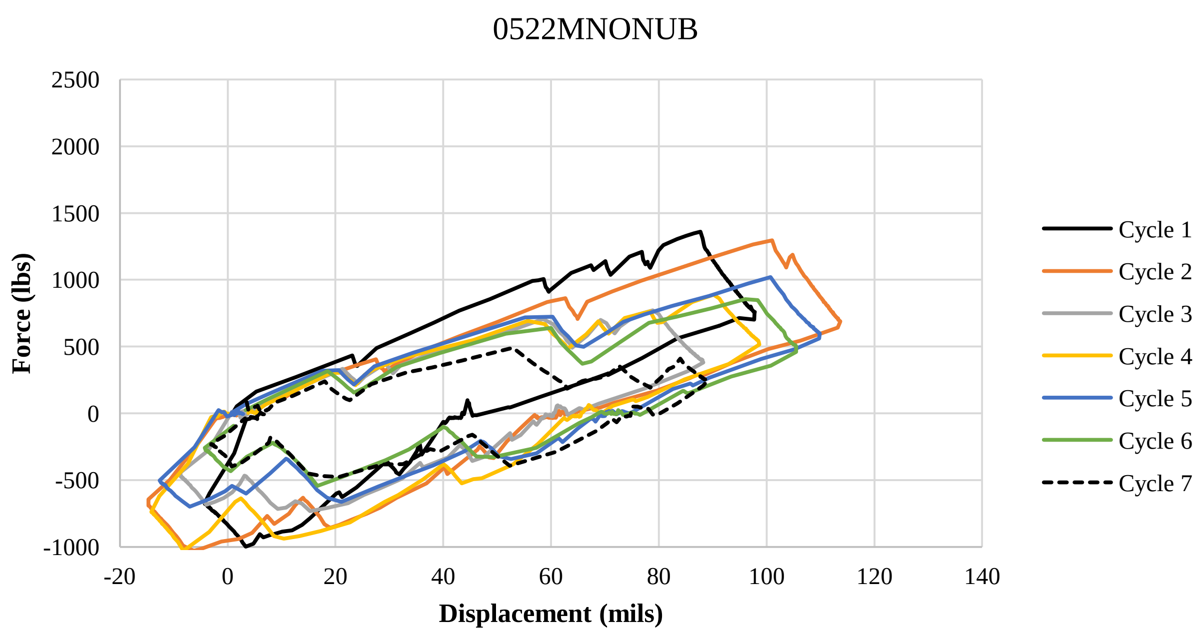

Figure C.26. MNONU Force vs. Displacement (Tested on 5/26/15)

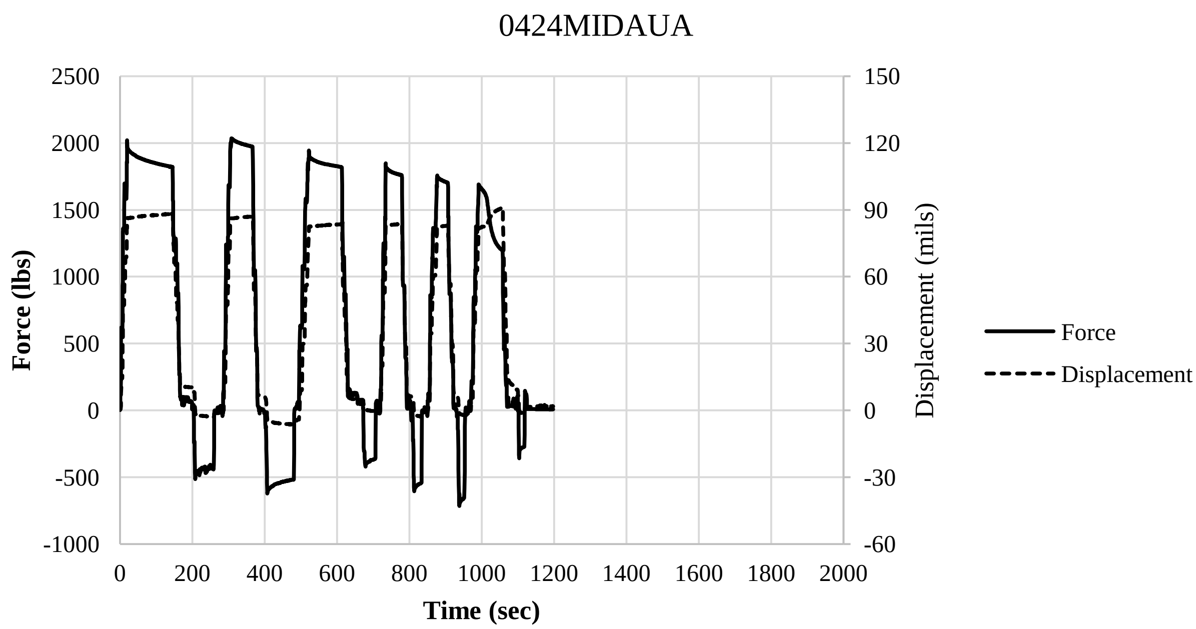

Figure C.27. MIDAU Force and Displacement vs. Time (Tested on 4/29/15)

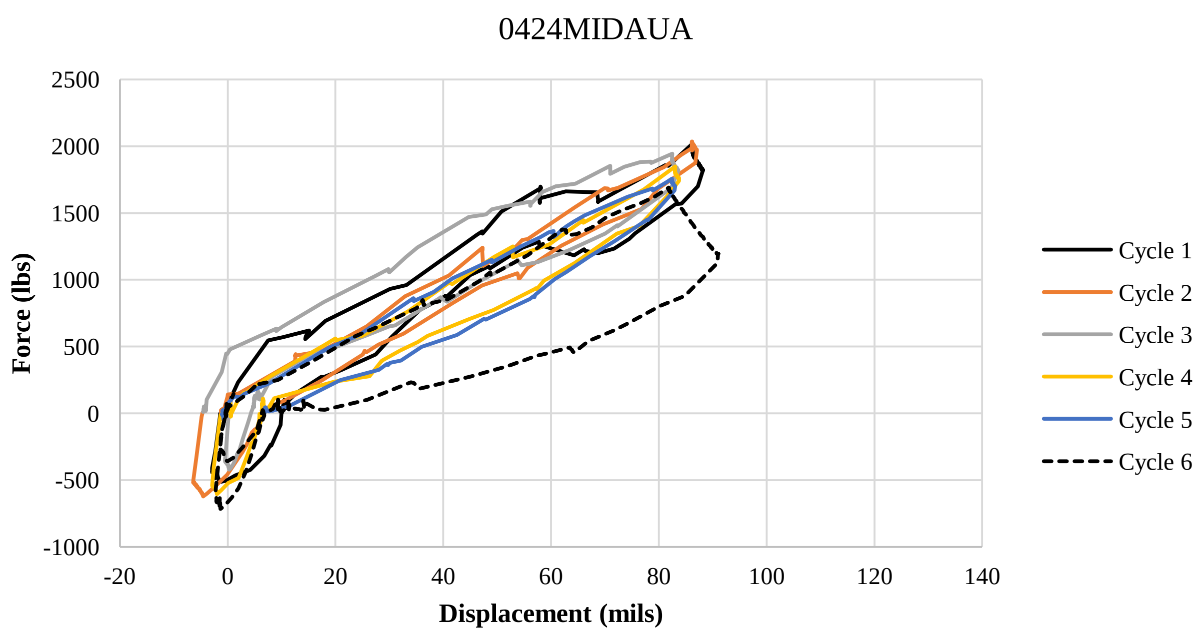

Figure C.28. MIDAU Force vs. Displacement (Tested on 4/29/15)

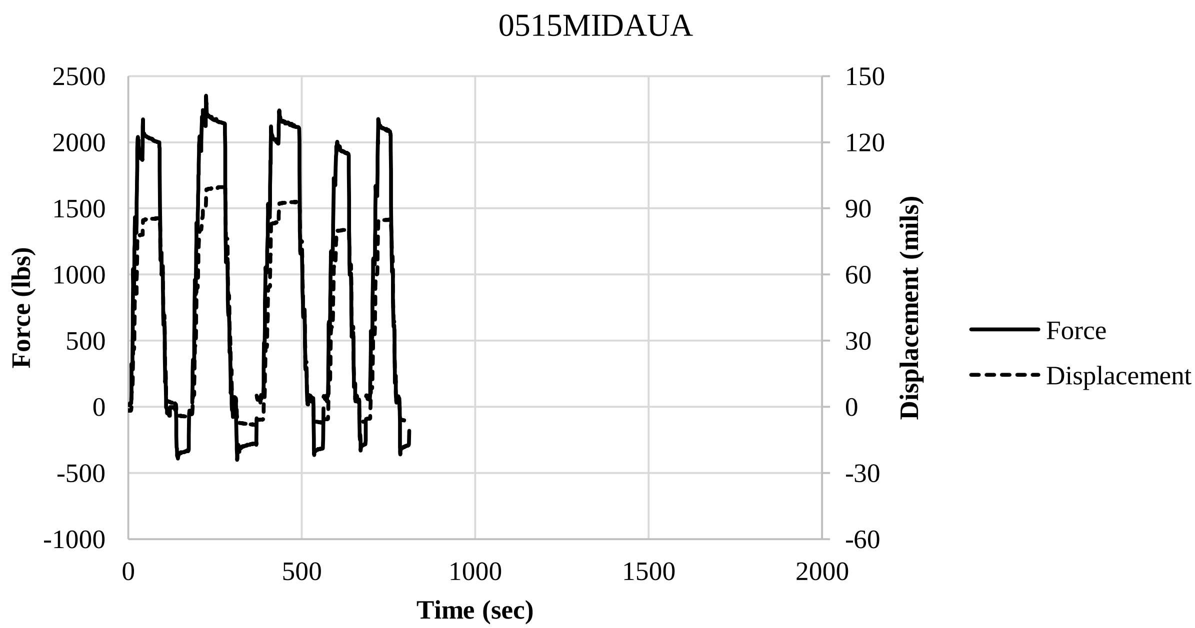

Figure C.29. MIDAU Force and Displacement vs. Time (Tested on 5/20/15)

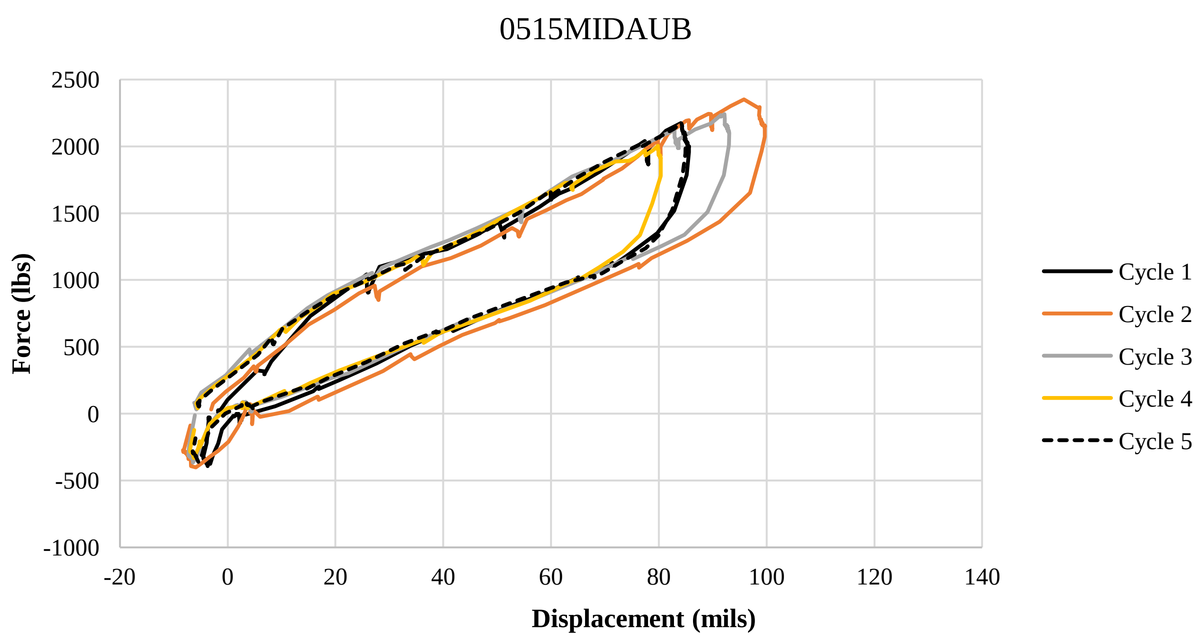

Figure C.30. MIDAU Force vs. Displacement (Tested on 5/20/15)

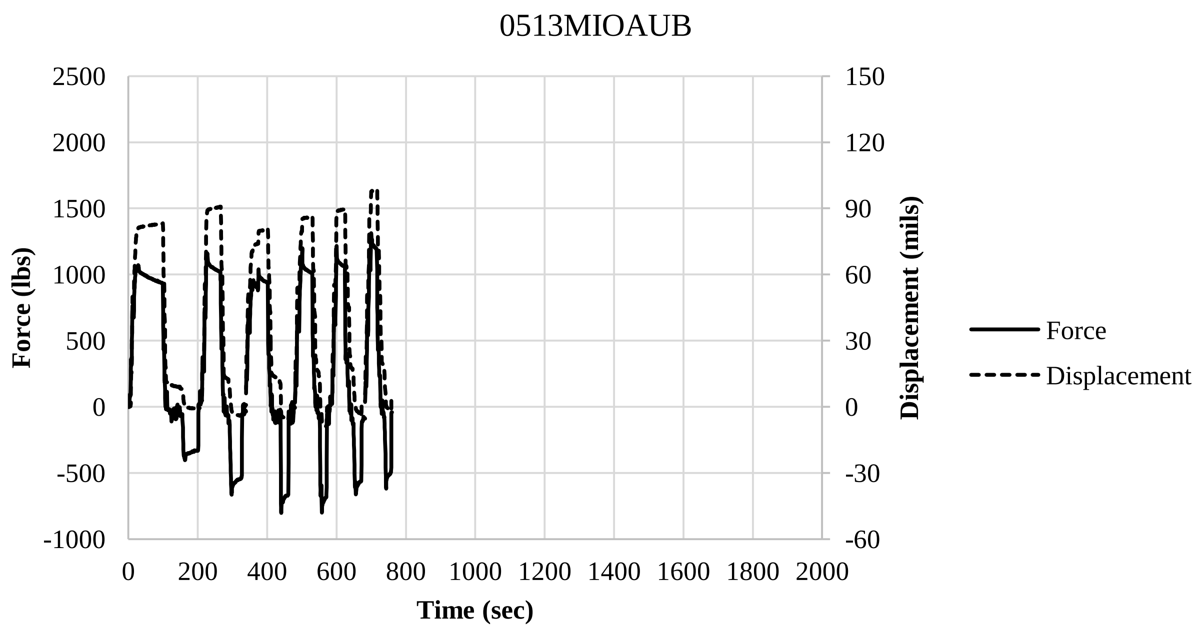

Figure C.31. MIOAU Force and Displacement vs. Time (Tested on 5/18/15)

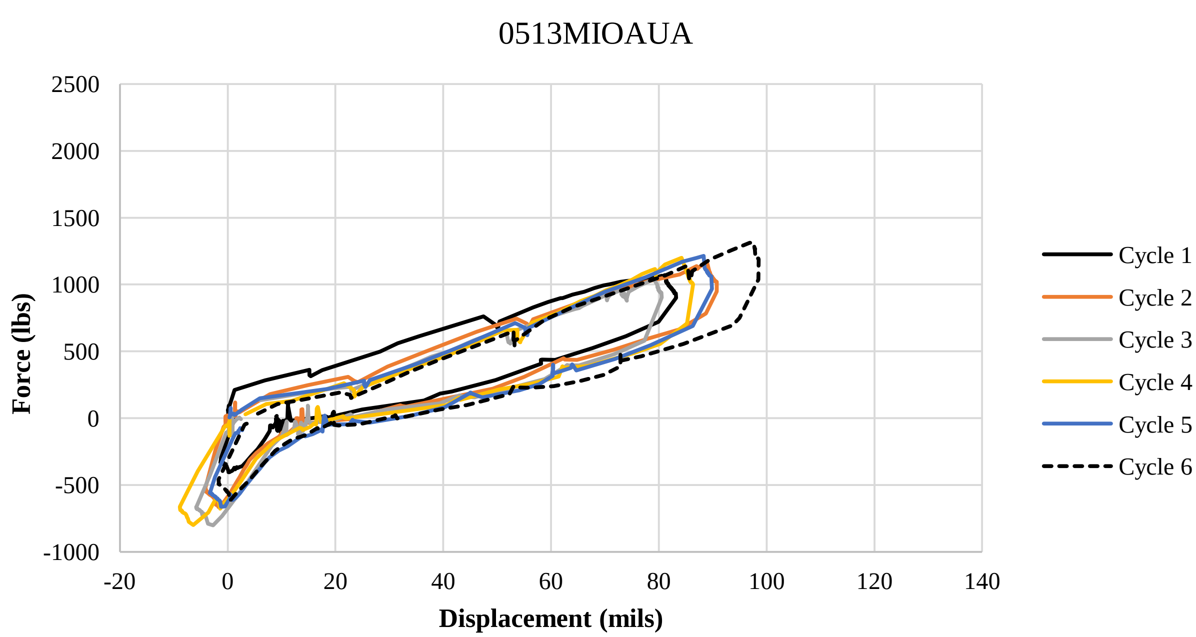

Figure C.32. MIOAU Force vs. Displacement (Tested on 5/18/15)

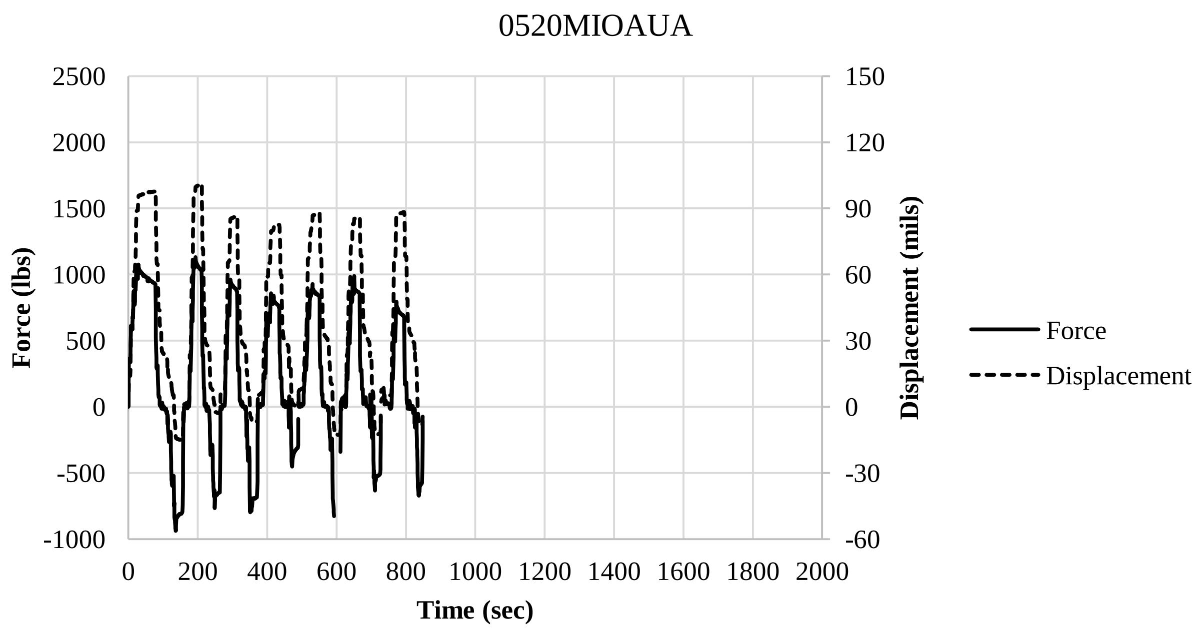

Figure C.33. MIOAU Force and Displacement vs. Time (Tested on 5/26/15)

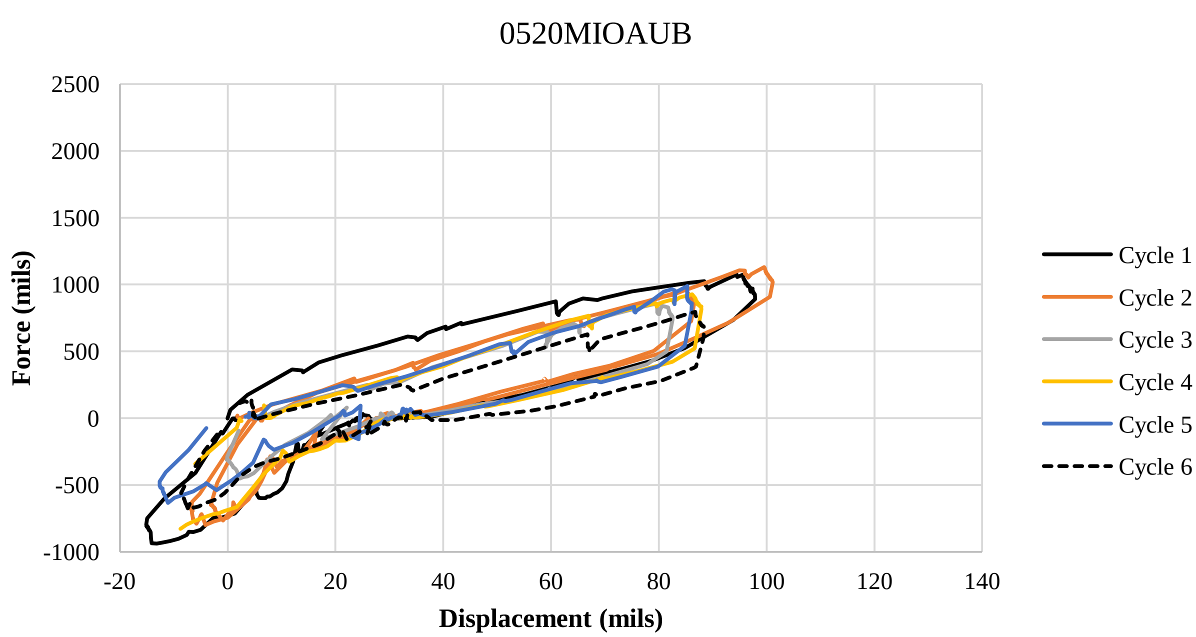

Figure C.34. MIOAU Force vs. Displacement (Tested on 5/26/15)

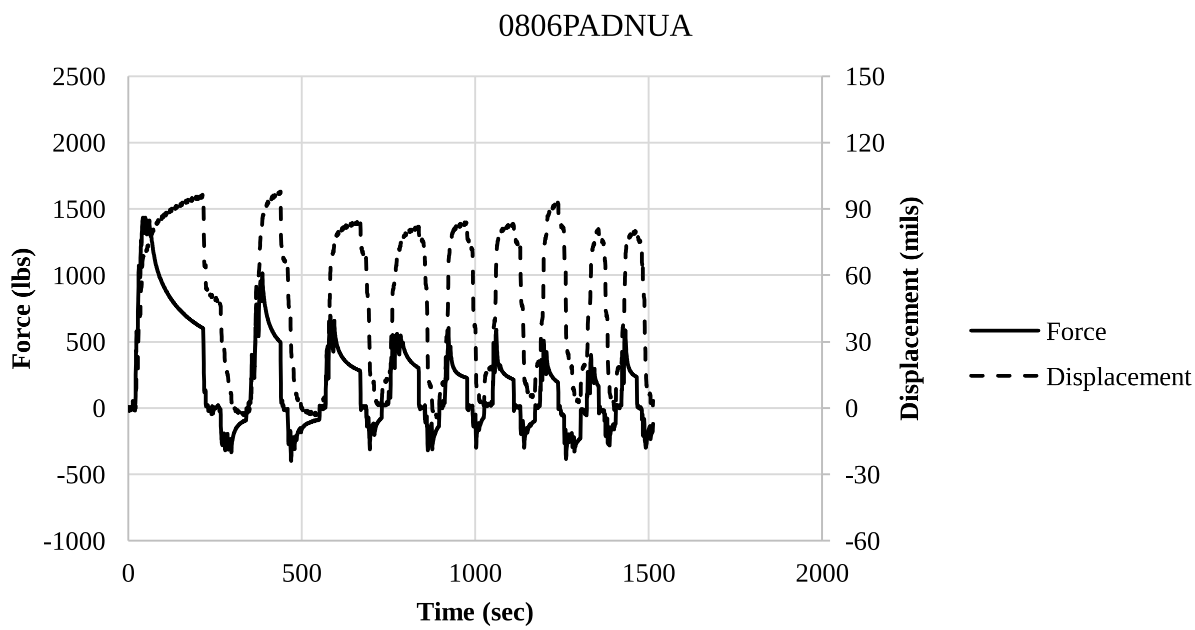

Figure C.35. PADNU Force and Displacement vs. Time (Tested on 8/11/15)

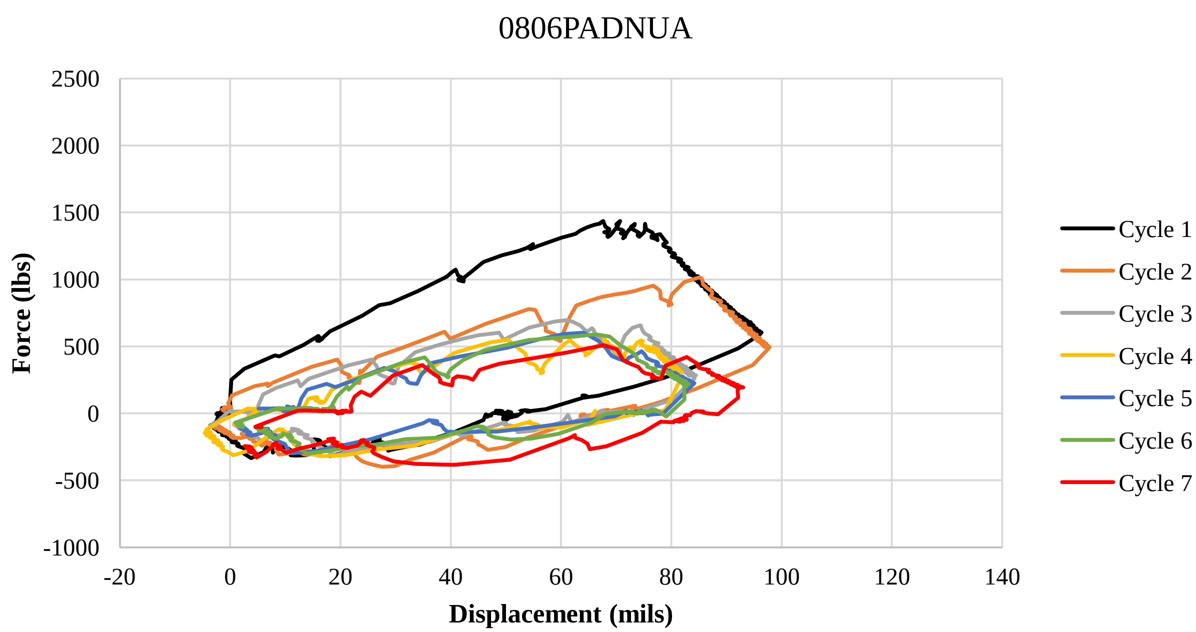

Figure C.36. PADNU Force vs. Displacement (Tested on 8/11/15)

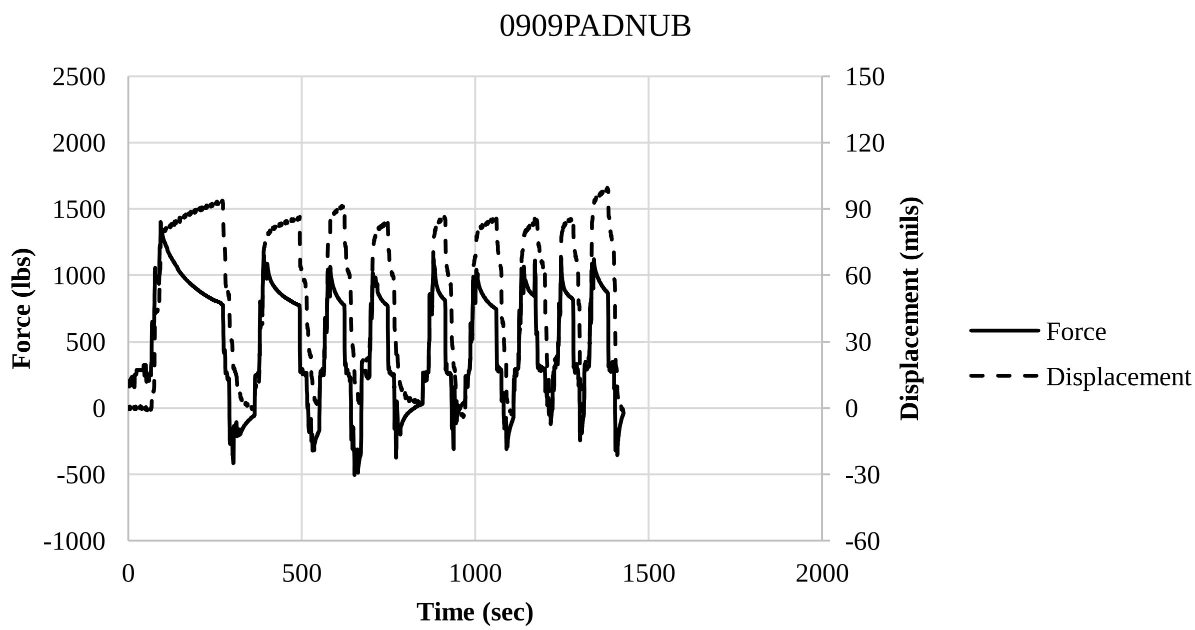

Figure C.37. PADNU Force and Displacement vs. Time (Tested on 9/16/15)

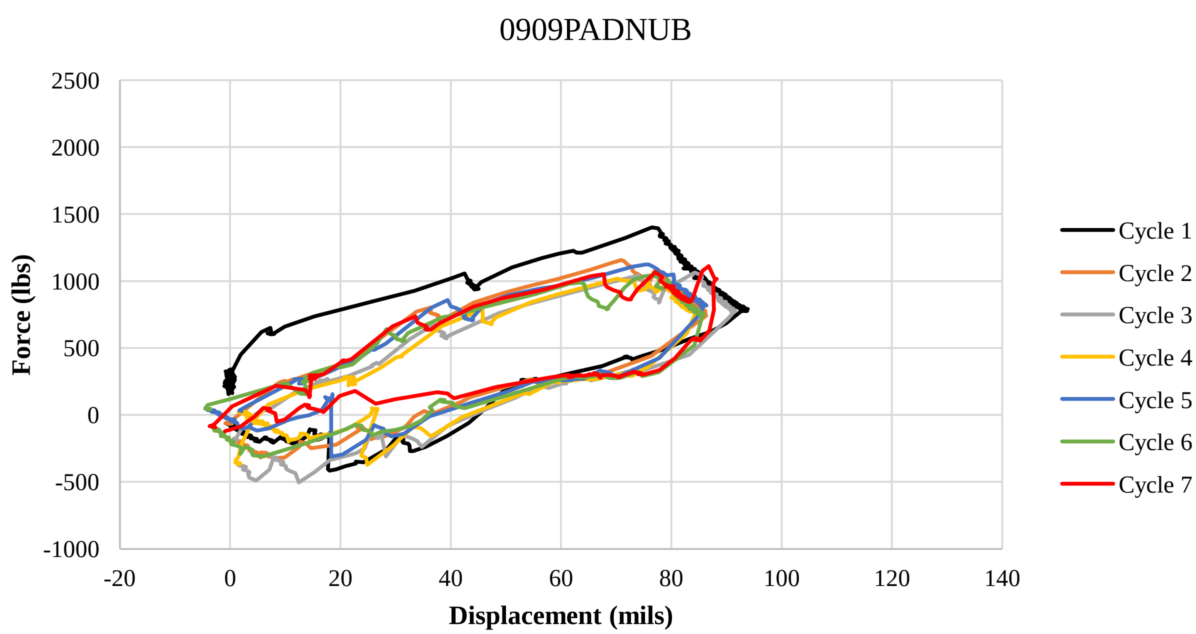

Figure C.38. PADNU Force vs. Displacement (Tested on 9/16/15)

APPENDIX D

RESULTS FROM THE REFLECTIVE CRACKING TEST

The following plots provide measured displacement of the overlay (TOP(OL)) and the existing (BOT(EXIST)) beam versus the applied force for each beam tested for reflective cracking.

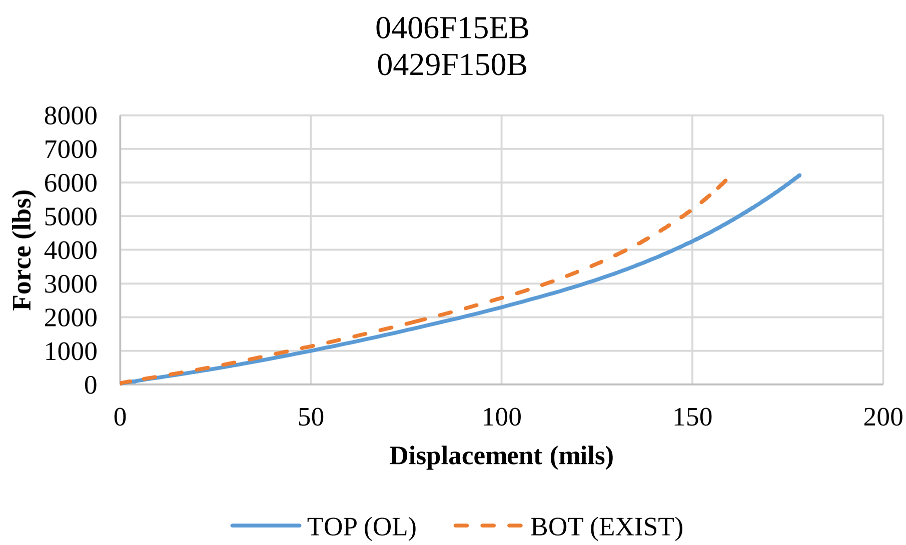

Figure D.1. F15 Force vs. Displacement (Tested on 5/4/15)

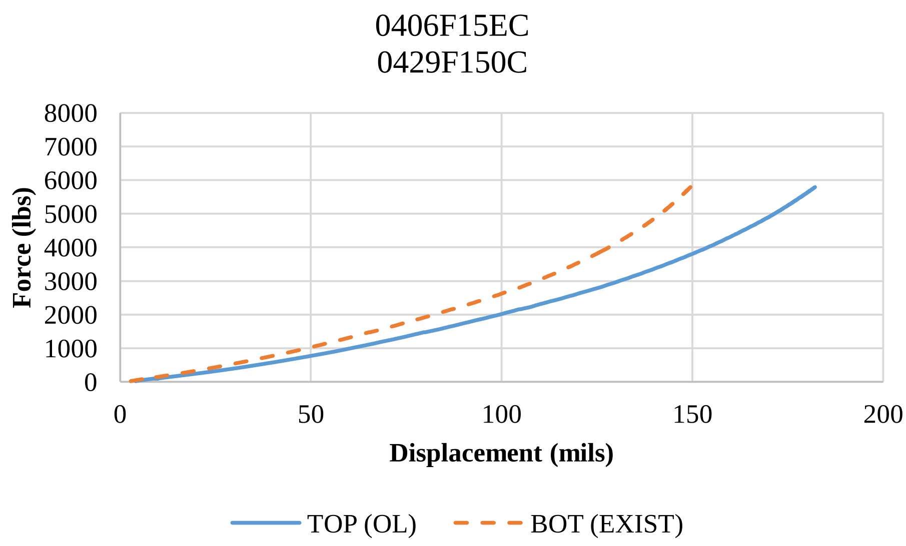

Figure D.2. F15 Force vs. Displacement (Tested on 5/4/15)

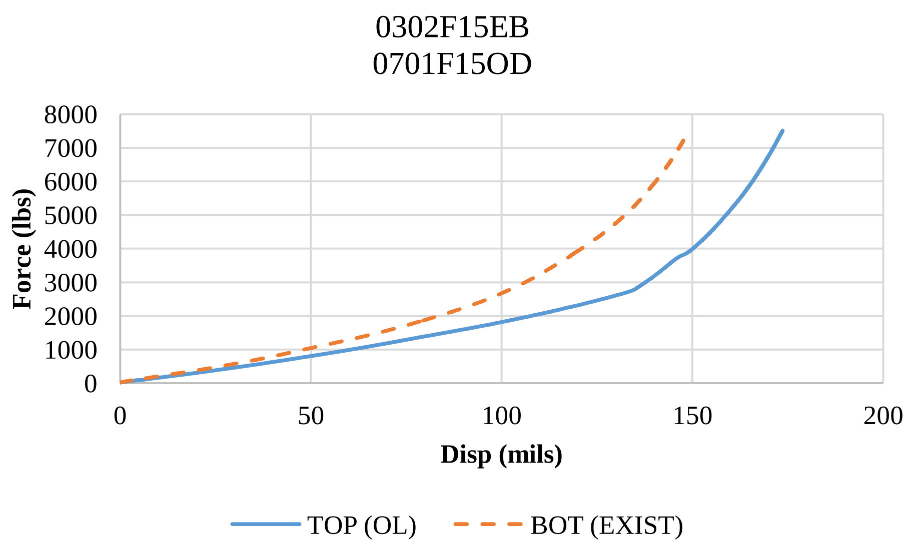

Figure D.3. F15 Force vs. Displacement (Tested on 7/6/15)

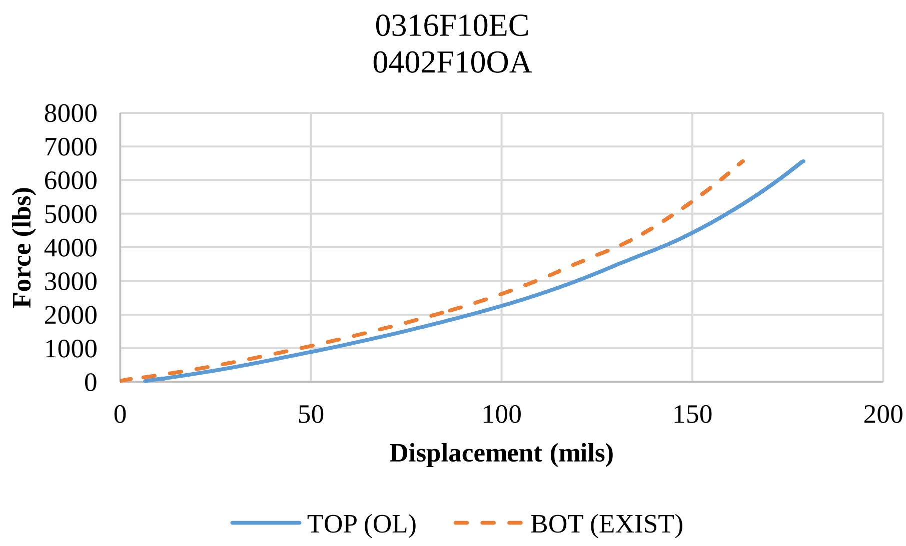

Figure D.4. F10 Force vs. Displacement (Tested on 4/7/15)

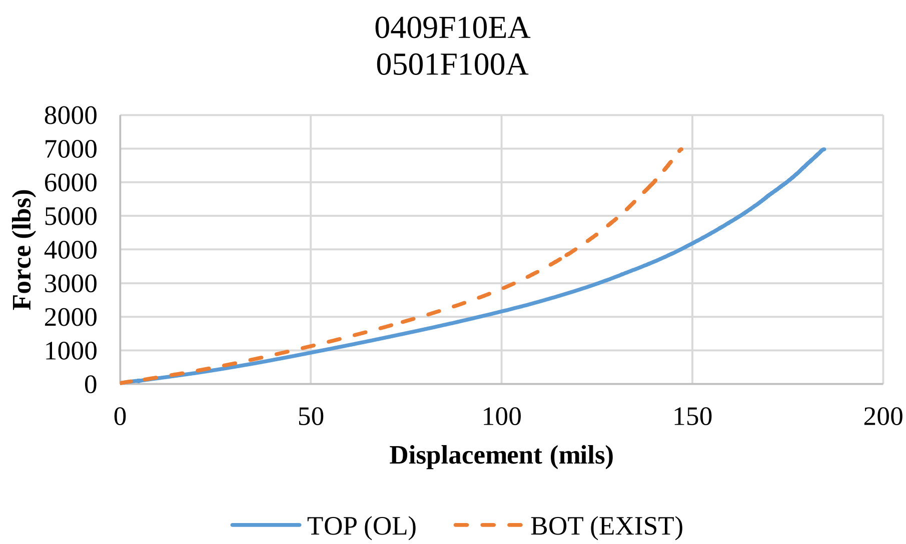

Figure D.5. F10 Force vs. Displacement (Tested on 5/6/15)

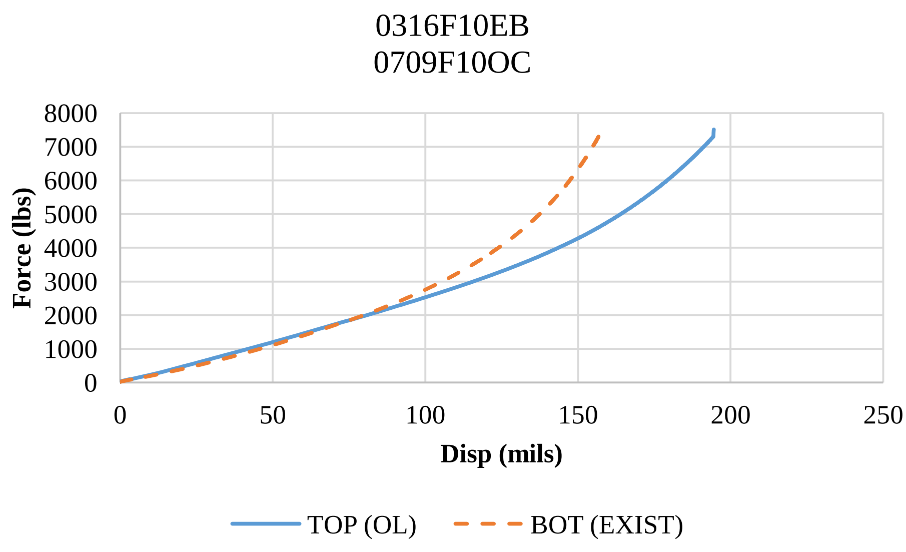

Figure D.6. F10 Force vs. Displacement (Tested on 7/14/15)

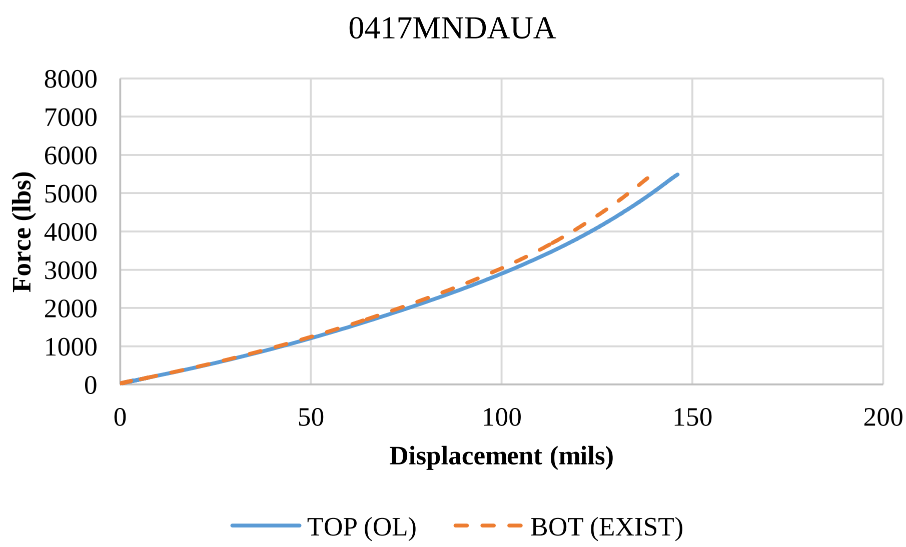

Figure D.7. MNDAU Force vs. Displacement (Tested on 4/22/15)

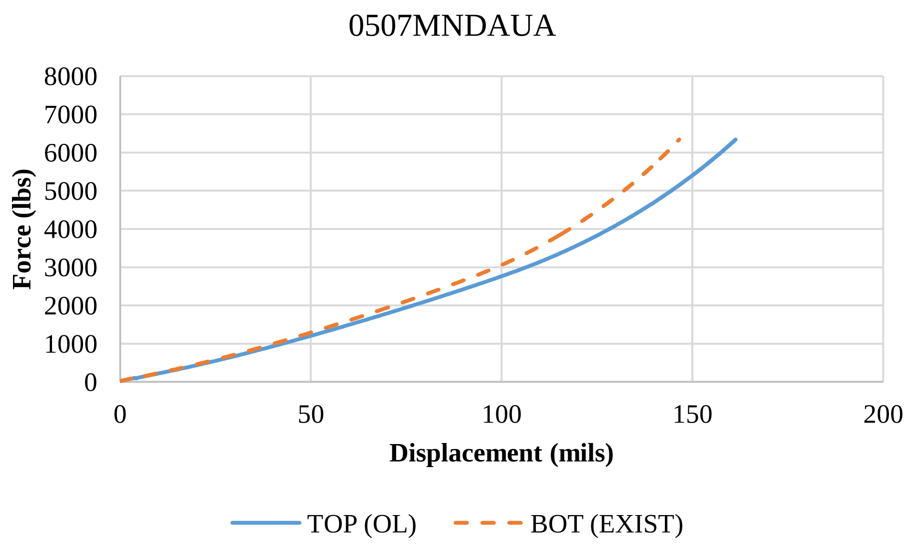

Figure D.8. MNDAU Force vs. Displacement (Tested on 5/12/15)

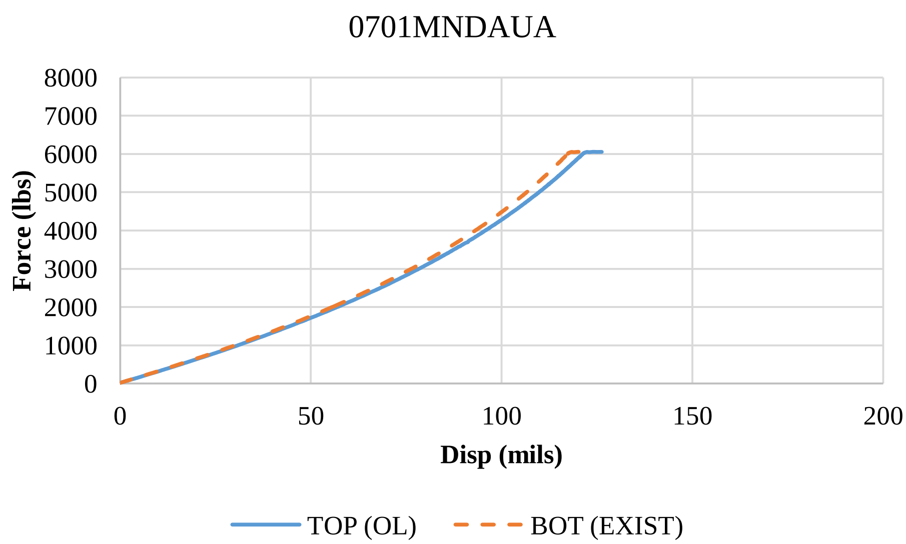

Figure D.9. MNDAU Force vs. Displacement (Tested on 7/6/15)

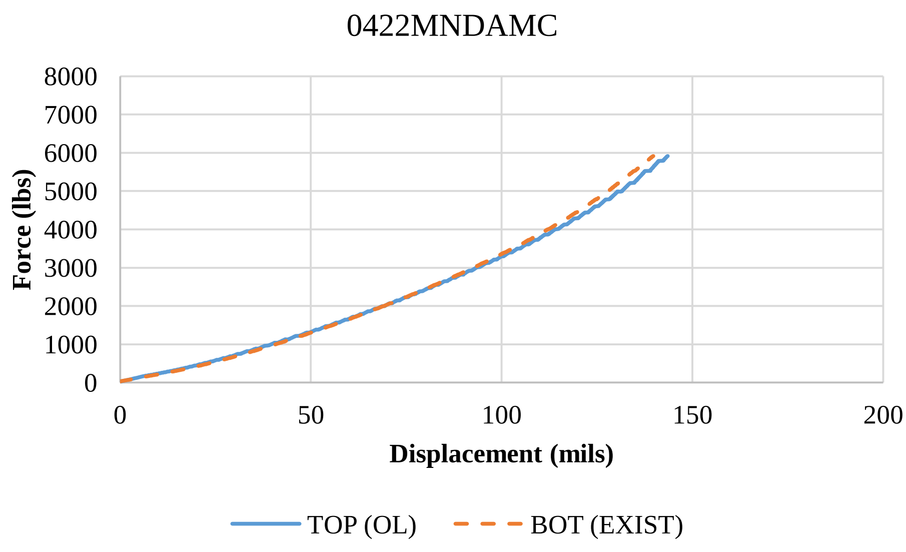

Figure D.10. MNDAM Force vs. Displacement (Tested on 4/27/15)

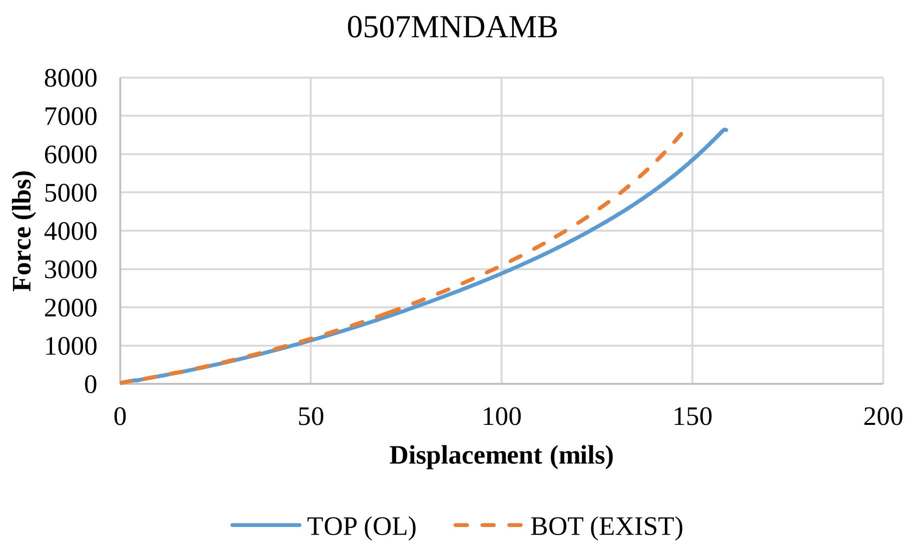

Figure D.11. MNDAM Force vs. Displacement (Tested on 5/12/15)

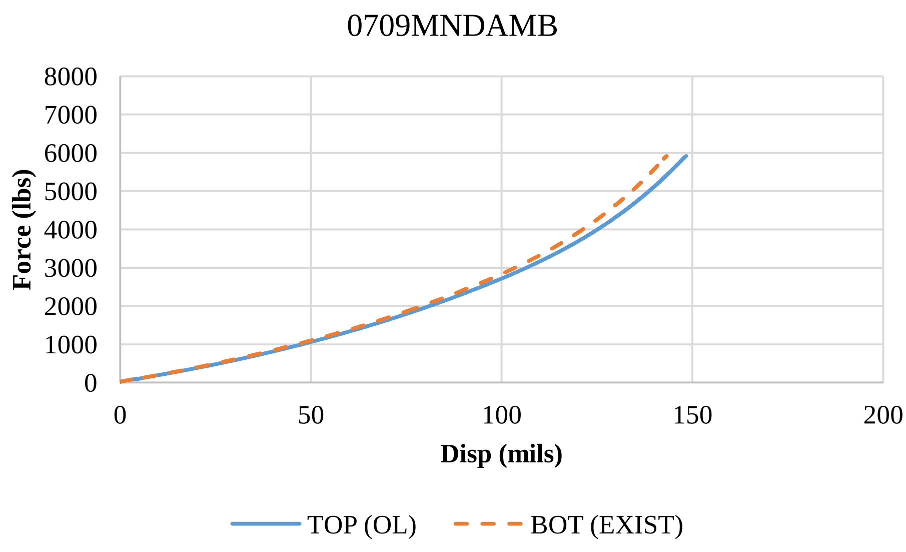

Figure D.12. MNDAM Force vs. Displacement (Tested on 7/14/16)

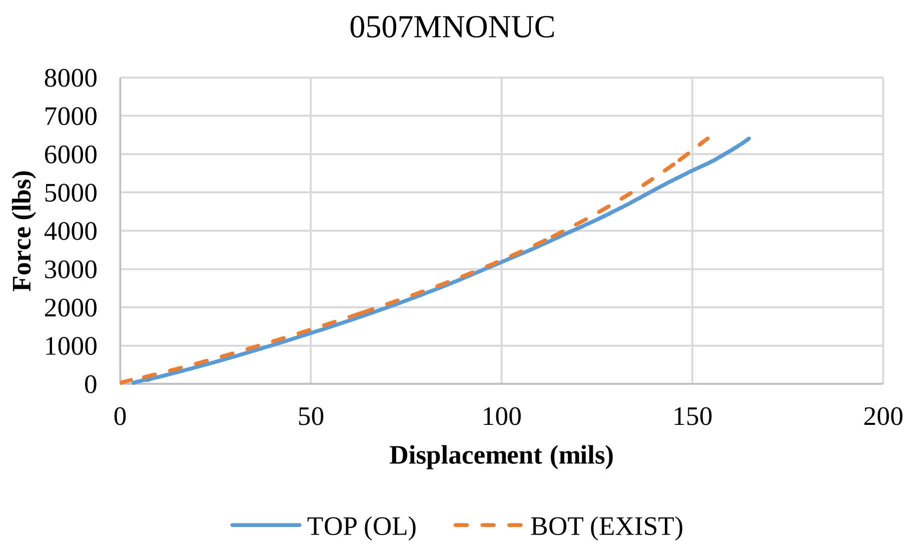

Figure D.13. MNONU Force vs. Displacement (Tested on 5/12/15)

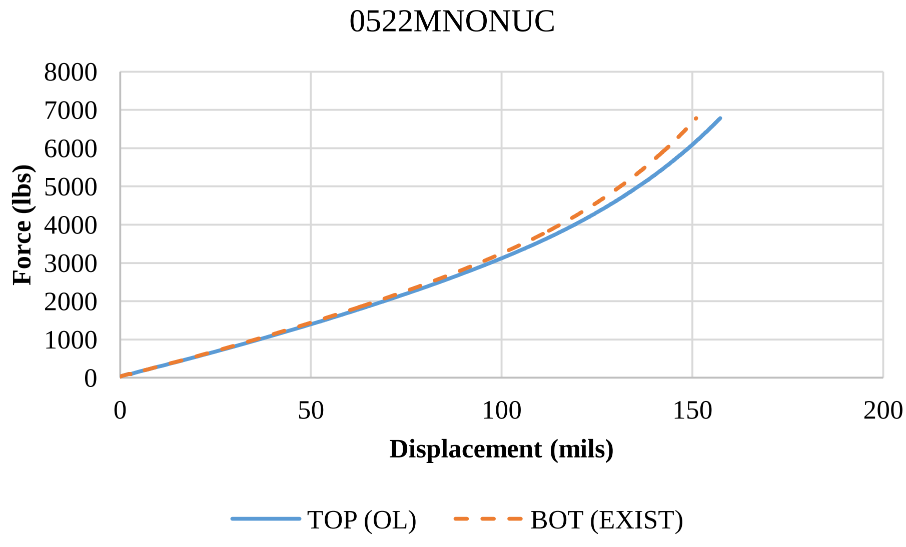

Figure D.14. MNONU Force vs. Displacement (Tested on 5/27/15)

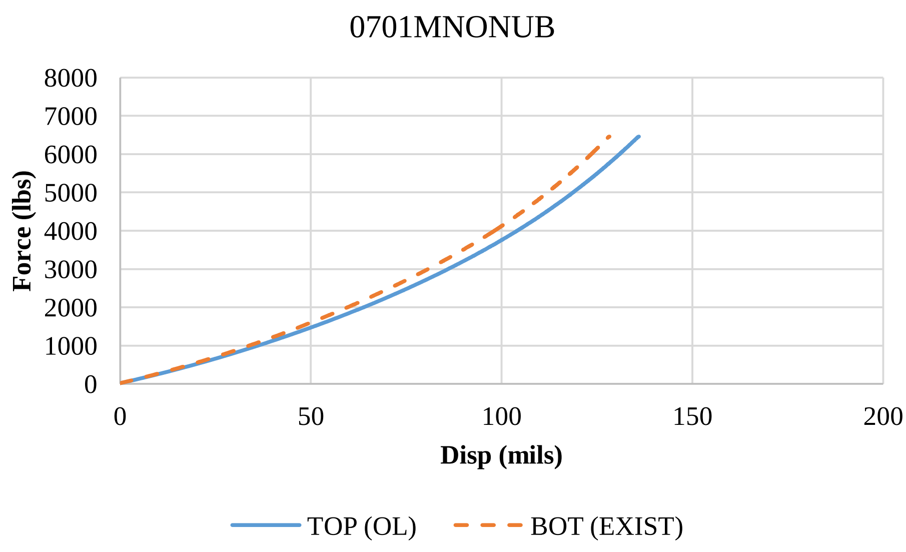

Figure D.15. MNONU Force vs. Displacement (Tested on 7/6/15)

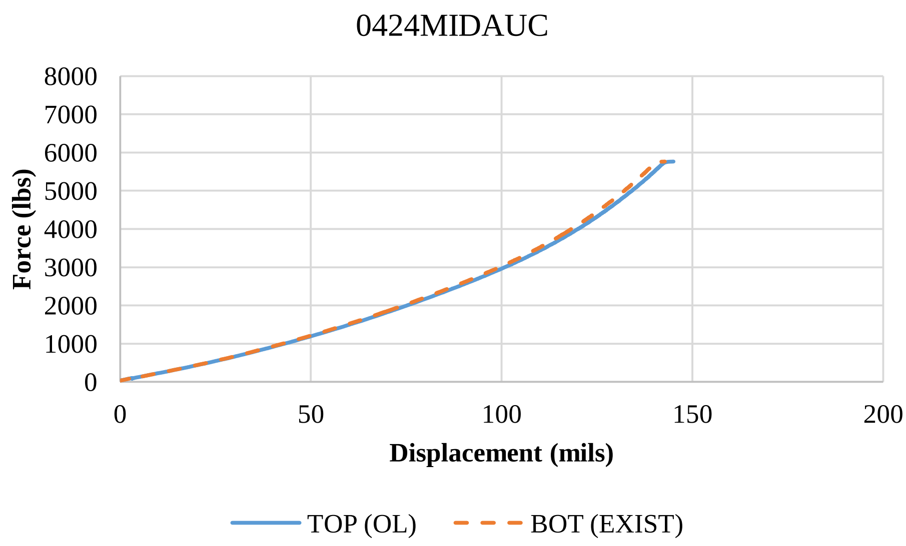

Figure D.16. MIDAU Force vs. Displacement (Tested on 4/29/15)

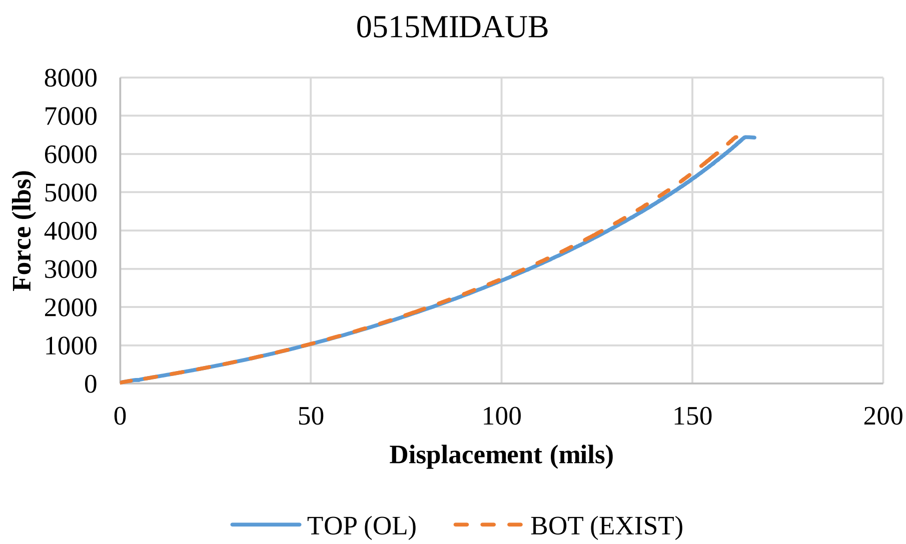

Figure D.17. MIDAU Force vs. Displacement (Tested on 5/20/15)

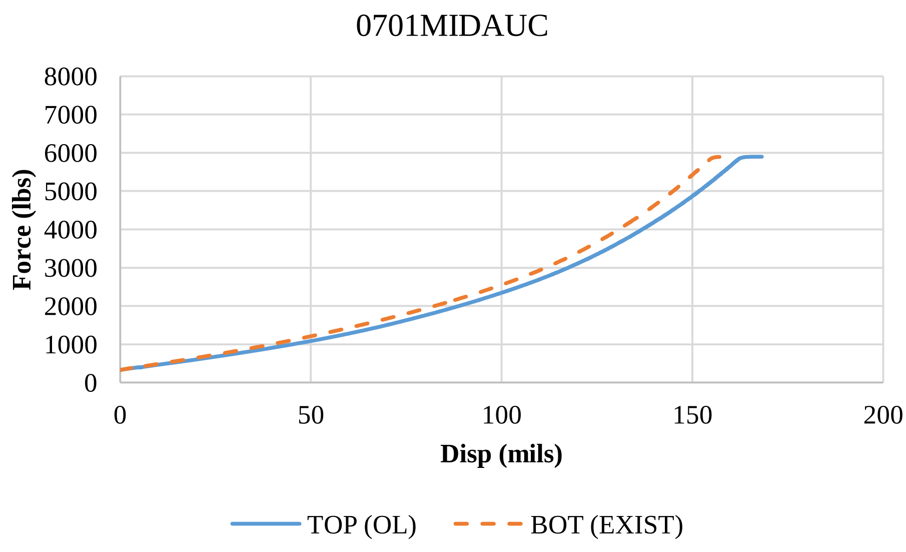

Figure D.18. MIDAU Force vs. Displacement (Tested on 7/6/15)

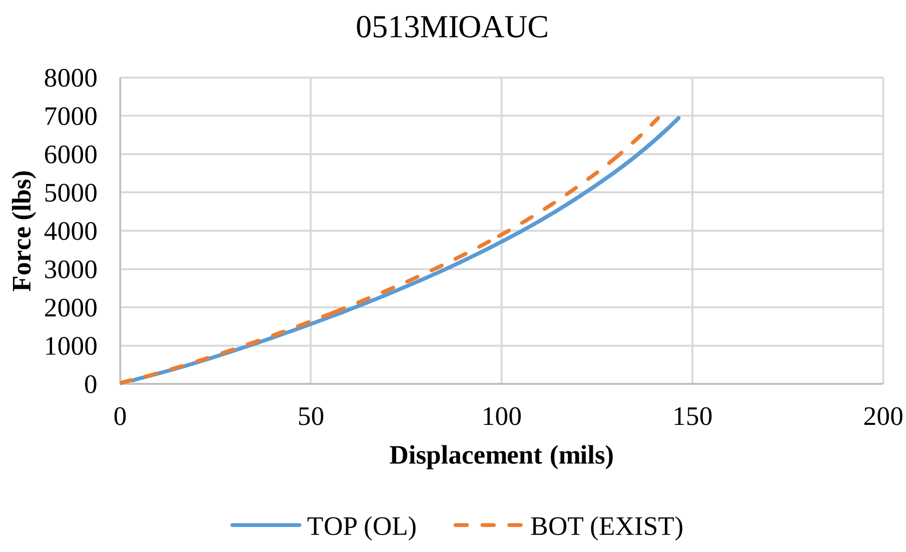

Figure D.19. MIOAU Force vs. Displacement (Tested on 5/18/15)

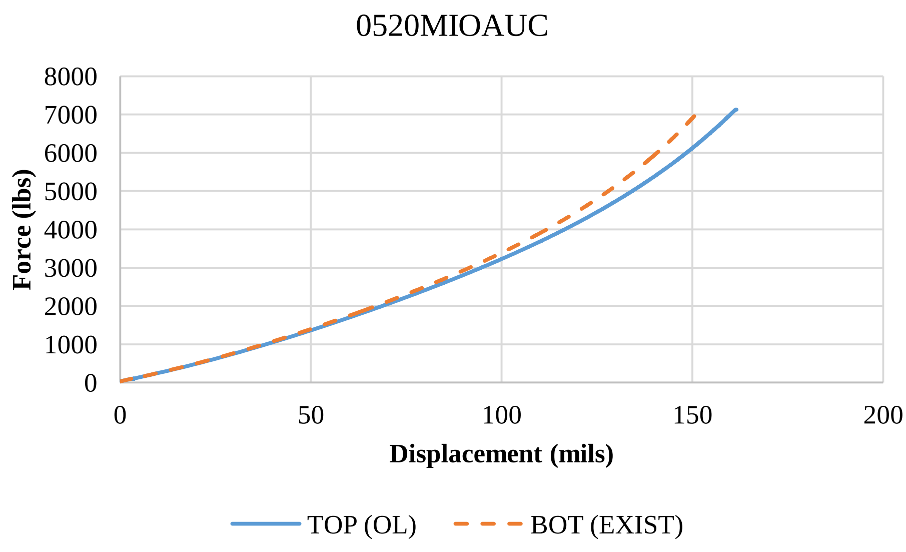

Figure D.20. MIOAU Force vs. Displacement (Tested on 5/25/15)

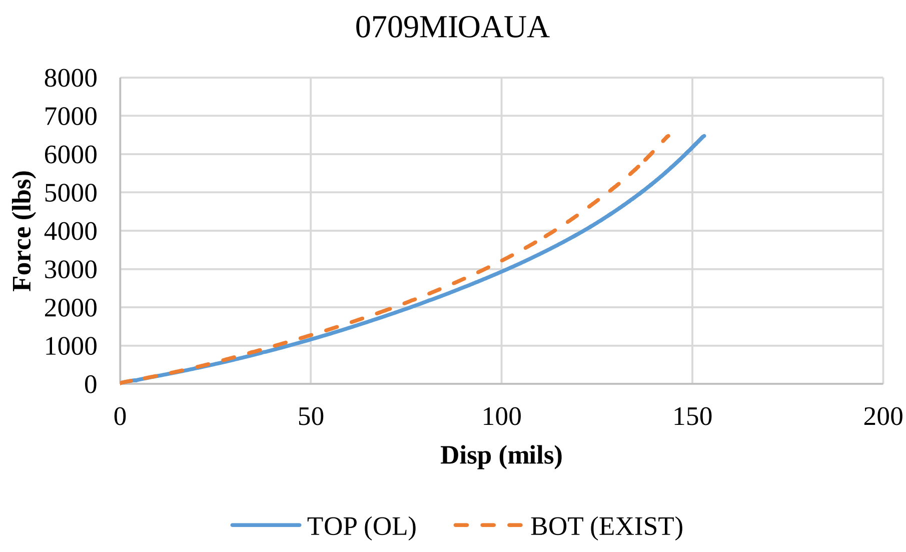

Figure D.21. MIOAU Force vs. Displacement (Tested on 7/14/15)

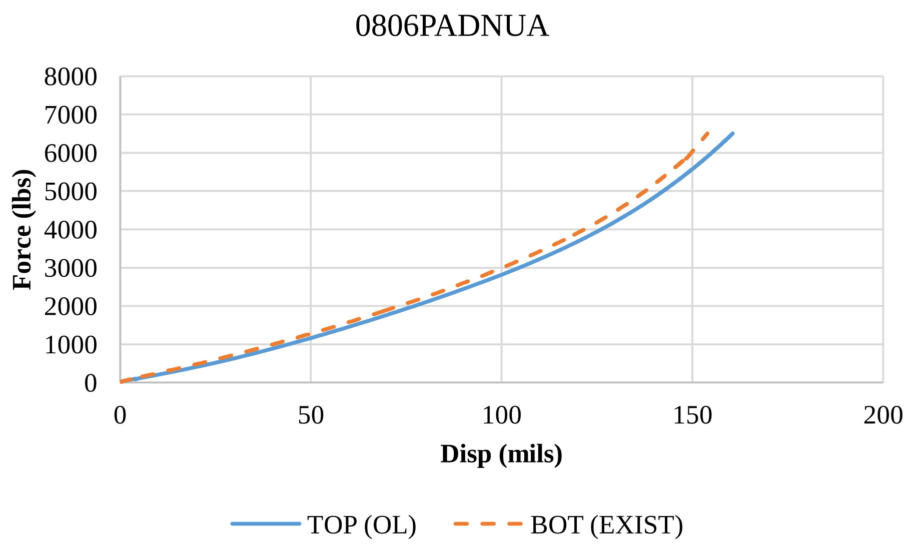

Figure D.22. PADNU Force vs. Displacement (Tested on 8/11/15)

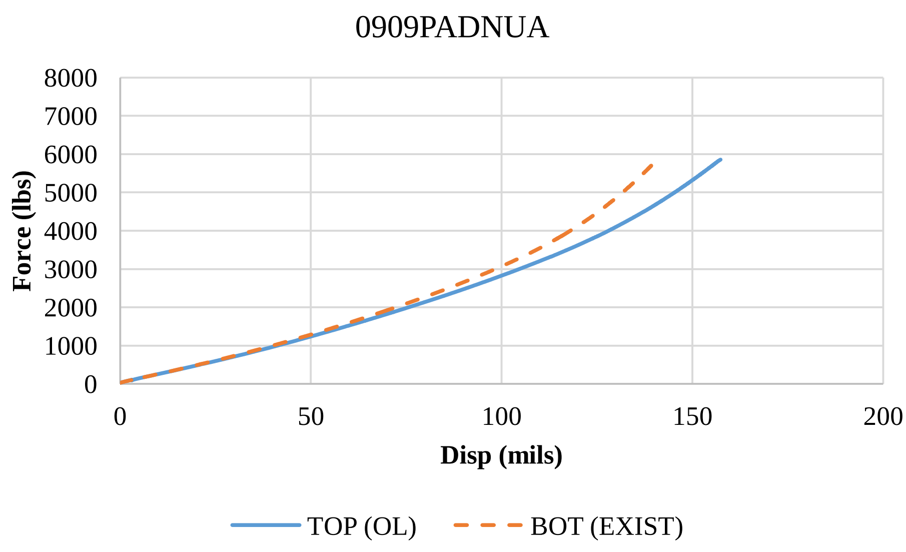

Figure D.23. PADNU Force vs. Displacement (Tested on 9/16/15)

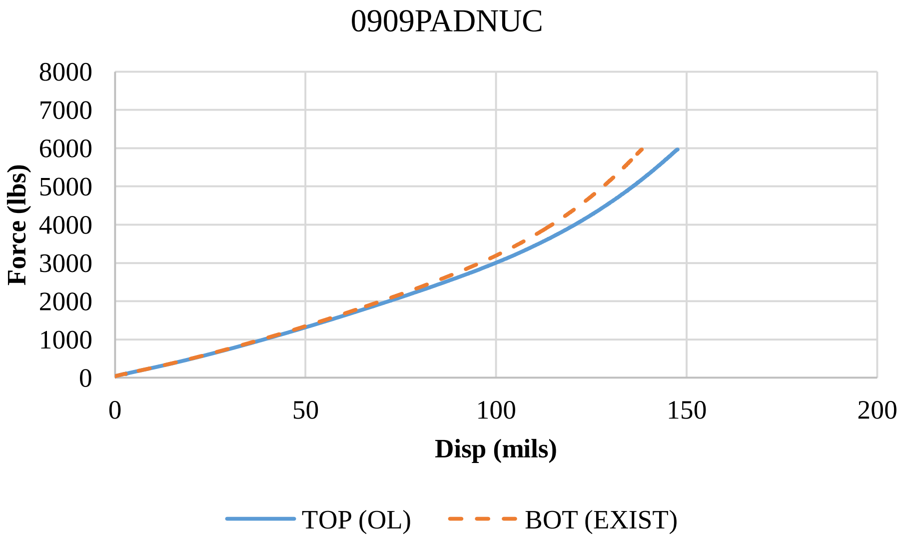

Figure D.24. PADNU Force vs. Displacement (Tested on 9/16/15)

APPENDIX E

RESULTS FROM THE DIRECT TENSION TEST

The direct tension test specimen results are shown below plotted as force versus displacement.

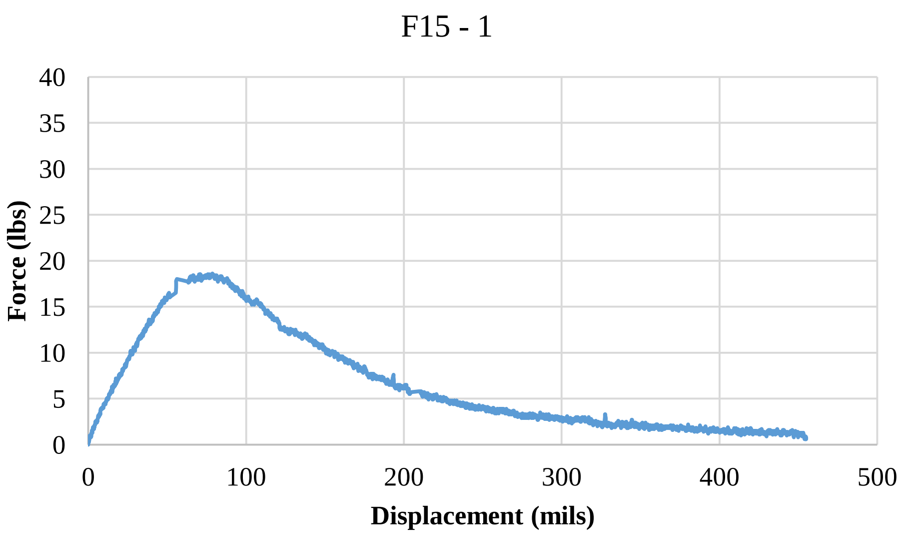

Figure E.1. F15 Specimen 1 Force vs. Displacement (Tested on 5/18/15)

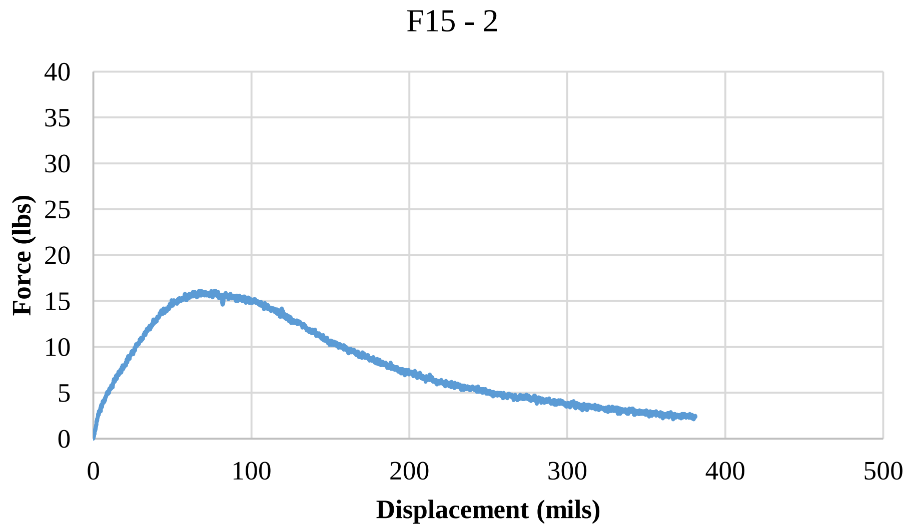

Figure E.2. F15 Specimen 2 Force vs. Displacement (Tested on 5/18/15)

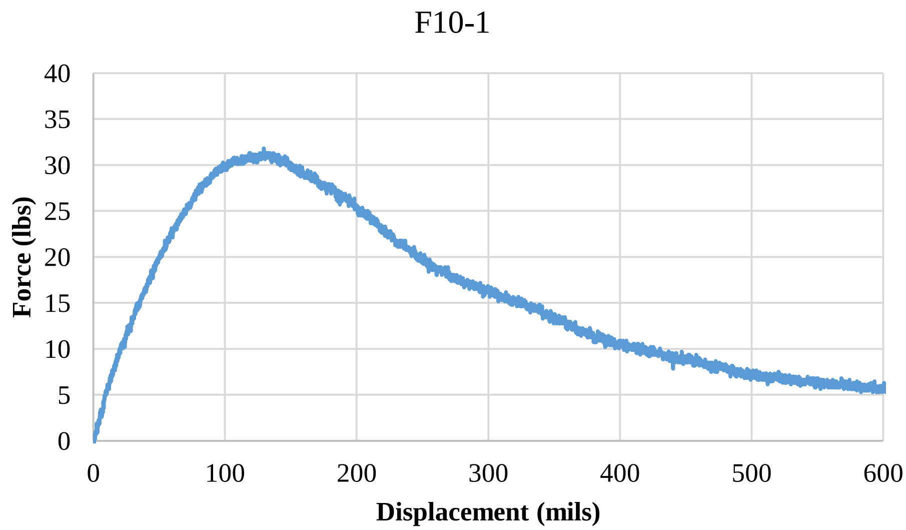

Figure E.3. F10 Specimen 1 Force vs. Displacement (Tested on 5/18/15)

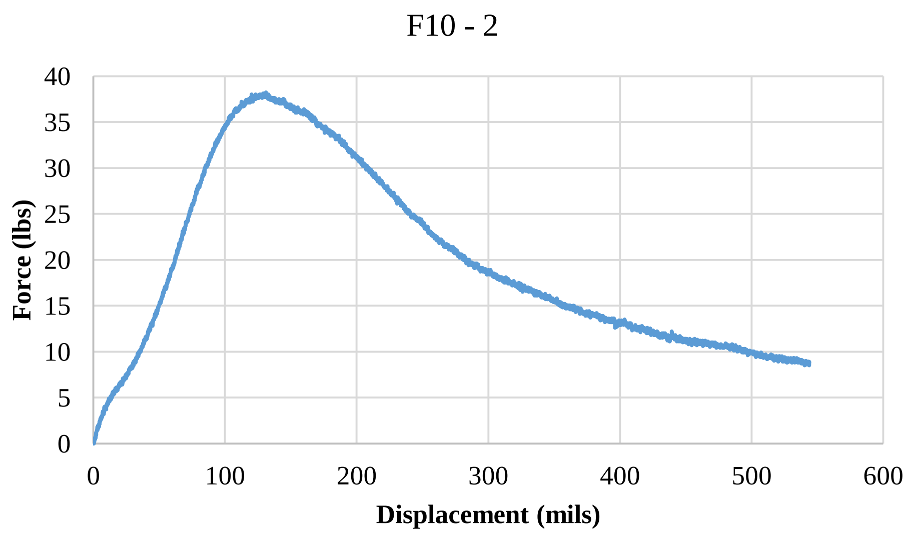

Figure E.4. F10 Specimen 2 Force vs. Displacement (Tested on 5/18/15)

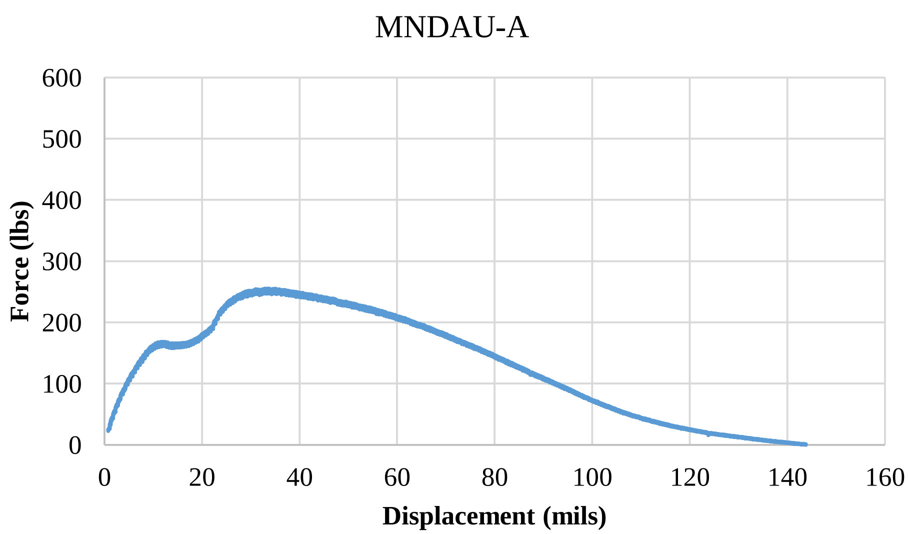

Figure E.5. MNDAU Specimen A Force vs. Displacement (Tested on 6/17/15)

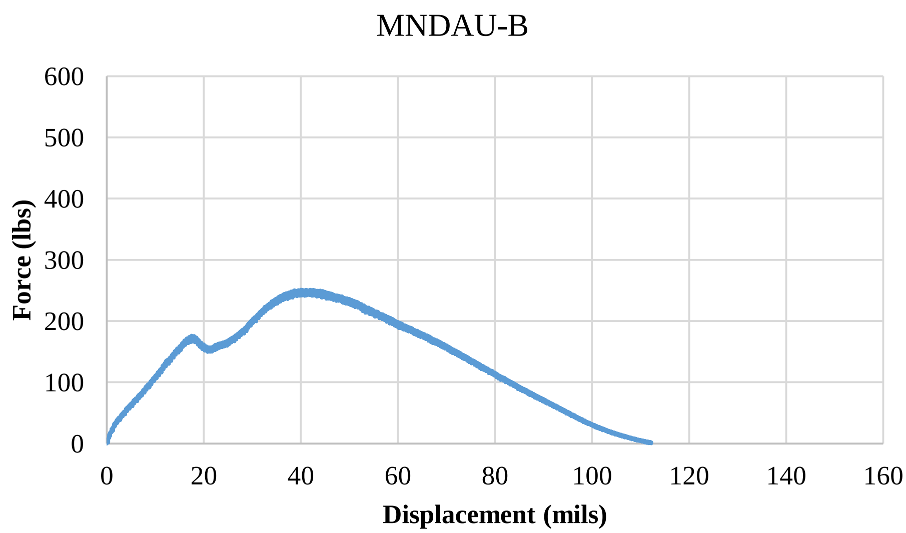

Figure E.6. MNDAU Specimen B Force vs. Displacement (Tested on 6/17/15)

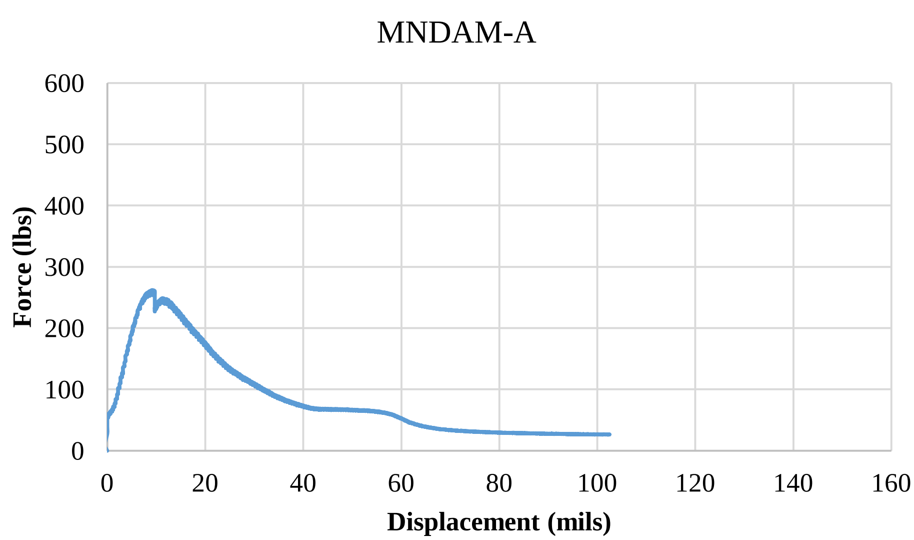

Figure E.7. MNDAM Specimen A Force vs. Displacement (Tested on 6/8/15)

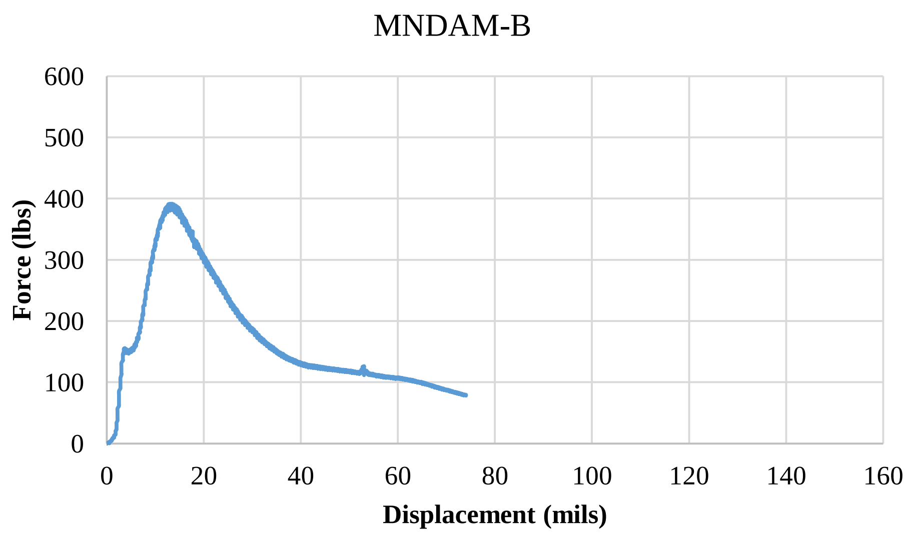

Figure E.8. MNDAM Specimen A Force vs. Displacement (Tested on 6/17/15)

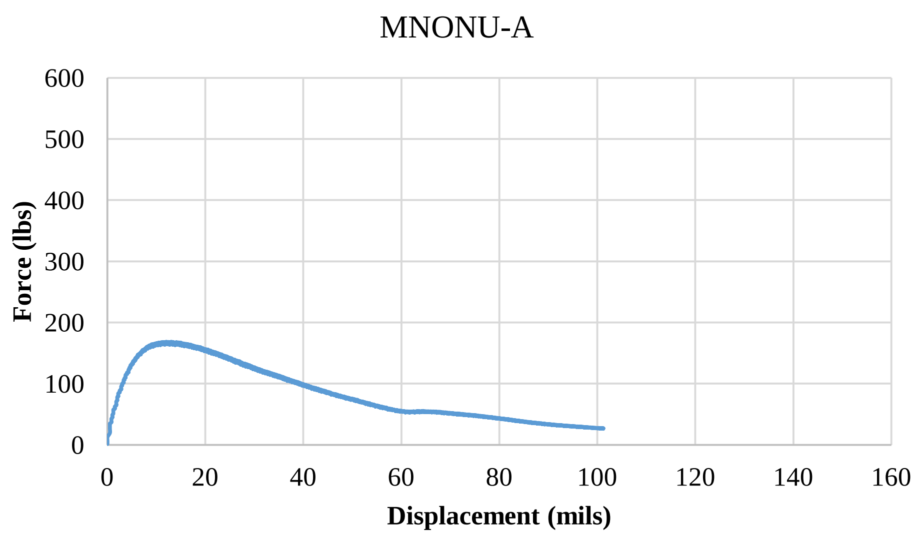

Figure E.9. MNONU Specimen A Force vs. Displacement (Tested on 6/5/15)

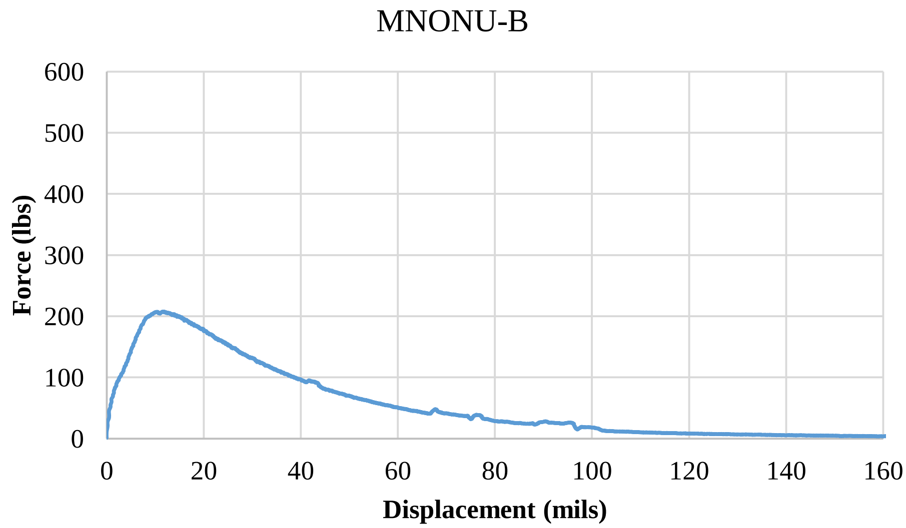

Figure E.10. MNONU Specimen B Force vs. Displacement (Tested on 6/17/15)

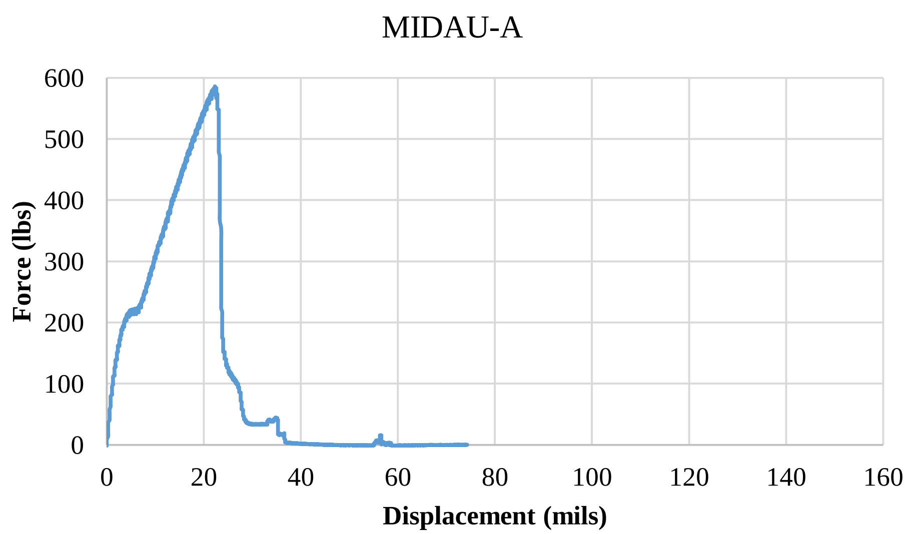

Figure E.11. MIDAU Specimen A Force vs. Displacement (Tested on 6/5/15)

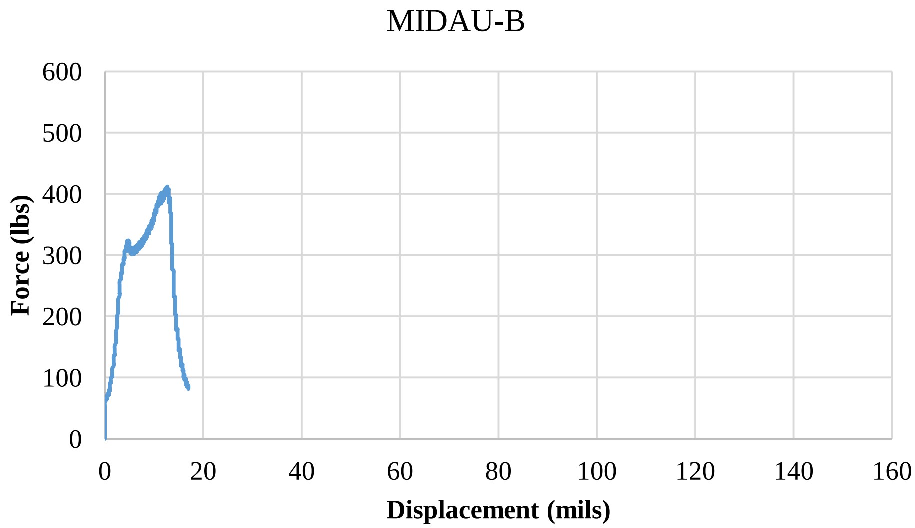

Figure E.12. MIDAU Specimen B Force vs. Displacement (Tested on 6/17/15)

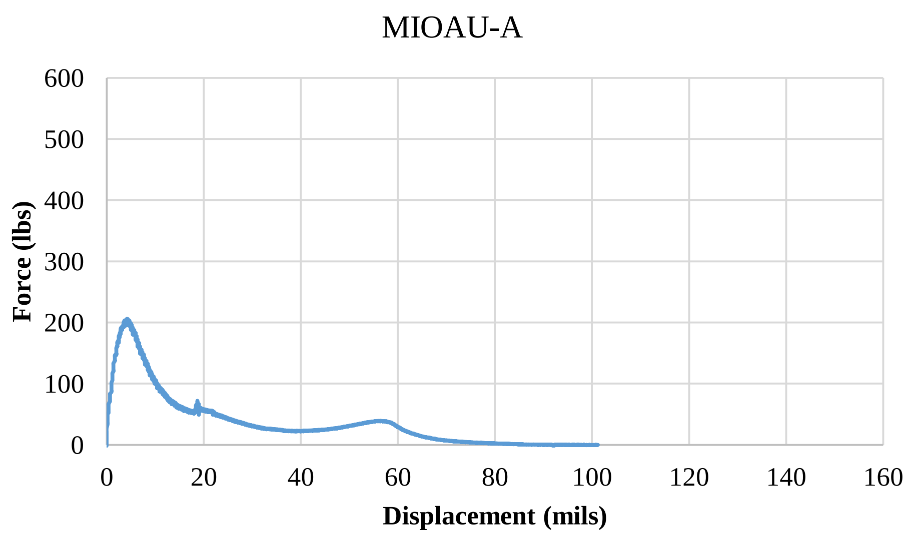

Figure E.13. MIOAU Specimen A Force vs. Displacement (Tested on 6/10/15)

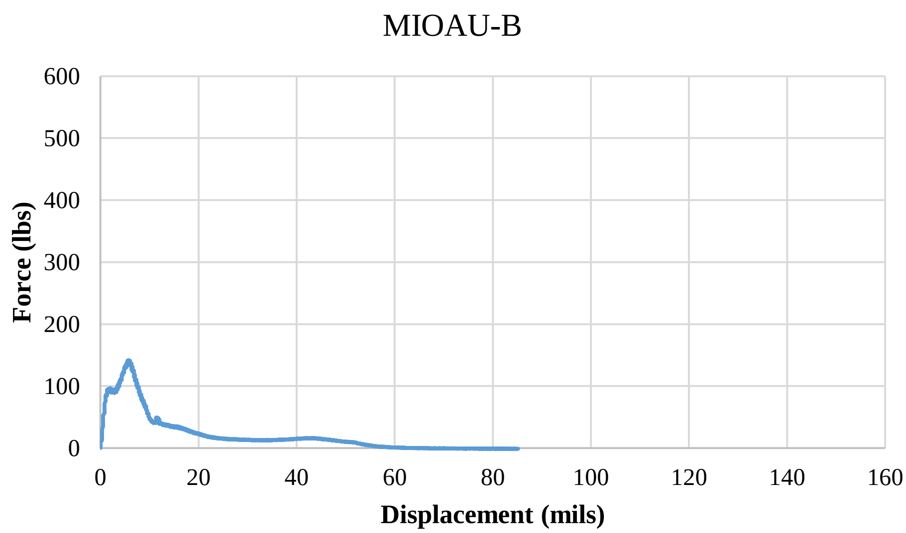

Figure E.14. MIOAU Specimen B Force vs. Displacement (Tested on 6/10/15)

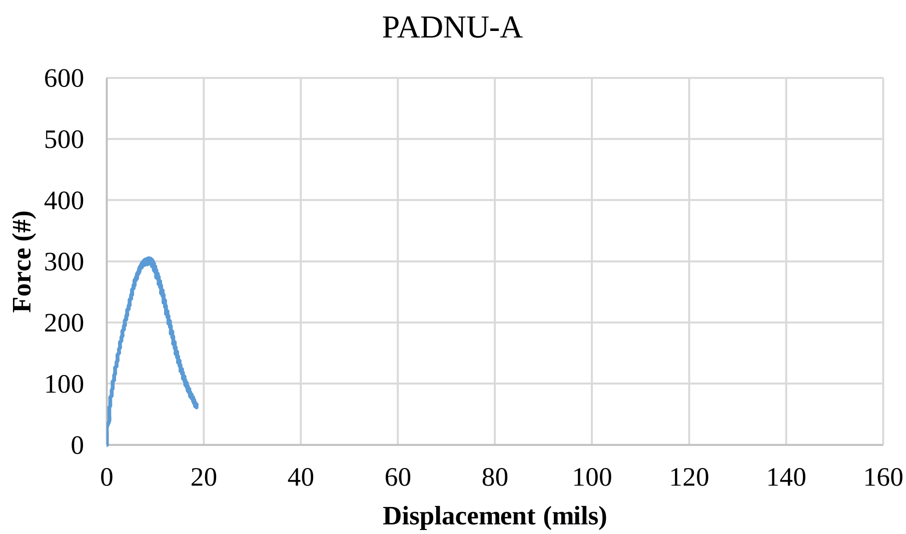

Figure E.15. PADNU Specimen A Force vs. Displacement (Tested on 9/14/15)

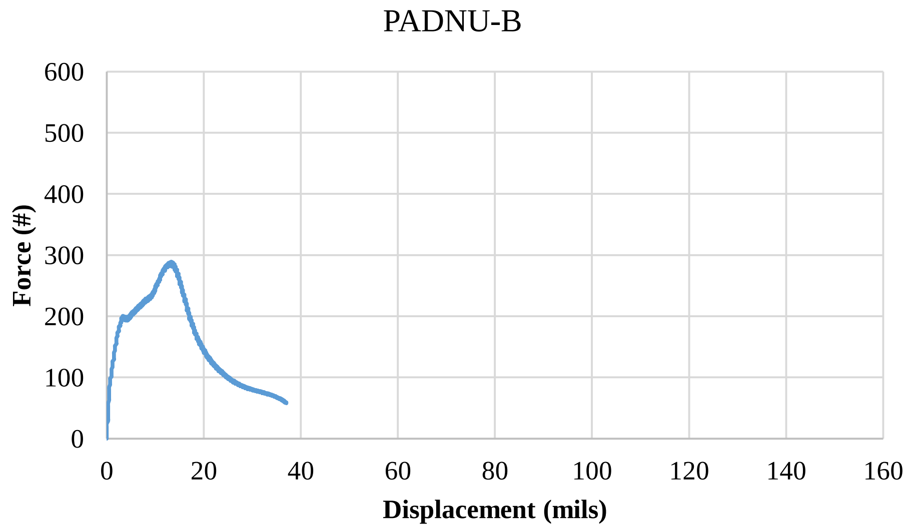

Figure E.16. PADNU Specimen B Force vs. Displacement (Tested on 9/14/15)

APPENDIX F

CALIBRATION DATABASE INFORMATION

For each calibration section, detailed information is presented in the following tables which are required for the faulting model calculation.

Table F.1. Calibration sections project information

Source	SHRP_ID or ID	Const. Date	Survey Date	Age, yrs	Est ESALs	Longitude, deg	Latitude, deg
LTPP	6_9048	9-Oct-70	24-Mar-04	33.48	2.41E+07	85.55	40.59
LTPP	6_9049	1-Jun-68	13-Nov-01	33.47	6.00E+06	95.71	39.09
LTPP	6_9107	1-Oct-88	13-Jun-02	13.71	8.45E+06	95.04	44.84
LTPP	8_9019	1-Feb-86	14-Aug-98	12.54	6.15E+06	90.7	32.36
LTPP	8_9020	1-Oct-86	24-Aug-98	11.90	7.69E+06	78.41	41.04
LTPP	18_9020	1-Jan-87	29-Apr-04	17.34	2.45E+07	96.37	31.9
LTPP	20_9037	1-Jan-78	12-May-94	16.37	8.56E+05	96.83	32.48
LTPP	27_9075	1-Jan-77	1-Jun-95	18.42	5.89E+05	116.7	32.84
LTPP	28_7012	1-Jul-85	7-Feb-12	26.62	1.71E+07	121.56	38.58
LTPP	42_1627	1-Sep-88	12-Nov-02	14.21	1.79E+07	120.55	39.31
LTPP	48_9167	15-Jun-88	29-Oct-12	24.39	1.50E+07	104.98	40.22
LTPP	48_9355	1-Mar-90	25-Mar-12	22.08	2.24E+07	104.99	40.39
LTPP	89_9018	1-Aug-87	21-Jul-05	17.98	1.99E+06	72.48	46.32
MnROAD	Cell105	30-Oct-08	14-Apr-11	2.45	2.45E+06	93.65	45.24
MnROAD	Cell205	30-Oct-08	14-Apr-11	2.45	2.45E+06	93.65	45.24
MnROAD	Cell305	30-Oct-08	14-Apr-15	6.46	6.46E+06	93.65	45.24
MnROAD	Cell405	30-Oct-08	14-Apr-15	6.46	6.46E+06	93.65	45.24
MnROAD	Cell505	12-Sep-11	16-Apr-15	3.59	3.59E+06	93.65	45.24
MnROAD	Cell605	12-Sep-11	16-Apr-15	3.59	3.59E+06	93.65	45.24
MDOT	03033	2009	2015	6.00	3.30E+06		
MDOT	03111	2004	2015	11.00	7.77E+06		
MDOT	09101	1990	2013	23.00	5.81E+06		
MDOT	16091	2008	2015	7.00	1.76E+06		
MDOT	19022	1991	2015	24.00	1.54E+07		
MDOT	25032	2004	2015	11.00	3.59E+06		
MDOT	39014	2004	2015	11.00	7.77E+06		
MDOT	41026	2007	2015	8.00	4.59E+06		
MDOT	41132	2000	2014	14.00	7.69E+06		
MDOT	47014	2001	2011	10.00	8.79E+06		
MDOT	56044	2010	2014	4.00	9.92E+05		
MDOT	65041	2003	2015	12.00	2.62E+06		
MDOT	70063	2004	2015	11.00	6.72E+06		
MDOT	71111	2006	2011	5.00	2.70E+06		

Table F.2. Calibration sections design features

SHRP_ID or ID	Lane Width, ft	Lane Width, ft	Tied PCC Shoulder	Avg Jt Spacing, ft	Dowel Diameter, in	Dowel Spacing, in	Drainage Type
6_9048	12	12	No, AC	15.5	None	None	None
6_9049	12	12	No, AC	15.5	None	None	None
6_9107	12	12	No, AC	13.5	None	None	Long Edgedrain
8_9019	12	12	No, PCC	13	None	None	None
8_9020	12	12	Yes	20	None	None	None
18_9020	12	12	No, AC	15.5	None	None	x-drain
20_9037	12	12	No, AC	15	0.5	30	None
27_9075	12	12	No, AC	15.5	None	None	None
28_7012	12	12	No, AC	21	1	12	None
42_1627	12	12	Yes	20.5	1.25	12	Long Edgedrain
48_9167	12	12	Yes	20	1.5	12	Long Edgedrain
48_9355	12	12	No	15	1.25	12	None
89_9018	12	12	Yes	15	1.25	12	None
Cell105	14	14	No, AC	15	None	None	Wick Drains
Cell205	14	14	No, AC	15	None	None	Wick Drains
Cell305	14	14	No, AC	15	None	None	Wick Drains
Cell405	14	14	No, AC	15	None	None	Wick Drains
Cell505	6.5	6.5	No, AC	6	None	None	Wick Drains
Cell605	6.5	6.5	No, AC	6	None	None	Wick Drains
03033	12	12	Yes	12	1.25	12	yes
03111	12	12	Yes	13	1.25	12	none
09101	12	12	Yes	14	1.25	12	Varies
16091	12	12	Yes	12	1.25	12	yes
19022	12	12	Yes	27	1.25	12	PDS at EOP
25032	12	12	Yes	14	1.25	12	none
39014	12	12	Yes	12	1.25	12	none
41026	12	12	Yes	14	1.25	12	18" PDS at EOP
41132	12	12	Yes	13	1.25	12	18" PDS at EOP
47014	12	12	Yes	13	1.25	12	18" PDS at EOP
56044	12	12	Yes	12	1.25	12	18" PDS at EOP
65041	12	12	Yes	11	1.25	12	none
70063	12	12	Yes	14	1.25	12	18" PDS at EOP
71111	12	12	Yes	14	1.25	12	6" open graded underdrain

Table F.3. Calibration sections structural details

SHRP_ID or ID	Overlay thickness, in	Overlay EMOD, psi	Overlay MOR, psi	Existing thickness, in	Existing EMOD, psi	Overlay CTE, in/in/degF	Overlay Cement Content, lbs
6_9048	6.4	3.81E+06	808	8.1	3.90E+06	5.50E-06	564
6_9049	7.5	3.51E+06	829	7.7	4.80E+06	5.50E-06	470
6_9107	8.8	3.09E+06	530	7.6	4.75E+06	5.50E-06	594.5
8_9019	9	3.37E+06	572	7.9	3.50E+06	5.50E-06	565
8_9020	8	3.44E+06	541	7.7	3.68E+06	5.50E-06	565
18_9020	10.2	4.05E+06	641	10.2	4.23E+06	5.50E-06	558
20_9037	5.8	3.31E+06	962	8.8	4.88E+06	5.50E-06	540
27_9075	5.9	4.25E+06	714	7.8	3.70E+06	5.50E-06	555
28_7012	10	4.23E+06	1022	9.4	5.00E+06	5.50E-06	549
42_1627	10.3	3.31E+06	696	9.7	4.25E+06	5.50E-06	541
48_9167	10.2	4.33E+06	858	8.4	4.85E+06	5.50E-06	414
48_9355	10.3	4.85E+06	877	9.9	4.98E+06	5.50E-06	354
89_9018	6.4	4.23E+06	810	8.9	3.80E+06	5.50E-06	573
Cell105	4.5	4.00E+06	660	7.1	4.63E+06	5.50E-06	550
Cell205	4.5	4.00E+06	660	7.1	4.63E+06	5.50E-06	550
Cell305	5	4.00E+06	660	7.1	4.63E+06	5.50E-06	550
Cell405	5	4.00E+06	660	7.1	4.63E+06	5.50E-06	550
Cell505	5	4.00E+06	660	7.1	4.63E+06	5.50E-06	550
Cell605	5	4.00E+06	660	7.1	4.63E+06	5.50E-06	550
03033	7	4.00E+06	625	9	4.50E+06	5.50E-06	550
03111	7	4.00E+06	625	9	4.50E+06	5.50E-06	550
09101	7	4.00E+06	625	9	4.50E+06	5.50E-06	550
16091	7	4.00E+06	625	9	4.50E+06	5.50E-06	550
19022	7	4.00E+06	625	9	4.50E+06	5.50E-06	550
25032	7	4.00E+06	625	9	4.50E+06	5.50E-06	550
39014	7	4.00E+06	625	9	4.50E+06	5.50E-06	550
41026	7	4.00E+06	625	9	4.50E+06	5.50E-06	550
41132	7	4.00E+06	625	9	4.50E+06	5.50E-06	550
47014	7	4.00E+06	625	9	4.50E+06	5.50E-06	550
56044	7	4.00E+06	625	9	4.50E+06	5.50E-06	550
65041	7	4.00E+06	625	9	4.50E+06	5.50E-06	550
70063	7	4.00E+06	625	9	4.50E+06	5.50E-06	550
71111	7	4.00E+06	625	9	4.50E+06	5.50E-06	550

BIBLIOGRAPHY

AASHTO. *AASHTO Guide for the Design of Pavement Structures.* Washington, D.C., 1993.

ABAQUS. *ABAQUS Theory Manual* (6.11), 2011.

ASTM International. Standard Test Method for Repetitive Static Plate Load Tests of Soils and Flexible Pavement Components, for Use in Evaluation and Design of Airport and Highway Pavements. ASTM Standard D1195/D1195M. West Conshocken, PA, 2009.

ASTM International. Standard Test Method for Static Modulus of Elasticity and Poisson's Ratio of Concrete in Compression. ASTM Standard C 469. West Conshocken, PA, 2014.

ASTM International. Standard Test Method for Compressive Strength of Cylindrical Concrete Specimens. ASTM Standard C 39. West Conshocken, PA, 2005.

ASTM International. Standard Test Method for Flexural Strength of Concrete (Using Simple Beam with Third-Point Loading). ASTM Standard C 78. West Conshocken, PA, 2015.

ASTM International. Standard Practice for Making and Curing Concrete Test Specimens in the Laboratory. ASTM Standard C 192. West Conshocken, PA, 2013.

ASTM International. Standard Test Method for Measuring Pavement Macrotexture Depth Using a Volumetric Technique. ASTM Standard E 965. West Conshocken, PA, 2015.

Applied Research Associates (ARA), Inc., ERES Division. *Guide for Mechanistic-Empirical Design of New and Rehabilitated Pavement Structures*. Final Report NCHRP 1-37A. Transportation Research Board of the National Academies, Washington, D.C., 2004.

Bhatti, M.A., Barlow, J.A., and J.W. Stoner. *Modeling Damage to Rigid Pavements Caused by Subgrade Pumping*. ASCE, Journal of Transportation Engineering, Vol. 122, No. 1, Jan-Feb 1996, pp. 12-21.

Christory, J.P. *Assessment of PIARC Recommendations on the Combating of Pumping in Concrete Pavements*. Proceedings of the Second International Workshop on the Design and the Evaluation of Concrete Pavements, Siguenza, Spain, 1990.

De Beer, M. *Erodibility of Cementitious Subbase Layers in Flexible and Rigid Pavements*. Second International Workshop on the Theoretical Design of Concrete Pavements, Siguenza, Spain, 1990.

Dempsey, B.J. *Laboratory and Field Studies of Channeling and Pumping*. Transportation Research Board, Transportation Research Record 849, 1982, pp. 1-12.

DeSantis, J., Vandenbossche, J.M., Alland, K., Sachs, S.G., Burnham, T., and A. Montenegro. *Joint Performance in Bonded Concrete Overlays of Asphalt.* Eleventh International Conference on Concrete Pavements, San Antonio, Texas, 2016.

ERES Consultants, Inc. *Evaluation of unbonded Portland cement concrete overlays.* National Cooperative Highway Research Program Report No. 415, Transportation Research Board, Washington, D.C, 1999.

Harrington, D., Degraaf, D., and R. Riley. *Guide to Concrete Overlay Solutions*. National Concrete Pavement Technology Center (CP Tech Center), Iowa State University, 2007.

Hoegh, K., Lederle, R., and L. Khazanovich. *Use of a Non-Woven Fabric Interlayer to Mitigate Reflective Cracking in an Unbonded Concrete Overlay*. 10th International Conference of Concrete Pavements, Quebec City, Quebec, Canada, 2012.

Janssen, D.J. and M.B. Snyder. *The Temperature-Moment Concept for Evaluating Pavement Temperature Data.* Journal of Infrastructure Engineering. Vol.6, No.2, pp. 81-83, 2000.

Khazanovich, L. *Structural Analysis of Multi-Layered Concrete Pavement Systems.* Ph.D. thesis. University of Illinois, Urbana, 1994.

Khazanovich, L., Yu, H.T., Rao, S., Galasova, K., Shats, E., and R. Jones. *ISLAB2000 - Finite Element Analysis Program for Rigid and Composite Pavements. User's Guide*. ERES Consultants, Champaign, Illinois, 2000.

Larson, G., and B. Dempsey. *Enhanced integrated climatic model version*. University of Illinois, Urbana, IL, 2003.

Maitra, S. R., Reddy, K. S., and L.S. Ramachandra. *Experimental Evaluation of Interface Friction and Study of Its Influence on Concrete Pavement Response*. Journal of Transportation Engineering, 135(8), 563–572, 2009.

Mallela, J., Titus Glover, L., Darter, M.I., Von Quintus, H., Gotlif, A., Stanley, M., and S. Sadasivam. *Guidelines for Implementing NCHRP 1-37A M-E Design Procedures in Ohio: Volume 1— Summary of Findings, Implementation Plan, and Next Steps.* FHWA Report No. FHWA/OJ-2009/9A, pp. 1-112, 2009.

MATLAB and Statistics Toolbox Release 2013a, The MathWorks, Inc., Natick, Massachusetts, United States.

Montgomery, *D. Design and Analysis of Experiments 8th Edition*. John Wiley & Sons, Inc., New York, 2012.

Owusu-Antwi, E.B., Titus-Glover, L., Khazanovich, L., and J.R. Roesler. *Development and Calibration of Mechanistic-Empirical Distress Models for Cost Allocation*. Final Report, Federal Highway Administration, Washington, DC, March 1997.

Packard, R.G. *Design Considerations for Control of Joint Faulting of Undoweled Pavements.* Proceedings of the International Conference on Concrete Pavement Design. Lafayette, IN: Purdue University, 1977.

PIARC Technical Committee on Concrete Roads. *Combating Concrete Pavement Slab Pumping*, 1987.

Rasmussen, R. and S. Garber. *Nonwoven Geotextile Interlayers for Separating Cementitious Pavement Layers: German Practice and US Field Trials.* FHWA, U.S. Department of Transportation. 2009.

Rasmussen, R., and D.K. Rozycki. *Characterization and modeling of axial slab-support restraint*. Transportation Research Record: Journal of the Transportation Research Board, 1778(1), 26–32, 2001.

Ruiz, J. M., Kim, P. J., Schindler, A. K., and R. Rasmussen. *Validation of HIPERPAV for Prediction of Early-Age Jointed Concrete Pavement*. Transportation Research Record: Journal of the Transportation Research Board, 1778(1), 17–25, 2001.

Sachs, S.G., Vandenbossche, J.M., and M.B. Snyder. *Calibration of National Rigid Pavement Performance Models for the Pavement Mechanistic-Empirical Design Guide*. Transportation Research Board, Transportation Research Record 2524, pp. 59-67, 2014.

Simpson, A.L., Rauhut, J.B., Jordahl, P.R., Owusu-Antwi, E.B., Darter, M.I., and R. Ahmad. *Early Analysis of LTPP General Pavement Studies Data, Volume 3: Sensitivity Analyses for Selected Pavement Distresses*. Report SHRP-P-393, Strategic Highway Research Program, Washington, DC, 1994.

Smith, K., Yu, T., and D. Peshkin. *Portland Cement Concrete Overlays: State of the Technology Synthesis*. Federal Highway Administration, 2002.

Titus-Glover, L., Owusu-Antwi, E.B., and M.I. Darter. *Design and Construction of PCC Pavements, Volume III: Improved PCC Performance.* Report No. FHWA-RD-98-113, Federal Highway Administration, Washington, DC, January 1999.

Totsky, O.N. *Behavior of Multi-Layered Plates and Beams on Winkler Foundation* (in Russian). *Stroitel'naya Mekhanika i Raschet Sooruzhenii,* No. 6, Moscow, pp. 54-58, 1981.

Van Wijk, A.J. *Rigid Pavement Pumping: (1) Subbase Erosion and (2) Economic Modeling*. Joint Highway Research Project File 5-10, School of Civil Engineering, Purdue University, West Lafayette, Indiana, May, 16, 1985.

Wu, C.L., Mack, J.W., Okamoto, P.A., and R.G. Packard. *Prediction of Faulting of Joints in Concrete Pavements.* Proceedings, Fifth International Conference on Concrete Pavement Design and Rehabilitation, Vol. 2., Purdue University, West Lafayette, IN, April 1993.

Yu, H.T., Darter, M.I., Smith, K.D., Jiang, J., and L. Khazanovich. *Performance of Concrete Pavements Volume III - Improving Concrete Pavement Performance.* Final Report, Contract DTFH61-91-C-00053, Federal Highway Administration, McLean, VA, 1996.